Technische Universität München
Fakultät für Physik

Abschlussarbeit im Masterstudiengang Kern-, Teilchen- und Astrophysik

Resonance Extraction in Diffractive 3π Production using 190 GeV/c π^- at the COMPASS Experiment (CERN)

Resonanzparameterbestimmung für Diffraktive 3π Produktion mittels 190 GeV/c π^- am COMPASS Experiment (CERN)

Stephan Schmeing

16. Juni 2014

Erstgutachter (Themensteller): Prof. S. Paul
Zweitgutachter: PD Dr. H. Kroha

Contents

Abstract

In this thesis the resonance extraction from the world's largest data sample on diffractively produced $\pi^-\pi^+\pi^-$ final states is presented. The data were collected during the COMPASS 2008 hadron run using an incoming beam of π^- at 190 GeV/c momentum on a proton target. The amount of data allows for the first time a thorough inclusion of the dependence on the squared four-momentum transfer t' in the partial-wave analysis. This novel analysis method on the one hand improves the separation of the resonant and non-resonant contributions to the final state. On the other hand it allows to extract for the first time the t' dependence of individual resonances in great detail.

The resonance extraction was systematically studied in the mass range of $0.9 \leq m_{3\pi} \leq 2.3\,\mathrm{GeV}/c^2$ and in the range of $0.1 \leq t' \leq 1.0\,\mathrm{GeV}^2/c^2$. It has been observed that due to many local solutions reproducible results can only be achieved by performing a large amount of different fits using randomly distributed starting values. To cope with the numerous results a new selection method was developed in order to extract the relevant physical solutions. This is necessary, because the best results that show the lowest deviation from the data in terms of χ^2 lead to partly unphysical parameters.

With this method a set of six selected partial waves based on previous publications and belonging to $J^{PC} = 0^{-+}, 1^{++}, 2^{-+}, 2^{++}$ and 4^{++} have been analysed observing ambiguous solutions. These ambiguities are resolved by increasing the number of included partial waves to a total of 13. With around 68 000 data points and slightly above 620 free parameters this is by far the most extensive analysis performed in this field.

Besides the six established resonances belonging to the studied waves, excitations of the $a_1(1260)$ and $a_2(1320)$ mesons have been observed. Additionally the discovery of a new excited a_1 decaying into $f_0(980)\pi$ from a previous analysis of this data sample could be confirmed, assigning a mass of $m_{a_1(1420)} = 1408\,\mathrm{MeV}/c^2$ and a width of $\Gamma_{a_1(1420)} = 157\,\mathrm{MeV}/c^2$.

Zussamenfassung

In dieser Arbeit wird die Extraktion von Resonanzparametern für die weltweit größte gesammelte Menge an Daten mit diffraktiv erzeugten $\pi^-\pi^+\pi^-$ Endzuständen vorgestellt. Die Daten wurden 2008 während der COMPASS Strahlzeit mittels eines auf ein Ziel aus flüssigem Wasserstoff gerichteten π^- Strahls mit einem Impuls von 190 GeV/c gesammelt. Diese Menge an Daten erlaubt zum ersten Mal eine vollständige Berücksichtigung der Abhängigkeit vom Viererimpulsübertrages t' in der Partialwellenanalyse. Dies ermöglicht einerseits eine bessere Trennung von resonanten und nicht resonanten Beiträgen zum Endzustand und andererseits erstmalig die Extraktion der detaillierten t'-Abhängigkeiten einzelner Resonanzen.

Die Resonanzparameterbestimmung wurde systematisch im Massenbereich von $0.9 \leq m_{3\pi} \leq 2.3\,\mathrm{GeV}/c^2$ und im Impulsübertragsbereich von $0.1 \leq t' \leq 1.0\,\mathrm{GeV}^2/c^2$ untersucht. Es wurde beobachtet, dass aufgrund vieler lokaler Lösungen reproduzierbare Ergebnisse nur mittels einer großen Anzahl von Wiederholungen der Parameteranpassung mit zufällig verteilten Startwerten erreichbar sind. Um die vielen Lösungen bewältigen zu können wurde ein neuartige Auswahlmethode entwickelt, die die relevanten physikalischen Lösungen auswählt. Dies ist notwendig, weil die am besten zu den Daten passenden Lösungen zum Teil nicht-physikalische Resonanzparameter aufweisen.

Mit dieser Methode wurden sechs Partialwellen mit $J^{PC} = 0^{-+}, 1^{++}, 2^{-+}, 2^{++}$ und 4^{++} untersucht, wobei für diesen auf früheren Publikationen basierenden Satz an Wellen mehrdeutige Lösungen gefunden wurden. Diese Mehrdeutigkeit konnte mittels einer Erweiterung auf insgesamt 13 verwendete Wellen aufgelöst werden, was zu der mit ungefähr 68 000 Datenpunkten und etwas über 620 freien Parametern mit Abstand umfangreichsten Analyse in diesem Feld führte.

Neben den sechs zu den untersuchten Wellen gehörenden etablierten Resonanzen, wurden auch angeregte Zustände des $a_1(1260)$ und $a_2(1320)$ Mesons beobachtet. Weiterhin konnte die Entdeckung eines neuen, bisher unbekannten angeregten a_1, welches in $f_0(980)\pi$ zerfällt, aus einer vorangegangenen Analyse dieser Daten bestätigt werden. Es wurden eine Masse von $m_{a_1(1420)} = 1408\,\mathrm{MeV}/c^2$ und eine Breite von $\Gamma_{a_1(1420)} = 157\,\mathrm{MeV}/c^2$ gemessen.

Chapter 1

Introduction

1.1 The light meson sector

Despite the fact that in the discovery rush from the late 1940's to the 1960's light mesons[1], meaning those containing only u,d and s quarks, were one of the first unstable hadrons observed by cosmic ray and accelerator experiments, there remain quite a lot of unanswered questions. This is due to exactly the same reason as the early discovery of light mesons: The small mass of their constituents.

While with the development of the **Q**uantum **C**hromo**D**ynamics (QCD) in the 1960's and the discovery of the asymptotic freedom in the early 1970's high-energy reactions could be well described, QCD perturbation theory breaks down for low energies corresponding to long distances. For mesonic systems that contain at least one heavy quark, like the c or the b, a non-relativistic description in terms of potentials is quite a good approximation, but for light mesons more complex models and calculations are needed. More on this topic can be found in section 1.1.2.

With all the success in high-energy reactions and the heavy-quark systems, the light-meson sector became more or less neglected until its revival around the turn of the millennium due to the observation of mesons with potentially gluonic degrees of freedom by several experiments like BNL852, e.g. [2], and VES, e.g. [3]. Even though these candidates were found, they are still strongly disputed, since there are quite heavy disagreements in between experiments and even in between different publications from the same experiment. After a short discussion of mesonic models, where the relevant quantum numbers are introduced, this topic will be further discussed in section 1.1.3.1.

1.1.1 Constituent Quark Model

The simplest mesonic model is the constituent quark model, developed independently by Gell-Mann and Zweig (see [4–6]), where the meson is a bound system of a quark-antiquark pair. Each quark has a charge of either $^2/_3$ or $-^1/_3$ and each antiquark has a charge of either $-^2/_3$ or $^1/_3$, so the bound system always has an integer charge between -1 and 1. Both quark and antiquark are fermions with a spin of $\frac{1}{2}$. The total intrinsic spin of the

[1] For the sake of a short introduction a basic knowledge of terminology in particle physics will be supposed. In case needed please refer to standard textbooks like [1].

system can therefore be either $S = 0$ or $S = 1$ with up to three different spin projections S_z:

$$\begin{aligned} \frac{1}{\sqrt{2}}(|\uparrow\downarrow\rangle - |\downarrow\uparrow\rangle) \quad & S = 0 \quad S_z = 0 \\ \frac{1}{\sqrt{2}}(|\uparrow\downarrow\rangle + |\downarrow\uparrow\rangle) \quad & S = 1 \quad S_z = 0 \\ |\uparrow\uparrow\rangle \quad & S = 1 \quad S_z = +1 \\ |\downarrow\downarrow\rangle \quad & S = 1 \quad S_z = -1 \end{aligned}$$

The coupling of the total spin S with the relative orbital angular momentum L between the quarks results in the total angular momentum J of the quark-antiquark pair, which is normally referred to as the spin of the meson:

$$|L - S| \leq J \leq L + S$$

Combining the positive intrinsic parity of the quark with the negative one of the antiquark and multiplying the parity of the spatial wave function the total parity P of the $q\bar{q}$-state is:

$$P = (+1)(-1)(-1)^L = (-1)^{L+1}$$

The naturality η is defined to be $\eta = +1$ for natural spin-parity $P = (-1)^J$ and $\eta = -1$ in case of $P = (-1)^{J+1}$. This results in:

$$\eta = P(-1)^J \tag{1.1}$$

Its further importance will be discussed with the introduction of the reflectivity in section 3.1.

The C-parity is strictly only defined for eigenstates under charge-conjugation, which are in the case of light mesons the neutral states with the third component of the isospin $I_3 = 0$, but by convention the whole isospin triplets are assigned the C-parity of their $I_3 = 0$ state:

$$C = (-1)^{L+S}$$

For example the π^- is therefore assigned the C-parity $C = +1$ of the π^0, because it is part of the π isospin triplet with $l = 0$ and $S = 0$.

A more proper way to handle the charged light mesons is to define a new operation called G-parity, which is the charge-conjugation followed by a charge flip realised via a rotation by 180° around the y-axis in isospin-space:

$$G = C \cdot e^{i\pi I_2} = (-1)^{L+S+I}$$

Since the rotation in isospin-space only works for mesons made of u and d quarks as intended, only for these mesons the G-parity is a good quantum number. However, flavour-neutral combinations of strange, charm or bottom mesons can also be eigenstates of the G-parity. Therefore strong decays, like e.g. $\phi(1020) \to K\overline{K}$, still conserve G-parity.

With this formulae the possible quantum numbers for mesons in the constituent quark model can be calculated as shown in table 1.1, leaving the following combinations of J^{PC} that are not allowed in this simple model and therefore denoted as spin-exotic:

$$J^{PC} = 0^{--}, \text{even}^{+-}, \text{odd}^{-+}$$

L	S	J	I	$I^G J^{PC}$	nomenclature
0	0	0	0	0^+0^{-+}	η
			1	1^-0^{-+}	π
	1	1	0	0^-1^{--}	ω
			1	1^+1^{--}	ρ
1	0	1	0	0^-1^{+-}	h_1
			1	1^+1^{+-}	b_1
	1	0	0	0^+0^{++}	f_0
			1	1^-0^{++}	a_0
		1	0	0^+1^{++}	f_1
			1	1^-1^{++}	a_1
		2	0	0^+2^{++}	f_2
			1	1^-2^{++}	a_2
2	0	2	0	0^+2^{-+}	η_2
			1	1^-2^{-+}	π_2
	1	1	0	0^-1^{--}	ω
			1	1^+1^{--}	ρ
		2	0	0^-2^{--}	ω_2
			1	1^+2^{--}	ρ_2
3	1	2	0	0^+2^{++}	f_2
			1	1^-2^{++}	a_2

Table 1.1: Possible quantum numbers for mesons in the constituent quark model for a spin $J \leq 2$.

1.1.2 Quantum Chromodynamics

The constituent quark model is very successful describing most mesons, but measurements of the current masses of light quarks show that these masses are negligible compared to the quark masses, which are assigned in the constituent quark model. This deviation points to the fact that the meson masses are dominated by non-perturbative dynamics of the gluonic field. In order to describe the dynamics inside the meson more realistically a description based on QCD is needed. However, a perturbative treatment is in this case impossible and therefore either an effective model has to be build out of the QCD or it has to be calculated numerically.

At the beginnings of numerical QCD calculations missing processing power prevented quantitative results, but inspired from their qualitative achievements the flux-tube model was proposed in the 1980 [7, 8]. In this model a tube-shaped gluonic field of constant energy density, the flux-tube, connects the quark and the antiquark. Since the effects of virtual quark-antiquark pairs are neglected the model is considered a phenomenological approximation.

One of the important effects of the flux-tube is that it can be excited and therefore adds additional freedom to the possible quantum numbers, so all J^{PC} combinations, including the exotic ones, which are forbidden in the constituent quark model, can be achieved.

With the flux-tube in its ground state the spectrum from the constituent quark model is reproduced. The new mesonic states with an excited gluonic field configuration are called hybrids.

However, in the flux-tube model there exists not only the possibility to connect the quarks by a flux-tube, but also the possibility to close the flux-tube onto itself and completely leave out the quarks. These mesons are called glueballs, but have not yet been observed. The reason for the uncertainty of their existence is simply that for the lightest predicted glueballs the J^{PC} quantum numbers are not exotic and therefore not easily distinguishable from constituent quark states. Despite its nice features recent studies showed that, when this model is applied to light quarks, the flux-tube breaks down because of pion production out of the vacuum [9].

However, due to the technological improvements of the last 30 years numerical calculations from first principles are now possible in the framework of lattice QCD [10]. These computing power intense calculations are done on an euclidean space-time grid with lattice spacing a. In the limit of $a \to 0$ continuum field theory is reached, but since the required processing power is proportional to a^{-6} the grid is as coarse as possible [11], being, for example, in the case of the calculation shown in figure 1.1 $a = 0.12\,\text{fm}$.

The current computing power also limits the number of quark-antiquark loops that can be included. In order to reduce these the mass of the quarks is increased artificially. As a reference on how close masses are to the physical point the pion mass is used. This is as an example $m_\pi = 396\,\text{MeV}/c^2$ for the recent calculation [12] shown in figure 1.1. Even if the masses do not correspond to the physical masses the light-meson spectrum is reproduced quite well and predictions should be taken seriously.

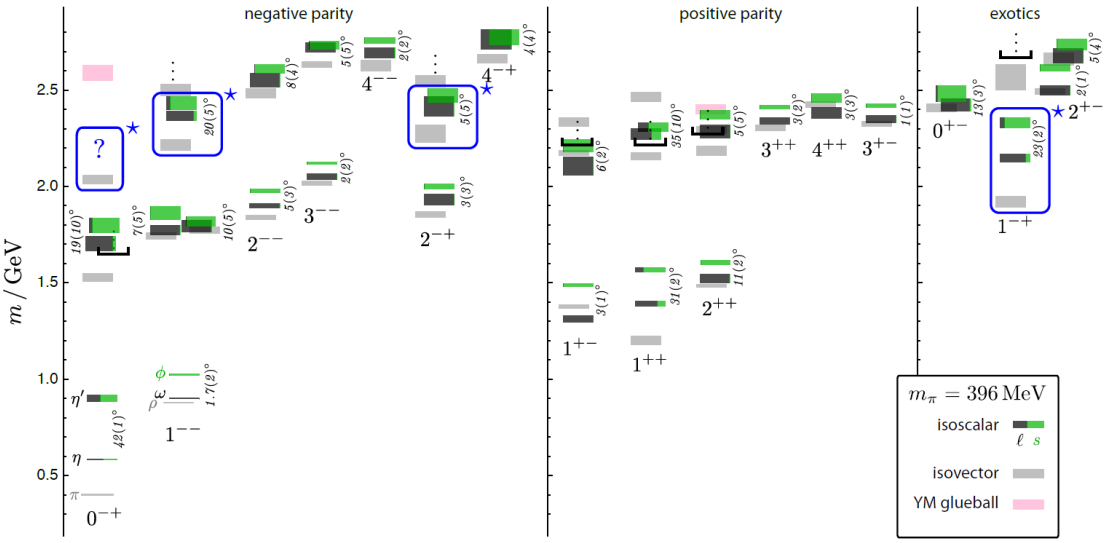

Figure 1.1: Light-meson spectrum from lattice QCD calculations [12].

One of this predictions is, for example, that the lightest hybrid super-multiplet[2] with

$$J^{PC} = 0^{-+}, 1^{--}, 2^{-+}, 1^{-+}$$

includes as the lightest spin-exotic the heavily disputed isovector $\pi_1(1600)$ (see section 1.1.3.1).

However, lattice QCD currently assumes that all states are stable and therefore does not give any information on decay widths or branching ratios between decays.

1.1.3 Open Questions

1.1.3.1 Confirmation or Falsification of Resonances

With all the predicted states from models and lattice QCD calculations, precise experimental measurements with a good handle on the systematics become more and more important. Currently there are 178 light unflavoured mesons listed in the Review of Particle Physics [13] of which only 47 are confirmed. This is partly due to the complexity of the analysis needed to disentangle the resonances, but also due to a strong dependence on the model used to describe the measured data.

A good example for both is again the search for the spin-exotic $\pi_1(1600)$ in diffractive-dissociation data of the $\pi^-\pi^+\pi^-$ final state. In this channel the first observation was done by BNL E852 seeing a clear peak at $1.6\,\mathrm{GeV}/c^2$ (see figure 1.2a [2]). Later the same collaboration published a result with an extended analysis model, where the spin-exotic state is not visible anymore (see black markers in figure 1.2b [14]). Then the VES group confirmed the $\pi_1(1600)$ again, but did see a broad structure instead of a narrow peak (see figure 1.2c [15]) and finally the COMPASS collaboration claimed to see a resonant structure with a mass of $1.66\,\mathrm{GeV}/c^2$ (see figure 1.2d [16]).

1.1.3.2 Nature of States

An even more complex question than the existence of a state is to determine its inner structure. A convincing answer on whether and to what degree a state is a simple quark-antiquark system, a hybrid, a glueball or something else can only be given by a matching of theoretical decay predictions and experimental data, but at the moment for most states theory as well as experiment are lacking the necessary precision by far. So all current discussions on this topic have to be seen as hints on whether a model or calculation is favoured or disfavoured by the data, which help to improve understanding and thereby the theoretical and experimental work.

Here the already addressed search for spin-exotic mesons, like the $\pi_1(1600)$, is crucial to confirm or falsify the constituent quark model. However, there are also intense studies in the region of non-exotic quantum numbers. A hot hybrid candidate is the $\pi_2(1880)$ since its closeness to the $\pi_2(1670)$ makes an explanation as a radial excitation unlikely.

[2] The term 'super-multiplet' is historical and denotes a grouping of ordinary flavour multiplets of a given J^{PC} to a bigger one with the same modes of excitation, e.g. all multiplets with $L = 2$. Assuming perfect flavour, spin and isospin symmetry they are supposed to have the same mass.

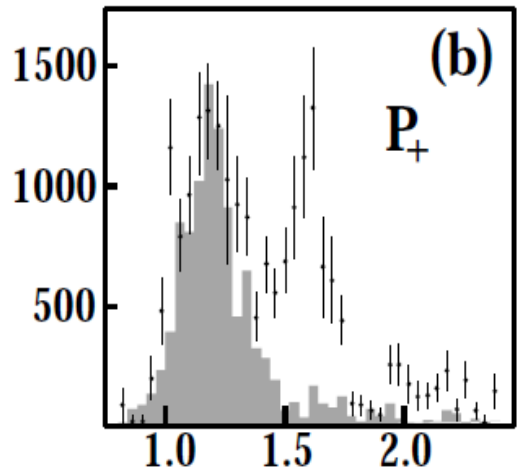

(a) BNL E852 [2]

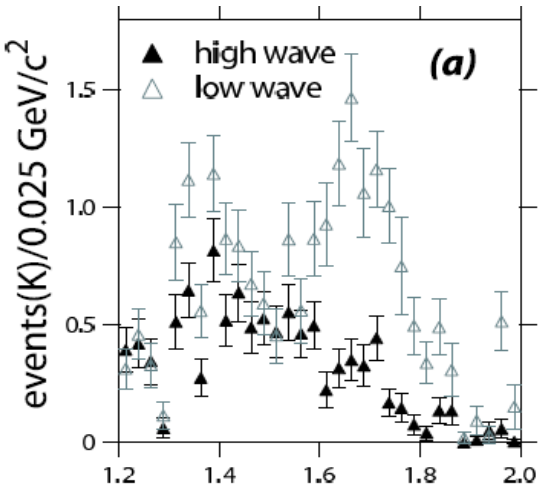

(b) BNL E852 [14]

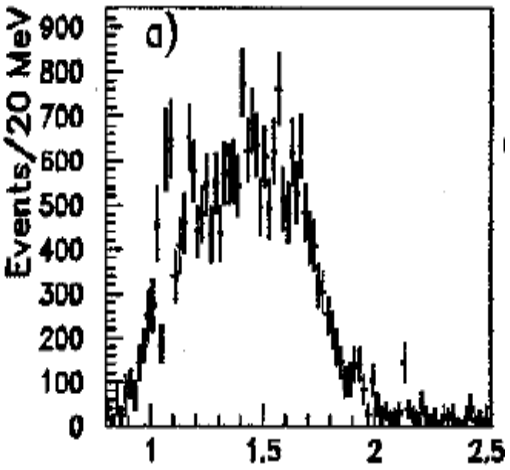

(c) VES [15]

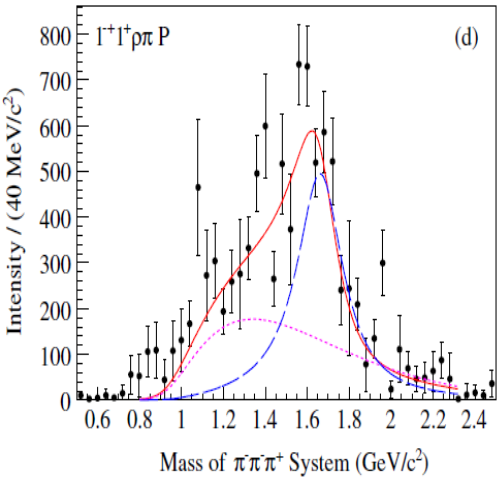

(d) COMPASS [16]

Figure 1.2: Overview of analyses investigating the spin-exotic $J^{PC} = 1^{-+}$ meson $\pi_1(1600)$ in the $\pi^-\pi^+\pi^-$ channel [17].

Alternatively [18] proposed that both resonances are just a different manifestation of the same resonance shifted by an interference effect.

For a further discussion of the potential of diffractive dissociation into the $\pi^-\pi^+\pi^-$ final state at COMPASS refer to section 1.3.3. For a detailed report on the current status of hybrid and glueball searches in general please refer to [19].

1.2 The COMPASS Experiment at CERN

In order to contribute to, amongst others, the open questions discussed in the previous section the **CO**mmon **M**uon and **P**roton **A**pparatus for **S**tructure and **S**pectroscopy (COMPASS), was set up at the M2 beam line of the **S**uper **P**roton **S**ynchrotron (SPS) at CERN. It is a high-luminosity fixed-target experiment dedicated to study the structure and dynamics of hadrons in the non-perturbative regime of QCD. While here only a short overview is given, the spectrometer is discussed in more detail in section 2.1.

In the meson sector the collaboration uses, for example, inverse kinematics for Compton scattering with virtual photons called Primakoff reactions to study the hadronic structure of unstable particles [20–22]. Furthermore central production [23, 24] and diffractive scattering of mesons on nuclei are used in order to investigate gluonic states, like hybrids and glueballs [16, 25, 26]. For additional information on the physics program please refer to [27–29]. The case of diffractive dissociation into $\pi^-\pi^+\pi^-$ is explained further in section 1.3 and analysed in chapter 3, 4 and 5.

Due to COMPASS origin as a merging of two separately proposed experiments, HMC [30] for structure measurements with muons and CHEOPS [31] for hadron spectroscopy, it can measure with various beams and targets. For example a positive muon beam is used for spin physics, a positive hadron beam for central production and a negative hadron beam for diffractive dissociation analysed in this thesis. COMPASS started data taking in 2002, but except of a two-week pilot run using a lead target in 2004 (see [16] for results) the first hadron-beam data were collected in 2008 on a 40 cm long liquid hydrogen target. The energy of the negative secondary hadron beam was $E_{\text{Lab}} \approx 190\,\text{GeV}$, corresponding to a centre-of-mass energy of $\sqrt{s} \approx 20\,\text{GeV}$.

1.3 Diffractive Dissociation of Pions at 190 GeV

This thesis analyses the diffractive dissociation of a beam π^- on a proton into the $\pi^-\pi^+\pi^-$ final state in the 2008 COMPASS data, thereby continuing the work of [17]. Similar analyses are also in progress for other final states, in example for the isospin-partner $\pi^-\pi^0\pi^0$ [32].

Diffractive dissociation denotes the soft scattering of a beam particle on a target particle resulting in an excitation of the beam followed by its decay into the final state. In the case of this analysis the beam particle is a π^- and the target particle is a proton. During the scattering process the π^- is assumed to get excited into an intermediate state X^-, which dissociates into the $\pi^-\pi^+\pi^-$ final state. A schematic drawing of this $\pi^- p \to \pi^-\pi^+\pi^- p_{\text{recoil}}$ process is shown in figure 1.3.

That X^- is dominated by resonances is one of the few necessary assumptions, since it allows to factorise the production from the decay. Furthermore isospin and G-parity are

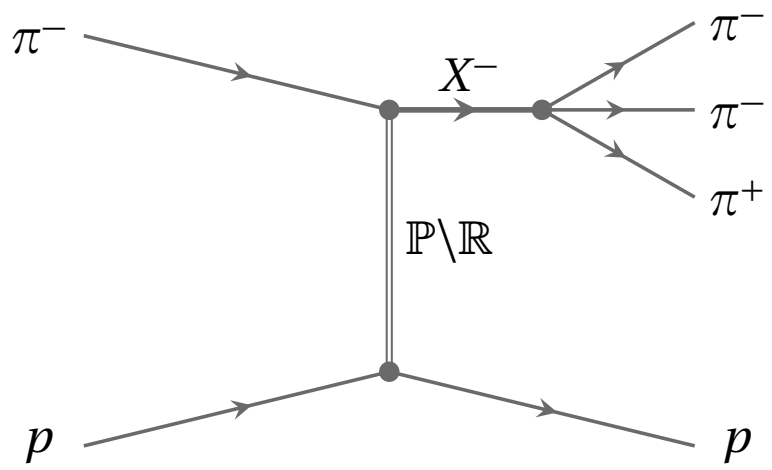

Figure 1.3: Schematic drawing of single-diffractive dissociation of π^- into $\pi^-\pi^+\pi^-$ on a proton target [17].

assumed to be conserved in the interaction vertices. The only other assumptions, being the isobar model in combination with no final state interaction and the used wave sets, will be explained in section 3.1.

The four-momentum of the intermediate state is calculated from the four-momenta of the final-state pions:

$$p_X = \sum_{i=1}^{3} p_{\pi,i}$$

The invariant mass is then calculated from the four-momentum:

$$m_X^2 = m_{3\pi}^2 = \frac{p_X^2}{c^2}$$

The extraction of resonance parameters, which will be described in chapter 4, is performed in the range of:

$$0.9 \leq m_X \leq 2.3\,\mathrm{GeV}/c^2$$

The squared four-momentum transfer t from the beam to the recoil particle is calculated as following:

$$t = (p_{\pi_{\mathrm{beam}}} - p_X)^2 < 0$$

Even for zero scattering angles, meaning forward scattering of the pion, t has a small deviation from zero, which is needed to excite the beam particle to a mass m_X. Since this minimal momentum transfer is purely due to kinematics and therefore clouds the information on the physics of the production mechanism, it is usually subtracted:

$$t' \equiv |t| - |t|_{\mathrm{min}} \geq 0$$

However, $|t|_{\mathrm{min}}$ is typically well below $10^{-3}\,\mathrm{GeV}^2/c^2$ and the range of analysed four-momentum transfer in this thesis is:

$$0.1 \leq t' \leq 1.0\,\mathrm{GeV}^2/c^2$$

Therefore to a very good approximation:

$$t' \approx |t|$$

In the observed region of diffractive scattering, where the centre-of-mass energy is much larger than the squared four-momentum transfer, Regge theory predicts the strong interaction to be dominated by Pomeron exchange, which is interpreted as a long-range gluonic interaction. With the RRE_{nf} parametrisation from [33] the percentage of Pomeron exchange was estimated by [34] to be 85%. In any case the true nature of the exchange does not matter to the analysis and only the conservation of G-parity and isospin mentioned above is crucial. A couple of quantum numbers consistent with Pomeron exchange are used in the analysis, but all of them are well backed by the data. Still some brief information on the production mechanism and references to further readings will be provided for interested readers in the following subsection.

1.3.1 The Pomeron

The basic idea of Regge physics is that not just a single particle is exchanged like the pion in Yukawa's theory [35], but in principle infinitely many. This sum of infinitely many particles that are exchanged in the same interaction is called a Regge trajectory or simply Reggeon. For a mathematical description of these trajectories Regge continued the angular momentum into the complex plane [36]. This interpolation can only be unique if the trajectories are split into even- and odd-signatured ones, which means that they contain only particles with even or odd angular momentum L.

This finally results in Regge trajectories containing families of bound states, where the total angular momentum J rises in steps of 2, e.g. $\{a_2(1320), a_4(2040), \dots\}$ or $\{\rho(770), \rho_3(1690), \dots\}$. These trajectories are visualised in the so-called Chew-Frautschi plot shown in figure 1.4.

Later it was shown that the so-called Sommerfeld-Watson transform, which transforms the sum over all particles on a trajectory in an integral over the complex angular momentum plane, made it possible to do an analytical continuation from the formation-experiment channel to the high-energy diffractive-scattering channel, studied in this thesis. In the Chew-Frautschi plot (see figure 1.4) this means to continue the approximately linear Regge trajectories to negative values of the squared mass, which of course only make sense if the interpretation is changed from a squared mass to the squared four-momentum transfer t.

Comparing the predictions from Regge theory for the total cross section $\sigma_{\text{tot}}(s)$ in scattering experiments with real data it was found that in theory $\sigma_{\text{tot}}(s)$ falls with rising centre-of-mass energy $\sqrt{s}$, but in reality it rises. To explain this behaviour an until then unknown trajectory with an intercept slightly above 1 was introduced.

This trajectory is called Pomeron trajectory or simply Pomeron [37]. In comparison to normal Regge trajectories it has a much lower slope. Bound states on this trajectory have to carry the quantum numbers of the vacuum, so they have to be flavourless hadrons with even parity and C-parity as well as positive naturality [38].

Up to now no state was found to lie on that trajectory. However, the still doubted $f_2(1910)$ with $J^{PC} = 2^{++}$ is a possible candidate [39] and support comes from lattice QCD

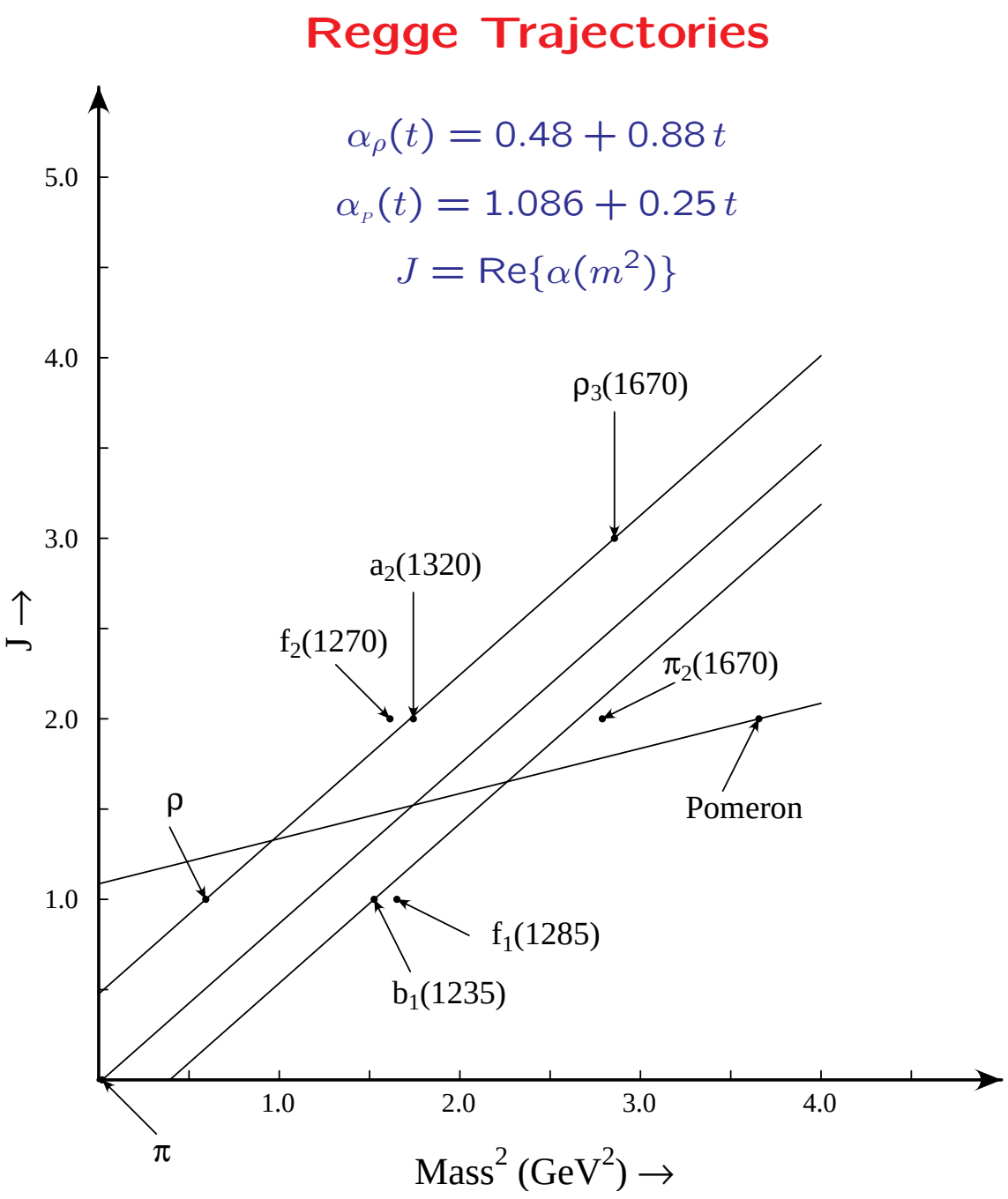

Figure 1.4: Mesonic Regge trajectories [34].

calculations predicting a glueball with $J^{PC} = 2^{++}$(see figure 1.1), but a real matching between lattice QCD and measurements is only possible if branching ratios for decays at physical masses can be predicted.

However, the $f_2(1910)$ cannot be observed in this analysis due to its quantum numbers. For further details please refer to section 1.3.3. In general the derivation of Regge theory from QCD is still an open question. For a more thorough introduction to Regge physics please refer to [39].

1.3.2 Alternative Production Mechanisms

After this short excursion on Regge theory and the Pomeron a for this thesis more relevant aspect has to be discussed. Besides the quasi-elastic scattering via Pomeron exchange also alternative production mechanism occur. One of them is the so-called Deck-effect [40] shown in figure 1.5. It denotes a decay of an incident high-energy beam pion into a $\pi^+\pi^-$ resonance and a single pion, followed by a quasi-elastic scattering of either the 2π resonance or the pion on the proton. Since this non-resonant production of a 3π final state can so far not be separated and does not have well-defined quantum numbers it ends up in the analysis as a broad background beneath the resonances.

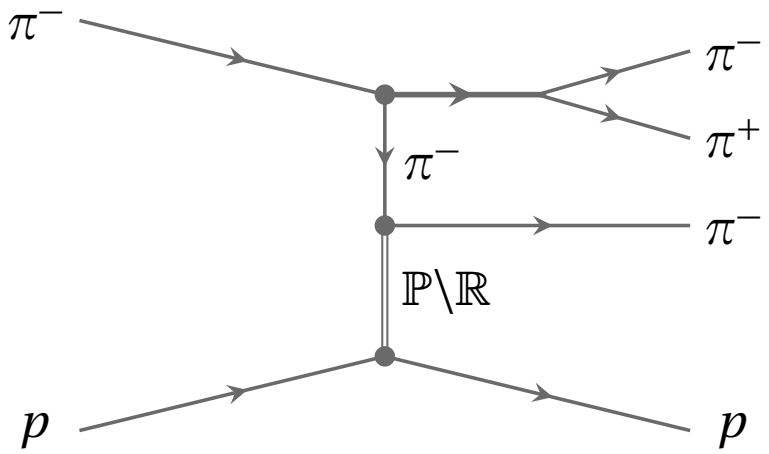

Figure 1.5: Schematic drawing of one possible amplitude for the Deck-effect in π^- into $\pi^-\pi^+\pi^-$ reactions [17].

An on the level of event selection (section 2.2) mostly separable production mechanism is the so-called central production shown in figure 1.6 as one case of multi-Regge exchange[3].

1.3.3 Observables at COMPASS

Using the previously explained production mechanism via a Pomeron with $I^G = 0^+$ the potential of diffractive dissociation into 3π at 190 GeV can be evaluated. The π^- beam has

[3] The Deck-effect is in some sense a special case of multi-Regge exchange, but it depends on the used model, whether it is truly multi-Regge.

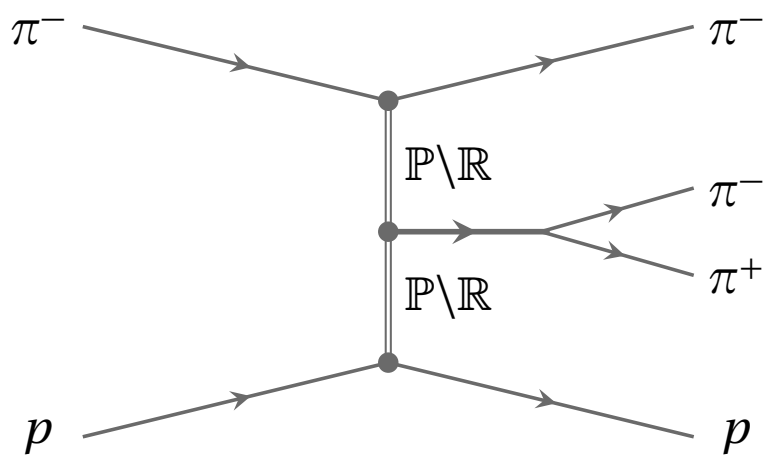

Figure 1.6: Schematic drawing of central production as one case of multi-Regge exchange [17].

$I^G = 1^-$ and isospin as well as G-parity are conserved in strong interactions. Therefore the resonance X^- also has to have $I^G = 1^-$.

This part can also be reconstructed from the $\pi^-\pi^+\pi^-$ final state, thereby omitting the quantum numbers of the Pomeron. In this case the calculation of the G-parity is similar:

$$G(X^-) = G(\pi)^3 = (-1)^3 = -1$$

However, for the isospin it has to be considered that the three observed pions have a total charge of -1. This can only be achieved if the resonance is at least part of an isospin triplet. Since flavour-exotic mesons with isospin $I = 2$ have not been observed so far, $I = 1$ can be assumed.

Independent on how it has been determined $I^G = 1^-$ directly results in $C = +1$ for the neutral member of the isospin triplet, since:

$$\begin{aligned} & G = (-1)^{L+S+I} = C \cdot (-1)^I \\ \Rightarrow \quad & -1 = C \cdot (-1) \\ \Leftrightarrow \quad & C = +1 \end{aligned}$$

A direct calculation via $C(X^-) = C(\pi^-) \cdot C(\mathbb{P}) = (+1) \cdot (+1) = +1$ is not valid, because the π^- is not a C-parity eigenstate.

To calculate the producible J^P quantum numbers of the resonance X^- takes a little more effort. Using $J^{PC} = 0^{-(+)}$ of the beam pion and, for example, $J^{PC} = 2^{++}$ as the dominant quantum numbers of the Pomeron trajectory the total spin S is:

$$\begin{aligned} & |J(\pi^-) - J(\mathbb{P})| \leq S \leq J(\pi^-) + J(\mathbb{P}) \\ \Leftrightarrow \quad & |0 - 2| \leq S \leq 0 + 2 \\ \Leftrightarrow \quad & S = 2 \end{aligned}$$

L	$J^P(X^-)$
0	2^-
1	$1^+, 2^+, 3^+$
2	$0^-, 1^-, 2^-, 3^-, 4^-$
3	$1^+, 2^+, 3^+, 4^+, 5^+$
4	$2^-, 3^-, 4^-, 5^-, 6^-$

Table 1.2: Possible J^P quantum numbers of 3π resonance X^- for angular momentum $L \leq 4$.

This has to be combined with the possible angular momentum L between both particles:

$$|L - S| \leq J(X^-) \leq L + S$$

The parity for this state is then:

$$P(X^-) = P(\pi^-) \cdot P(\mathbb{P}) \cdot (-1)^L = (-1) \cdot (+1) \cdot (-1)^L = (-1)^{L+1}$$

The possible J^P up to $L = 4$ are listed in table 1.2.

It is obvious that in principle all J^P quantum numbers except 0^+ can be produced, which is not altered by choosing other allowed quantum numbers for the Pomeron. In terms of observable states this means that all a_J and π_J except a_0 are possible. Though the a_0 decay into 3π is forbidden by conservation of angular momentum and parity [41] it is also not observed in its dominant decay into $\pi^-\eta$ [25], which further supports this production mechanism.

Table 1.3 is an overview on all observed states as given in [13], which can in principle be studied in this analysis. Of course it is obvious that due to the high number only a part of them will be studied in this thesis.

1.3.4 Overview on the analysis procedure

In order to extract the resonance parameters of the intermediate state X^- first the data corresponding to diffractive dissociation into the $\pi^-\pi^+\pi^-$ final state are selected (chapter 2) and then they are binned in the invariant mass $m_{3\pi}$ and the squared four-momentum transfer t' as well as separated into partial waves (chapter 3). Finally the resonance parameters are determined from the $m_{3\pi}$ mass dependence in a combined fit of all t' bins and a selected sub set of partial waves (chapter 4).

The new thorough inclusion of the four-momentum transfer t' into the analysis provides for the first time at the level of resonance extraction a good handle on the separation of the single diffractive dissociation from alternative production processes, which is an open problem since the 1960's. This significantly reduces the model dependence and thereby increases the precision of the measurement. Furthermore it allows for the first time to study the t' dependences for individual resonances (chapter 5).

However, with the huge amount of COMPASS 2008 data and thereby strongly reduced statistical errors the systematic effects dominate the precision of the measurement and therefore have to be studied extensively. In the scope of this thesis this is done at the level

Particle	$I^G J^{PC}$	Mass[MeV/c^2]	Width[MeV/c^2]	Status
$\boldsymbol{a_1(1260)}$	1^-1^{++}	1230 ± 40	250 to 600	Established
$a_1(1640)$	1^-1^{++}	1647 ± 22	254 ± 27	Omitted from Summary
$a_1(1930)$	1^-1^{++}	$1930\,^{+30}_{-70}$	155 ± 45	Further
$a_1(2095)$	1^-1^{++}	$2096 \pm 17 \pm 121$	$451 \pm 41 \pm 81$	Further
$a_1(2270)$	1^-1^{++}	$2270\,^{+55}_{-40}$	$305\,^{+70}_{-40}$	Further
$\boldsymbol{a_2(1320)}$	1^-2^{++}	$1318.3\,^{+0.5}_{-0.6}$	107 ± 5	Established
$a_2(1700)$	1^-2^{++}	1732 ± 16	194 ± 40	Omitted from Summary
$a_2(1950)$	1^-2^{++}	$1950\,^{+30}_{-70}$	$180\,^{+30}_{-70}$	Further
$a_2(1990)$	1^-2^{++}	$2050 \pm 10 \pm 40$	$190 \pm 22 \pm 100$	Further
		$2003 \pm 10 \pm 19$	$249 \pm 23 \pm 32$	
$a_2(2030)$	1^-2^{++}	2030 ± 20	205 ± 30	Further
$a_2(2175)$	1^-2^{++}	2175 ± 40	$310\,^{+90}_{-45}$	Further
$a_2(2255)$	1^-2^{++}	2255 ± 20	230 ± 15	Further
$a_3(1875)$	1^-3^{++}	$1874 \pm 43 \pm 96$	$385 \pm 121 \pm 114$	Further
$a_3(2030)$	1^-3^{++}	2031 ± 12	150 ± 18	Further
$a_3(2275)$	1^-3^{++}	2275 ± 35	$350\,^{+100}_{-50}$	Further
$\boldsymbol{a_4(2040)}$	1^-4^{++}	$1996\,^{+10}_{-9}$	$255\,^{+28}_{-24}$	Established
$a_4(2255)$	1^-4^{++}	2237 ± 5	291 ± 12	Further
		2255 ± 40	$330\,^{+110}_{-50}$	
$a_6(2450)$	1^-6^{++}	2450 ± 130	400 ± 250	Omitted from Summary
$\boldsymbol{\pi(1300)}$	1^-0^{-+}	1300 ± 100	200 to 600	Established
$\boldsymbol{\pi(1800)}$	1^-0^{-+}	1812 ± 12	208 ± 12	Established
$\pi(2070)$	1^-0^{-+}	2070 ± 35	$310\,^{+100}_{-50}$	Further
$\pi(2360)$	1^-0^{-+}	2360 ± 25	$300\,^{+100}_{-50}$	Further
$\boldsymbol{\pi_1(1400)}$	$\boldsymbol{1^-1^{-+}}$	1354 ± 25	330 ± 35	Established
$\boldsymbol{\pi_1(1600)}$	$\boldsymbol{1^-1^{-+}}$	$1662\,^{+8}_{-9}$	241 ± 40	Established
$\pi_1(2015)$	$\boldsymbol{1^-1^{-+}}$	$2014 \pm 20 \pm 16$	$230 \pm 32 \pm 73$	Further
		$2001 \pm 30 \pm 92$	$333 \pm 52 \pm 49$	
$\boldsymbol{\pi_2(1670)}$	1^-2^{-+}	1672.2 ± 3.0	260 ± 9	Established
$\boldsymbol{\pi_2(1880)}$	1^-2^{-+}	1895 ± 16	235 ± 34	Established
$\pi_2(2005)$	1^-2^{-+}	$1974 \pm 14 \pm 83$	$341 \pm 61 \pm 139$	Further
		2005 ± 15	200 ± 40	
$\pi_2(2100)$	1^-2^{-+}	2090 ± 29	625 ± 50	Omitted from Summary
$\pi_2(2285)$	1^-2^{-+}	$2285 \pm 20 \pm 25$	$250 \pm 20 \pm 25$	Further
$\pi_4(2250)$	1^-4^{-+}	2250 ± 15	215 ± 25	Further

Table 1.3: Parameters of already observed 3π resonances as given in [13], which can be studied at COMPASS. If entries are bold in the first column they are established states and if they are bold in the second column they have exotic quantum numbers. States with unknown quantum numbers are omitted.

of resonance extraction. Since this thesis presents the first resonance extraction performed with the improved analysis framework and the first extraction from the COMPASS 2008 data sample, which allows to study the whole spectrum in unprecedented detail, it will concentrate on the sectors with rather well-established ground-states, being a_1, a_2, a_4, π_2 and to some extend π.

Chapter 2

Event Selection

As a first step of any analysis the events of interest have to be filtered out of the huge amount of data taken. This chapter describes the selection criteria applied in [17], after giving a short overview on the COMPASS Spectrometer, which helps understanding the choices in the event selection.

2.1 The COMPASS Spectrometer

To meet all the requirements from the different experimental areas the COMPASS spectrometer needs a large and uniform acceptance over a wide kinematic range, good kinematic reconstruction capabilities and the ability to measure extremely small scattering angles. In order to achieve this it has been designed as a two-stage magnetic spectrometer. Since this thesis will focus on the final step of the data analysis, where most issues concerning apparatus effects are already accounted for, the further discussion of the experimental setup will be very brief. For additional information please refer to the technical reports [42, 43].

In order to create the secondary beam, that will later be focused on the COMPASS target, the intense primary proton beam with $E_{\text{Lab}} \approx 400\,\text{GeV}$ from the SPS is focused onto a Beryllium production target of a length of up to 500 mm. Various targets with different length can be used to fit the secondary beam intensity to the experimental needs. For the 2008 hadron run the highest possible intensity was desired, because of the large amount of data needed to disentangle the complex contributions to the hadronic spectrum. Therefore the maximum of 500 mm has been chosen for the target length, resulting in an average beam intensity of $5 \cdot 10^6\,\text{s}^{-1}$ [43] producing in total over 1 PB of data per year [44]. After the production target the secondary beam is collimated and the desired momentum range is filtered in an approximately 1 km long beam line using several magnets.

In front of the target two Cherenkov counters were installed to distinguish the different beam-particle species. A silicon tracking telescope is used to measure the direction of the beam particles. Their momenta have to be reconstructed from the outgoing final-state particles. In order to ensure exclusivity of the measured reactions a **R**ecoil **P**roton **D**etector (RPD) consisting of two concentric barrels of scintillators was build around the target.

Behind the target a 50 m long two-stage spectrometer is positioned for tracking and calorimetry at forward angles. A schematic view of it is shown in figure 2.1. The spectrometer has a wide angular acceptance of $\Delta\Theta = \pm 180\,\text{mrad}$ and a large overall acceptance $\times$ reconstruction efficiency of about 50% for the complete reconstruction of an event with three charged tracks over a wide range in $m_{3\pi}$ and four-momentum transfer t' (see [17, 45]).

The particle tracking close to the beam (2.5 to 20 cm radial distance) was done by so-called **S**mall-**A**rea **T**rackers (SAT) consisting of Micromegas[1] and GEM[2] detectors due to their high-rate capabilities. For regions further away from the beam axis with lower rates large drift chambers, MWPCs[3] and straw-tube trackers are used as **L**arge-**A**rea **T**rackers (LAT). The first spectrometer stage has a momentum resolution of $1\% \lesssim \frac{\delta p}{p} \lesssim 3\%$ and the second spectrometer stage with an angular acceptance of $\Delta\Theta = \pm 30\,\text{mrad}$ measures particles with momenta above $5\,\text{GeV}/c$ and improves the momentum resolution to $\frac{\delta p}{p} \lesssim 0.4\%$ [43]. Both stages are also fully equipped with electromagnetic calorimeters for neutral-particle detection, but since this analysis uses only charged tracks they will not be further discussed. Particle identification is only performed in the first spectrometer stage by a RICH[4] achieving kaon-pion separation at 95% confidence level for particle momenta in between 9.5 and $50\,\text{GeV}/c$ [24].

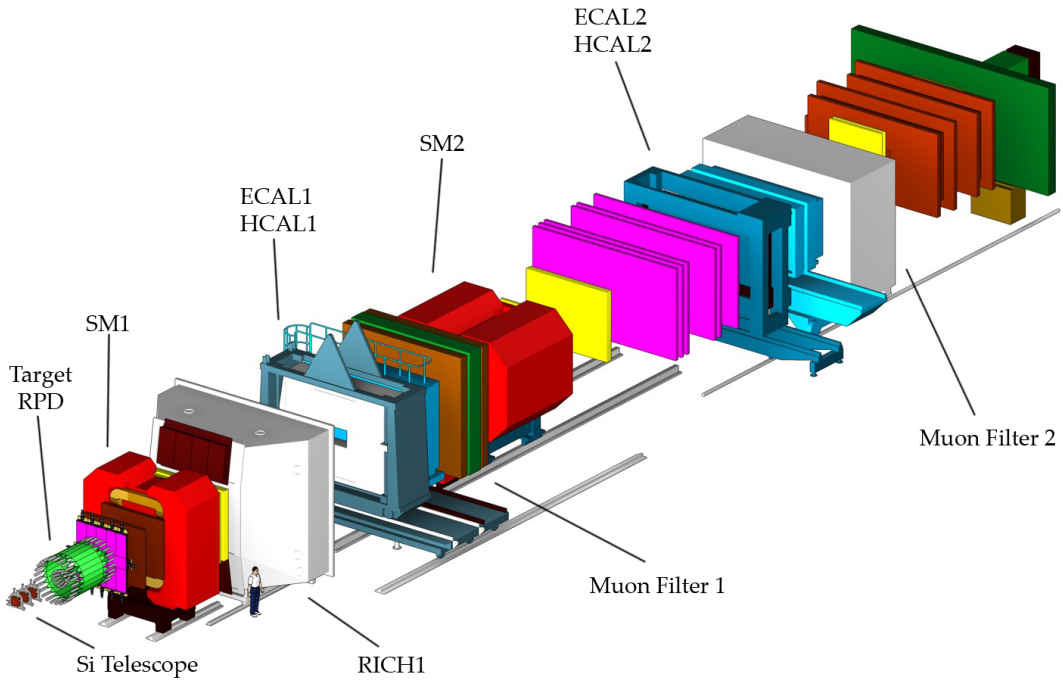

Figure 2.1: Schematic view of the COMPASS experiment for the 2008 hadron run.

[1] **Micro-Me**sh **Ga**seous **S**tructure
[2] **G**as **E**lectron **M**ultiplier
[3] **M**ulti**W**ire **P**roportional **C**hamber
[4] **R**ing-**I**maging **C**herenkov **D**etector

2.2 Selection Criteria

The selection starts with a separation of the diffractive dissociation process into $\pi^-\pi^+\pi^-$ from all other studied channels, followed by a removal of parasitic events. At the end less than 1% of the total events survive all selection cuts. Still the $\pi^-\pi^+\pi^-$ channel has the highest diffractive dissociation cross-section at COMPASS. In the following the general idea of the cuts will be explained, but for a detailed description please refer to [17].

The first cuts are rather straight forward as given by the event topology: There should be exactly one interaction point of a beam pion and a target proton for each event, which is called primary-vertex. By allowing only one interaction point the so called pile up, where multiple reactions happen in the same event, is suppressed.

Naturally for the $\pi^-\pi^+\pi^-$ final state there should be exactly three charged tracks detected by the tracking system. Furthermore it is required that the complete set of track parameters is reconstructed, as needed for the further analysis, and that the net charge of the three final-state particles should be the same as the one of the incoming pion, namely -1.

After this coarse preselection already 93.2% of the events are ruled out. Now more advanced cuts are needed to clean the sample. For the beam-time cut the time of the incident π^- as measured by the beam telescope is compared to the time reconstructed for the event. If they match within the combined time resolution, the event is accepted by this cut.

The next cut requires the **D**iffractive **T**rigger 0 (DT0) to have fired. Since there are a couple of different triggers depending on the physics of interest, not all recorded events are due to the DT0, which is designed to select diffractive-dissociation events. The trigger combines the signals of the beam counter, the RPD and some veto detectors. The beam counter is a scintillator disc, which verifies together with the scintillating fibre detector FI01X that a beam particle is hitting the target. The beam veto on the other hand suppresses events, where beam particles missed the target, because they result in unwanted tracks that do not originate from the target.

The part that is triggering on diffractive reactions is the RPD shown in figure 2.2. The production mechanism described in section 1.3 leads to a recoil proton, which in the lab frame is a slow charged particle leaving the target under a large angle with respect to the beam axis. The RPD is designed to measure these particles. Therefore the DT0 requires signals in both RPD rings.

The last two components of the trigger are the so-called sandwich veto, which rejects events, where particles emerging from the target are outside of the geometrical acceptance of the detector, and the so-called beam killers, which are placed on the beam axis in the second part of the spectrometer and prevent a trigger signal in case they are both traversed by a particle. The beam killers are necessary since only a small fraction of the beam particles actually do interact in the target. The whole DT0 trigger system is sketched in figure 2.3.

In addition to its use in the trigger system the RPD information permits to reconstruct tracks of the recoil particle. Of course there should be exactly one such track, namely the one of the recoil proton. With a cut on the target position reactions in the material around

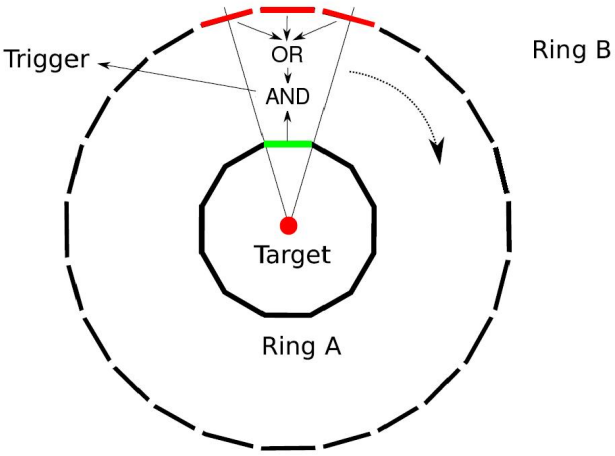

Figure 2.2: RPD trigger scheme based on the segmented scintillator rings [17].

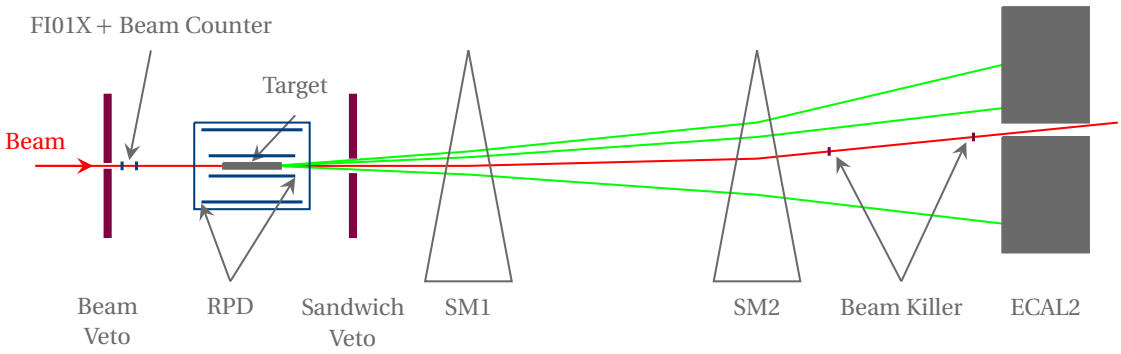

Figure 2.3: Scheme of the DT0: The main component is the RPD (blue), triggering on slow charged particles leaving the target. In addition upstream of the target the beam trigger (blue) is tagging single incoming beam particles. The veto system (red), consisting of beam veto, sandwich veto and beam killer, is completing the DT0 system [17].

the cylindrical liquid hydrogen target, i.e. the cooling pipe and the exit windows, can be sorted out.

The following two cuts are done in order to ensure exclusivity, meaning that all final-state particles have been reconstructed. Non-exclusive events can happen, for example, due to inefficiencies in the detector or reconstruction or due to neutral particles, because the calorimeter information is not used. Furthermore additional particles can hit the detector, which are not from the target region and did not trigger the vetos.

The first cut is on energy conservation, but since the momentum of the beam pion is not measured its energy has to be calculated from the momentum of the three reconstructed pions as described by [46]. After the calculation a 2σ cut on the Gaussian peak at $\sim 191\,\text{GeV}$ in the energy spectrum shown in figure 2.4 is applied. The resulting $\sigma \approx 1.9\,\text{GeV}$ agrees well with the expected 1% beam energy spread [47].

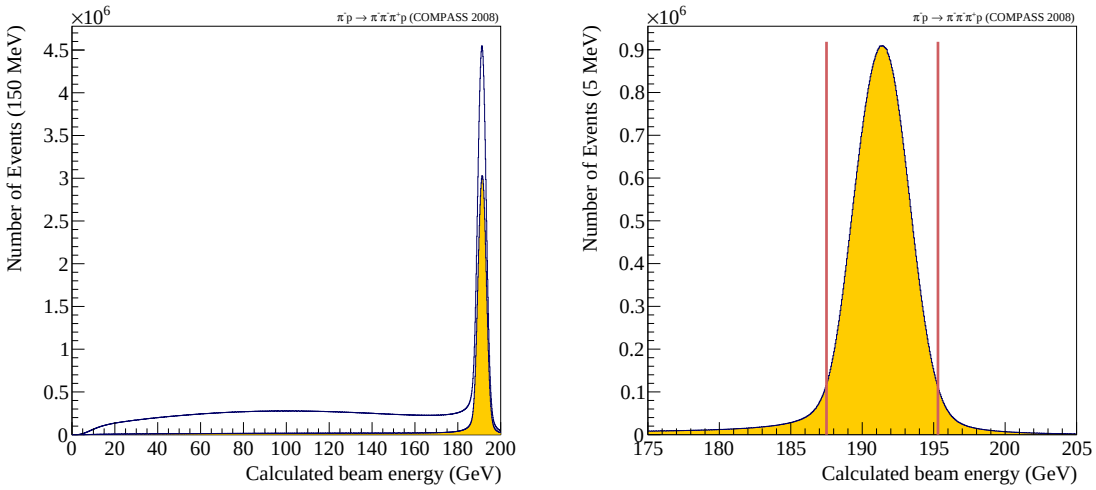

Figure 2.4: Calculated beam energy, before (unfilled histogram) and after the coplanarity cut (filled histogram). The red lines indicate the 2σ cut on the energy peak [17].

The coplanarity cut uses the fact that due to momentum conservation no net transverse momentum with respect to the beam is allowed, which requires that the difference of the azimuthal angle ϕ of the recoil proton and the excited state X^- is $\Delta\phi = 180°$. However this is slightly softened by taking into account the geometry of the RPD as well as the effect of multiple scattering in the inner ring.

Additionally cuts on the four-momentum transfer t' are introduced to clean the sample. The low-momentum cut at $0.1\,\mathrm{GeV}^2/c^2$ removes pile-up and noise in the region below the acceptance of the RPD and the high-momentum cut at $1.0\,\mathrm{GeV}^2/c^2$ keeps the probability for multi-Regge exchange and excitations of the target proton low.

So far all incident and final-state particles were treated as pions (pion hypotheses) and this will be kept for the further analysis, but the negative secondary hadron beam consists at the COMPASS target of $\sim 97\%\ \pi^-$, $\sim 2\%\ K^-$, $\sim 1\%\ \overline{p}$ and a negligible amount of muons and electrons. To suppress the small background contribution the CEDAR and RICH detectors are used to veto clearly identified particles that are not a pion. For more information please refer to [17].

Additionally to the non-pionic background there exists background due to other production processes as explained in section 1.3.2. The central production as one of these can be separated from diffractive dissociation via the kinematic variables rapidity y and Feynman's x_F, defined in [13] as:

$$y = \frac{1}{2} \ln \frac{E + p_z}{E - p_z} \qquad \text{and} \qquad x_F \approx \frac{2 p_{z,CM}}{\sqrt{s}}$$

with the energy E of the particle and its momentum component p_z along the beam axis in the laboratory frame and the centre-of-mass energy $\sqrt{s}$ and the momentum component along the beam axis $p_{z,CM}$ in the centre-of-mass frame.

The typical kinematics for central production contain a fast π^- and a centrally produced $\pi^+\pi^-$ system. Quantifying this leads to a cut on a rapidity gap between the fast π^- and

the $\pi^+\pi^-$ system of 4.5 in combination with x_F larger than 0.9. For more information please refer to [17].

Finally the mass range is limited to $0.5 \leq m_{3\pi} \leq 2.5\,\mathrm{GeV}/c^2$ as in previous experiments. The range starts considerably lower than the lightest observed 3π resonance at $1.2\,\mathrm{GeV}/c^2$ and can be extended in the future up to higher masses due to the large data sample and the excellent acceptance of the apparatus.

Chapter 3

Partial-Wave Decomposition of the $\pi^-\pi^+\pi^-$ Final State

This chapter will describe the main results of a partial-wave decomposition in bins of the invariant mass $m_{3\pi}$ and the squared four-momentum transfer t', which were developed in [17] and which constitute the basis of this thesis.

3.1 PWA Method

The invariant mass distributions of the selected data sample are shown in figure 3.1. The 2π invariant mass spectrum contains both possible $\pi^+\pi^-$ combinations for each event, since the two final-state π^- are indistinguishable. While the clearly visible resonant structures in the 3π mass distribution confirm the assumption that the intermediate state X^- is dominated by resonances and therefore production and decay are factorisable, the visible resonances in the 2π mass spectrum suggest the use of the isobar model. This model assumes that multi-body decays can be described as a tree of successive two-body decays. In the case of the 3π final state this means that the intermediate state X^- decays into a so-called bachelor π^- and a 2π resonance, the isobar, which then continues to decay into a π^+ and π^-. This decay sequence is illustrated in figure 3.3.

The use of the isobar model is further supported by the Dalitz plots in figure 3.2, which show that the occurrence of specific isobars depends on the invariant three-pion mass $m_{3\pi}$ as one would expect it due to the larger phase-space for higher masses as well as the different possibilities for the intermediate states X^- and thereby different quantum numbers.

As the schematic sketch in figure 3.3 already suggest it is further assumed that no final-state interaction disturbs the phase-space distributions, which are fitted in the first partial-wave analysis step that is described in the remainder of this section.

The goal of this step is now to disentangle the different contributing X^- and their decay channels. In order to do so a description of the decay kinematics is needed. Each two-body decay vertex has five degrees of freedom, e.g. the masses of the mother and the two daughter particles plus two decay angles, which define the direction of the daughter particles. Counting two decay vertices the total number of degrees of freedom is 10, but since the final state is fixed to three pions and the isobar enters as the daughter of the first decay and as the mother of the second decay only six variables remain. Finally describing the decay for a given mass $m_{3\pi}$ of the intermediate state X^-, which is a property of the production, the degrees of freedom reduce to five. These five variables, which are here

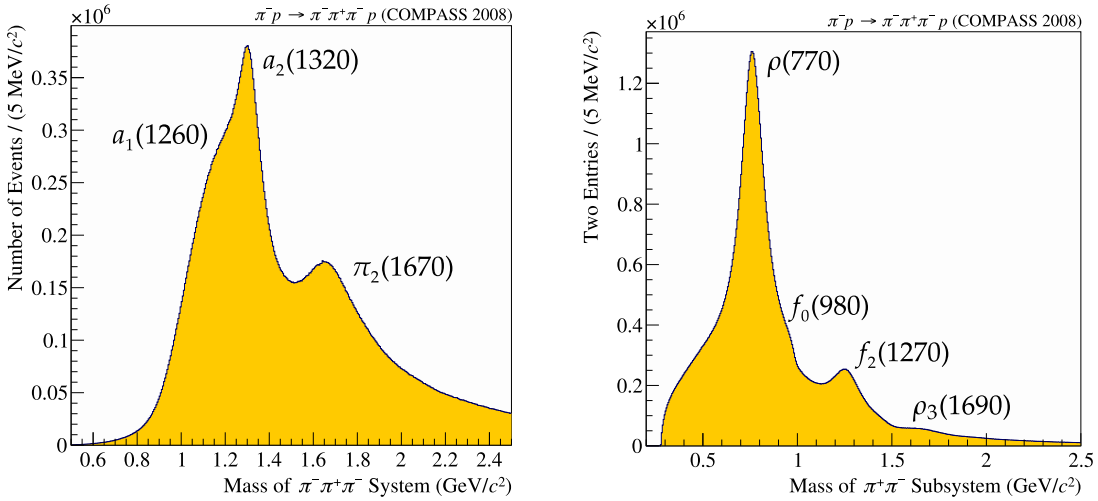

Figure 3.1: 3π (left) and 2π (right) invariant-mass spectrum after event selection. In both spectra clear structures are visible. While the 3π mass distribution is dominated by a peak attributed to the $a_2(1320)$ with a low-mass shoulder corresponding to the $a_1(1260)$ and a smaller $\pi_2(1670)$ peak at higher masses, the largest contribution to the 2π mass spectrum is the $\rho(770)$, followed by the $f_2(1270)$. Moreover the $f_0(980)$ and the $\rho_3(1690)$ appear as high-mass shoulders [45].

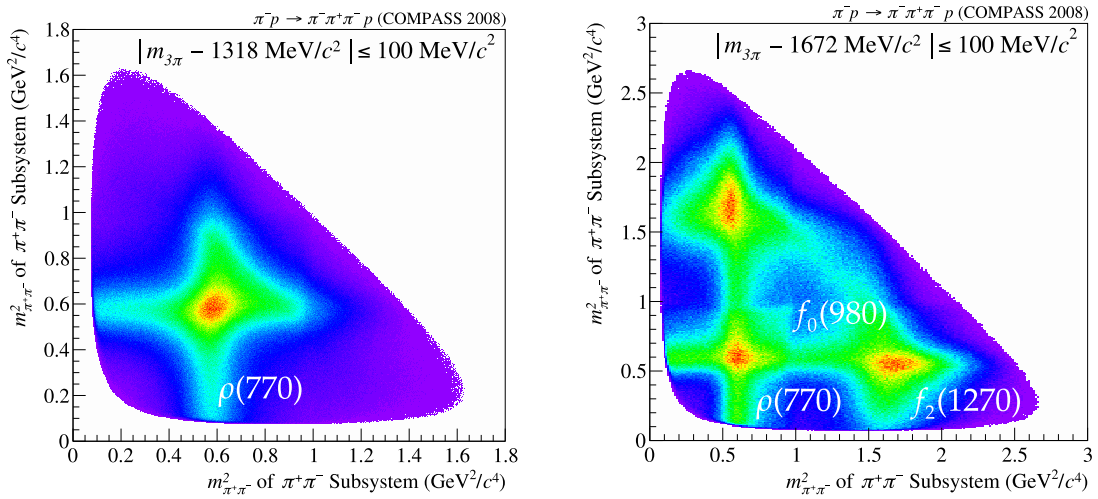

Figure 3.2: Dalitz plots for selected 3π mass ranges of the $a_2(1320)$ (left) and the $\pi_2(1670)$ (right) with linear z-axis. In both plots clear bands at $0.6\,\mathrm{GeV}^2/c^4$ corresponding to the $\rho(770)$ are visible. For the $\pi_2(1670)$ additional $f_2(1270)$ bands at $1.6\,\mathrm{GeV}^2/c^4$ and sharp edges at $1.0\,\mathrm{GeV}^2/c^4$ associated to the $f_0(980)$ can be seen [45].

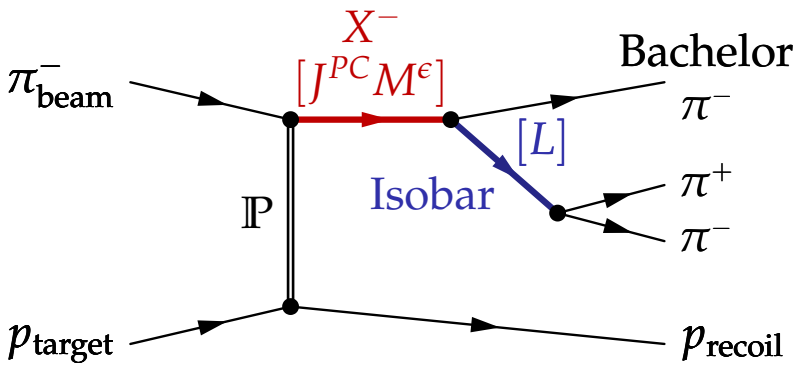

Figure 3.3: Schematic drawing of single-diffractive dissociation of π^- into $\pi^-\pi^+\pi^-$ on a proton target in the isobar approximation without final-state interaction [45].

chosen to be the mass of the isobar and the four decay angles, are in the following denoted by τ.

The τ distribution depends on the quantum numbers of the intermediate state X^- and the isobar as well as on the orbital angular momentum between the isobar and the bachelor pion. The angular momentum between the π^+ and π^- in the isobar decay also plays a role, but, since pions are spin-less particles, it is equal to the spin of the isobar. In addition to the so far discussed $I^G J^{PC}$ of X^- the spin projection M is important for the distribution. In contrast to the other quantum numbers M needs a reference axis. The natural choice is to take the quantisation axis along the beam direction. Combining this with the definition of the y-axis along the normal of the production plane, which is spanned by the incoming beam and the outgoing X^-, results in the used Gottfried-Jackson Frame [48].

In order to account for parity conservation in the strong-interaction process a transformation from the canonical basis to the reflectivity basis [49] is performed. This transformation combines states of opposite spin projection M. Therefore in the reflectivity basis M is now limited to values between 0 and J. However, a new quantum number, the eigenvalue of the reflectivity operator, is added. The operator is defined as the parity operator followed or preceded by a rotation around the normal of the production plane. For bosons its eigenvalue, denoted reflectivity ε, can take on ± 1. This corresponds in the Gottfried-Jackson Frame to the naturality of the exchange particle defined in equation 1.1 and therefore $\varepsilon = +1$ is related to all trajectories with natural spin-parity, in particular the Pomeron.

Having a set of properly defined quantum numbers, they describe the spatial distributions of the decay particles completely except of two unknown couplings appearing in the decay vertices. Assuming that they do not depend on the kinematics, the couplings can be absorbed into the production amplitudes, which bundles the unknown parts into the complex functions $T^{\varepsilon}_{\alpha}(m_X, t')$ called transition amplitudes, because they carry information about the production as well as the decay. Doing this leaves the decay amplitudes $\psi^{\varepsilon}_{\alpha}(m_X, \tau)$ completely defined and calculable. The factorisation of the two amplitudes is of course only possible, because the intermediate state X^- is as we have seen dominated by resonances.

The index α denotes the so-called partial wave containing the quantum numbers $I^G J^{PC} M$ of the intermediate state X^-, the isobar ξ and the orbital angular momentum L between the isobar and the bachelor pion. In short-hand notation a partial wave is fully defined by $I^G J^{PC} M^\varepsilon \xi \pi L$ or leaving out $I^G = 1^-$, because it is predetermined by the final state, simply $J^{PC} M^\varepsilon \xi \pi L$. Since the partial waves normally interfere with each other they have to be summed up coherently to obtain the seven-dimensional intensity distribution, but an advantage of the used reflectivity base is that waves with different reflectivities do not interfere and can therefore be summed up incoherently. This is described by the following equation:

$$\mathcal{I}(m_X, t', \tau) = \sum_{\varepsilon=\pm 1} \left| \sum_\alpha T^\varepsilon_\alpha(m_X, t') \psi^\varepsilon_\alpha(m_X, \tau) \right|^2 \tag{3.1}$$

In order to eliminate the dependence of the decay and transition amplitudes on m_X and t' the analysis is performed in bins, which for m_X are chosen to be equidistant and of size $20\,\mathrm{MeV}/c^2$. The t' binning, on the other hand, was chosen as given in table 3.1 in order to distribute the events equally. This together with the correlation of the t' and the invariant mass distribution of the 3π system is shown in figure 3.4.

Bin	**t' range [GeV$^2/c^2$]**
1	0.100 to 0.113
2	0.113 to 0.127
3	0.127 to 0.144
4	0.144 to 0.164
5	0.164 to 0.189
6	0.189 to 0.220
7	0.220 to 0.262
8	0.262 to 0.326
9	0.326 to 0.449
10	0.449 to 0.724
11	0.724 to 1.000

Table 3.1: t' binning used in the analysis.

Since the transition amplitudes T^ε_α are not unique due to arbitrary complex phases, instead the so-called spin-density matrix $\rho^\varepsilon_{\alpha\beta}$ is used as defined in equation 3.2 represented in the Chung-Trueman parametrisation [49].

$$\rho^\varepsilon_{\alpha\beta} = T^\varepsilon_\alpha T^{\varepsilon *}_\beta \tag{3.2}$$

For a single kinematic bin in the $(m_{3\pi}, t')$ plane the intensity therefore reads:

$$\mathcal{I}(\tau) = \sum_{\varepsilon=\pm 1} \sum_{\alpha,\beta} \rho^\varepsilon_{\alpha\beta} \psi^\varepsilon_\alpha(\tau) \psi^{\varepsilon *}_\beta(\tau) \tag{3.3}$$

This parametrisation of the now only five-dimensional intensity distribution is fitted to the measured data using a maximum-likelihood method resulting in a spin-density matrix

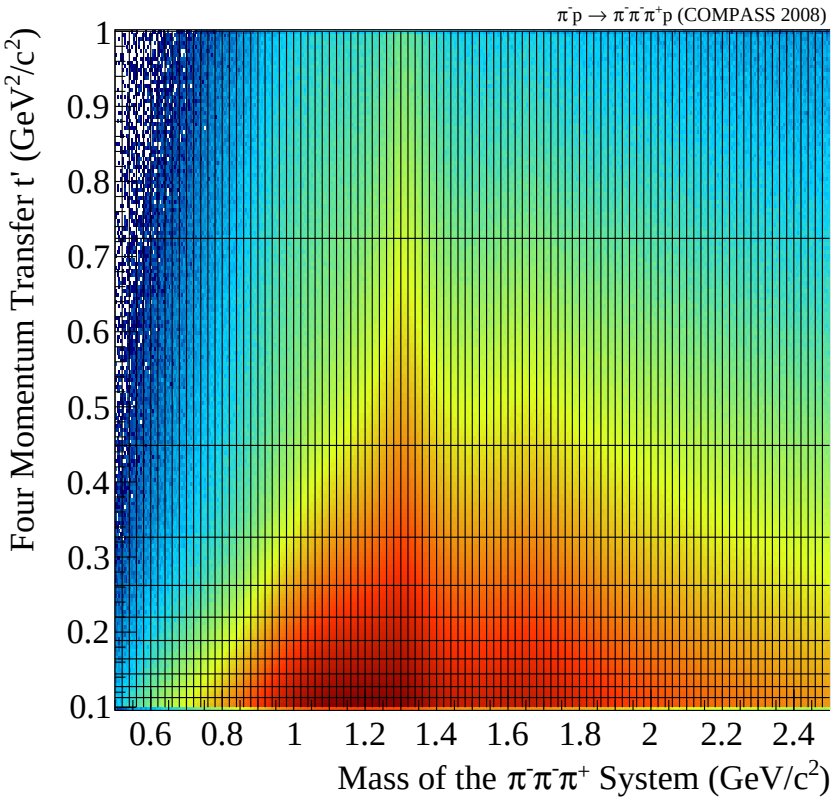

Figure 3.4: Intensity distribution with logarithmic z-axis binned in the invariant mass $m_{3\pi}$ and the squared four-momentum transfer t'. Equidistant mass bins of 20 MeV/c^2 and 11 t' bins with equal intensity are chosen [17].

for each $(m_{3\pi}, t')$ bin, which is referred to as mass-independent fit. The mass dependence of $\rho^{\varepsilon}_{\alpha\beta}(m_{3\pi}, t')$ is then analysed in the mass-dependent fit explained in chapter 4.

Since both final-state π^- are indistinguishable this is taken into account in the analysis by calculating $\psi^{\varepsilon}_{\alpha}(\tau)$ for both possibilities and adding them coherently, thereby respecting interferences. This method is denoted Bose symmetrisation, because the coherent sum constructs a wave function that is symmetric under the exchange of the two π^-.

While the $m_{3\pi}$ spectrum is binned in order to remove the dependence on $m_{3\pi}$, the one on the isobar mass $m_{2\pi}$ has to be known precisely at this step, because it influences the decay. How $m_{2\pi}$ is parametrised for the individual isobars can be found in [17]. Here only the used isobars are listed in table 3.2.

The next step is to calculate all possible partial waves for these isobars, but as they are in principal infinitely many, one important decision is how to truncate the partial-wave expansion of equation 3.3. The goal is to describe the data with the minimum amount of partial waves, that is with the minimum number of free parameters. Including to many insignificant waves will lead to overfitting. On the other hand, if important waves are

Particle	J^{PC}
$(\pi\pi)_S$	0^{++}
$f_0(980)$	0^{++}
$f_0(1500)$	0^{++}
$f_2(1270)$	2^{++}
$\rho(770)$	1^{--}
$\rho_3(1690)$	3^{--}

Table 3.2: Used isobars with their J^{PC} [17]. $(\pi\pi)_S$ denotes a parametrisation for the broad component of isobars decaying with an orbital angular momentum 0.

missing, intensity may be wrongly attributed to other waves and can even create artificial structures, like shown in figure 1.2a for the case of the BNL E852 $\pi_1(1600)$ search.

Since in general the wave intensity is expected to decrease for larger J, M and L, [17] started with about 160 waves by including all with total spin $J \leq 6$, $M \leq 1$ and positive reflectivity $\varepsilon = +1$ and adding some specific waves with, for example, negative reflectivity $\varepsilon = -1$ or $M = 2$. Taking mostly $\varepsilon = +1$ is motivated by the Pomeron dominance at COMPASS beam energies. Step by step waves with insignificant intensities over the whole $m_{3\pi}$ and t' range were removed and finally a set of 88 waves remained. This constitutes the largest wave set used in an analysis of this kind so far and reflects the size of the data set.

The 88 used waves are listed in table 3.3. In order to get an estimator on how much each wave contributes their intensities, summed over all $m_{3\pi}$ and t' bins, are given normalised to the total number of events. However, due to interference effects between the waves the sum of these relative intensities is slightly larger than 100%.

An additional complication arises from the fact that in the low-mass region, which corresponds to small phase-space volume, the fit has problems to distinguish between certain waves. This typically leads to fit instabilities, where waves have unphysically large intensities in the low-mass region, but are destructively interfering so that the net result is again compatible with the data. These artifacts mostly involve waves with high-mass isobars, which therefore have high physical 3π-mass thresholds. Also wave pairs where isobar spin and the angular momentum L between the isobar and bachelor pion are interchanged, like for the $1^{++}1^+\rho(770)\pi D$ and $1^{++}1^+f_2(1270)\pi P$ waves, are sensitive to these effects. This can be largely suppressed by applying the mass thresholds listed in table 3.3 during the fitting.

Finally in order to account for background contributions, where the three pions are uncorrelated, for example, from not discriminated pile-up, a special wave, the so-called flat wave, that has an isotropic phase-space distribution is added incoherently to equation 3.3:

$$\mathcal{I}(\tau) = \sum_{\varepsilon=\pm1} \sum_{\alpha,\beta} \rho^{\varepsilon}_{\alpha\beta} \psi^{\varepsilon}_{\alpha}(\tau) \psi^{\varepsilon *}_{\beta}(\tau) + T^2_{\text{flat}}$$

$J^{PC}M^{\varepsilon}$	Isobar	L	T[GeV/c^2]	I[%]
FLAT			—	3.09
$0^{-+}0^{+}$	$(\pi\pi)_S$	S	—	7.96
$0^{-+}0^{+}$	$f_0(980)$	S	1.20	2.44
$0^{-+}0^{+}$	$\rho(770)$	P	—	3.55
$0^{-+}0^{+}$	$f_0(1500)$	S	1.70	0.10
$0^{-+}0^{+}$	$f_2(1270)$	D	—	0.22
$1^{++}0^{+}$	$\rho(770)$	S	—	32.65
$1^{++}1^{+}$	$\rho(770)$	S	—	4.10
$1^{++}0^{+}$	$\rho(770)$	D	—	0.90
$1^{++}1^{+}$	$\rho(770)$	D	—	0.56
$1^{++}0^{+}$	$(\pi\pi)_S$	P	—	4.07
$1^{++}1^{+}$	$(\pi\pi)_S$	P	1.10	0.18
$1^{++}0^{+}$	$f_2(1270)$	P	1.22	0.44
$1^{++}1^{+}$	$f_2(1270)$	P	—	0.49
$1^{++}0^{+}$	$f_2(1270)$	F	—	0.14
$1^{++}0^{+}$	$f_0(980)$	P	1.18	0.25
$1^{++}1^{+}$	$f_0(980)$	P	1.14	0.08
$1^{++}0^{+}$	$\rho_3(1690)$	D	—	0.12
$1^{++}0^{+}$	$\rho_3(1690)$	G	—	0.04
$1^{-+}1^{+}$	$\rho(770)$	P	—	0.85
$2^{++}1^{+}$	$\rho(770)$	D	—	7.66
$2^{++}2^{+}$	$\rho(770)$	D	—	0.33
$2^{++}1^{+}$	$f_2(1270)$	P	1.00	0.48
$2^{++}2^{+}$	$f_2(1270)$	P	1.40	0.01
$2^{++}1^{+}$	$\rho_3(1690)$	D	0.80	0.02
$2^{-+}0^{+}$	$f_2(1270)$	S	—	6.72
$2^{-+}1^{+}$	$f_2(1270)$	S	1.10	0.87
$2^{-+}2^{+}$	$f_2(1270)$	S	—	0.11
$2^{-+}0^{+}$	$f_2(1270)$	D	—	0.91
$2^{-+}1^{+}$	$f_2(1270)$	D	—	0.20
$2^{-+}2^{+}$	$f_2(1270)$	D	—	0.08
$2^{-+}0^{+}$	$f_2(1270)$	G	—	0.08
$2^{-+}0^{+}$	$\rho(770)$	P	—	3.83
$2^{-+}1^{+}$	$\rho(770)$	P	—	3.33
$2^{-+}2^{+}$	$\rho(770)$	P	—	0.16
$2^{-+}0^{+}$	$\rho(770)$	F	—	2.19
$2^{-+}1^{+}$	$\rho(770)$	F	—	0.30
$2^{-+}0^{+}$	$\rho_3(1690)$	P	1.00	0.23
$2^{-+}1^{+}$	$\rho_3(1690)$	P	1.30	0.11
$2^{-+}0^{+}$	$(\pi\pi)_S$	D	—	2.96
$2^{-+}1^{+}$	$(\pi\pi)_S$	D	—	0.38
$2^{-+}0^{+}$	$f_0(980)$	D	1.16	0.55
$3^{-+}1^{+}$	$\rho(770)$	F	—	0.05
$3^{-+}1^{+}$	$f_2(1270)$	D	1.34	0.03
$3^{++}0^{+}$	$\rho(770)$	D	—	0.89
$3^{++}1^{+}$	$\rho(770)$	D	—	0.99
$3^{++}0^{+}$	$\rho(770)$	G	—	0.36
$3^{++}1^{+}$	$\rho(770)$	G	—	0.12
$3^{++}0^{+}$	$f_2(1270)$	P	0.96	0.43
$3^{++}1^{+}$	$f_2(1270)$	P	1.14	0.45
$3^{++}0^{+}$	$\rho_3(1690)$	S	1.38	0.43
$3^{++}1^{+}$	$\rho_3(1690)$	S	1.38	0.15
$3^{++}0^{+}$	$\rho_3(1690)$	I	—	0.01
$3^{++}0^{+}$	$(\pi\pi)_S$	F	1.38	0.23
$3^{++}1^{+}$	$(\pi\pi)_S$	F	1.38	0.32
$4^{-+}0^{+}$	$\rho(770)$	F	—	0.98
$4^{-+}1^{+}$	$\rho(770)$	F	—	0.38
$4^{-+}0^{+}$	$f_2(1270)$	D	—	0.30
$4^{-+}1^{+}$	$f_2(1270)$	D	—	0.14
$4^{-+}0^{+}$	$f_2(1270)$	G	1.60	0.01
$4^{-+}0^{+}$	$(\pi\pi)_S$	G	1.40	0.28
$4^{++}1^{+}$	$\rho(770)$	G	—	0.76
$4^{++}2^{+}$	$\rho(770)$	G	—	0.03
$4^{++}1^{+}$	$\rho_3(1690)$	D	1.70	0.01
$4^{++}1^{+}$	$f_2(1270)$	F	—	0.18
$4^{++}2^{+}$	$f_2(1270)$	F	—	0.02
$5^{++}0^{+}$	$\rho(770)$	G	—	0.33
$5^{++}0^{+}$	$\rho_3(1690)$	D	1.36	0.02
$5^{++}0^{+}$	$f_2(1270)$	F	0.98	0.11
$5^{++}1^{+}$	$f_2(1270)$	F	—	0.09
$5^{++}0^{+}$	$f_2(1270)$	H	—	0.02
$5^{++}0^{+}$	$(\pi\pi)_S$	H	—	0.13
$5^{++}1^{+}$	$(\pi\pi)_S$	H	—	0.08
$6^{-+}0^{+}$	$(\pi\pi)_S$	I	—	0.11
$6^{-+}1^{+}$	$(\pi\pi)_S$	I	—	0.05
$6^{-+}0^{+}$	$\rho(770)$	H	—	0.70
$6^{-+}1^{+}$	$\rho(770)$	H	—	0.14
$6^{-+}0^{+}$	$\rho_3(1690)$	F	—	0.05
$6^{-+}0^{+}$	$f_2(1270)$	G	—	0.05
$6^{++}1^{+}$	$\rho(770)$	I	—	0.04
$6^{++}1^{+}$	$f_2(1270)$	H	—	0.03
$1^{++}1^{-}$	$\rho(770)$	S	—	0.30
$1^{-+}0^{-}$	$\rho(770)$	P	—	0.26
$1^{-+}1^{-}$	$\rho(770)$	P	—	0.67
$2^{++}0^{-}$	$\rho(770)$	D	—	0.31
$2^{++}0^{-}$	$f_2(1270)$	P	1.18	0.18
$2^{++}1^{-}$	$f_2(1270)$	P	1.30	0.33
$2^{-+}1^{-}$	$f_2(1270)$	S	—	0.18

Table 3.3: Used wave set with applied threshold T and relative total intensity I. It contains 80 amplitudes with positive and 7 with negative reflectivity [17]. Note that due to interference the sum of the intensities results in 105.47%.

3.2 Spin-density matrix in bins of $m_{3\pi}$ and t'

Since the spin-density matrix $\rho^{\varepsilon}_{\alpha\beta}$ from equation 3.2 is Hermitian it is represented as an upper triangular matrix. By enumerating the partial waves α and β this leads to:

$$\rho^{\varepsilon} = \begin{pmatrix} T^{\varepsilon}_1 T^{\varepsilon *}_1 & T^{\varepsilon}_1 T^{\varepsilon *}_2 & \cdots \\ & T^{\varepsilon}_2 T^{\varepsilon *}_2 & \cdots \\ & & \ddots \end{pmatrix} \tag{3.4}$$

Note that the diagonal elements are the squared absolute values of the transition amplitudes and are therefore real. They are in the following denoted as "intensity" of a partial wave. The off-diagonal elements describing the interferences between waves are in general complex, but the information on their absolute value is already included in the intensities and therefore only their argument, referred to as "relative phase", is of interest. Furthermore the fact that waves with different reflectivities are not interfering leads to a block-diagonal form of the spin-density matrix:

$$\rho = \begin{pmatrix} \text{Flat} & 0 & 0 \\ 0 & \rho^{+1} & 0 \\ 0 & 0 & \rho^{-1} \end{pmatrix}$$

Of course not all 88 intensities and 3181 relative phases can be discussed. Therefore only some common features of the waves, which are later used for the resonance extraction described in chapter 4, are pointed out here. More information on the possible interpretations of the results at this stage of the analysis is available in [17].

The waves with the largest total intensities are $1^{++}0^+\rho(770)\pi S$ and $2^{++}1^+\rho(770)\pi D$ shown in figure 3.5. While in the 1^{++} wave a broad peak attributed to the $a_1(1260)$ is visible, the narrow peak in the 2^{++} wave is due to the $a_2(1320)$. Comparing the lowest and the second highest t' bin a clear shift of the peak position is observable in the 1^{++} wave, while the $a_2(1320)$ peak is completely unaffected. This indicates that the 1^{++} wave has strong contributions from non-resonant production processes.

A further feature in the high-t' region of the $1^{++}0^+\rho(770)\pi S$ is the shoulder at the side of the main resonance due to a second interfering resonance in this wave. This is more prominent in the $2^{-+}0^+ f_2(1270)\pi S$ wave plotted in figure 3.6, where the $\pi_2(1880)$ is visible as a slight bump on the falling flank of the $\pi_2(1670)$ peak. The second wave in figure 3.6, denoted $0^{-+}0^+ f_0(980)\pi S$, shows a problem that can occur for the applied thresholds. While the intensity going to a physical thresholds should continuously drop and finally reach zero, here it is cut off at non-zero intensities, because a higher threshold had to be used due to instabilities in the fit. In order to minimise this effect the thresholds have been chosen as low as possible. However, the $\pi(1800)$ peak is not affected and therefore the chosen threshold has only a minor influence on the resonance extraction in this wave.

So far only waves with relatively large intensities were shown, hence in figure 3.7 two waves, namely $4^{++}1^+\rho(770)\pi G$ and $1^{++}0^+ f_0(980)\pi P$, with total relative intensities around or below 1% are plotted. As the broad high-mass $a_4(2040)$ peak in the 4^{++} wave demonstrates, a clear signal can also be found in small-intensity waves. The same is

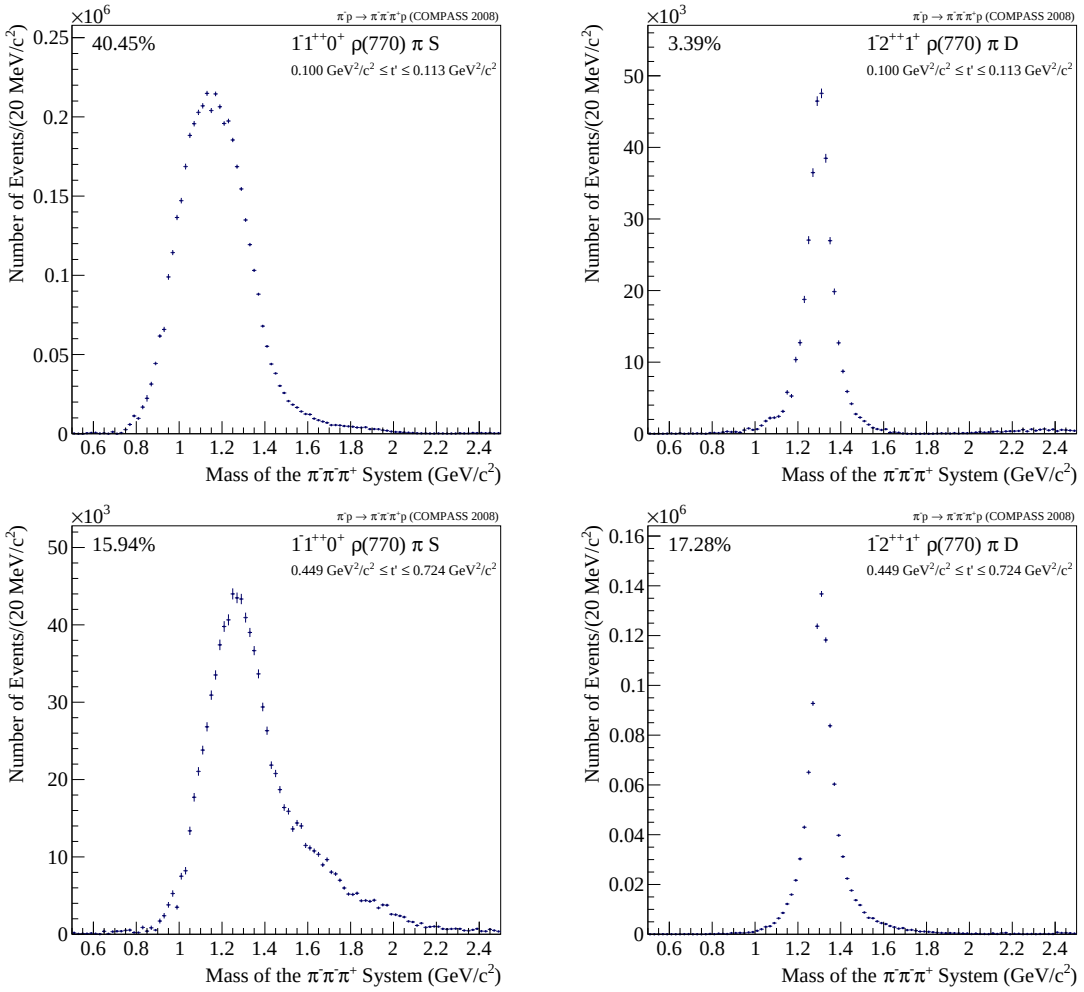

Figure 3.5: Intensities of the $1^{++}0^{+}\rho(770)\pi S$ (left) and $2^{++}1^{+}\rho(770)\pi D$ (right) waves for the lowest (upper row) and the second highest (lower row) t' bin [17]. The percentages give the intensity integrals normalised to the total number of events in the respective t' bin.

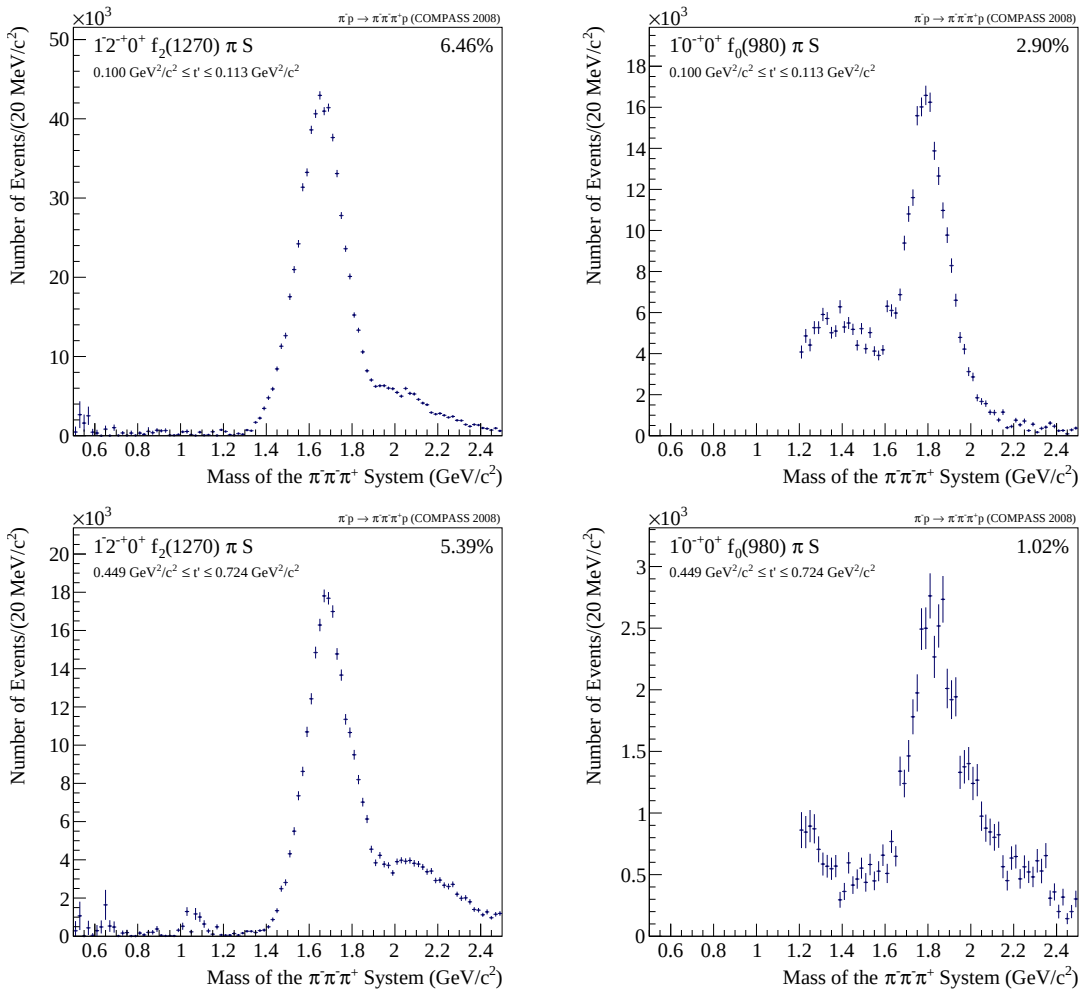

Figure 3.6: Intensities of the $2^{-+}0^+ f_2(1270)\pi S$ (left) and $0^{-+}0^+ f_0(980)\pi S$ (right) waves for the lowest (upper row) and the second highest (lower row) t' bin [17]. The percentages give the intensity integrals normalised to the total number of events in the respective t' bin.

true for the 1^{++} wave, but here additionally to the isolated, narrow peak visible at about $1.4\,\mathrm{GeV}/c^2$ in the low-t' region, for high t' a broad structure at higher masses emerges. The peak at $1.4\,\mathrm{GeV}/c^2$ is peculiar due to its extremely steep rise and the fact that so far no resonance with this quantum numbers has been observed at this position. In chapter 4 a possible interpretation as an $a_1(1420)$ resonance will be discussed.

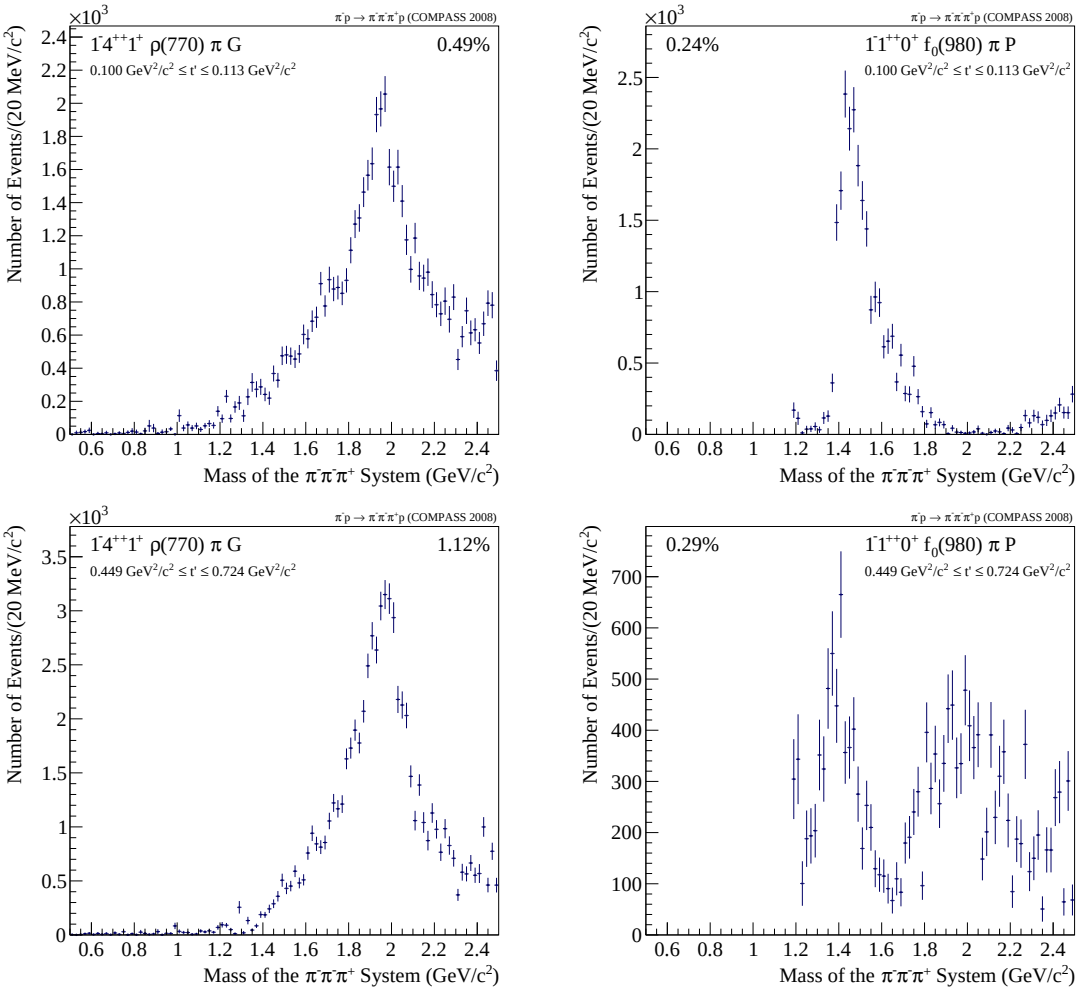

Figure 3.7: Intensities of the $4^{++}1^{+}\rho(770)\pi G$ (left) and the $1^{++}0^{+}f_0(980)\pi P$ (right) waves for the lowest (upper row) and the second highest (lower row) t' bin [17]. The percentages give the intensity integrals normalised to the total number of events in the respective t' bin.

Since the interference terms are an important aspect in the identification of resonances two examples, namely the relative phase motions of the $2^{++}1^{+}\rho(770)\pi D$ wave with respect to the $1^{++}0^{+}\rho(770)\pi S$ and the $2^{-+}0^{+}f_2(1270)\pi S$ wave, are shown in figure 3.8. The common phase motion at about $1.3\,\mathrm{GeV}/c^2$ is related to the $a_2(1320)$. The opposite direction of the phase motion is due to the fact that for the plots on the left side the phase of the 1^{++} wave is subtracted from the 2^{++} wave, while for the plots on the right side

the 2^{++} wave is subtracted from the 2^{-+} wave. The difference in strength results from a different interference with the other given wave. Like the $a_2(1320)$ peak the related phase motion does not change with t'. However, the low- and high-mass parts of the relative phases do.

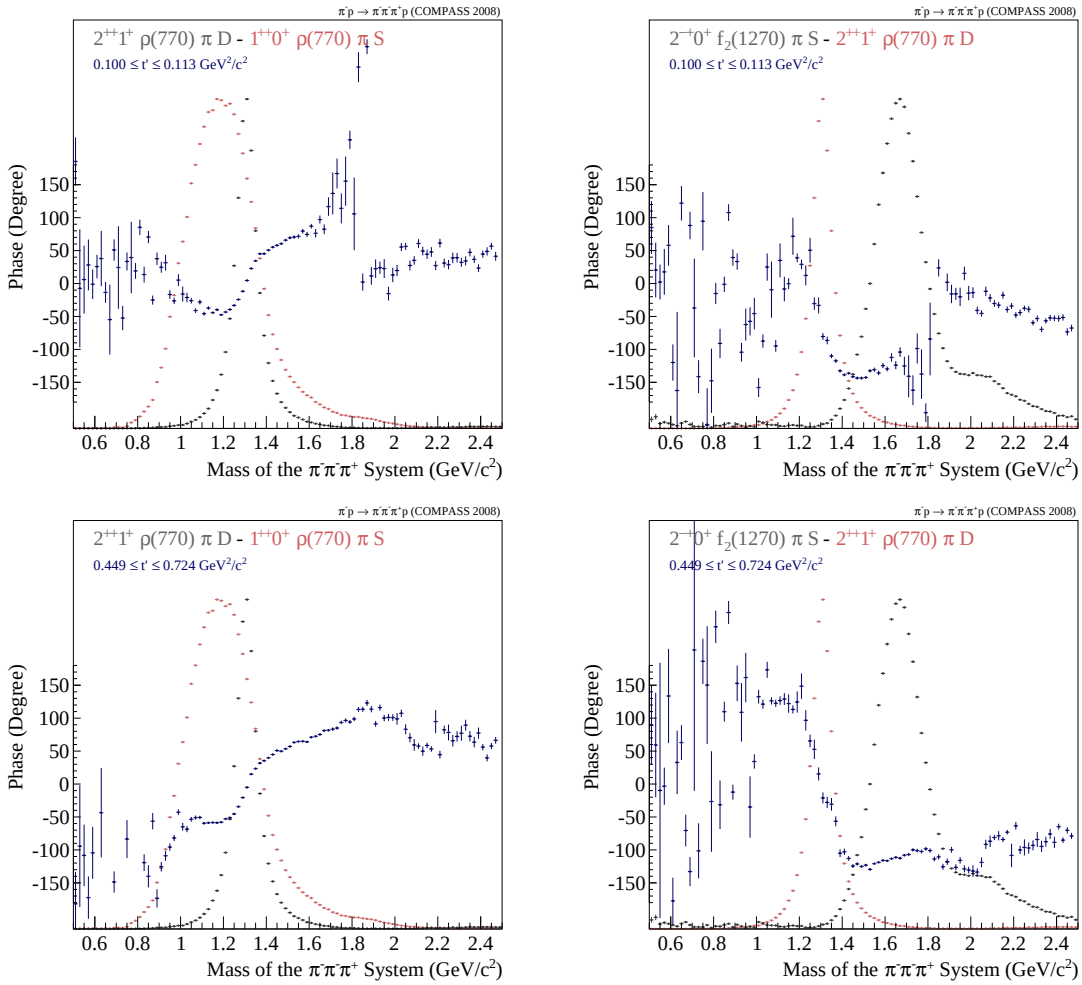

Figure 3.8: Relative phase motions of the $2^{++}1^+\rho(770)\pi D$ wave with respect to the $1^{++}0^+\rho(770)\pi S$ (left) and the $2^{-+}0^+ f_2(1270)\pi S$ (right) wave for the lowest (upper row) and the second highest (lower row) t' bin [17]. The intensities of the corresponding waves are also plotted (red, grey) in order to make the correlation to the phases easier to observe.

Chapter 4

Extraction of Resonance Parameters

4.1 Fit of $m_{3\pi}$ dependence

Having the data binned in the invariant mass $m_{3\pi}$ and the squared four-momentum transfer t' as well as separated into partial waves, this information can now be used to extract resonances. However, since the t' dependence of resonances and even more so the non-resonant contributions has not been studied extensively so far, no assumptions are made at this point, but instead the t' spectra are later extracted for further studies as described in chapter 5. Therefore the resonant contributions in the different partial waves are determined by modelling only their $m_{3\pi}$ dependence. The resonance parameters are estimated fitting the spin-density matrices $\rho^{\varepsilon}_{\alpha\beta}$ resulting from the mass-independent fit using a χ^2 minimisation.

For this purpose $\rho^{\varepsilon}_{\alpha\beta}$ is parametrised in the following way:

$$\begin{aligned}\rho^{\varepsilon}_{\alpha\beta}(m_{3\pi}, t') = &\left[\varphi^{\varepsilon}_{\alpha}(m_{3\pi}) \sum_{k(\alpha)} C^{\varepsilon}_{\alpha k}(t') D_k(m_{3\pi}, t'; \xi_k)\right] \Psi(m_{3\pi}) \\ &\cdot \left[\varphi^{\varepsilon}_{\beta}(m_{3\pi}) \sum_{k(\beta)} C^{\varepsilon}_{\beta k}(t') D_k(m_{3\pi}, t'; \xi_k)\right]^*\end{aligned} \tag{4.1}$$

$D_k(m_{3\pi}, t'; \xi_k)$ denotes dynamic terms, meaning resonant and non-resonant contributions. The ξ_k are the free shape parameters of each term k. For resonances ξ_k represents mass and width and for non-resonant contributions some general shape parameters b and c_i with $i = 1, 2, 3$. Each dynamic term is multiplied by a so-called coupling $C^{\varepsilon}_{\alpha k}(t')$, before the contributions in a single wave are summed coherently. Finally $\varphi^{\varepsilon}_{\alpha}(m_{3\pi})$ is the phase space for a decay into partial wave (α, ε) and $\Psi(m_{3\pi})$ describes the decreasing probability for the production of high-mass intermediate states X^-.

The resonant terms are described with relativistic Breit-Wigner amplitudes as in equation 4.2, where m_0 denotes the mass and Γ_0 the total width of the resonance.

$$D_k(m_{3\pi}; m_0, \Gamma_0) = \frac{\sqrt{m_0 \Gamma_0}}{m_0^2 - m_{3\pi}^2 - i m_0 \Gamma(m_{3\pi})} \tag{4.2}$$

The Breit-Wigner intensity as a function of mass is plotted in figure 4.1a for the case of a narrow, isolated resonance, while the phase of the amplitude δ is shown in figure 4.1b. It rises from 0° to 180° and passes 90° at the peak position m_0 of the resonance.

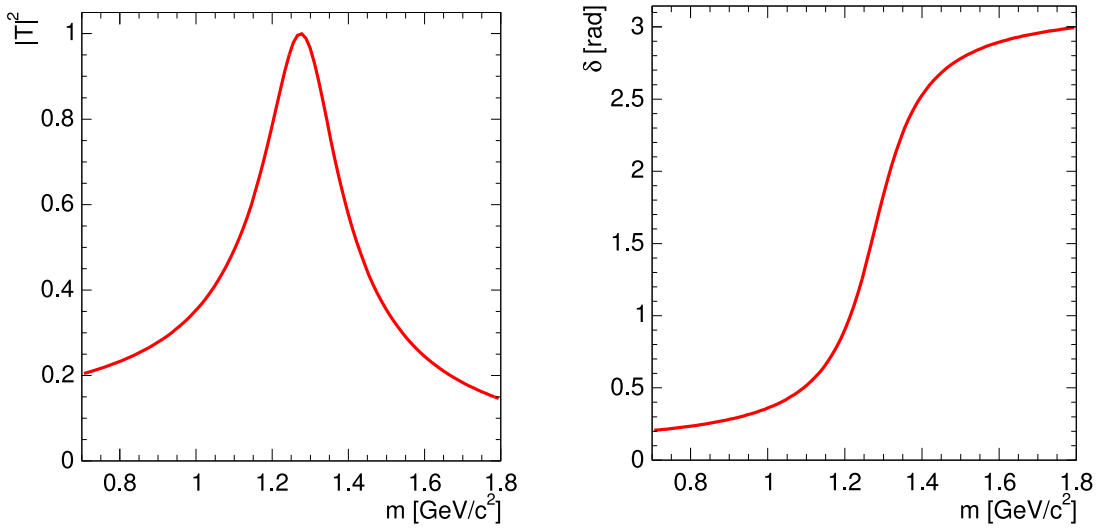

(a) Intensity (b) Phase

Figure 4.1: Example of a simple relativistic Breit-Wigner [50].

The mass-dependent width $\Gamma(m_{3\pi})$ in the denominator takes into account the decay phase space, which is described by including the dominant decay channels. In the numerator on the contrary the phase-space for a decay into the particular partial wave, where the resonance is measured in, has to be considered for the mass-dependence. Therefore to be able to use the same amplitude for multiple waves this part is factored out and accounted in the factor $\varphi_\alpha^\varepsilon(m_{3\pi})$ in equation 4.1. Such a parametrisation is used to model the well-known resonances $a_1(1260)$ and $a_2(1320)$. However, due to a lack of knowledge about their dominant decays $\Gamma(m_{3\pi})$ is reduced to a constant for all other resonances considered here:

$$\Gamma(m_{3\pi}) = \Gamma_0$$

For the $a_1(1260)$ the so-called Bowler parametrisation [51] is used, where the phase-space $\varrho_{\rho\pi}^{1^+S}(m)$ for a $\rho\pi$ S-wave decay with an orbital angular momentum S is explicitly calculated taking into account the width of the $\rho(770)$:

$$\Gamma(m_{3\pi}) = \Gamma_0 \frac{m_0}{m_{3\pi}} \frac{\varrho_{\rho\pi}^{1^+S}(m_{3\pi})}{\varrho_{\rho\pi}^{1^+S}(m_0)} \tag{4.3}$$

The mass-dependent width of the $a_2(1320)$ is approximated by taking into account its decay into $\eta\pi$ with a branching fraction $x = 20\%$ and by attributing the remaining branching fraction of $(1-x) = 80\%$ to the $\rho(770)\pi$ channel:

$$\Gamma(m_{3\pi}) = \Gamma_0 \frac{m_0}{m_{3\pi}} \left[(1-x) \frac{q_\rho(m_{3\pi}) F_L^2(q_\rho(m_{3\pi}))}{q_\rho(m_0) F_L^2(q_\rho(m_0))} + x \frac{q_\eta F_L^2(q_\eta(m_{3\pi}))}{q_\eta(m_0) F_L^2(q_\eta(m_0))} \right]$$

In contrast to the $a_1(1260)$ the $\rho(770)$ is here treated as a stable particle. The break-up momenta of the $\rho(770)\pi$ and $\eta\pi$ decays are denoted $q_\rho(m)$ and $q_\eta(m)$. Their general form

is with the pion mass m_π and the isobar mass m_{Isobar}:

$$q_{\text{Isobar}}(m) = \frac{\sqrt{(m^2 - (m_\pi + m_{\text{Isobar}})^2)\,(m^2 - (m_\pi - m_{\text{Isobar}})^2)}}{2m} \tag{4.4}$$

The Blatt-Weisskopf centrifugal-barrier factors $F_L(q)$ by [52] account for the orbital angular momentum $L = 2$ in both two-body decays.

The coherently added non-resonant terms account for alternative production processes, like the Deck-effect (see section 1.3.2). Unfortunately there are no generally accepted parametrisations available and therefore a phenomenological approach was chosen, which, as shown in section 4.4.4, introduces a large systematic uncertainty. For partial waves with a significant non-resonant contribution the non-resonant terms are modelled with the free parameters b and c_i according to:

$$D_k(m_{3\pi}, t'; b, c_0, c_1, c_2) = (m_{3\pi} - m_{\text{threshold}})^b e^{(c_0 + c_1 t' + c_2 t'^2) q(m_{3\pi})^2} \tag{4.5}$$

The break-up momenta $q(m_{3\pi})$ are the same function as for the resonances using the isobar given in the respective partial wave. $m_{\text{threshold}}$ is an empirical value fixed to 0.5.

In order to stabilise the fit by reducing the total number of free parameters for smaller waves or waves with small non-resonant contributions the simpler parametrisation in equation 4.6 was used for the non-resonant terms, which corresponds to equation 4.5 where all free parameters except c_0 are set to zero. In both cases the non-resonant amplitudes are purely real.

$$D_k(m_{3\pi}; c_0) = e^{c_0 q(m_{3\pi})^2} \tag{4.6}$$

How the different contributions manifest themselves in the intensity spectra of the two dominant waves is shown in figure 4.2. In the logarithmic scale it is visible that the model contains two resonances in each of these waves. The ones at lower masses are the ground states $a_1(1260)$ for the 1^{++} wave and $a_2(1320)$ for the 2^{++} wave. The resonances at higher masses are associated excited states and denoted a_1' and a_2'. While the a_1' appears as a shoulder, the a_2' is an example that due to interferences a resonances can also create a pronounced dip.

The relative phases for multiple interfering resonances are illustrated exemplarily in figure 4.3, which shows the part of the spin-density matrix that contains the $1^{++}0^+\rho(770)\pi S$ and the $2^{++}1^+\rho(770)\pi D$ waves. Here the phase motion of the narrow $a_2(1320)$ is nicely visible at $1.3\,\text{GeV}/c^2$, but its low- and high-mass behaviour gets distorted by additional resonances in both waves. The purely real non-resonant terms only contribute to the phase in form of an offset.

The couplings multiplied to the dynamical terms $D_k(m_{3\pi}, t'; \xi_k)$ are complex and determine the strength of each component as well as the phases relatively to the other dynamical terms and thereby the interferences. There exists one such coupling for each term in each wave for each t' bin and since they all have to be extracted from the data they are the largest fraction in terms of number of fit parameters. However, they are luckily entering equation 4.1 at maximum quadratically and can therefore be determined much more reliable than the shape parameters ξ_k.

The parametrisation of the spin-density matrix in principal has to be applied to all 3269 elements with the exception of the flat wave, but this is practically not possible. Therefore

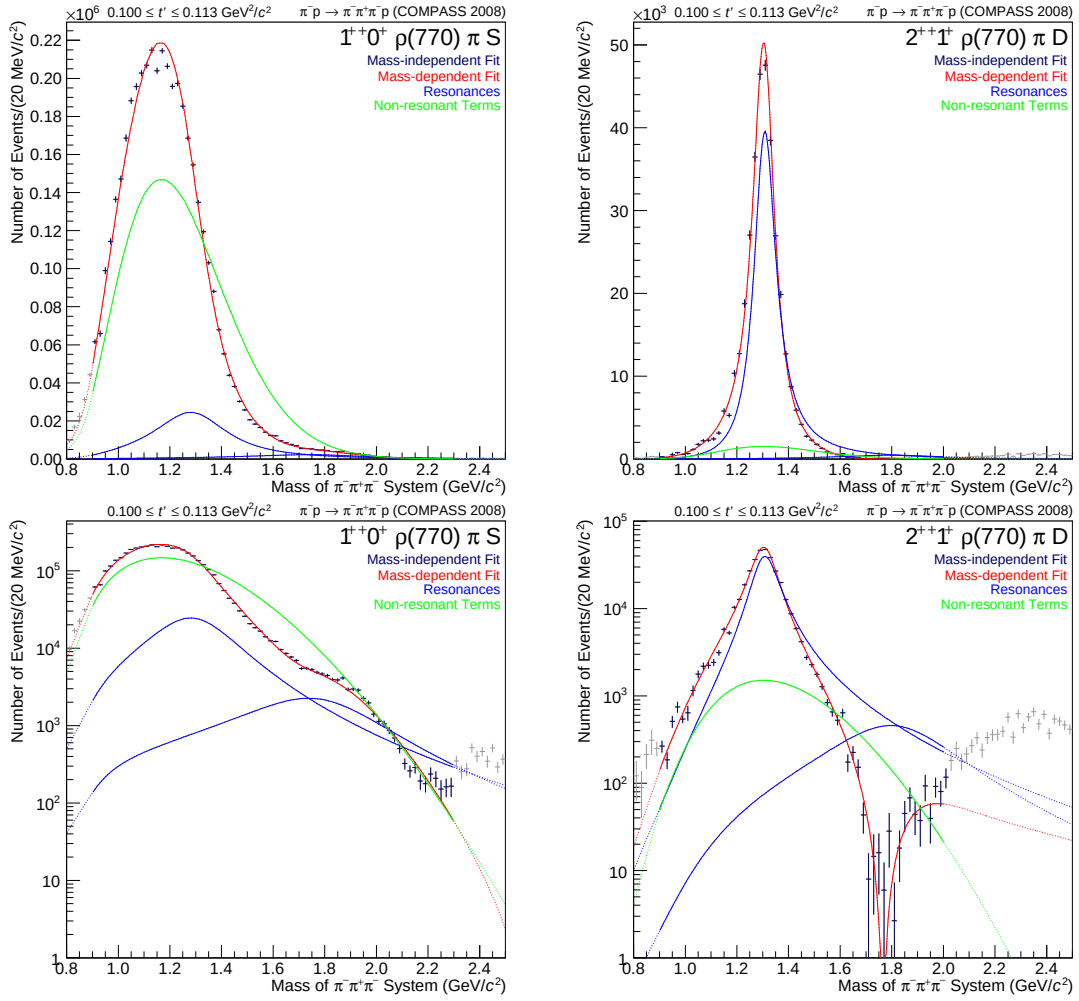

Figure 4.2: Intensity of the $1^{++}0^{+}\rho(770)\pi S$ (left) and the $2^{++}1^{+}\rho(770)\pi D$ (right) partial waves for the lowest t' bin in linear (upper row) and logarithmic scale (lower row). The red line represents the total mass-dependent fit, whereas the other lines show the individual components, being the resonant terms (blue) and the non-resonant terms (green). While the lines are solid inside and dotted outside of the fit range of the mass-dependent fit, the markers representing the mass-independent fit are blue inside and grey outside of this fit range.

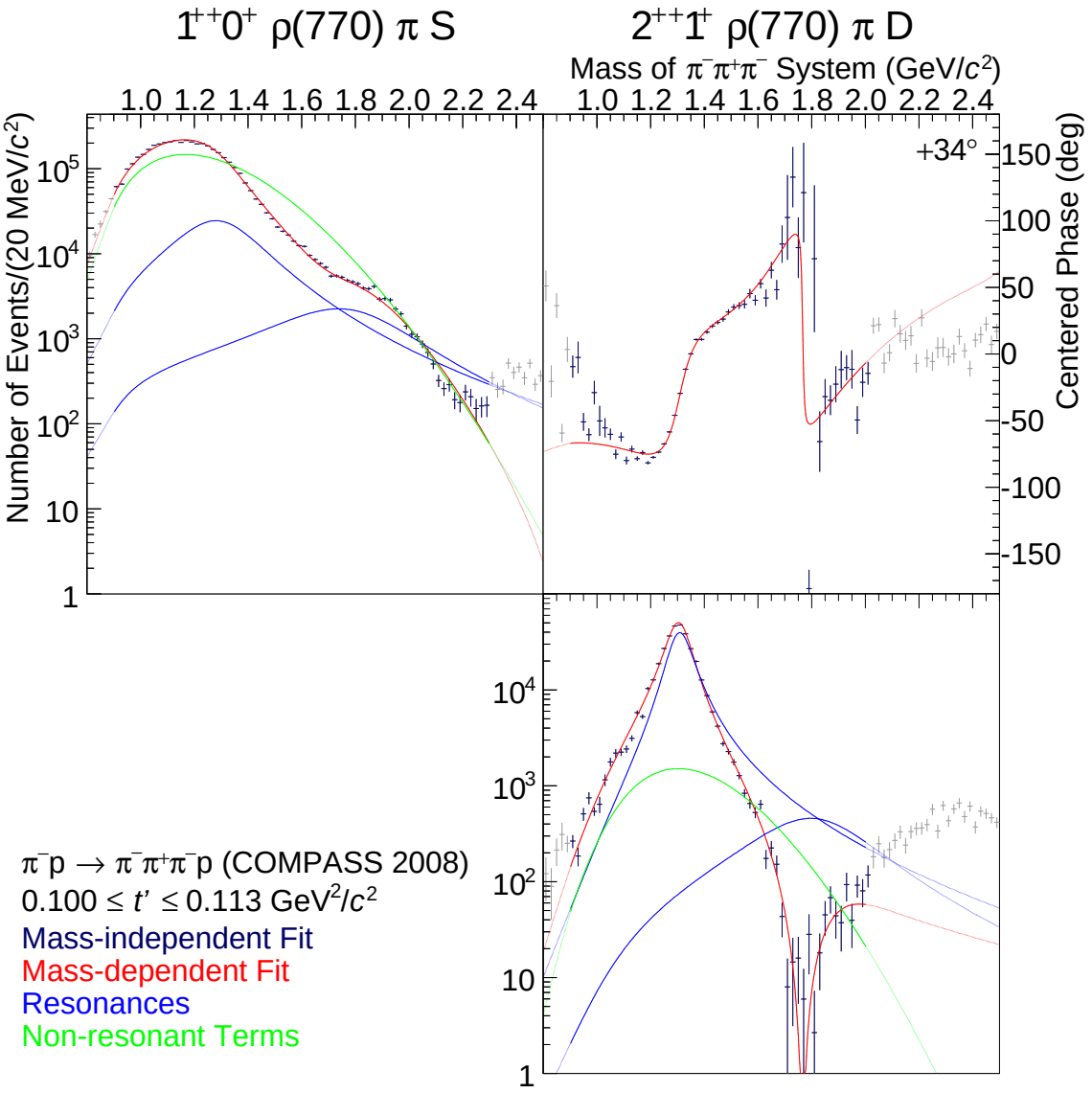

Figure 4.3: Part of the fitted spin-density matrix showing the $1^{++}0^{+}\rho(770)\pi S$ and the $2^{++}1^{+}\rho(770)\pi D$ wave for the lowest t' bin. The colour scheme is the same as in figure 4.2. The plots along the diagonal show the partial-wave intensities. The relative phase presented in the upper right plot is given in the form "column − row" and is shifted by $-34°$ in order to be centred in the range between $-180°$ and $+180°$. The offset that has to be added to the values on the axis in order to receive the non-shifted phase is denoted in the right corner of the plot. Furthermore the individual components of the phase are not drawn.

as a minimal starting set the waves from a previous analysis [16] were chosen, except that the $1^{-+}1^{+}\rho(770)\pi P$ wave has been replaced by the $1^{++}0^{+}f_0(980)\pi P$ wave in order to clarify the resonance behaviour of the newly discovered narrow, isolated peak structure in it. All six fitted partial waves are listed in table 4.1.

The three largest waves are described by two resonances and the more elaborate parametrisation of the non-resonant terms (equation 4.5), whereas the three smaller waves are only allowed to have a single resonance and the simplified non-resonant parametrisation (equation 4.6). While the lower limits of the fit ranges result from a too sparsely populated phase-space that leads to uncertain data points, the upper limits are due to arising new features that are not explainable by the given model, like, for example, the occurrence of a third resonance.

Partial wave	**Resonances**	**Non-resonant term**	**Fit range[GeV/c^2]**
$1^{++}0^{+}\rho(770)\pi S$	$a_1(1260), a_1'$	eq. 4.5	0.90 to 2.30
$2^{++}1^{+}\rho(770)\pi D$	$a_2(1320), a_2'$	eq. 4.5	0.90 to 2.00
$2^{-+}0^{+}f_2(1270)\pi S$	$\pi_2(1670), \pi_2(1880)$	eq. 4.5	1.40 to 2.30
$0^{-+}0^{+}f_0(980)\pi S$	$\pi(1800)$	eq. 4.6	1.20 to 2.30
$4^{++}1^{+}\rho(770)\pi G$	$a_4(2040)$	eq. 4.6	1.25 to 2.30
$1^{++}0^{+}f_0(980)\pi P$	$a_1(1420)$	eq. 4.6	1.30 to 1.60

Table 4.1: Wave set with six waves.

The 6×6 spin-density sub matrix corresponding to the wave set of table 4.1 is shown for the lowest t' bin in figure 4.4. However, the fit is performed in all t' bins at the same time, where the shape parameters ξ_k are identical in each t' bin. The behaviour as a function of t' has to be explained only by the couplings and the explicit t' dependence of the shape of some of the non-resonant terms. This means that the fit has to describe roughly 14 900 data points with in total 352 real parameters: 319 for the couplings, 18 for the resonances and 15 for the non-resonant terms.

In order to see why the separation in t' and thereby the large number of couplings is needed the intensities of the $1^{++}0^{+}\rho(770)\pi S$ wave are shown in figure 4.5 for all eleven t' bins. While a shift of the $a_1(1260)$ peak with t' was already visible in the mass-independent fit, it can now be discussed in terms of the applied model. In the low-t' region the peak is on the low-mass side of the real resonance peak, whereas for high t' it is on the high-mass side. It is explained in the given model by a shift of the relative phase between the $a_1(1260)$ and the non-resonant terms of about 180° over the shown t' range. Thereby these two components interfere at low t' constructively below the Breit-Wigner resonance, where the phase of its amplitude is approximately 0°, and destructively above it, where the phase of the amplitude is approximately 180°, while it is exactly the other way round at high t'.

In the $2^{++}1^{+}\rho(770)\pi D$ wave plotted in figure 4.6 the steadiness of the $a_2(1320)$ peak is now attributed to the comparatively small non-resonant contribution. In logarithmic scale, however, the dip in the high-mass tail vanishes for high t'. This can be explained by a change of the relative intensity of the a_2' with respect to the $a_2(1320)$ in combination with a slight shift in their relative phase away from a completely destructive interference.

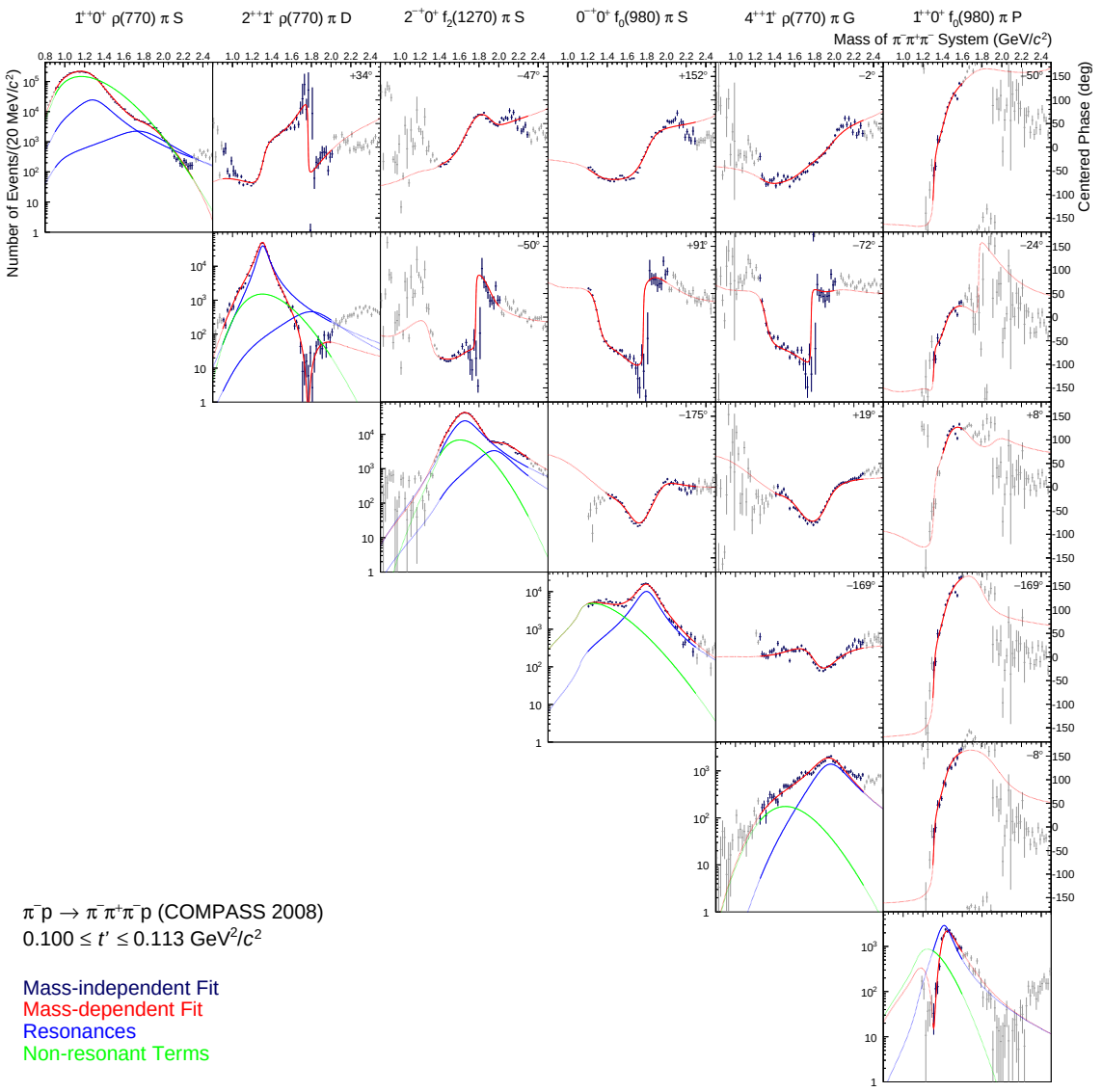

Figure 4.4: Fitted spin-density sub matrix for the lowest t' bin containing the waves from table 4.1 in the same order. An enlarged version can be found in section A.1 in the appendix. The colour scheme is described in figure 4.2 and the plotting of the relative phases is commented in figure 4.3.

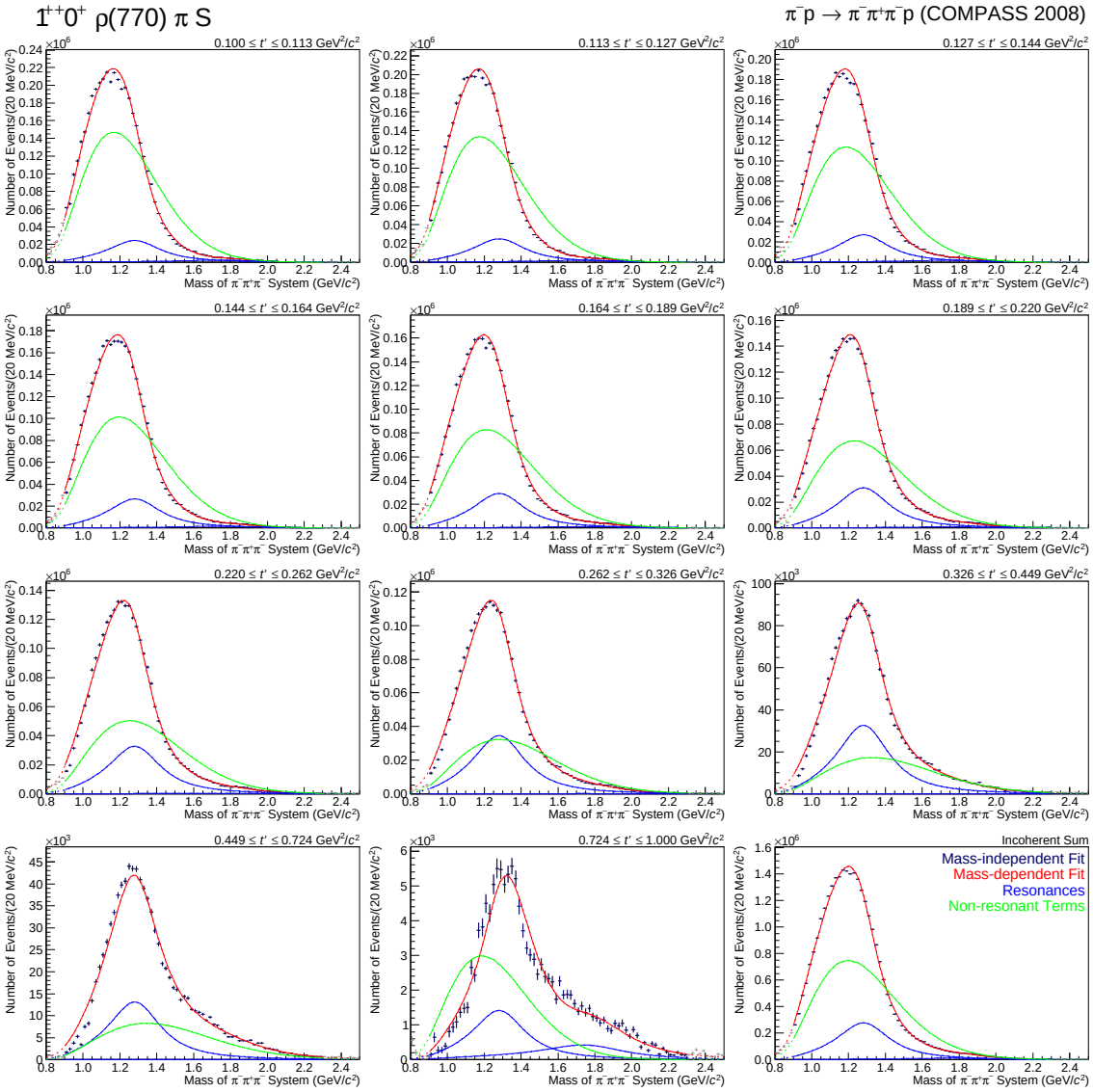

Figure 4.5: Intensity of the $1^{++}0^{+}\rho(770)\pi S$ wave as a function of t' in linear scale. t' is increasing first from left to right and then from top to bottom. The lower right corner shows the intensity sum of all eleven t' bins. The colour scheme is the same as in the previous plots and described in figure 4.2.

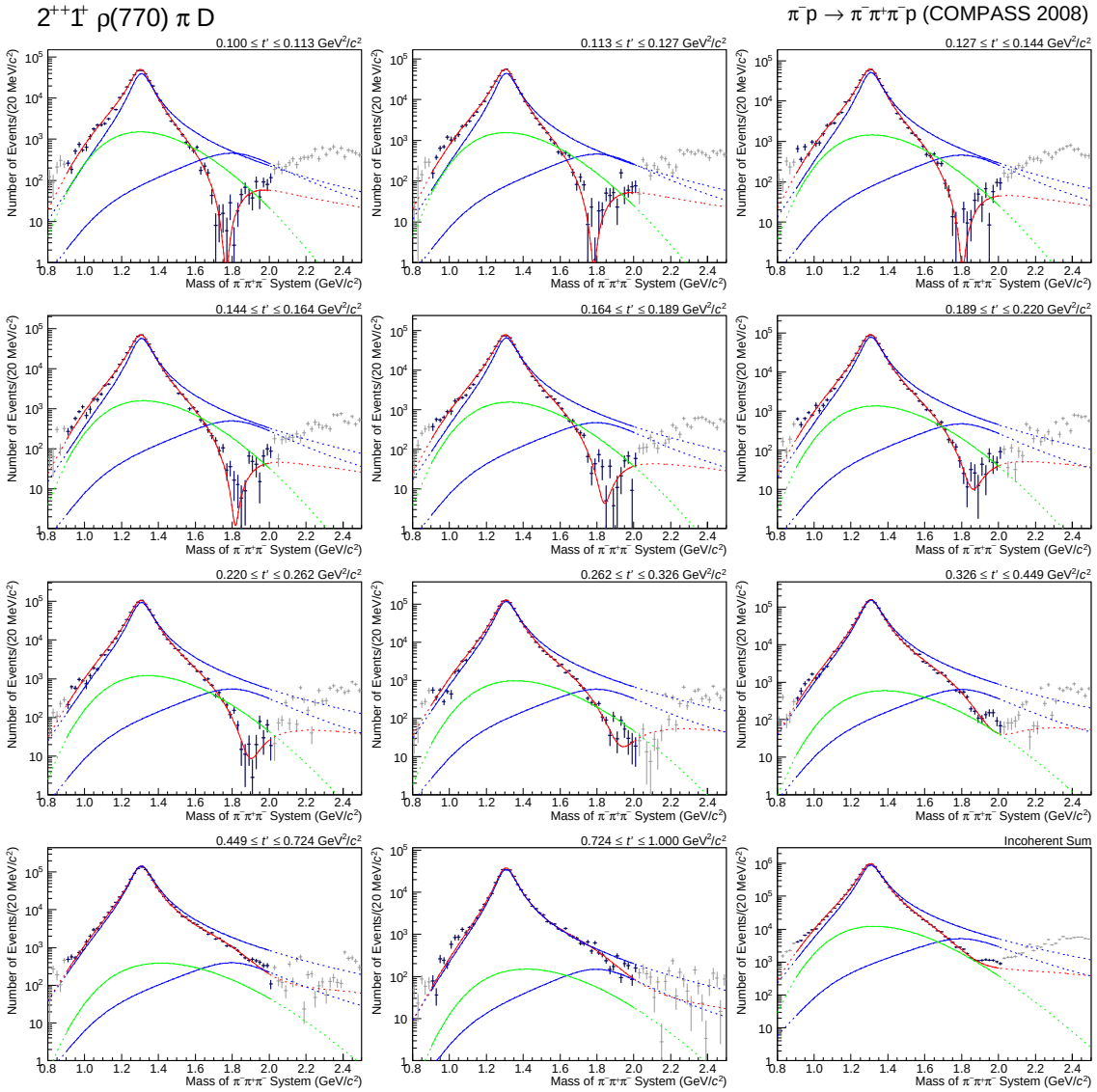

Figure 4.6: Intensity of the $2^{++}1^{+}\rho(770)\pi D$ wave as a function of t' in logarithmic scale. The ordering in t' is the same as in figure 4.5. The colour scheme is described in figure 4.2.

Having seen how the model is able to describe the features of the established resonances, it is interesting to look at how well it can explain the newly found potential resonance in the $1^{++}0^{+}f_0(980)\pi P$ wave. Considering the intensity shown in figure 4.7 the fit is matching the data consistently with the exception of the highest t' bin, where the signal looses its significance. Furthermore the relative phases with respect to other waves given in figure 4.8 feature in all t' bins a significant phase motion, so it can be safely concluded that the $a_1(1420)$ is consistent with a Breit-Wigner resonance description.

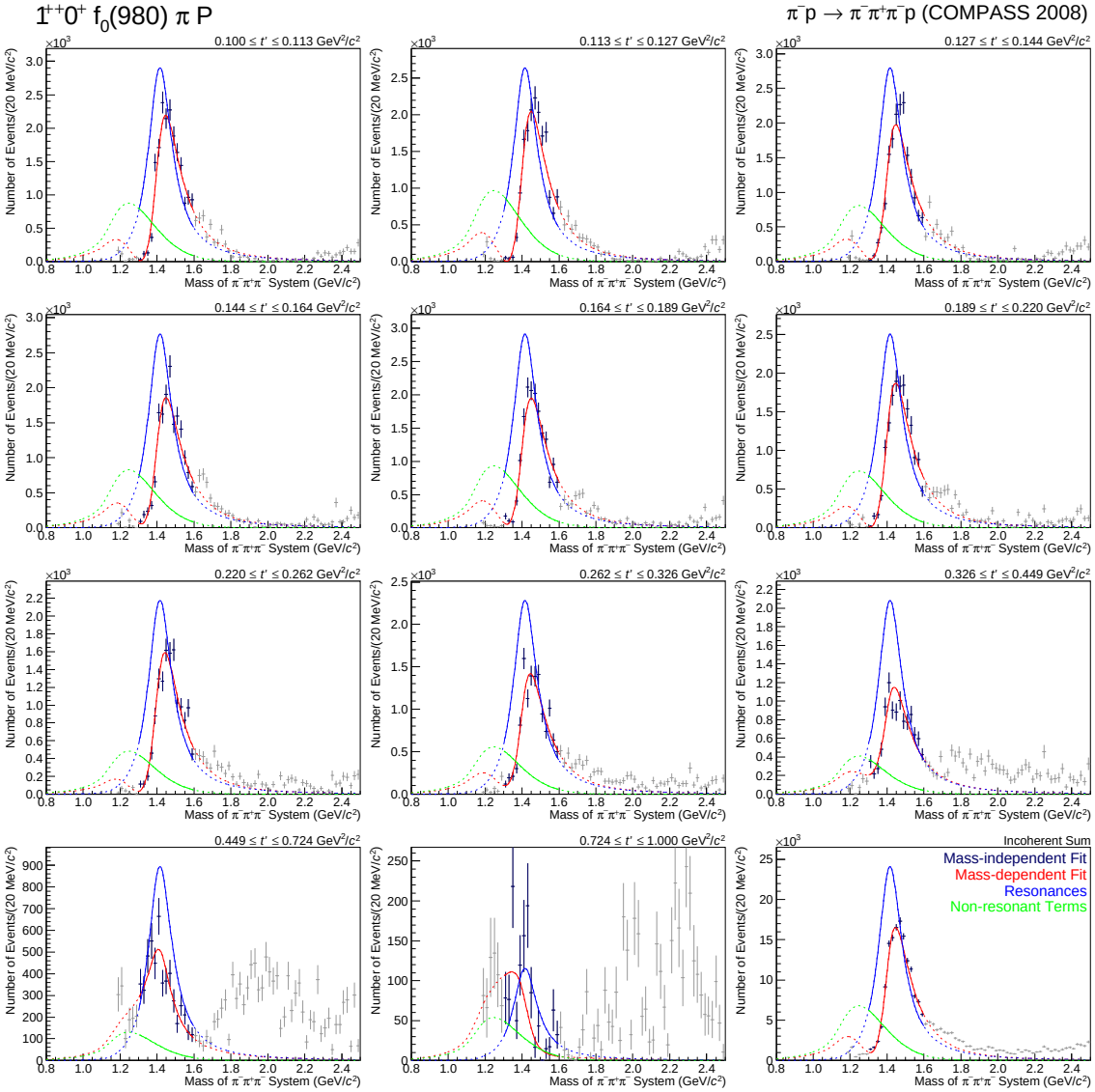

Figure 4.7: Intensity of the $1^{++}0^{+}f_0(980)\pi P$ wave as a function of t' in linear scale. The ordering in t' is the same as in figure 4.5. The colour scheme is described in figure 4.2.

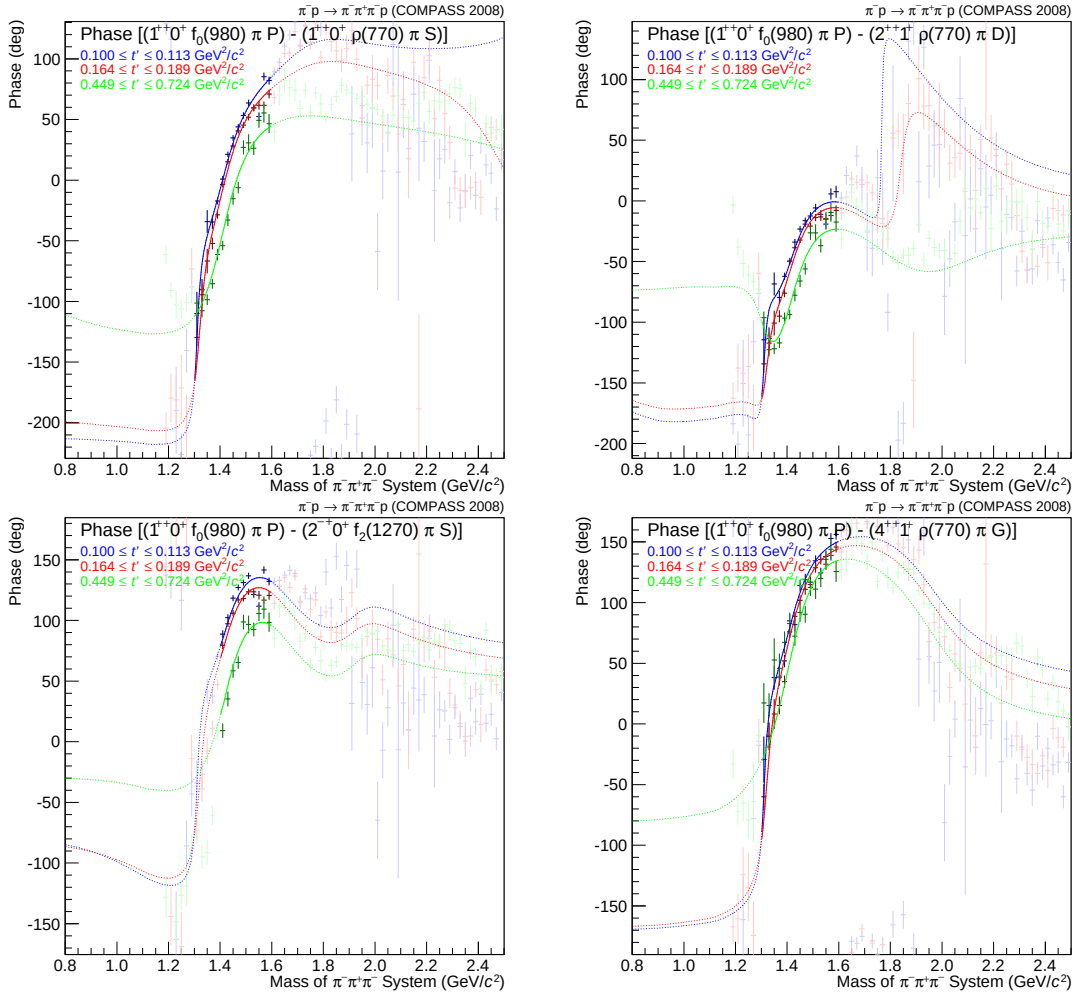

Figure 4.8: Phase of the $1^{++}0^+ f_0(980)\pi P$ wave relative to the $1^{++}0^+\rho(770)\pi S$ (upper left), $2^{++}1^+\rho(770)\pi D$ (upper right), $2^{-+}0^+ f_2(1270)\pi S$ (lower left) and $4^{++}1^+\rho(770)\pi G$ (lower right) waves for the lowest (blue), intermediate (red) and second highest (green) t' bin.

4.2 Systematic Studies of the Fit Procedure

What so far has been neglected is that the result described in the previous section was not obtained by performing only a single fit, but in fact was selected from a set of 1000. This turned out to be necessary, because the fit result is observed to be dependent of the way the fit is performed. This can be seen in the distribution of the found χ^2 values in figure 4.9, where different starting values and different orders of releasing the parameters were chosen for the same model fitted to the same data. In the ideal case the fit should always converge to the same minimum, but the χ^2 values are obviously spread over a wide range with some values that are more frequently appearing than others. However, it gets even more complicated, because many of these solutions are not "physical" in the sense that the fitter uses the given freedom in a way it is not intended. For example, in

some fit results the resonant term of the excited resonance is assigned nearly the same mass as the ground state in the same partial wave in order to compensate imperfections in the peak description of the ground-state resonance, which contradicts the model intention. Such "unphysical" solutions unfortunately include the ones with the lowest χ^2, but before it can be discussed, how to properly handle this, it has to be explained, how the different fits are performed.

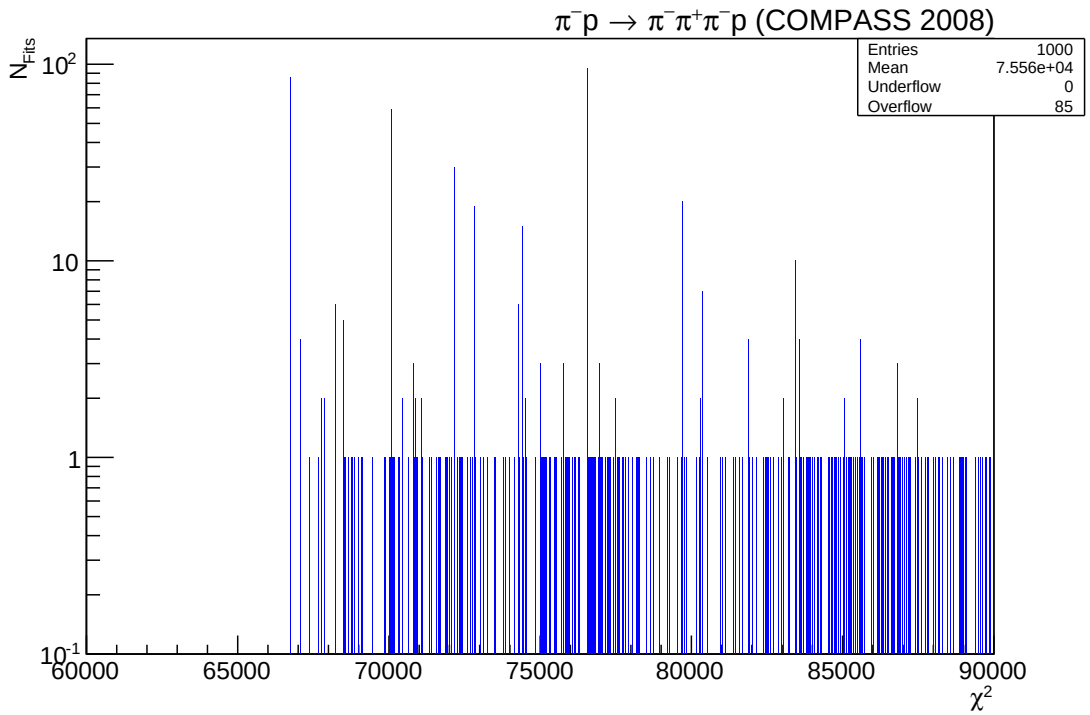

Figure 4.9: Distribution of χ^2 values resulting from fits with random starting values and different orders of releasing the fit parameters.

In a first step 250 different sets of starting values are generated by drawing the dynamical parameters ξ_k uniformly from certain ranges, which are based on previous fits as well as on the values and errors listed in [13]. The chosen intervals and the distribution of the starting values for the $a_1(1260)$ and the a_1' can be seen in figure 4.10. One important observation is that the starting values of the fits resulting in the best χ^2 are fairly equally spread over the whole range. This is the same for all other dynamical parameters and shows that changes of the starting range are not likely to cause any systematic effects.

After the creation of the 250 sets of starting values, for each of them the best start values for the couplings are determined. This can be done separately for all t' bins, because they are only connected by the dynamical parameters. Since for the lowest t' bin basically no expectation values exist, the real and imaginary parts of the couplings are each drawn uniformly 25 times in the range between -1 and $+1$. These are then used as starting values for 25 fits, where the ξ_k are fixed to the previously drawn values. Finally the

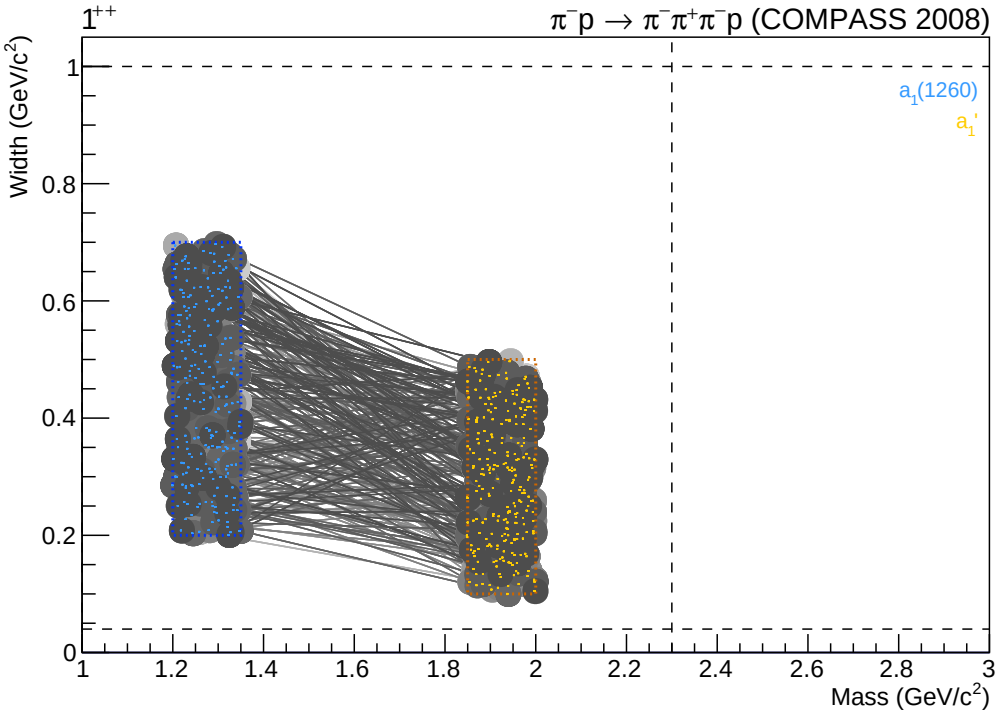

Figure 4.10: Start-value distribution for the mass and the width of $a_1(1260)$ (blue) and a_1' (yellow). The shading of the discs around the coloured dots indicate the resulting χ^2 values from best (dark grey) to worst (light grey) in 10 grey scales grouping always 10% of the fits. The lines in the same grey shades connect the parameter values of the same fit. The ranges where the starting values are uniformly drawn from are indicated by the dotted rectangles. The horizontal black broken lines at widths of 40 and 1000 MeV/c^2 show the limits applied to all resonances in the fit. The mass limits are 1 and 3 GeV/c^2, respectively, and are indicated by the range of the x-axis. The vertical broken line is the upper limit of the fit range of the partial waves, which contain the plotted resonances. For the $1^{++}0^+\rho(770)\pi S$ wave shown here the lower limit is at 0.9 GeV/c^2 and therefore below the general mass limit of 1 GeV/c^2 and not drawn.

couplings from the fit with the best χ^2 are chosen. This procedure can now either be repeated independently for all other t' bins or one can exploit the fact that the couplings should not vary strongly from bin to bin and therefore take the values from the lower neighbouring t' bin as starting values. Both methods are complimentary and therefore both are applied, choosing at the end the solution with the lowest χ^2 for the couplings. It should be noted that for a set of dynamical parameters close to their later determined optimum values in the χ^2 minimum both methods yield the same values.

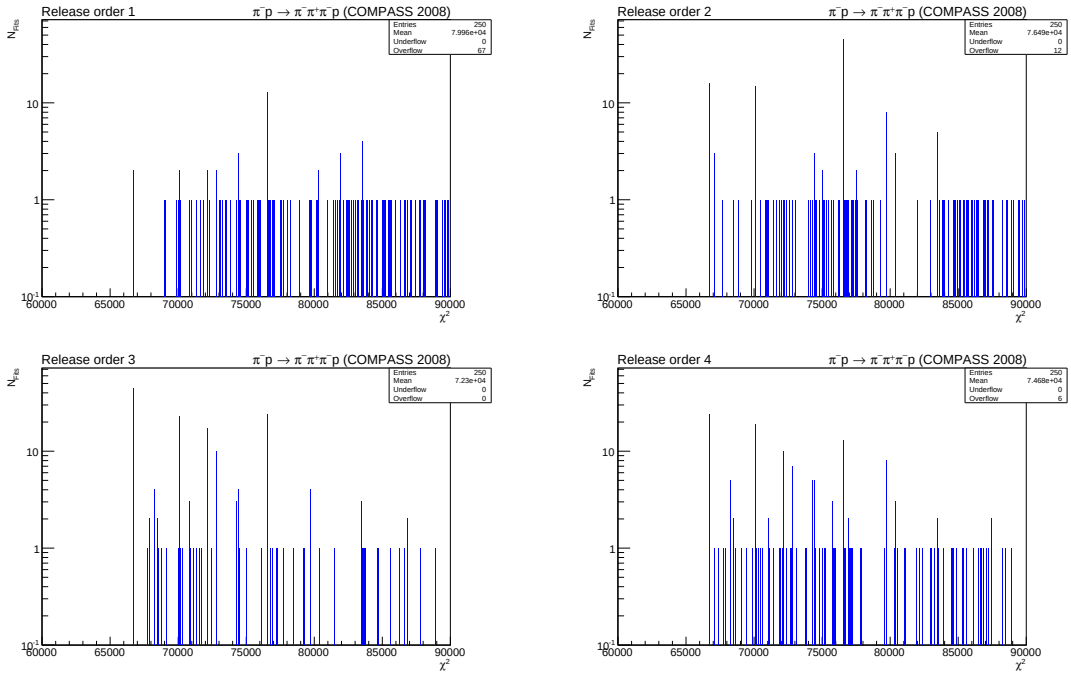

Figure 4.11: Distributions of χ^2 values resulting from fits with random starting values split into the individual release orders described on page 48.

Having now obtained 250 sets of randomly distributed ξ_k with their individually best couplings, they are used as starting values for the final fits, but as previously mentioned the results also depend on the order of releasing the parameters. Looking at figure 4.11, which shows the previously given distribution of χ^2 values separated into the four used release orders, it is evident that the more frequent χ^2 values appear in all of them, but have strongly varying probabilities. The parameter release orders were chosen with the purpose of enhancing the probability of convergence to the global minima, but keeping the introduced method bias minimal. Furthermore it was paid attention that they explore diverse paths to the solution. This resulted in the following four methods, where all couplings are free during the whole fit and the shape parameters are partially released in up to four steps, so that in the end all parameters are free:

Method 1: All dynamical parameters ξ_k are released from the beginning and the fitter has to determine the optimal way to the minimum by itself. Thereby no additional bias is introduced.

Method 2: In a first step only the shape parameters of the non-resonant terms are released, since they are in general much less well-known then the ones of the resonances. In a second step additionally all remaining shape parameters are released.

Method 3: In a first step only the dynamical parameters of the non-resonant terms of the three waves with the highest intensity, namely $1^{++}0^{+}\rho(770)\pi S$, $2^{++}1^{+}\rho(770)\pi D$ and $2^{-+}0^{+}f_2(1270)\pi S$, are freed. Then additionally the resonance parameters of these three waves, denoted major waves, are released and in a final step all the remaining ones are released. Thereby the largest contributions to the χ^2 are fitted first.

Method 4: This is a combination of the previous two release orders by first fitting the shape parameters of the non-resonant terms of the major waves, then additionally those of the non-resonant terms of the so-called minor waves, then the resonance parameters of the large waves and finally those of the small waves.

Using these methods on all 250 sets of starting parameters results in the 1000 fits, whose χ^2 values are shown in figures 4.9 and 4.11. The topic of the rest of this section will now be, how to find the best physical solution.

Starting with the resulting distributions for the mass and width of the $a_1(1260)$ and the a_1' in figure 4.12 the first observation is that for some fits the estimated parameters have extremely large error bars, while for others the parameters are at the introduced limits. The large error bars are due to a failed convergence, whereas the fits at the limits are in a region, which is either ruled out by the scope of the given model or by physical arguments.

In detail the low-mass limit is set to $1\,\mathrm{GeV}/c^2$, since there are no known 3π resonances below that value. The high-mass limit was chosen to be $3\,\mathrm{GeV}/c^2$, because the maximum fit range is $2.3\,\mathrm{GeV}/c^2$ and anything above that contributes only via its tail thereby causing only negligible phase motion. The limits on the width at $40\,\mathrm{MeV}/c^2$ and $1\,\mathrm{GeV}/c^2$ are defined by mostly the same arguments. Excited resonances are not expected to be drastically smaller than their ground states and if they are extremely wide their phase motion is changing so slowly with mass that they cannot be distinguished from the non-resonant terms anymore. So by removing those unphysical fits only around 500 remain. They still spread over a fairly wide range in terms of parameter and χ^2 values as can be seen in figures 4.13 and 4.14. The three smaller $0^{-+}0^{+}f_0(980)\pi S$, $4^{++}1^{+}\rho(770)\pi G$ and $1^{++}0^{+}f_0(980)\pi P$ waves are not shown, because the fit always finds roughly the same parameter values.

In the distribution of χ^2 values in figure 4.13 can be seen that most minima are found only rarely. One possible explanation is that these are local minima into which the fitter gets trapped. The observation that none of them are found with a lower χ^2 than the lowest frequently occurring minimum leads to the impression that the fitter gets caught by ripples in the χ^2 manifold, while approaching another minimum. Therefore these spurious solutions are removed by requiring that a similar χ^2 has to be found a number of times within intervals of 0.01. In order to determine a proper threshold on how many fits have to result in a specific χ^2 in order to accept the solution, the histogram in figure 4.13 is projected onto the y-axis. This projections shows how often $N_{\mathrm{same}\chi^2}$ fits with similar χ^2 have been found. After multiplying each $N_{\mathrm{same}\chi^2}$ bin in the projection with its x-value

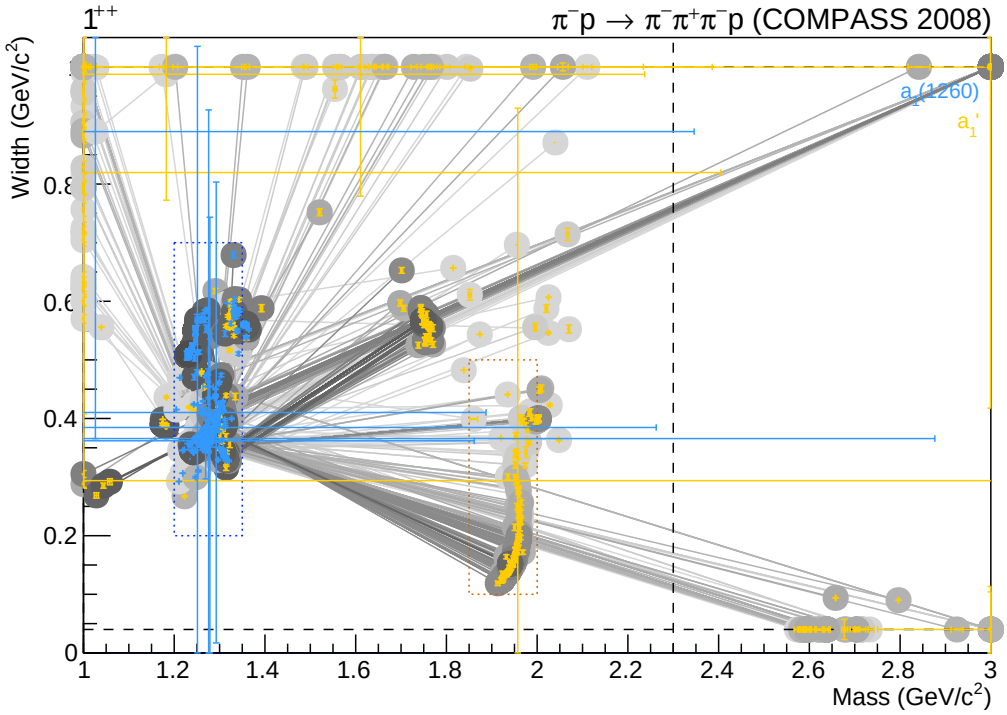

Figure 4.12: Masses and widths of the $a_1(1260)$ (blue) and the a_1' (yellow) for all 1000 fits. The used plotting scheme is explained in figure 4.10 with the exception that in this plot the statistical errors given by the fitter are drawn in addition.

$N_{\text{same}\chi^2}$ an interpretation as a not normalised probability of a fit to result in such a χ^2 becomes possible. This is plotted in figure 4.15.

First a strong decrease of the probability with $N_{\text{same}\chi^2}$ is observable as it is expected for spurious solutions. Then the distribution rises again linearly due to the frequently found minima. Furthermore large gaps are eminent for the region above the spurious solutions. Therefore the cut is chosen to be in the first pronounced gap that has at least three not populated $N_{\text{same}\chi^2}$ bins. After applying this cut the distribution of the resonance parameters looks much cleaner (see figure 4.16).

However, looking in more detail at the 1^{++} resonances the a_1' has for the best fits in terms of χ^2 a mass that is just about 70 MeV/c^2 larger than the one of the $a_1(1260)$. In this solution the fitter misuses the a_1' to better describe the rising flank of the $a_1(1260)$ peak, as can be seen in figure 4.17a, instead of using it to describe the shoulder in the high-mass tail of the $a_1(1260)$. This gives a first hint that the chosen parametrisation of the $a_1(1260)$ and the non-resonant term are not sufficient to describe the peak shape within the extremely small statistical errors of the $1^{++}0^+\rho(770)\pi S$ wave. However, since these solutions are not physical, they are removed.

In order to generalise this cut it has to be defined, when exactly two resonances in one wave are too close. As an universal measure the phase motion of the resonant terms was

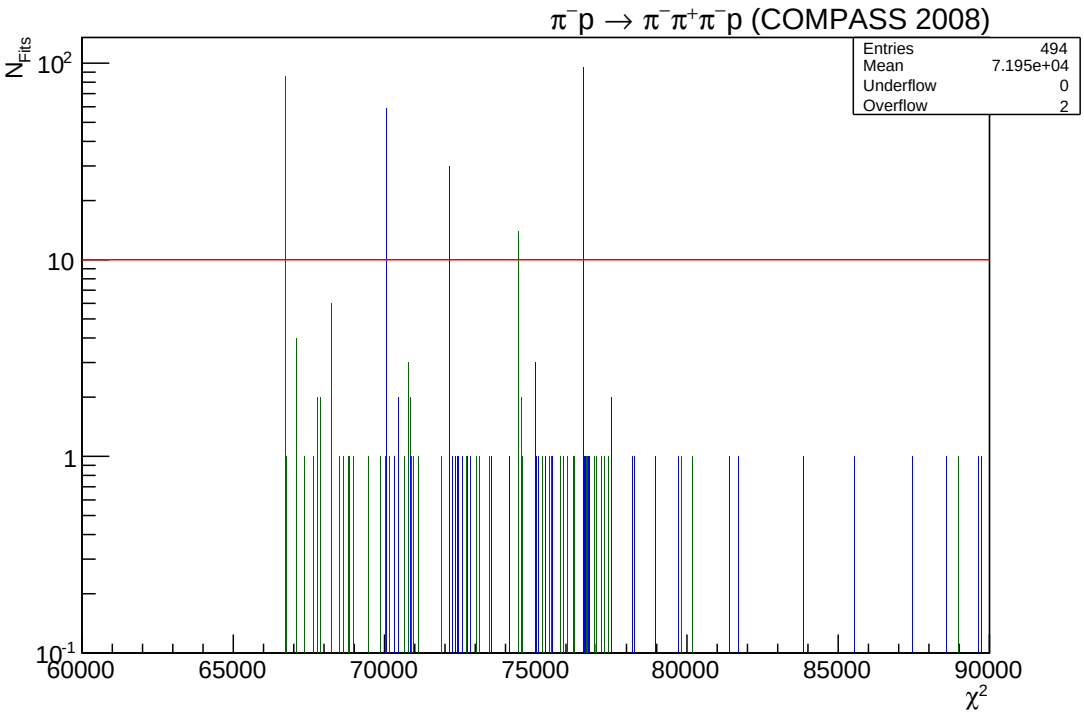

Figure 4.13: Distribution of χ^2 values of converged fits that are not at a parameter limit and cut away (green) or kept (blue) by the later applied physical and model-based restrictions. The red line indicates the cut on spurious solutions applied in the next step. The histogram is binned in steps of 0.01.

chosen defining the centre range by going 22.5° up and down from the phase at the peak mass m_0 and taking the corresponding masses, so that one fourth of the whole phase motion is included in this interval. Then all solutions are removed, where the centre ranges of resonances in the same wave are overlapping.

Furthermore resonances that have a mass outside of the fit range of their wave are contributing only via their tales, which in general have only a slow phase motion and therefore are hard to distinguish from the non-resonant terms. So they are either an indication for another resonance closely above the fit range or simply misused by the fitter as an additional non-resonant term. In the parameter distributions of the $2^{++}1^{+}\rho(770)\pi D$ wave in figure 4.16 one solution is above the fit range, which goes up to $2\,\mathrm{GeV}/c^2$. The corresponding intensity in this partial wave is shown in figure 4.17b and indicates that a third resonance might occur shortly above the fit range. However, including this third resonance and extending the fit range results almost always in unphysical solutions, where one of the resonances becomes extremely broad and works more like a non-resonant term. A typical example is shown in figure 4.18b.

Additionally it may happen that the mass ordering of the resonances in one wave is inverted. Since the parametrisation of the first and the second resonance are in general

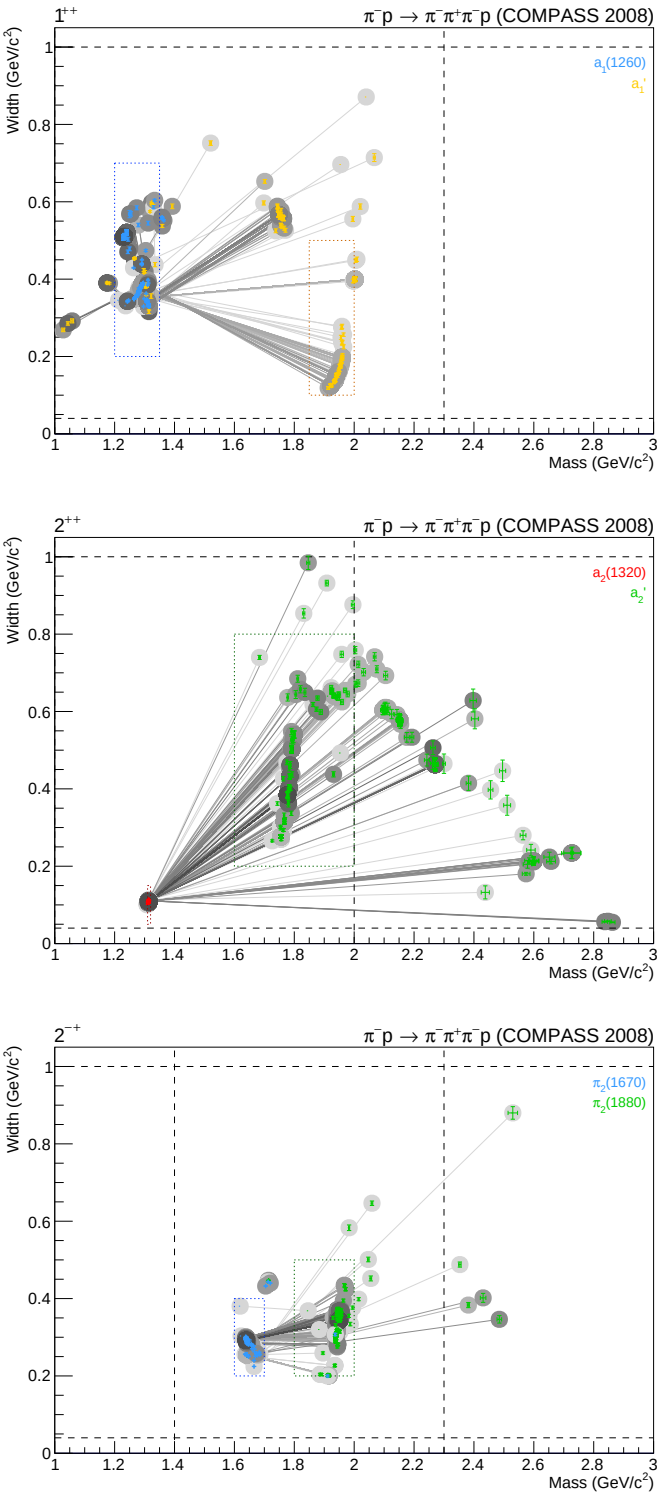

Figure 4.14: Parameter values of $a_1(1260)$ (top, yellow), a_1' (top, blue), $a_2(1320)$ (centre, red), a_2' (centre, green), $\pi_2(1670)$ (bottom, blue) and $\pi_2(1880)$ (bottom, green) for converged fits not at a parameter limit. An explanation of the used plotting scheme can be found in figure 4.12.

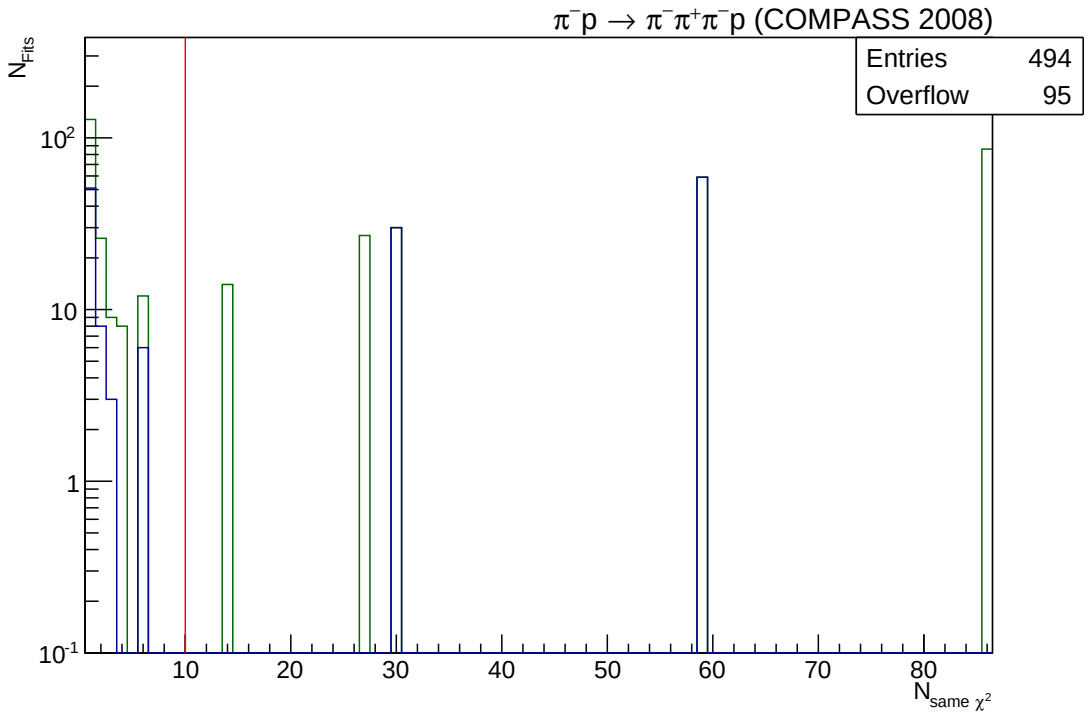

Figure 4.15: Projection of the distribution of χ^2 values in figure 4.13 on the y-axis followed by a multiplication of each $N_{\text{same}\chi^2}$ bin with its x-value $N_{\text{same}\chi^2}$. The histogram can be interpreted as a not normalised probability of a fit to result in a χ^2 interval with $N_{\text{same}\chi^2}$ values. The fits that are cut away (kept) by later applied physical and model-based restrictions are indicated in green (blue). The red line shows the cut on spurious solutions performed in the next step.

not the same, a simple change in the assignment of the resonance labels is not possible. Therefore these solutions have to be removed as well. However, for the model used here all fits, where this occurs, belong to spurious solutions and therefore are already erased.

At the end, when all cuts are applied only about 180 fits corresponding to three different solutions remain. An overview of the exact numbers after each cut is listed in table 4.2, whereas the final parameter distributions are shown in figures 4.19 and 4.20.

Now that all this three solutions are valid, in principal the best in terms of χ^2 should be chosen, but as discussed earlier, the $a_1(1260)$ peak is not well described by the model and even after the unphysical solutions are removed this influences the χ^2. The influence can be shown by removing the contribution of the intensity of the $1^{++}0^+\rho(770)\pi S$ wave from the χ^2 value. The results are given in table 4.3. While the third solution is still the worst, the first and the second solution interchange their order with respect to χ^2. This means that while the first solution describes the $a_1(1260)$ intensity peak better, the second one does a better job for the rest of the data. The distance between the two best solutions in the a_1' parameters suggests that the fitter might have found two different excited resonances,

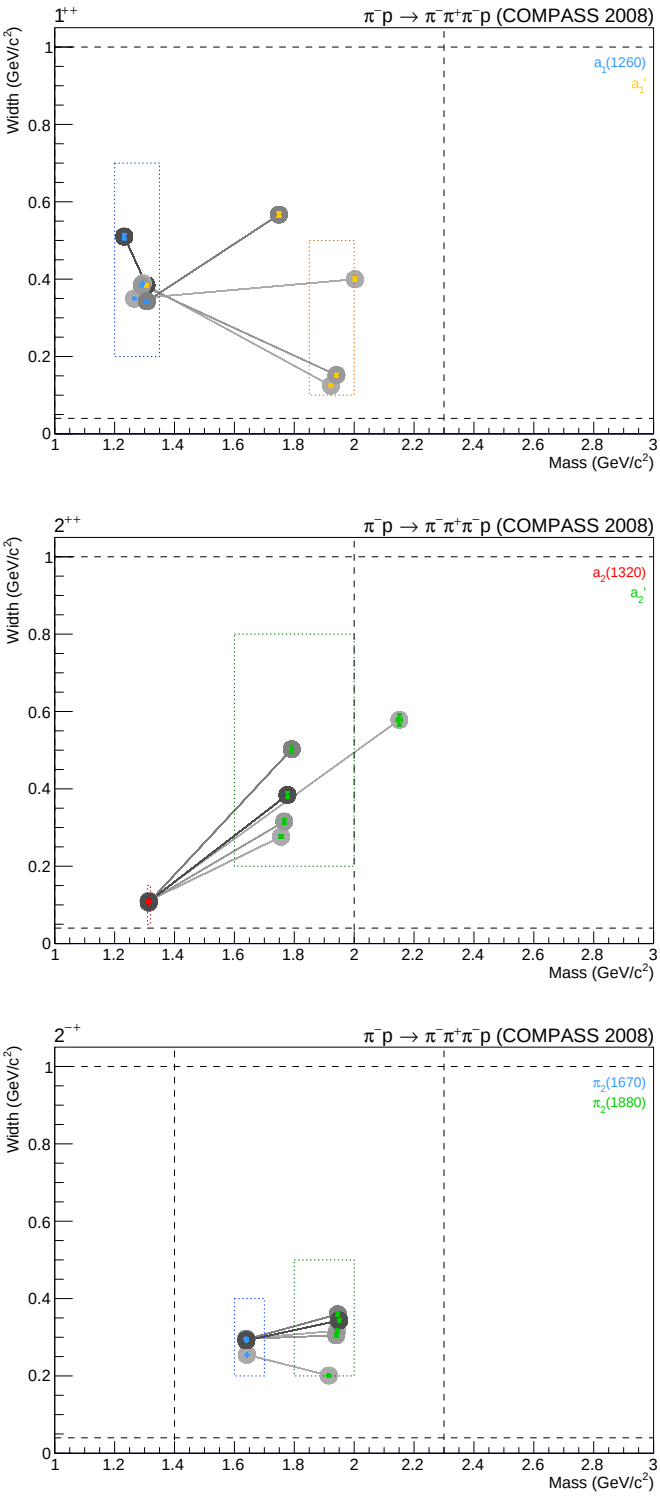

Figure 4.16: Parameter values of $a_1(1260)$ (top, yellow), a_1' (top, blue), $a_2(1320)$ (centre, red), a_2' (centre, green), $\pi_2(1670)$ (bottom, blue) and $\pi_2(1880)$ (bottom, green) after removing spurious solutions. An explanation of the used plotting scheme can be found in figure 4.12.

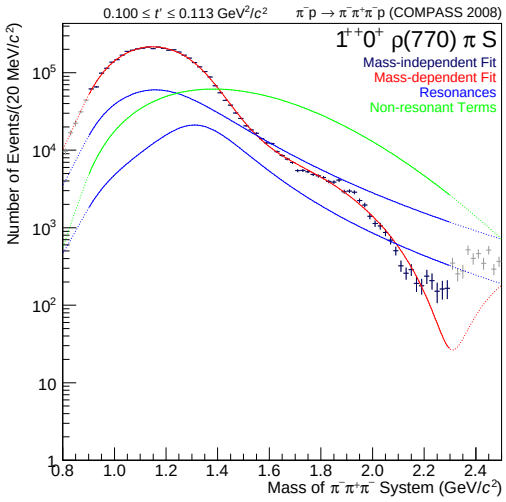

(a) Intensity of the $1^{++}0^{+}\rho(770)\pi S$ wave for the fit that is cut away due to the proximity of resonances.

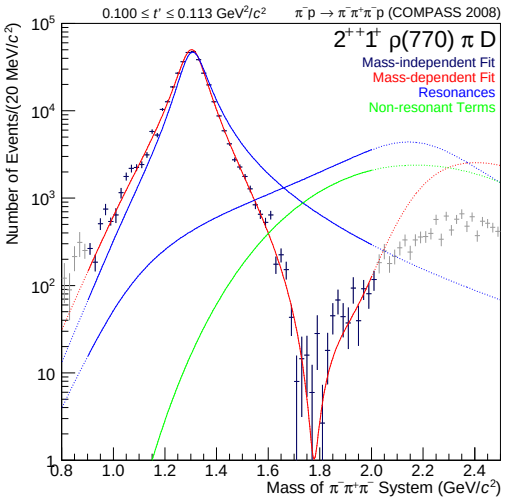

(b) Intensity of the $2^{++}1^{+}\rho(770)\pi D$ wave for the fit that is cut away due to a resonance mass outside the fit range.

Figure 4.17: Examples of physical cuts for the lowest t' bin in logarithmic scale. The colour scheme is described in figure 4.2.

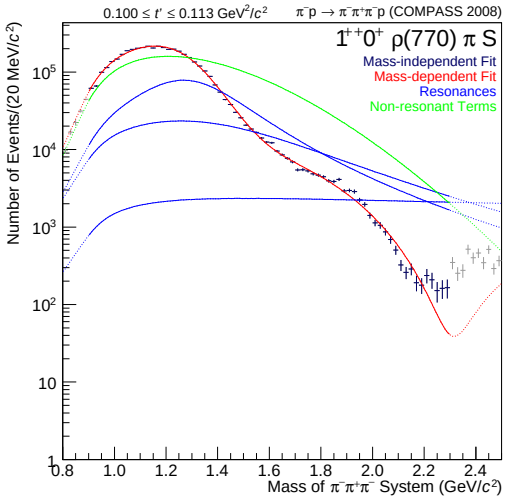

(a) Intensity of the $1^{++}0^{+}\rho(770)\pi S$ wave.

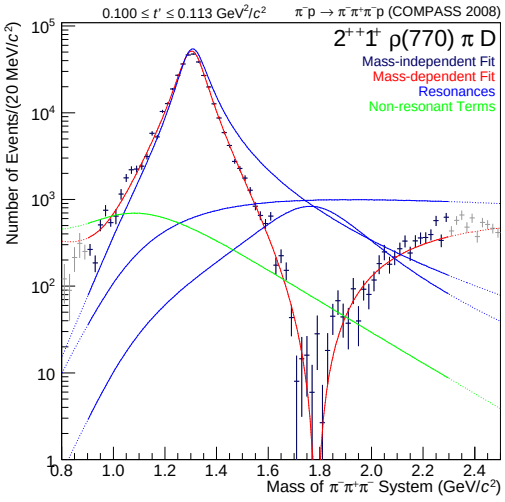

(b) Intensity of the $2^{++}1^{+}\rho(770)\pi D$ wave.

Figure 4.18: Examples of tried fits with three resonances in one wave for the lowest t' bin in logarithmic scale. The colour scheme is described in figure 4.2.

but unfortunately as shown in figure 4.18a the fitter does not give meaningful results when three resonances are included in the $1^{++}0^{+}\rho(770)\pi S$ wave. As this problem already emerged for the case of the 2^{++} sector, it seems to be a general property of the model described here. Therefore at this stage it cannot be decided, which solution should be preferred.

Cut	**Number of remaining fit results**
	1000
Failed convergence	924
Parameter close to limits	494
Spurious solutions	311
Interchange of resonance positions	311
Proximity of resonances	198
Resonances outside fit range	184

Table 4.2: Overview on the applied cuts.

Solution	1	2	3
Total χ^2	70 072	72 162	76 576
χ^2 without the intensity of the $1^{++}0^{+}\rho(770)\pi S$ wave	61 639	61 489	67 638

Table 4.3: χ^2 values of the three final solutions for the six-wave model.

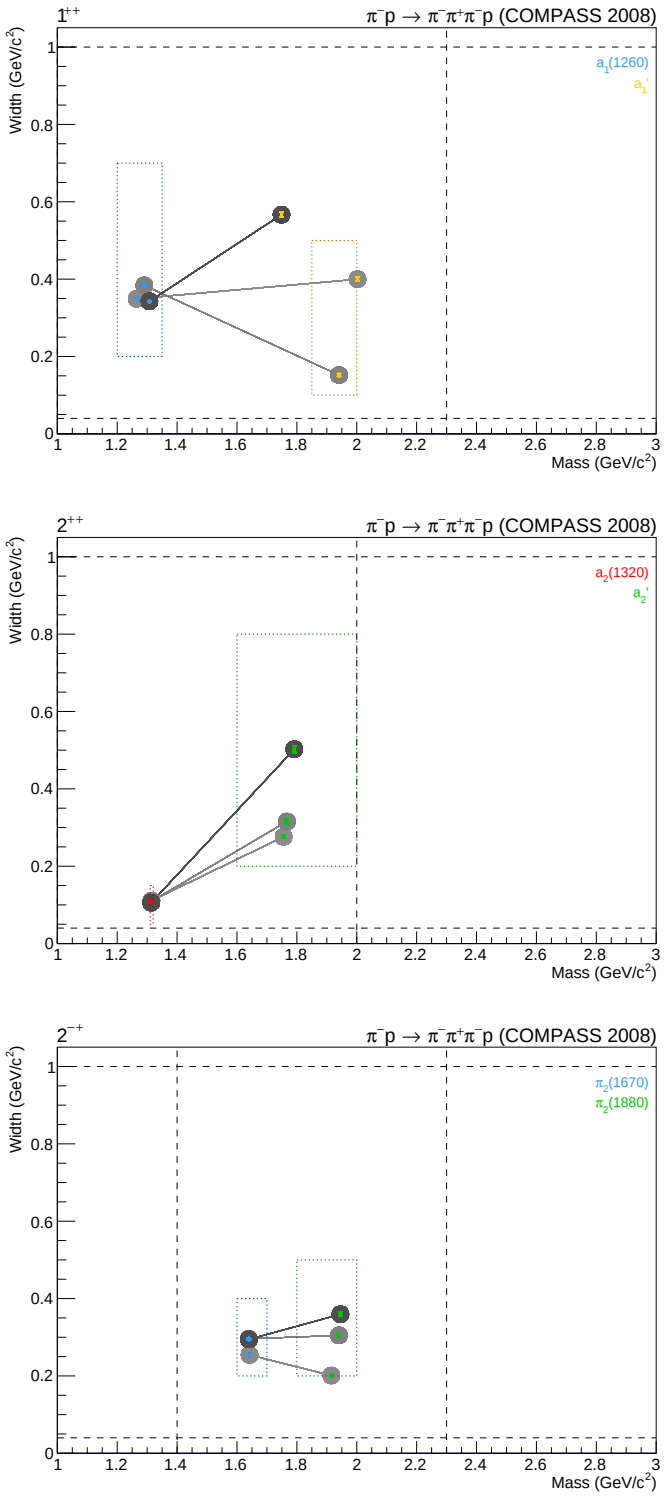

Figure 4.19: Parameter values of $a_1(1260)$ (top, yellow), a_1' (top, blue), $a_2(1320)$ (centre, red), a_2' (centre, green), $\pi_2(1670)$ (bottom, blue) and $\pi_2(1880)$ (bottom, green) after all cuts. An explanation of the used plotting scheme can be found in figure 4.12.

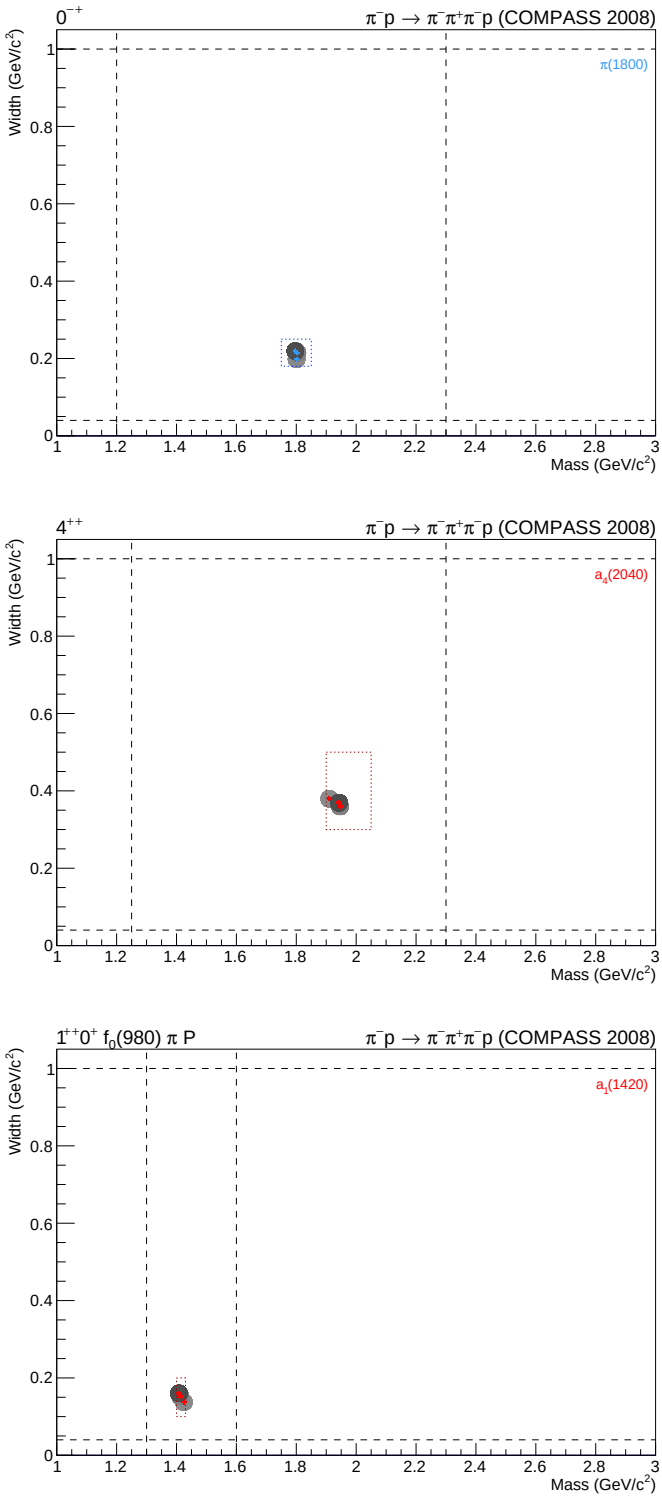

Figure 4.20: Parameter values of $\pi(1800)$(top, blue), $a_4(2040)$ (centre, red) and $a_1(1420)$ (bottom, red) after all cuts. An explanation of the used plotting scheme can be found in figure 4.12.

4.3 Extended Fit

In order to solve the ambiguities in the model with only six waves more information is included into the fit by adding seven further partial waves from the mass-independent fit. Table 4.4 list the extended wave set. The general idea was to stabilise the second resonances with waves, where they are more dominant, and thereby remove the ambiguities. Important is that no further resonances have been introduced into the fit. However, each of these seven new waves needs an own non-resonant term and an additional coupling for each term, including the resonances, in each t' bin, which results in a total of 802 real parameters for the description of now roughly 68 000 data points.

Partial wave		**Resonances**	**Non-resonant terms**	**Fit range [GeV/c^2]**
$1^{++}0^+ f_0(980)\pi P$		$a_1(1420)$	eq. 4.6	1.30 to 1.60
$1^{++}0^+ \rho(770)\pi S$		$a_1(1260), a_1'$	eq. 4.5	0.90 to 2.30
$1^{++}0^+ \rho(770)\pi D$	$*$	$a_1(1260), a_1'$	eq. 4.6	0.90 to 2.10
$2^{++}1^+ \rho(770)\pi D$		$a_2(1320), a_2'$	eq. 4.5	0.90 to 2.00
$2^{++}2^+ \rho(770)\pi D$	$*$	$a_2(1320), a_2'$	eq. 4.6	1.00 to 2.00
$2^{++}1^+ f_2(1270)\pi P$	$*$	$a_2(1320), a_2'$	eq. 4.6	1.00 to 2.00
$2^{-+}0^+ f_2(1270)\pi S$		$\pi_2(1670), \pi_2(1880)$	eq. 4.5	1.40 to 2.30
$2^{-+}1^+ f_2(1270)\pi S$	$*$	$\pi_2(1670), \pi_2(1880)$	eq. 4.6	1.40 to 2.30
$2^{-+}0^+ f_2(1270)\pi D$	$*$	$\pi_2(1670), \pi_2(1880)$	eq. 4.6	1.60 to 2.30
$2^{-+}0^+ \rho(770)\pi F$	$*$	$\pi_2(1670), \pi_2(1880)$	eq. 4.5	1.20 to 2.10
$0^{-+}0^+ f_0(980)\pi S$		$\pi(1800)$	eq. 4.6	1.20 to 2.30
$4^{++}1^+ \rho(770)\pi G$		$a_4(2040)$	eq. 4.6	1.25 to 2.30
$4^{++}1^+ f_2(1270)\pi F$	$*$	$a_4(2040)$	eq. 4.6	1.40 to 2.30

Table 4.4: Extended wave set with 13 waves. The asterisks mark new waves with respect to the smaller wave set with six waves. The ordering is chosen to match with the one in figure 4.25.

In order to decrease the number of fit parameters it is used that the relative branching ratios between the different considered decay channels of a resonance should not dependent on t'. So, for example, the intensity ratio between an $a_1(1260)$ in the $\rho(770)\pi S$ and in the $\rho(770)\pi D$ wave should be the same for all t' bins. Therefore the couplings $C^{\varepsilon}_{\alpha,k}(t')$ are separated into the t' dependence $\mathcal{C}_{J^{PC}M^{\varepsilon},k}(t')$ and the "branchings" $\mathcal{B}_{J^{PC}[\text{Isobar}]\pi L,k}$, which describe the decay dependence:

$$C^{\varepsilon}_{\alpha,k}(t') = \mathcal{B}_{J^{PC}[\text{Isobar}]\pi L,k} \cdot \mathcal{C}_{J^{PC}M^{\varepsilon},k}(t'). \tag{4.7}$$

The index $\alpha = J^{PC}M[\text{Isobar}]\pi L$ containing the partial wave was split up in order to do emphasise that the branchings $\mathcal{B}_{J^{PC}[\text{Isobar}]\pi L,k}$ are independent of t', the spin projection M and the reflectivity ε, while the t' dependences $\mathcal{C}_{J^{PC}M^{\varepsilon},k}(t')$ are independent of the decay described by $[\text{Isobar}]\pi L$. Since the different partial waves interfere, the branching as well as the t' dependences are in general complex.

Note that the t' dependence is different for different spin projections M and therefore this cannot be used to connect, for example, the couplings of the $a_2(1320)$ in the $2^{++}1^+\rho(770)\pi D$ wave with the ones in the $2^{++}2^+\rho(770)\pi D$ wave, but still it reduces the total number of parameters by 180 down to 622.

The way the random studies are performed does not need to be changed, except of a consistent extension of the definition of the major and minor waves. Considered as a major wave are now all waves containing the $a_1(1260)$, the $a_2(1320)$ or the $\pi_2(1670)$. Furthermore the number of fits has been increased to 10 000.

The effect of the cut on spurious solutions can be seen best in the distribution of χ^2 values shown in figure 4.21. There are in principal two groups of physical solutions that survive it. One with a χ^2 of about 325 000 that has two secondary minima, which are worse in χ^2 but do not vary strongly in the parameters, and one with a χ^2 of roughly 386 000. The parameter distribution after all cuts in figure 4.23 shows that the worse solution with a χ^2 of approximately 386 000 has an extremely light $a_1(1260)$. Table 4.6 shows that this solution in addition describes the $a_1(1260)$ peak worse than the first solution, so it can be safely rejected. Looking at figure 4.22 it can be seen that the proximity of the two a_1 resonances in the solution with the best χ^2 is much more pronounced than in the case of the smaller wave set. The precise numbers for all cuts are given in table 4.5. For the reason of completeness the plots after all cuts for the minor waves are given in figure 4.24

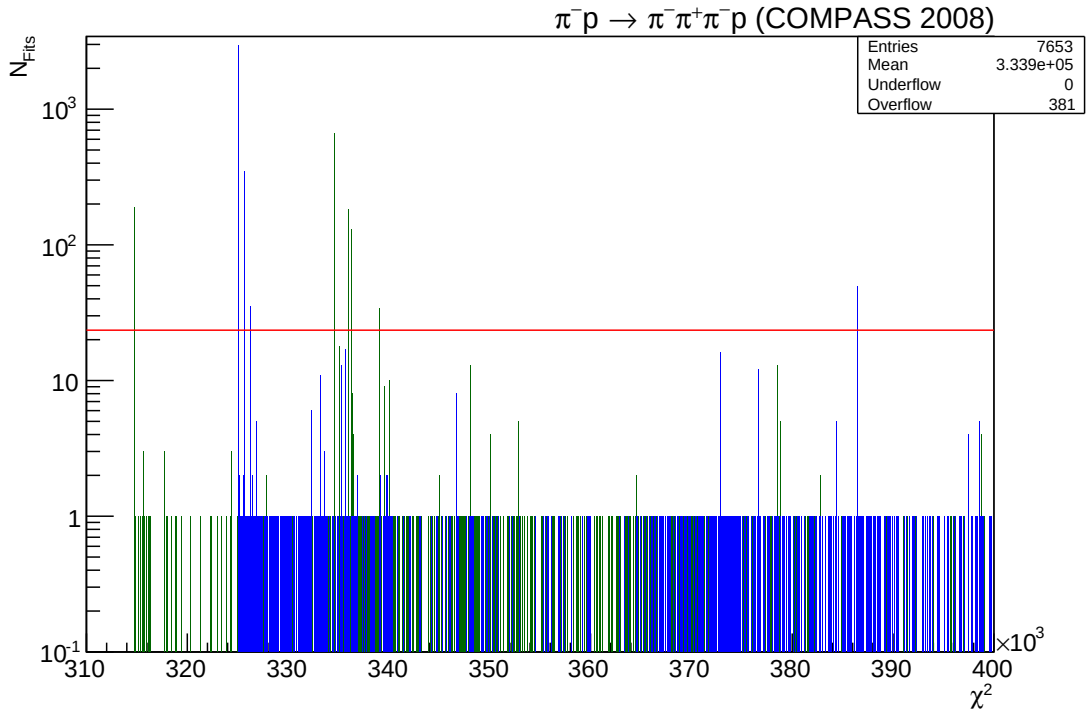

Figure 4.21: Distribution of χ^2 values before the removal of spurious solutions for the extended wave set. The plotting scheme is described in figure 4.13.

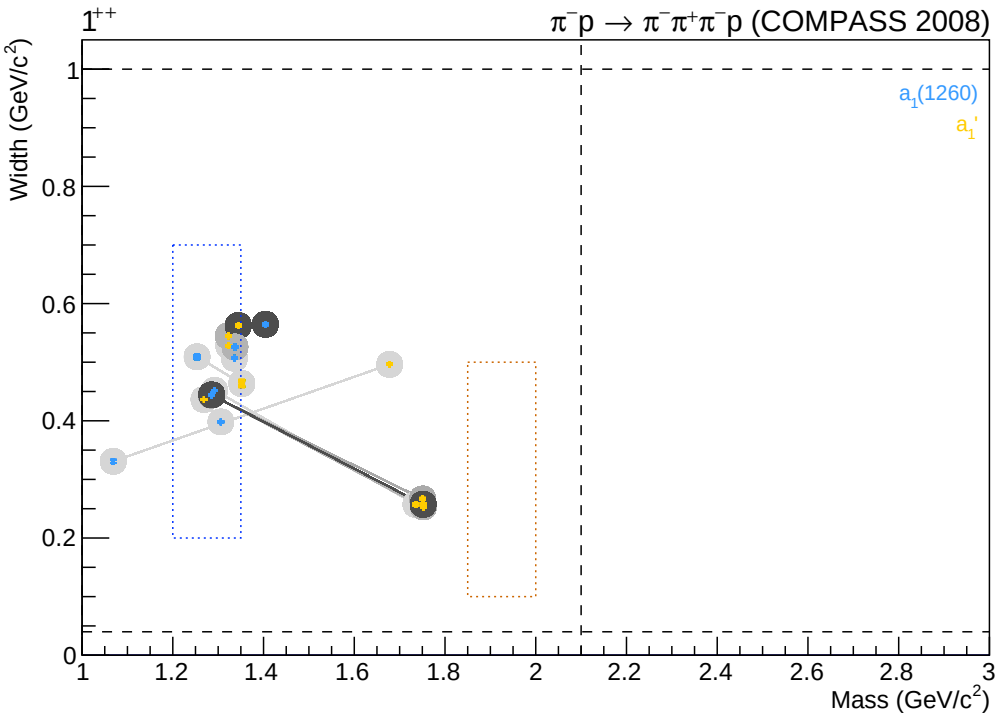

Figure 4.22: Mass and width of $a_1(1260)$ (blue) and a_1' (yellow) after the cut on spurious solutions. An explanation of the used plotting scheme can be found in figure 4.12. Note that these resonances are now fitted in two waves at the same time and therefore the vertical black broken line indicates the lower of the two upper ends of the individual fit ranges.

Cut	**Number of remaining fit results**
	9942
Failed convergence	9041
Parameter close to limits	7653
Spurious solutions	4753
Interchange of resonance positions	3736
Proximity of resonances	3523
Resonances outside fit range	3523

Table 4.5: Overview on the applied cuts for the extended wave set.

Solution	1	2
Total χ^2	325 125	386 466
χ^2 without the intensity of the $1^{++}0^+\rho(770)\pi S$ and D waves	297 718	356 470

Table 4.6: χ^2 values of the two final solutions for the extended wave set.

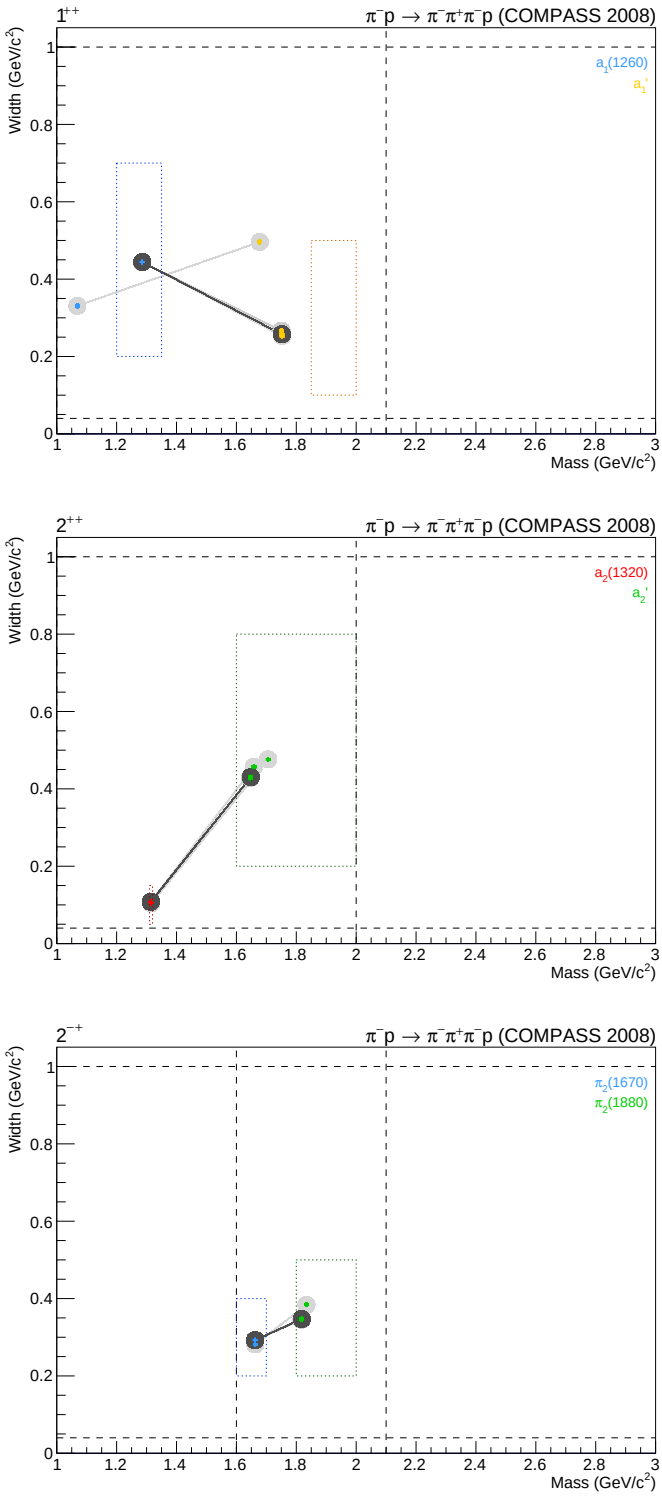

Figure 4.23: Parameter values of $a_1(1260)$ (top, yellow), a_1' (top, blue), $a_2(1320)$ (centre, red), a_2'(centre, green), $\pi_2(1670)$ (bottom, blue) and $\pi_2(1880)$ (bottom, green) for the extended wave set after all cuts. An explanation of the used plotting scheme can be found in figure 4.12.

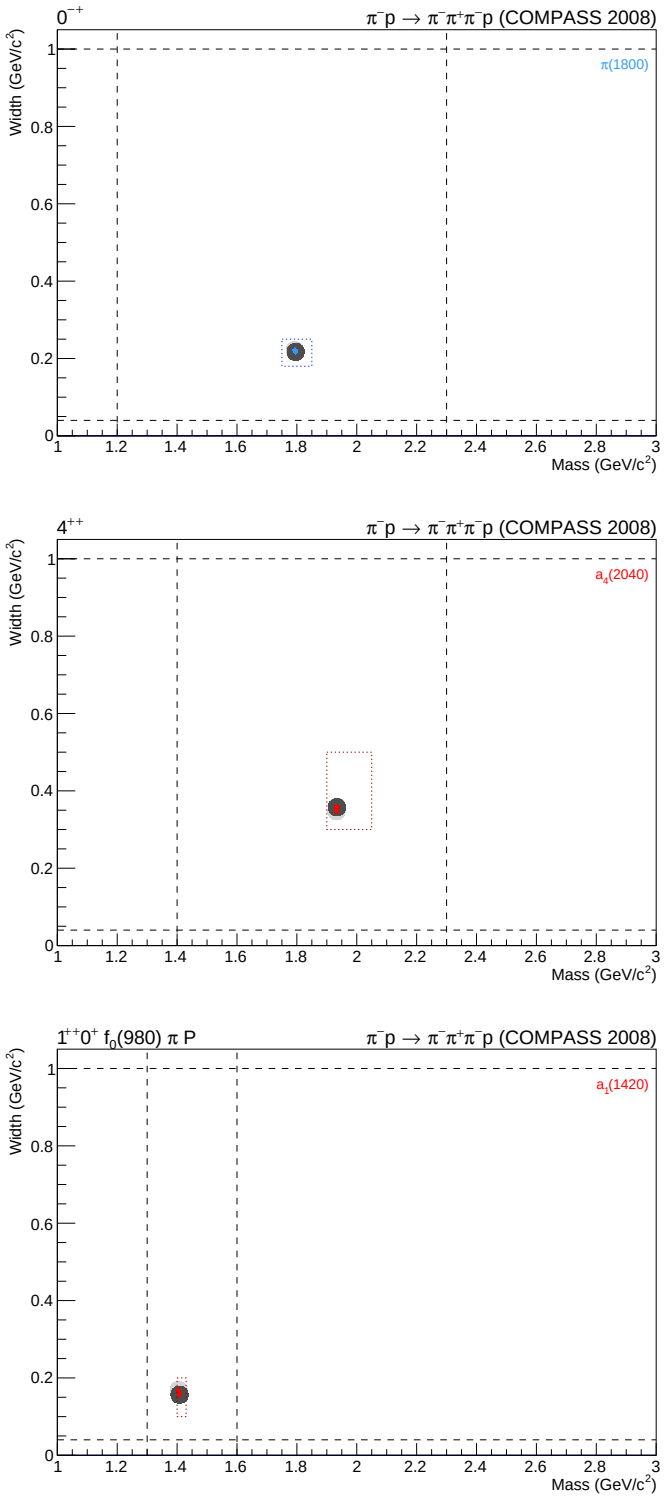

Figure 4.24: Parameter values of $\pi(1800)$(top, blue), $a_4(2040)$ (centre, red) and $a_1(1420)$ (bottom, red) for the extended wave set after all cuts. An explanation of the used plotting scheme can be found in figure 4.12.

In summary the extended wave set reaches its goal to solve the ambiguities observed in the smaller wave set. The spin-density matrix for the lowest t' bin in figure 4.25 gives an impression of the dimension of this fit and shows that the model describes the data overall fairly well. In order to illustrate this further figures 4.26, 4.27 and 4.28 show the intensities of the three largest waves as a function of t'. The peak shift of the $a_1(1260)$ and the destructive-interference dip of the $a_2(1320)$ and the a_2' are reproduced. As expected the bad description of the rising flank of the $a_1(1260)$ peak is not solved and in the additional $1^{++}0^+\rho(770)\pi D$ wave in figure 4.29 the agreement is even worse. Here the fit only coarsely describes the data. The improvement for higher t' leads to the conclusion that the difference is due to an insufficient description of the non-resonant term. This is further supported by the rather odd behaviour of the non-resonant contribution, which is growing, instead of decreasing, exponentially with mass. Attempts to solve the issue have not been successful so far.

Table 4.7 and Figure 4.30 compare the resonance parameters of the extended and the smaller wave set. The most striking changes are observable for the second resonances. The ambiguity for the a_1' was resolved with parameters that have more or less the mass of solution 1 and the width of solution 2 of the six-waves model. At the same time the $a_1(1260)$ mass decreases, which is likely to be caused by the $1^{++}0^+\rho(770)\pi D$ wave. The a_2' is getting considerably lighter with a width between both previous solutions. As figure 4.27 illustrates the mass of the a_2' is now below the interference dip. In contrast to the six-waves model this might provide the possibility to use a third a_2 resonance to describe the higher mass regions. However, this is left for further work.

The $\pi_2(1880)$ is also considerably lighter in combination with a slightly heavier $\pi_2(1670)$, which is mainly due to the newly introduced $2^{-+}0^+f_2(1270)\pi D$ wave in figure 4.31. Here the $\pi_2(1880)$ is the dominant contribution and can therefore be much better determined than before.

The statistical errors listed in table 4.7 are for the extended wave set at most $0.4\,\mathrm{MeV}/c^2$ in mass and $1.3\,\mathrm{MeV}/c^2$ in width. Compared to the also shown six-waves model they were considerably reduced by up to one order of magnitude. After this reduction the statistical errors are more than one order of magnitude smaller than the systematic ones determined in the next section. Therefore they are from now on neglected. All in all it can be said that the extension of the wave set has improved the fit quite considerably.

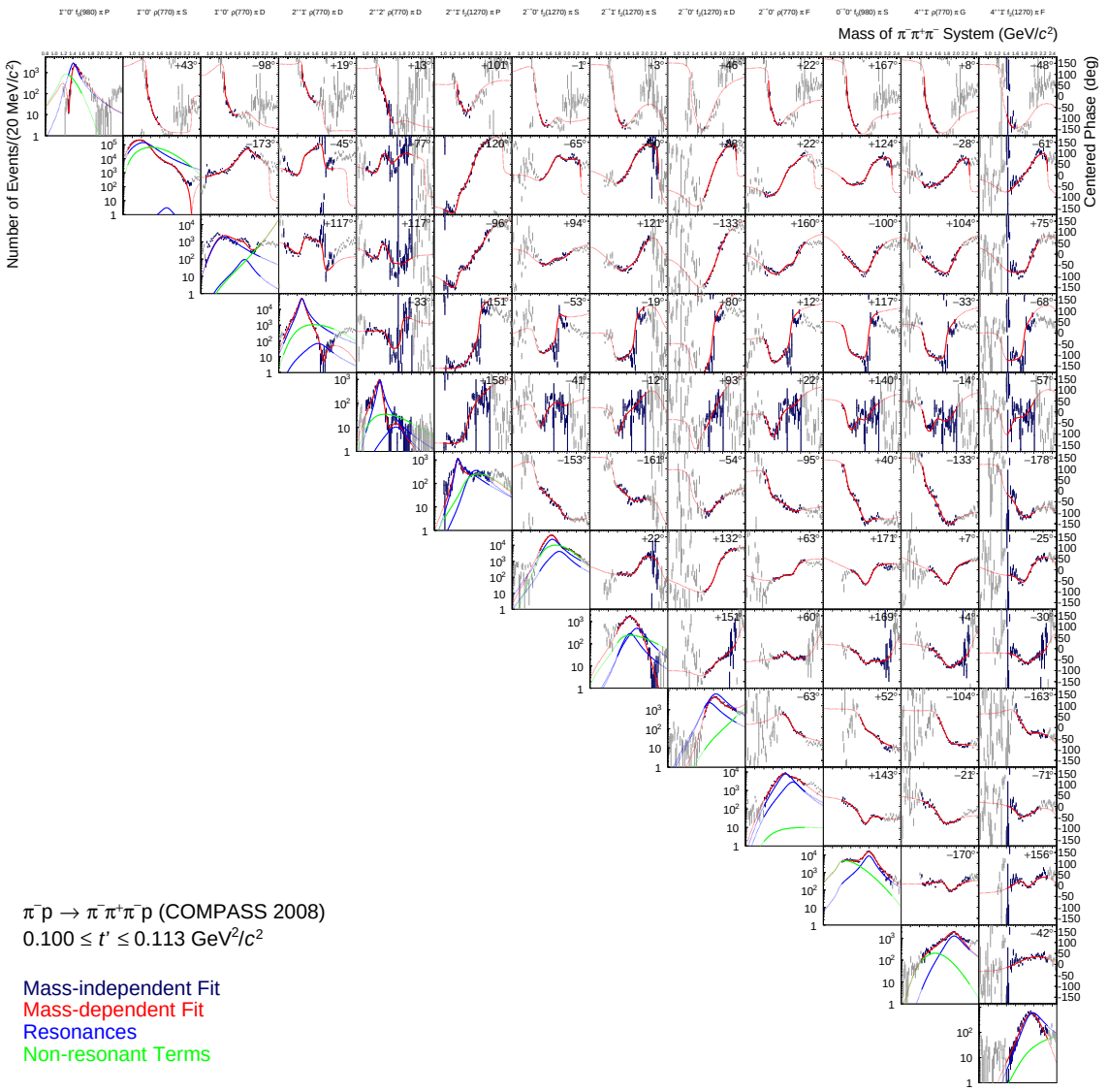

Figure 4.25: Fitted spin-density matrix for the lowest t' bin containing the waves from table 4.4 ordered in the same way. An enlarged version can be found in section A.2 in the appendix. The colour scheme is described in figure 4.2 and the plotting of the relative phases is commented on in figure 4.3.

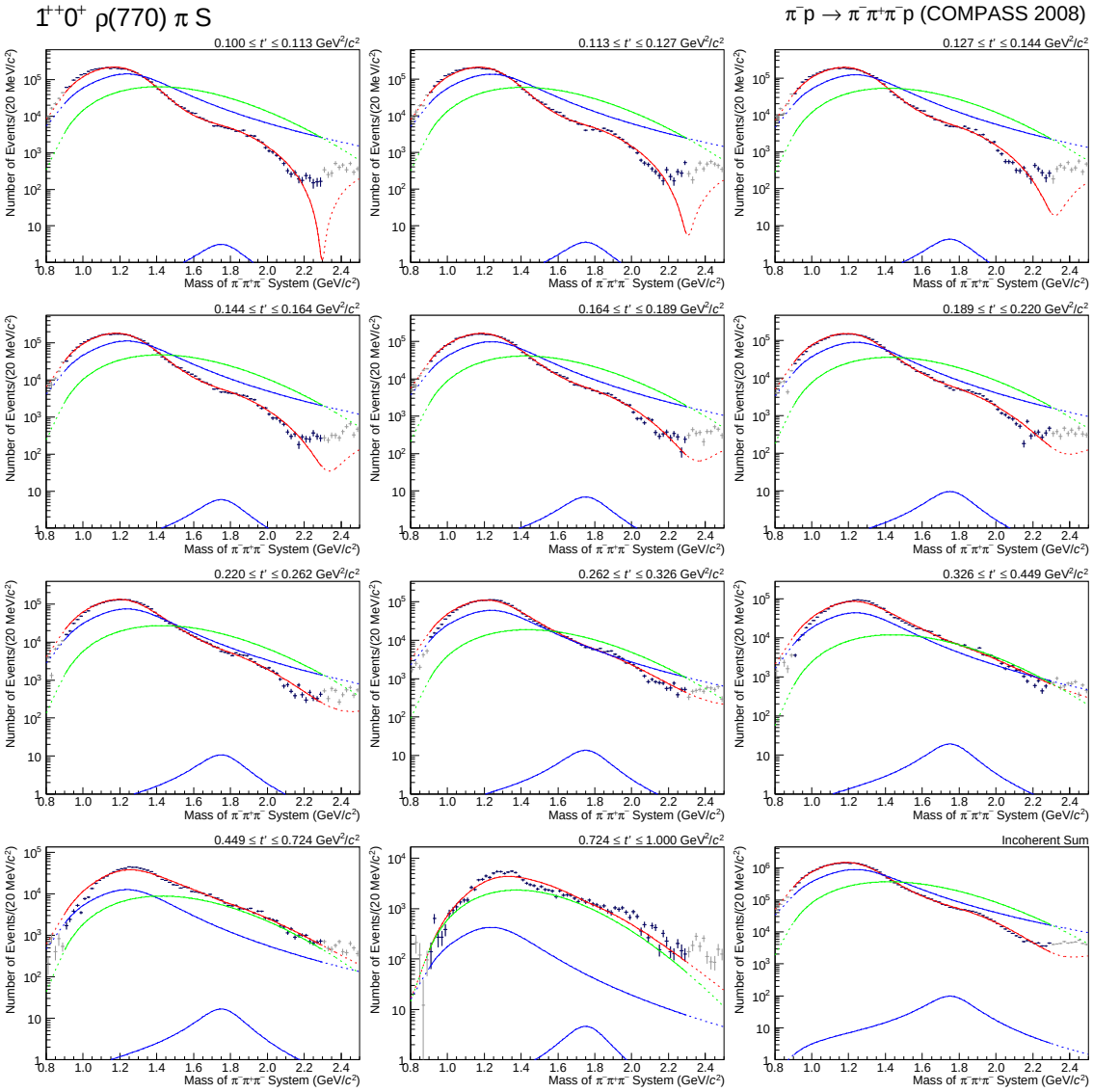

Figure 4.26: Intensity of the $1^{++}0^{+}\rho(770)\pi S$ wave as a function of t' in logarithmic scale. The ordering in t' is the same as in figure 4.5. The colour scheme is described in figure 4.2.

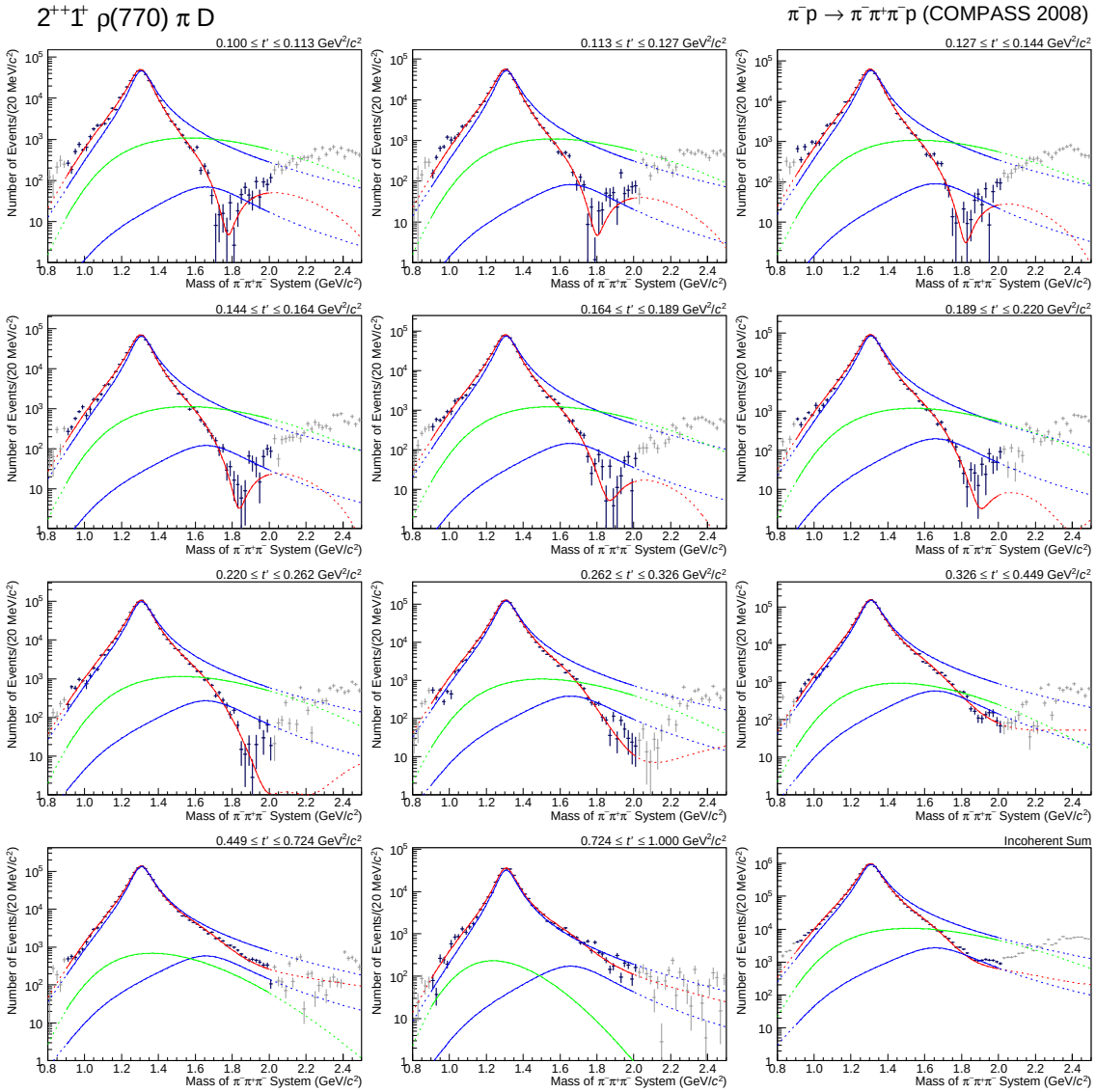

Figure 4.27: Intensity of the $2^{++}1^{+}\rho(770)\pi D$ wave as a function of t' in logarithmic scale. The ordering in t' is the same as in figure 4.5. The colour scheme is described in figure 4.2.

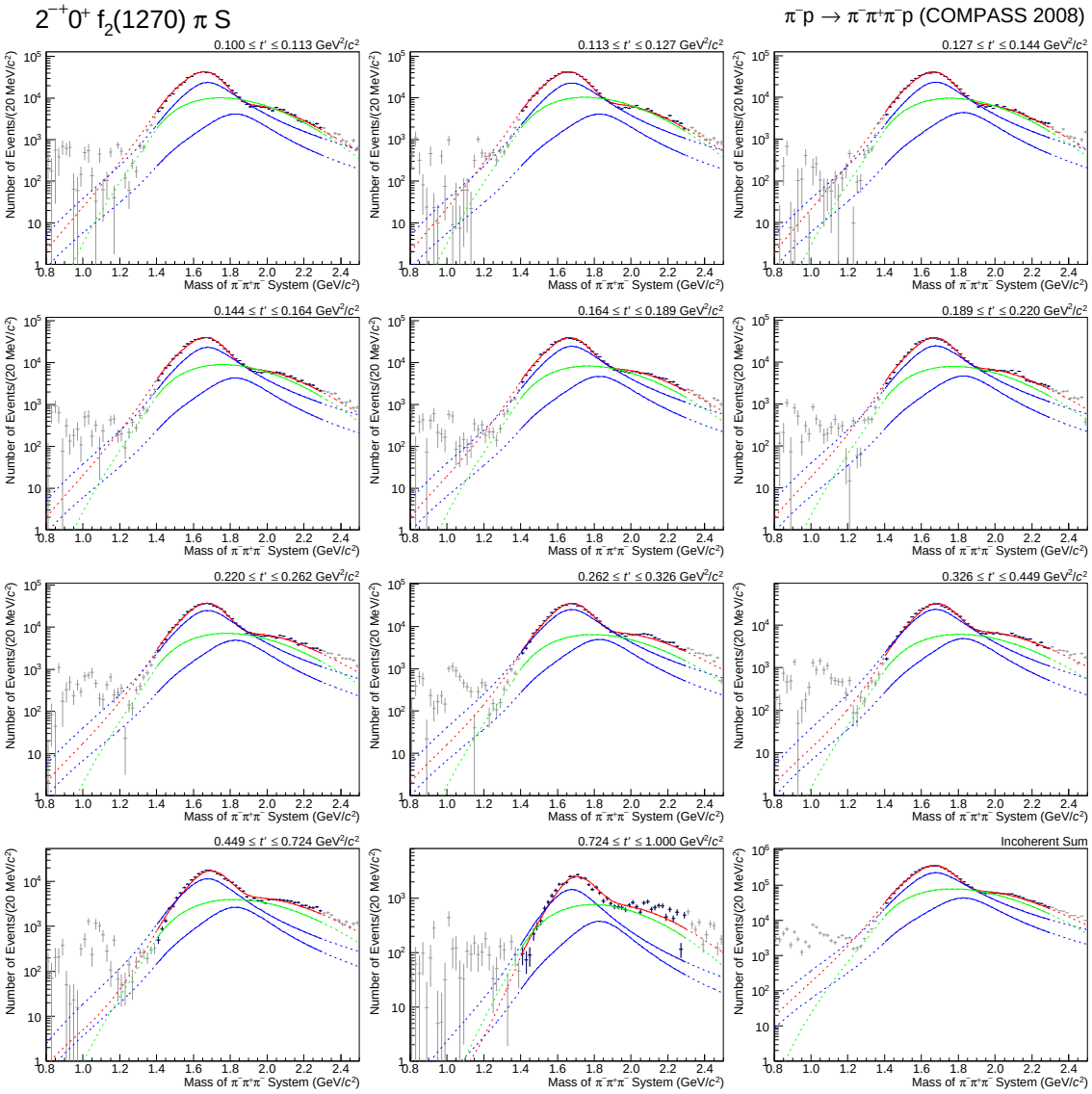

Figure 4.28: Intensity of the $2^{-+}0^{+}f_2(1270)\pi S$ wave as a function of t' in logarithmic scale. The ordering in t' is the same as in figure 4.5. The colour scheme is described in figure 4.2.

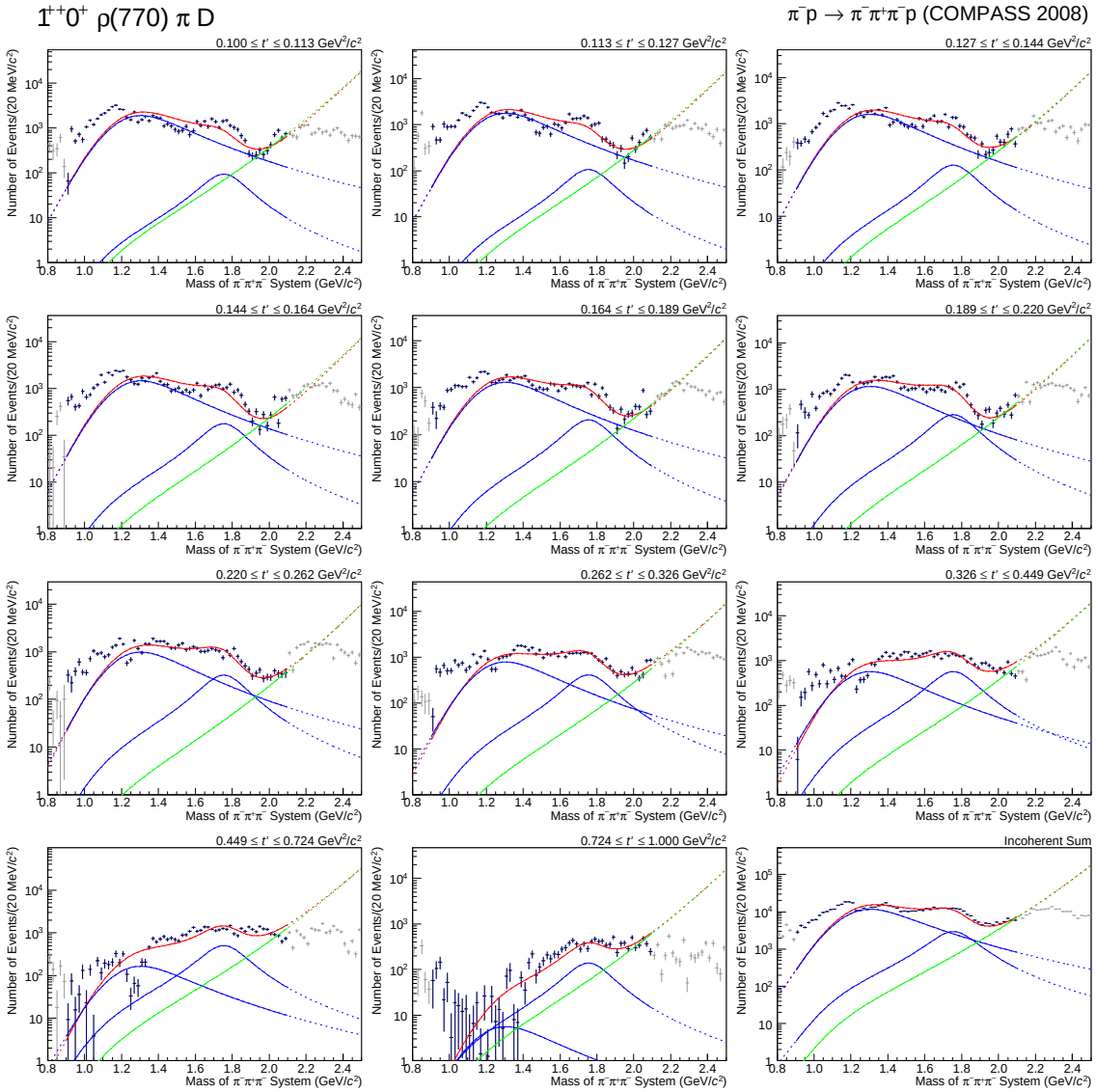

Figure 4.29: Intensity of the $1^{++}0^{+}\rho(770)\pi D$ wave as a function of t' in logarithmic scale. The ordering in t' is the same as in figure 4.5. The colour scheme is described in figure 4.2.

Resonance	Parameter	M[MeV/c^2]	A1[MeV/c^2]	A2[MeV/c^2]
$a_1(1260)$	Mass	1285.8 ± 0.1	1307.5 ± 0.3	1290.6 ± 0.4
	Width	444.3 ± 0.3	342.6 ± 1.0	383.7 ± 0.7
$a_1(1420)$	Mass	1408.1 ± 0.1	1408.6 ± 0.2	1412.6 ± 0.3
	Width	156.7 ± 0.5	160.1 ± 0.6	152.4 ± 0.8
a_1'	Mass	1751.9 ± 0.4	1748.7 ± 1.7	1940.9 ± 1.5
	Width	257.4 ± 1.3	566.7 ± 3.6	152.0 ± 3.1
$a_2(1320)$	Mass	1314.2 ± 0.0	1313.6 ± 0.1	1314.1 ± 0.1
	Width	108.0 ± 0.1	105.9 ± 0.1	109.0 ± 0.1
a_2'	Mass	1647.9 ± 0.2	1791.5 ± 1.9	1766.5 ± 1.6
	Width	430.2 ± 0.4	502.5 ± 4.2	315.6 ± 3.8
$a_4(2040)$	Mass	1933.7 ± 0.2	1942.5 ± 0.5	1946.4 ± 0.5
	Width	357.4 ± 0.6	369.1 ± 1.3	359.6 ± 1.1
$\pi(1800)$	Mass	1795.8 ± 0.1	1797.0 ± 0.2	1803.8 ± 0.2
	Width	217.2 ± 0.3	219.2 ± 0.5	214.5 ± 0.5
$\pi_2(1670)$	Mass	1662.5 ± 0.1	1640.2 ± 0.8	1639.3 ± 0.4
	Width	292.6 ± 0.2	294.6 ± 1.8	295.9 ± 0.5
$\pi_2(1880)$	Mass	1818.4 ± 0.1	1945.5 ± 2.0	1940.2 ± 0.8
	Width	347.0 ± 0.3	359.4 ± 3.3	304.8 ± 2.1

Table 4.7: Resonance parameters for the best solution of the extended wave set (M) and the two ambiguous solutions with the smaller wave set (A1 and A2). Where applicable the given resonance names are attributed by a rough accordance with the values in [13]. For the a_1' and a_2' no clear assignment is possible. The given errors are the statistical ones determined by the fitter.

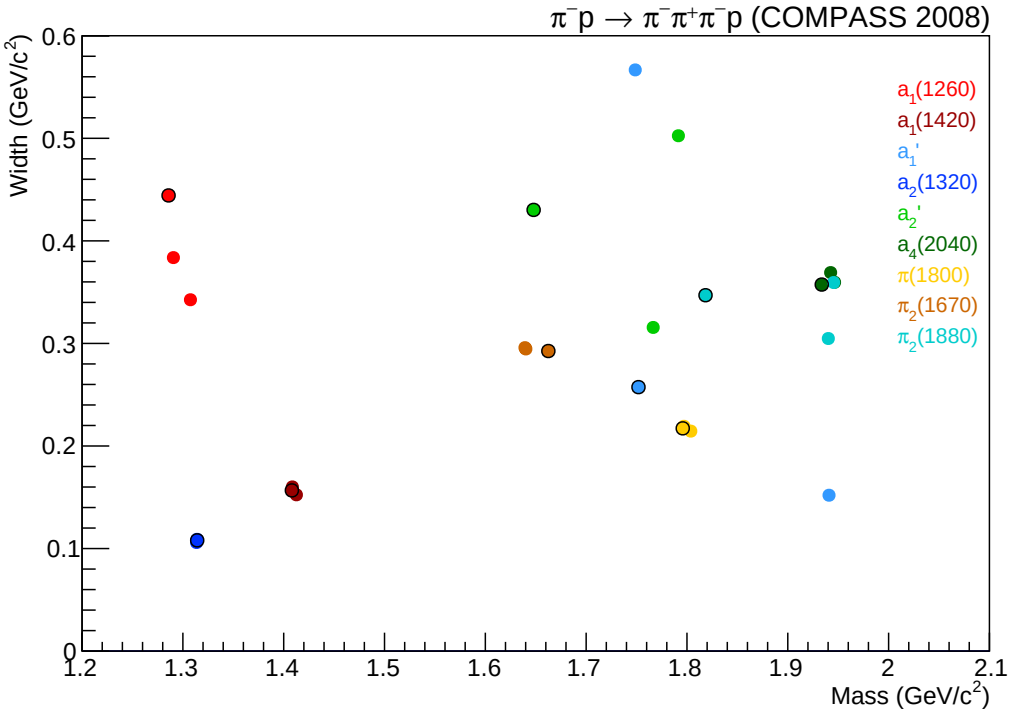

Figure 4.30: Mass and width of all measured resonances for the best solution of the extended wave set and the two ambiguous solutions with the smaller wave set. The black circle around the dots marks the solution from the extended wave set.

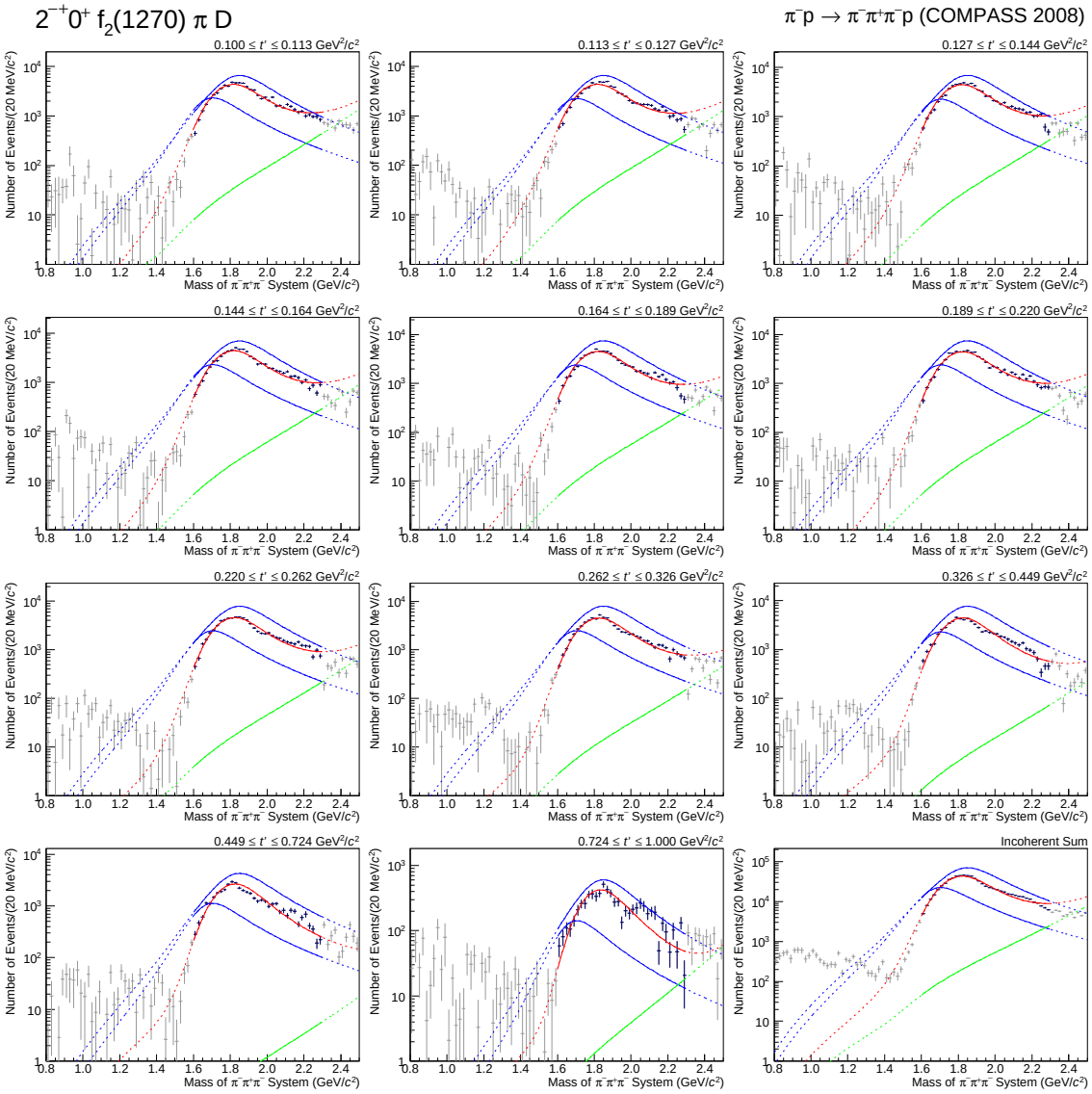

Figure 4.31: Intensity of the $2^{-+}0^{+}f_2(1270)\pi D$ wave as a function of t' in logarithmic scale. The ordering in t' is the same as in figure 4.5. The colour scheme is described in figure 4.2.

4.4 Systematic Studies of the Model

That the changes in the resonances parameters between the extended wave set and the smaller one were quite pronounced already hints that the systematic errors are by far the dominant ones. In order to get a good estimate on them 14 further studies with 1000 fits each were performed testing different aspects of the model and of the event selection. Since the amount of information used by the fitter for the smaller wave set is much less than for the extended fit, the smaller wave set is not included into the systematics. In the following the individual studies will be presented always comparing to the results of the 13 waves model from the previous section, being referred to as the main fit. The scale of the spread of the resonance parameters of all systematic studies is shown in figure 4.32. The $a_2(1320)$ is, as expected, extremely stable. Furthermore the $a_1(1420)$, $a_4(2040)$ and $\pi(1800)$ are rather stable as well, because they are not affected by other resonances in their waves. A larger spread of parameter values is observable for the $\pi_2(1670)$, $\pi_2(1880)$ and a_2'. Due to the strong non-resonant contributions in the $1^{++}0^+\rho(770)\pi S$ and D waves the $a_1(1260)$ parameters are less stable. The ones of the a_1' are for the same reason more or less undetermined.

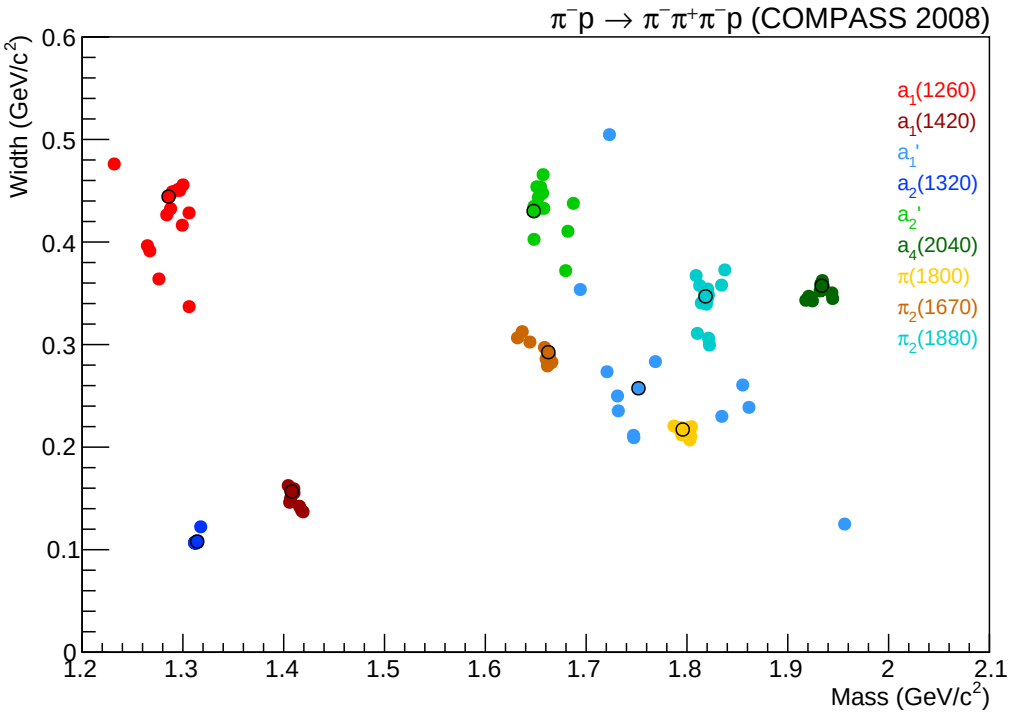

Figure 4.32: Resonance parameters estimated in the systematic studies. The black circle around the dots marks the solution from the main fit.

4.4.1 Reproducibility of Results

Having seen how large the discrepancies between fits with different models can be the most important study is whether the results are reproducible within one model. First it was checked, whether 1000 fits are enough to reproduce the fit result, using only the first 1000 fits of the larger study of the main fit. Then the fits were repeated on another computing cluster and finally the start-value range of the a_1' was shifted to demonstrate that the fit is insensitive to the particular choice of values as was already concluded in section 4.2 from the distribution of the starting values of fits that resulted in the best χ^2. The new start-value range is shown in figure 4.33. Table 4.8 summarises the resulting resonance parameters. The largest deviation between all four studies is 0.2 MeV/c^2, so the reproducibility can be considered as perfect. Additionally the spread of parameter values within the chosen solutions was checked, being at most 0.1 MeV/c^2, and is therefore also negligible. Summarising these studies, the results after the full procedure with random start values and applied cuts are the same. Since the spread of parameter values between the other systematic studies is much larger, their results will only be stated with a precision of 1 MeV/c^2.

Resonance	**Parameter**	**M[MeV/c^2]**	**A[MeV/c^2]**	**B[MeV/c^2]**	**C[MeV/c^2]**
$a_1(1260)$	Mass	1285.8	1285.7	1285.7	1285.7
	Width	444.3	444.3	444.3	444.3
$a_1(1420)$	Mass	1408.1	1408.1	1408.1	1408.1
	Width	156.7	156.7	156.7	156.7
a_1'	Mass	1751.9	1751.9	1751.9	1751.9
	Width	257.4	257.4	257.4	257.4
$a_2(1320)$	Mass	1314.2	1314.2	1314.2	1314.2
	Width	108.0	108.0	108.0	108.0
a_2'	Mass	1647.9	1647.9	1647.9	1647.9
	Width	430.2	430.3	430.3	430.4
$a_4(2040)$	Mass	1933.7	1933.7	1933.7	1933.7
	Width	357.4	357.4	357.4	357.4
$\pi(1800)$	Mass	1795.8	1795.8	1795.8	1795.8
	Width	217.2	217.2	217.2	217.2
$\pi_2(1670)$	Mass	1662.5	1662.5	1662.5	1662.5
	Width	292.6	292.6	292.6	292.6
$\pi_2(1880)$	Mass	1818.4	1818.4	1818.4	1818.4
	Width	347.0	347.0	347.0	347.0

Table 4.8: Table of resonance parameters for study on reproducibility. M denotes a study with 10 000 fits. A gives the result for the same study using only the first 1000 fits. B is a study with the same model, but determined on another computing cluster and C denotes a study were the starting values of the a_1' had been changed in order to be located around the resulting parameters for this resonance. The new range is shown in figure 4.33.

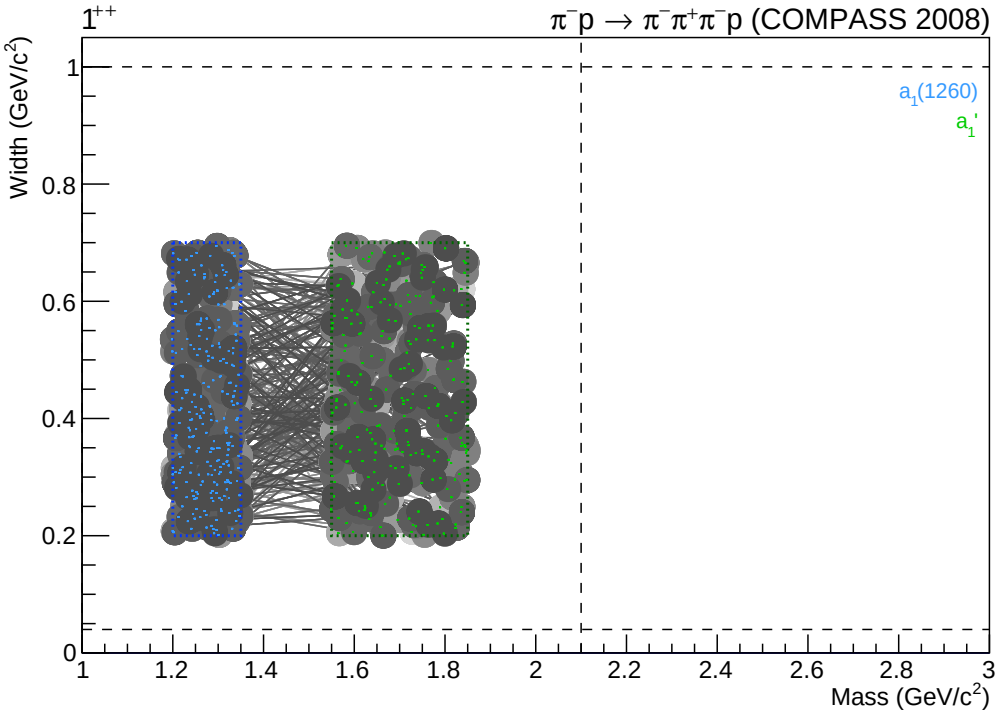

Figure 4.33: Alternative starting values for the a_1' (green) and unchanged starting values for the $a_1(1260)$ (blue). An explanation of the used plotting scheme can be found in figure 4.12.

4.4.2 Influence of the Branchings

The next study tries to estimate the influence of the branchings introduced in equation 4.7 by using independent couplings $C^{\varepsilon}_{\alpha,k}(t')$ for all waves instead. After all cuts four different solutions with the χ^2 values given in table 4.9 remained. They are resulting from two different solutions for the a_1 resonances, which both have again two different solutions for the $\pi_2(1880)$ as can be seen in figure 4.34. The two solutions with the narrower $\pi_2(1880)$ have nearly equal χ^2. However, after an exclusion of the $1^{++}0^+\rho(770)\pi S$ and D intensities from the χ^2 calculation, the difference between their χ^2 is increasing and therefore only solution 1 with the narrower a_1' is accepted.

Solution	1	2	3	4
Total χ^2	308635	308834	311495	311577
χ^2 without $1^{++}0^+\rho(770)\pi S, D$ intensity	284715	287683	290612	287509

Table 4.9: χ^2 values of the final solutions for the extended wave set without branchings.

The differences of solution 1 to the main fit are given in table 4.10 and figure 4.35. The largest change is seen in the a_1' resonance parameters, even though the general trend

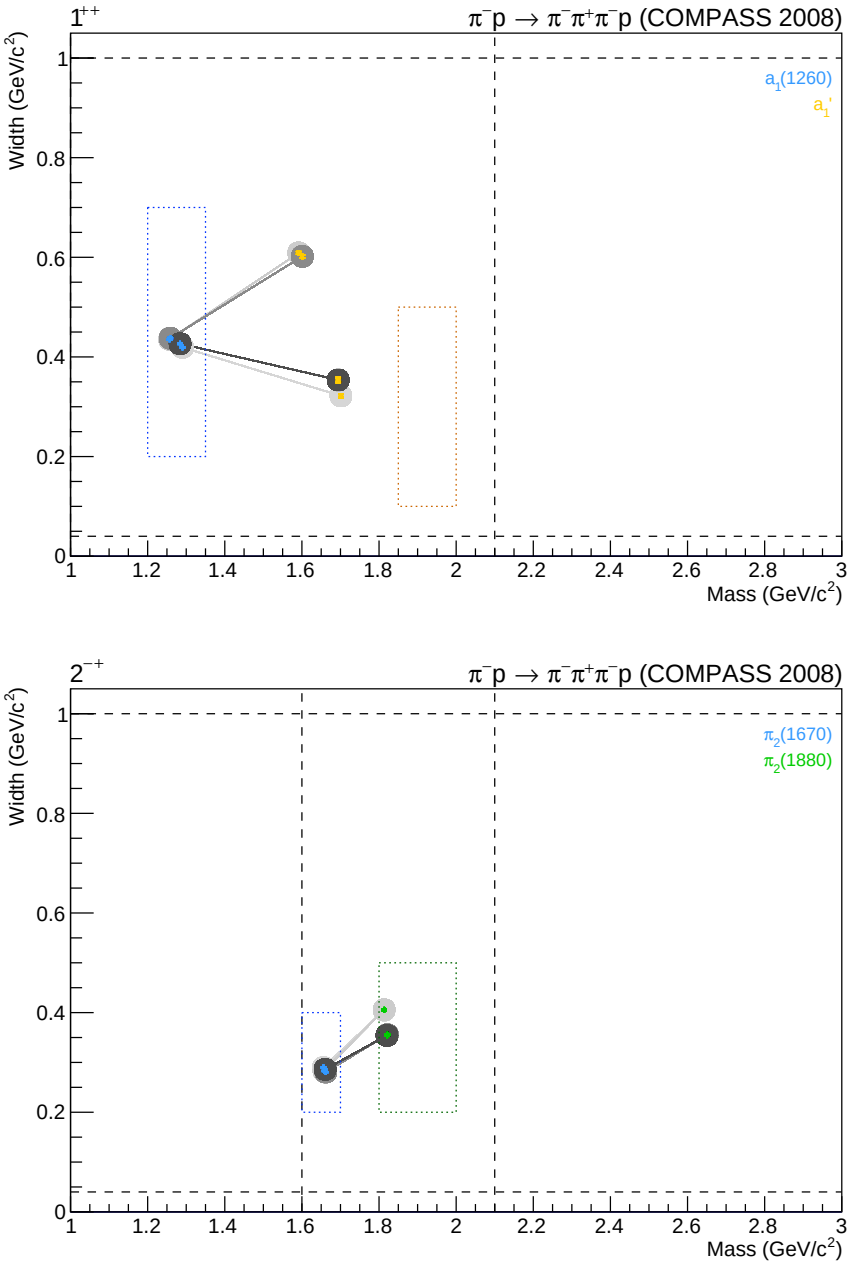

Figure 4.34: Parameter values of $a_1(1260)$ (top, yellow), a_1' (top, blue), $\pi_2(1670)$ (bottom, blue) and $\pi_2(1880)$ (bottom, green) for the extended wave set without branchings after all cuts. An explanation of the used plotting scheme can be found in figure 4.12.

that the first resonances are getting narrower and the second resonances are becoming broader is also true for the $a_1(1260)$, a_2', $\pi_2(1670)$ and $\pi_2(1880)$. Sitting in the tail of the insufficiently described $a_1(1260)$ peak it is not surprising that the a_1' changes the most and the fitter uses the additional freedom here to improve the description of the rising flank of the $a_1(1260)$ peak for higher t'. Summing up this study, the effect of the additional constraints is clearly visible and reflects that the separation between resonant and non-resonant terms done by the fitter is partly ambiguous. The effects of this uncertainty are the strongest for the 1^{++} waves, where the non-resonant contributions are the most prominent.

Resonance	**Parameter**	**M[MeV/c^2]**	**A[MeV/c^2]**
$a_1(1260)$	Mass	1286	1284
	Width	444	426
$a_1(1420)$	Mass	1408	1408
	Width	157	157
a_1'	Mass	1752	1694
	Width	257	354
$a_2(1320)$	Mass	1314	1314
	Width	108	108
a_2'	Mass	1648	1658
	Width	430	433
$a_4(2040)$	Mass	1934	1932
	Width	357	352
$\pi(1800)$	Mass	1796	1795
	Width	217	212
$\pi_2(1670)$	Mass	1662	1660
	Width	293	286
$\pi_2(1880)$	Mass	1818	1820
	Width	347	354

Table 4.10: Resonance parameters for study on branchings. M denotes the main fit. A is a study without further constraints through branchings, where the t' dependences of the same resonances in different waves are no longer coupled.

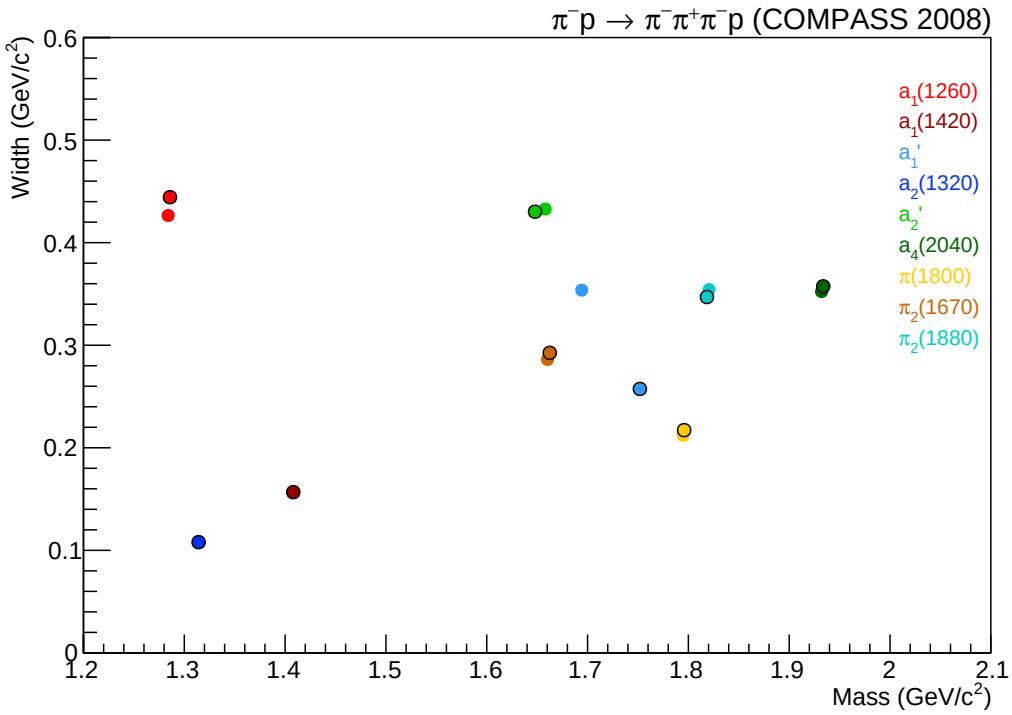

Figure 4.35: Resonance parameter overview for study on branchings. The black circle around the dots marks the solution from the main fit.

4.4.3 Study on the Choice of Wave Set

Having seen how strong the differences between the six waves and the thirteen waves are, one important study is how the resonance parameters depend on the wave set. Since using only six waves restricts the amount of information too much in order to include it in the systematic error estimation, only one or two waves are removed in the following. Starting by leaving out the $1^{++}0^{+}\rho(770)\pi D$ wave, so that the $a_1(1260)$ and a_1' are directly defined only by the $1^{++}0^{+}\rho(770)\pi S$ wave, results in a vast increase of unphysical solutions surviving the cut on spurious solutions and having a better χ^2 then the physical ones as can be seen in figure 4.36. Additionally it is the only case in all performed studies, where a solution with the best χ^2 from all that are marked as physical is removed as a spurious solution. This is shown in figure 4.37. However, lifting this cut and applying all others leads to figure 4.38, which shows that the best solution has an $a_1(1260)$ at around $1.05\,\mathrm{GeV}/c^2$, which just describes the rising flank of the resonance peak while the rest is described by the a_1'. This is clearly not a meaningful solution, but was just not filtered by the cuts on physics. At the end for this wave set without the $1^{++}0^{+}\rho(770)\pi D$ wave the same two classes of ambiguous solutions for the a_1' survive as in the case of only 6 waves. However, the exact a_1' parameters have changed. The a_2' and $\pi_2(1880)$, which also

significantly changed going from six to thirteen waves, reproduce roughly the main fit instead of the values from the small wave set.

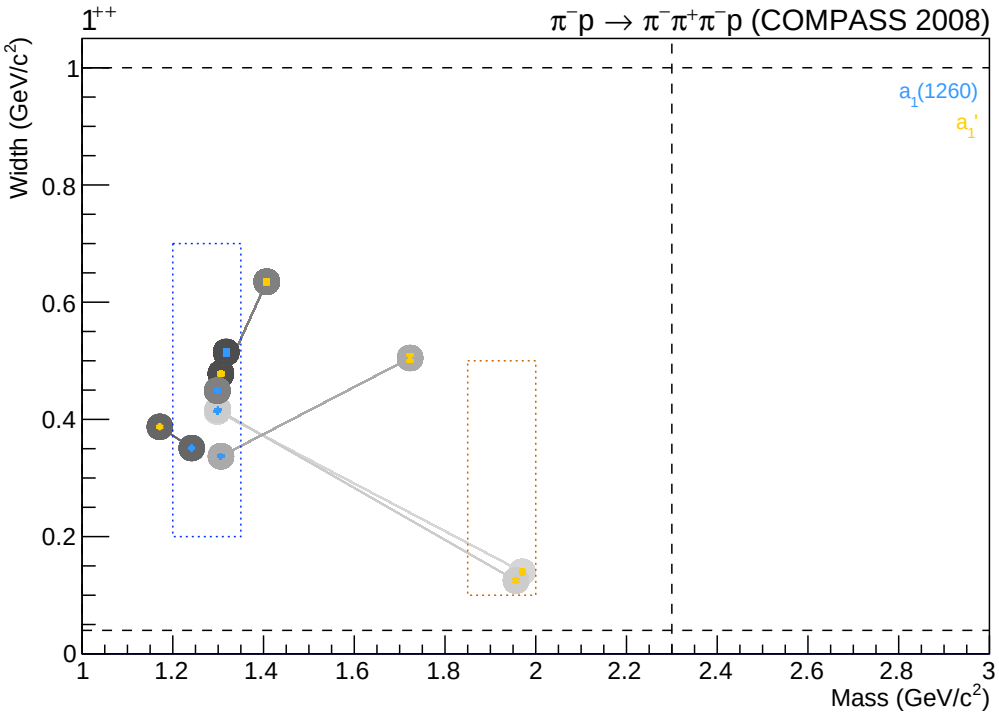

Figure 4.36: Mass and width of $a_1(1260)$ (blue) and a_1' (yellow) after the removal of spurious solutions for the extended wave set without the $1^{++}0^+\rho(770)\pi D$ wave. An explanation of the used plotting scheme can be found in figure 4.12.

Having observed a significant shift of the two π_2 resonances towards each other going from six to thirteen waves, it is interesting to study, whether this is only due to the $2^{-+}1^+f_2(1270)\pi D$ wave, where the $\pi_2(1880)$ is dominant, or is further amplified by the two other new waves in this sector. Therefore those are left out and only the $2^{-+}1^+f_2(1270)\pi S$ and $2^{-+}1^+f_2(1270)\pi D$ waves are included in this study. After removing the unphysical solutions that appear in most studies due to an interchange of resonance positions of the a_1 resonances shown in figure 4.39 the remaining solutions for the π_2 parameter are given in figure 4.40. Besides the two solutions that are roughly the same as the one of the main fit, there are two solutions with an unexpectedly wide $\pi_2(1670)$, which are later removed by the proximity cut. In comparison to the main fit (see figures 4.28, 4.31 and A.11) the narrower physical solution in figure 4.41 exhibits a peculiarly strong destructive interference. However, this behaviour is vanishing towards higher t' in contrast to the unphysical solution, where it continuous over the whole t' range. So it seems that the fits are distorted by the lack of information.

In general leaving out waves seems to amplify ambiguities and decrease the stability of the fits. While none of the two studies described above would be able to provide a

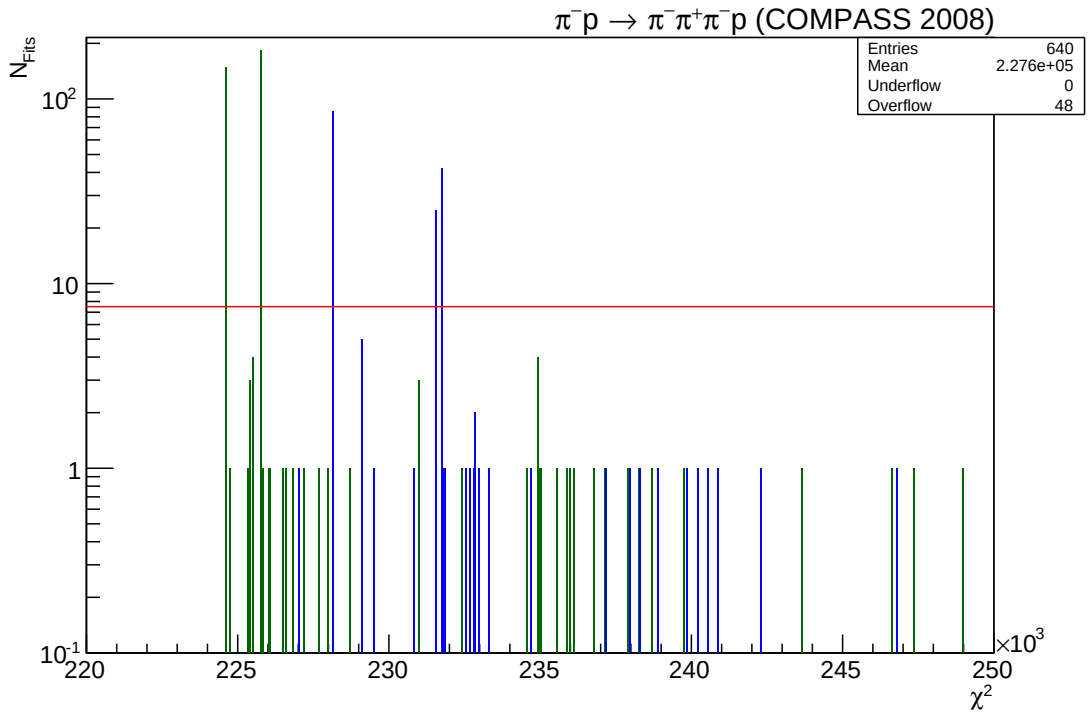

Figure 4.37: Distribution of χ^2 values before the removal of spurious solutions for the extended wave set without the $1^{++}0^+\rho(770)\pi D$ wave. The plotting scheme is described in figure 4.13.

reasonable main fit, they are still good to estimate the systematic errors. The resulting resonance parameters for these studies are compared to the main fit in table 4.11 and figure 4.42. They support that the large shift of the $\pi_2(1880)$ mass going from 6 to 13 waves is caused by the $2^{-+}1^+f_2(1270)\pi D$ wave while suggesting that the increase in the $\pi_2(1670)$ mass is due to the other two new 2^{-+} waves.

Additionally a study has been performed, where both waves containing the $a_1(1260)$ and a_1' are removed from the wave set, since there are still some issues with their description by the fit due to the large non-resonant contributions in them. That the maximum deviation for the other resonances is smaller than for the case of only leaving out the $1^{++}0^+\rho(770)\pi D$ wave can be seen as a slight hint that the shortcomings in describing the intensity distribution of the 1^{++} waves in the main fit do not significantly disturb the other resonances. However, comparing the results of the study without the $1^{++}0^+\rho(770)\pi D$ wave and the one without the $2^{-+}1^+f_2(1270)\pi S$ and $2^{-+}0^+\rho(770)\pi F$ waves it seems that the influences of the π_2 parameters on the other waves are more pronounced.

Resonance	Parameter	M[MeV/c^2]	A[MeV/c^2]	B[MeV/c^2]	C1[MeV/c^2]	C2[MeV/c^2]
$a_1(1260)$	Mass	1286	—	1265	1306	1299
	Width	444	—	396	337	416
$a_1(1420)$	Mass	1408	1410	1419	1409	1410
	Width	157	159	137	159	155
a_1'	Mass	1752	—	1835	1723	1956
	Width	257	—	230	505	125
$a_2(1320)$	Mass	1314	1314	1312	1314	1314
	Width	108	107	107	107	107
a_2'	Mass	1648	1648	1682	1657	1648
	Width	430	435	410	448	403
$a_4(2040)$	Mass	1934	1934	1918	1934	1933
	Width	357	362	343	357	357
$\pi(1800)$	Mass	1796	1794	1803	1795	1799
	Width	217	216	207	217	216
$\pi_2(1670)$	Mass	1662	1663	1644	1663	1659
	Width	293	293	302	289	297
$\pi_2(1880)$	Mass	1818	1814	1810	1820	1819
	Width	347	341	311	344	339

Table 4.11: Resonance parameters for study on wave set. Column M denotes the main fit. A is a study, where the $1^{++}0^+\rho(770)\pi S$ and D waves were removed. B denotes a study, where the $2^{-+}1^+f_2(1270)\pi S$ and the $2^{-+}0^+\rho(770)\pi F$ waves were left out. C1 and C2 are two ambiguous solutions for a study without the $1^{++}0^+\rho(770)\pi D$ wave.

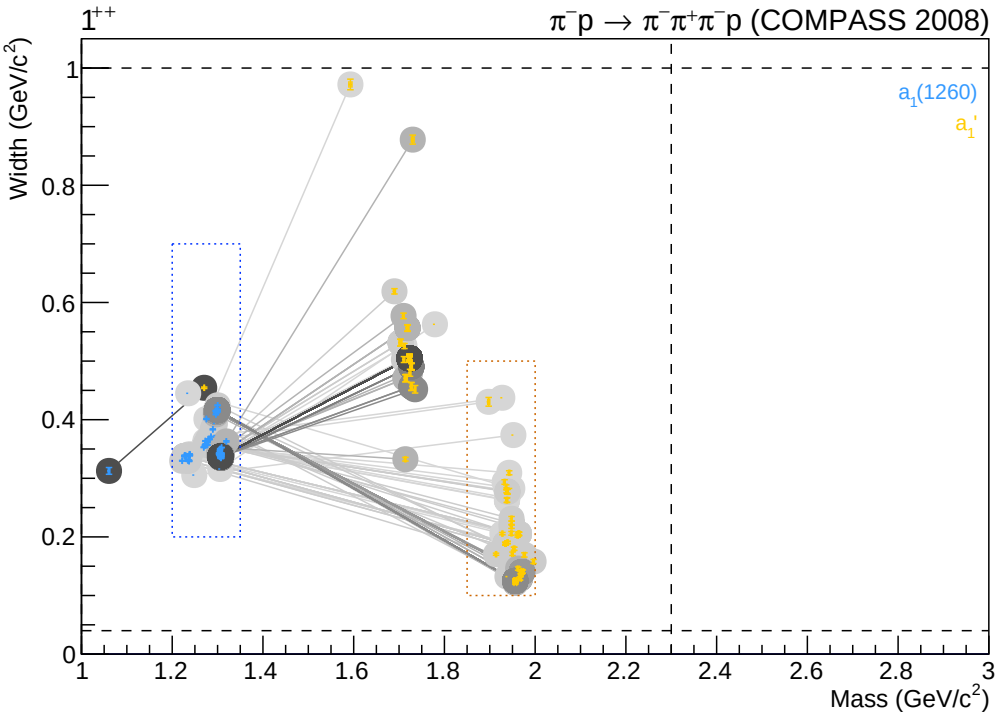

Figure 4.38: Mass and width of $a_1(1260)$ (blue) and a_1' (yellow) after all cuts leaving out the removal of spurious solutions for the extended wave set without the $1^{++}0^+\rho(770)\pi D$ wave. An explanation of the used plotting scheme can be found in figure 4.12.

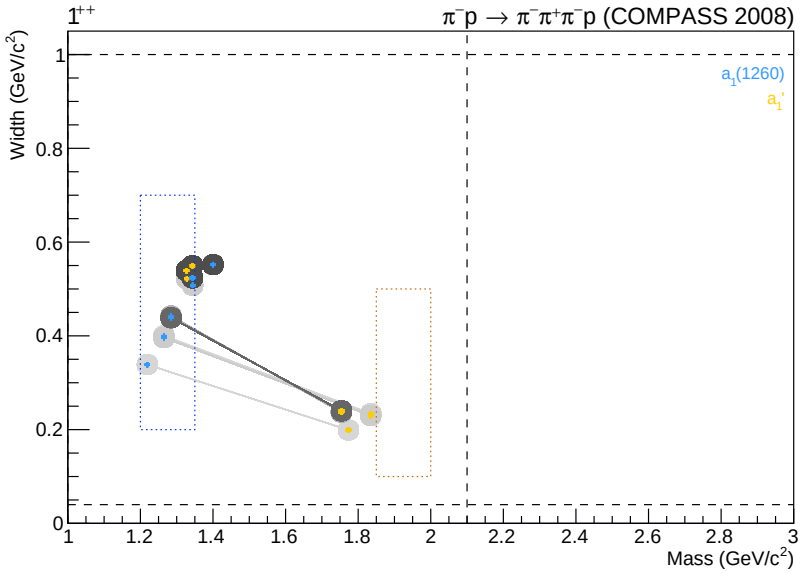

Figure 4.39: Mass and width of $a_1(1260)$ (blue) and a_1' (yellow) after the removal of spurious solutions for the extended wave set without the $2^{-+}1^+f_2(1270)\pi S$ and $2^{-+}0^+\rho(770)\pi F$ waves. An explanation of the used plotting scheme can be found in figure 4.12.

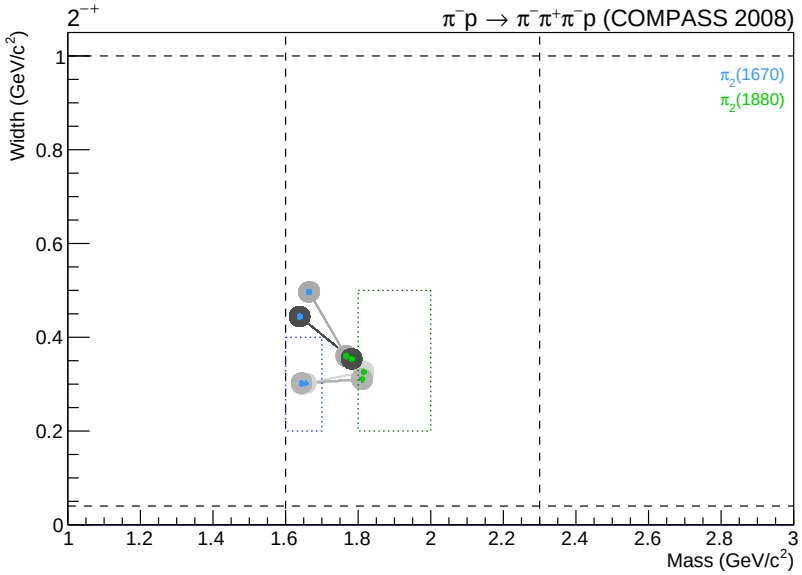

Figure 4.40: Mass and width of $\pi_2(1670)$ (blue) and $\pi_2(1880)$ (green) after the cut on the interchange of resonance positions for the extended wave set without the $2^{-+}1^+f_2(1270)\pi S$ and $2^{-+}0^+\rho(770)\pi F$ waves. An explanation of the used plotting scheme can be found in figure 4.12.

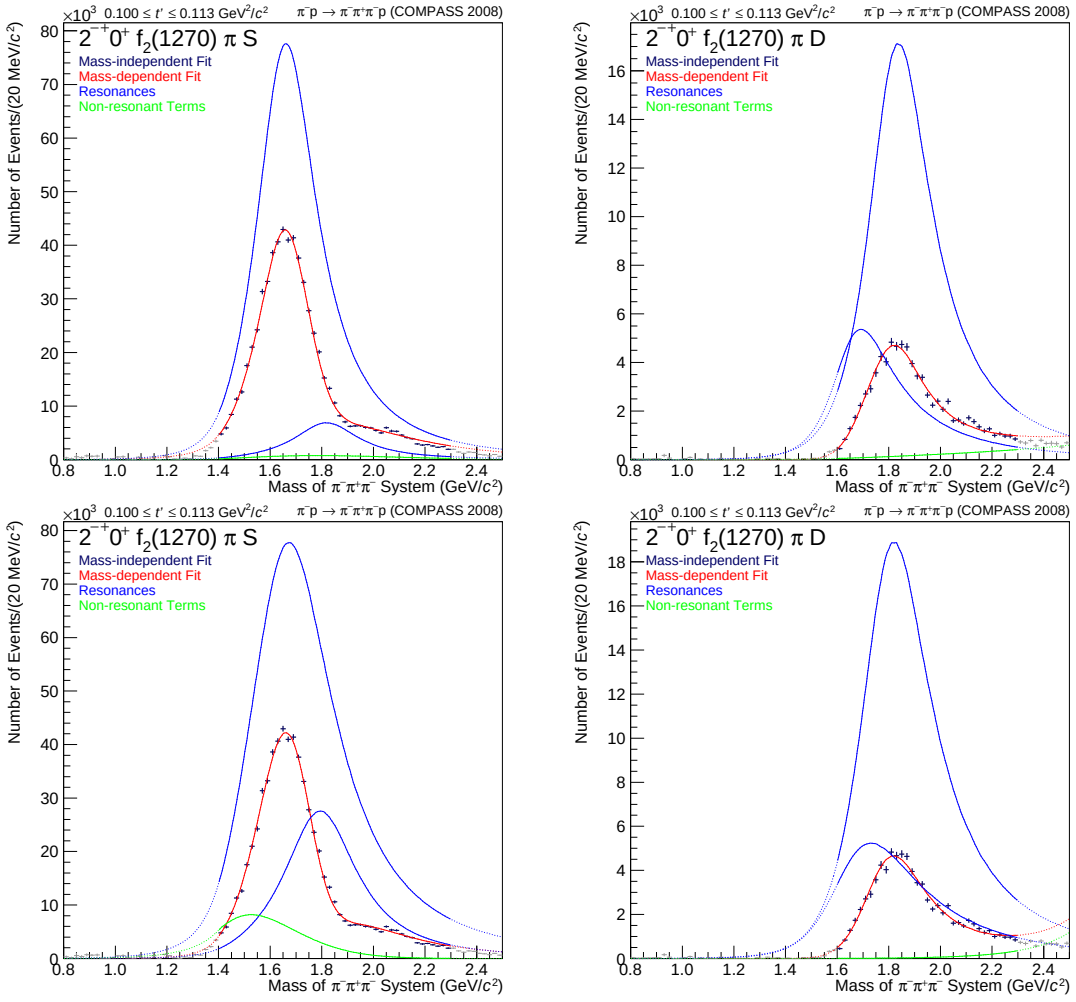

Figure 4.41: Intensity in the $2^{-+}1^{+}f_2(1270)\pi S$ (left) and the $2^{-+}1^{+}f_2(1270)\pi D$ (right) waves for the lowest t' bin in the best physical (upper row) and unphysical (lower row) solution after the cut on the interchange of resonance positions for a systematic study without the $2^{-+}1^{+}f_2(1270)\pi S$ and the $2^{-+}0^{+}\rho(770)\pi F$ waves. The colour scheme is described in figure 4.2.

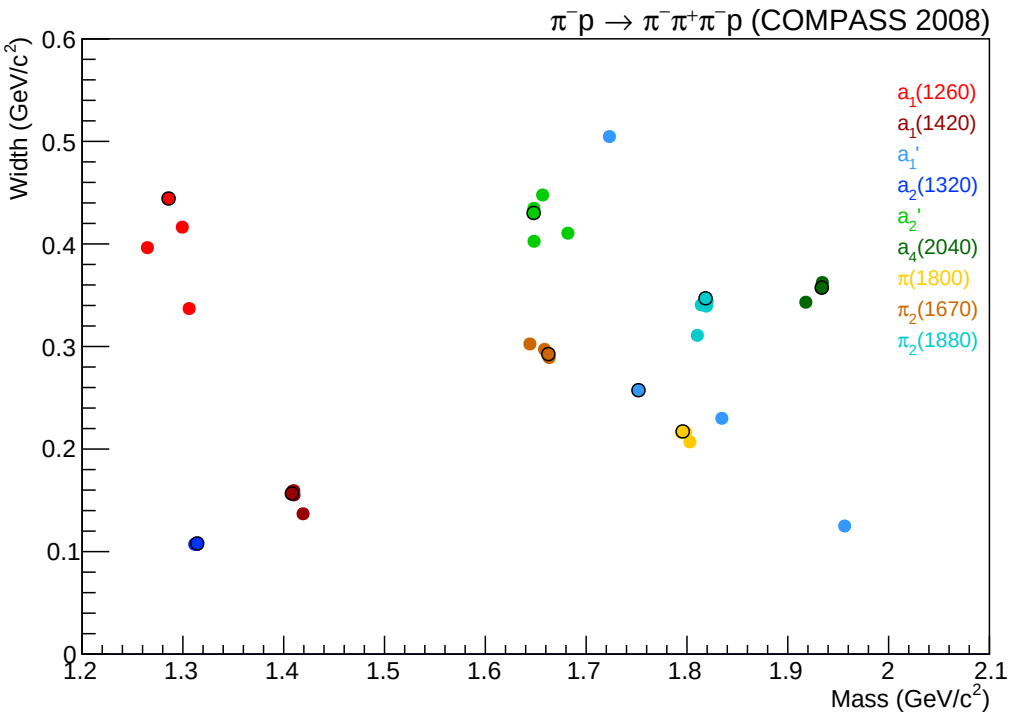

Figure 4.42: Resonance parameter overview for study on wave set. The black circle around the dots marks the solution from the main fit.

4.4.4 Study on the Choice of Parametrisation

Since it was observed that the description of the rising flanks of the $a_1(1260)$ peaks by the $a_1(1260)$ resonance term in combination with the non-resonant term of the $1^{++}0^+\rho(770)\pi S$ or D wave are insufficient, it is important to study the occurring deviations for different parametrisations. This is even more the case, because the non-resonant terms are parametrised phenomenologically.

One test was performed with a fixed-width Breit-Wigner instead of the Bowler parametrisation from equation 4.3 for the $a_1(1260)$. In addition three different parametrisations for the non-resonant terms, which are observed to be the strongest source of systematics besides the choice of the wave set, were tested. In one study all non-resonant terms use the simplest parametrisation (equation 4.6) and in another study only the parameter b was fixed to zero for all terms using the equation 4.5. Furthermore in order to check whether the description of the rising part of the $a_1(1260)$ peak can be better described by an increase in the freedom of the non-resonant contributions the following parametrisation was used in the $1^{++}0^+\rho(770)\pi S$ and D waves:

$$(m - m_{\text{threshold}})^{b_0+b_1 t'+b_2 t'^2} e^{(c_0+c_1 t'+c_2 t'^2)q^2} \tag{4.8}$$

As can be seen in table 4.12 the χ^2 shrinks with an increased freedom for the non-resonant contributions, which can be achieved with only slightly more parameters compared to the 68 255 data points. The most significant improvement is noticeable for the additional factor $(m - m_{\text{threshold}})^b$, which improves the χ^2 by more than 30 000. Extending this term further with a build-in t' dependence does succeed in describing the rise of the $a_1(1260)$ peak in the $1^{++}0^+\rho(770)\pi S$ wave, but leads to a suspicious result for the $1^{++}0^+\rho(770)\pi D$ wave shown in figure 4.43. Furthermore the fitter has huge problems converging and often runs into the parameter limits as can be seen in table 4.13.

Parametrisation of non-resonant term	χ^2	$N_{\text{parameter}}$
Extended parametrisation from equation 4.8	307 418	629
Main fit	325 125	622
$b = 0$ in parametrisation from equation 4.5	356 248	619
Parametrisation from equation 4.6 for all waves	366 348	610

Table 4.12: χ^2 values for different parametrisations of the non-resonant terms.

The resonance parameters resulting from the different studies are presented in table 4.14 and figure 4.44. While the change of the $a_1(1260)$ parametrisation is almost only changing the parameters of the a_1 resonances, the usage of the extended non-resonant term from equation 4.8 additionally influences the a_2'. The other two changes in the parametrisation influence all resonances considerably as can be expected, because they were applied to more waves. In waves with two resonances the first always gets lighter and the second heavier. For the simple parametrisation from equation 4.6 all resonances except the $\pi_2(1670)$ are additionally getting narrower. So, in general the large systematic effects from the non-resonant terms are clearly visible.

The test with the simpler fixed-width $a_1(1260)$ parametrisation results in the lightest and broadest $a_1(1260)$ of all systematic studies. However, since the parametrisations are

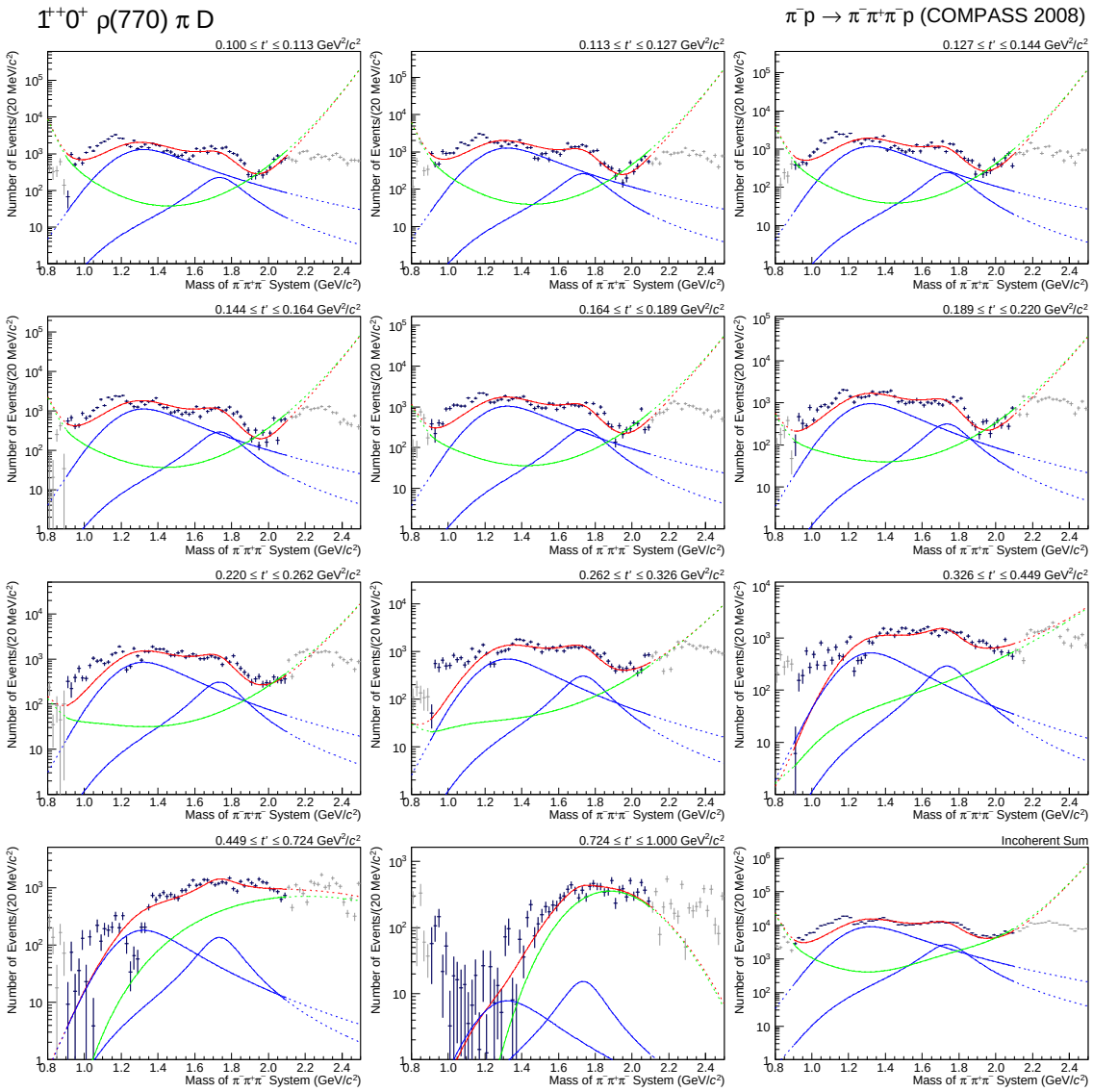

Figure 4.43: Intensity of the $1^{++}0^{+}\rho(770)\pi D$ wave as a function of t' in logarithmic scale for the study with the extended parametrisation of the non-resonant terms given in equation 4.8. The ordering in t' is the same as in figure 4.5. The colour scheme is described in figure 4.2.

Cut	Number of remaining fit results
	966
Failed convergence	681
Parameter close to limits	92
Spurious solutions	52
Interchange of resonance positions	52
Proximity of resonances	52
Resonances outside fit range	52

Table 4.13: Overview on the applied cuts for the study with the extended non-resonant terms from equation 4.8 in the $1^{++}0^{+}\rho(770)\pi S$ and D waves.

different the mass and width parameters slightly change in their meaning, so that they are not directly comparable. This effect is not taken into account and is left for a further study. Therefore the resulting systematic error might be somewhat overestimated.

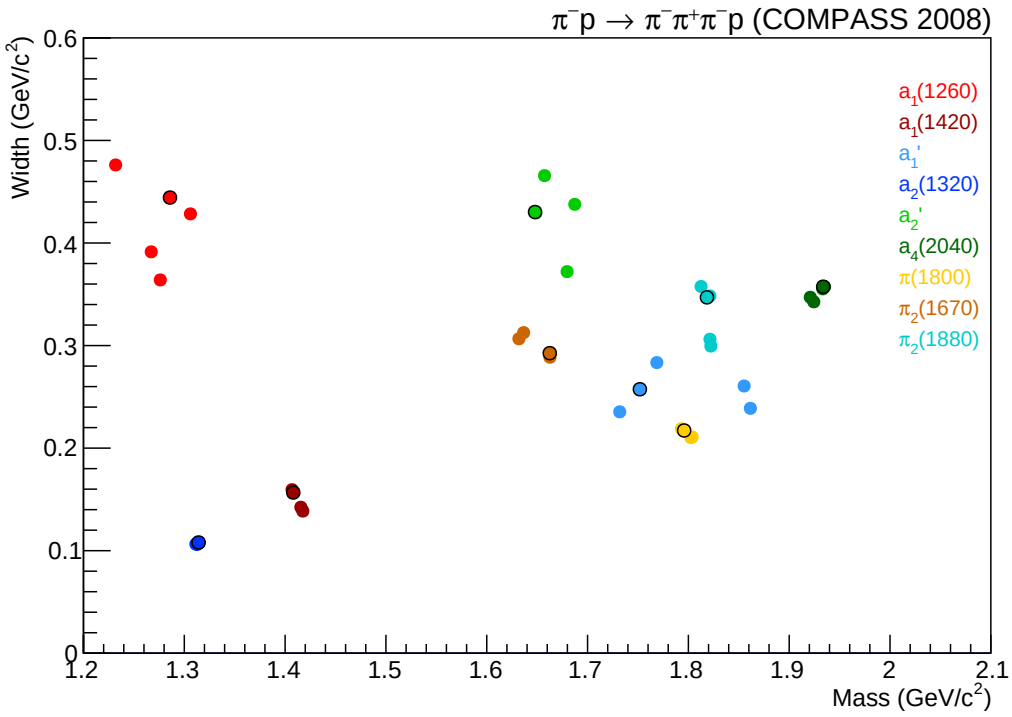

Figure 4.44: Resonance parameter overview for study on parametrisation of resonant and non-resonant terms. The black circle around the dots marks the solution from the main fit.

Resonance	Parameter	M[MeV/c^2]	A[MeV/c^2]	B[MeV/c^2]	C[MeV/c^2]	D[MeV/c^2]
$a_1(1260)$	Mass	1286	1232	1306	1267	1276
	Width	444	476	428	391	364
$a_1(1420)$	Mass	1408	1408	1407	1418	1416
	Width	157	157	160	139	142
a_1'	Mass	1752	1769	1732	1855	1862
	Width	257	283	235	261	239
$a_2(1320)$	Mass	1314	1314	1315	1312	1313
	Width	108	108	108	106	106
a_2'	Mass	1648	1649	1657	1687	1680
	Width	430	429	466	438	372
$a_4(2040)$	Mass	1934	1933	1935	1921	1924
	Width	357	355	357	347	343
$\pi(1800)$	Mass	1796	1796	1793	1802	1804
	Width	217	216	219	210	211
$\pi_2(1670)$	Mass	1662	1663	1663	1632	1637
	Width	293	292	289	307	313
$\pi_2(1880)$	Mass	1818	1821	1813	1822	1821
	Width	347	348	358	300	306

Table 4.14: Resonance parameters for study on parametrisationof resonant and non-resonant terms. M denotes the main fit. For A a fixed-width Breit-Wigner was used for the $a_1(1260)$ instead of the Bowler parametrisation. In B the non-resonant terms for the $1^{++}0^+\rho(770)\pi S$ and D waves have been extended as given in equation 4.8. C denotes a study, where the parameter b in equation 4.5 was fixed to 0 for all waves that use this non-resonant parametrisation. For D all waves have used the simplest non-resonant parametrisation given in equation 4.6.

4.4.5 Study on the Used Resonances

In order to check the significance of the not established resonances $a_1(1420)$, a_1' and a_2' they were removed from the model in three separate studies. The χ^2 values given in table 4.15 clearly show that the fitter has problems describing some features of the data without those resonances. For the $a_1(1420)$ the fitter was neither able to describe the intensity of the $1^{++}0^+f_0(980)\pi P$ wave nor its relative phase motions (see figure 4.15). In the case of the a_1' and a_2' the description of the waves, where these resonances are more dominant, also failed (see figures 4.46 and 4.47). However, the description of the $1^{++}0^+\rho(770)\pi S$ and the $2^{++}1^+\rho(770)\pi D$ wave did not suffer visibly. This includes the description of the interference dip for the 2^{++} wave, but in order to make up for the missing a_2' the fitter needs here a 14 MeV/c^2 broader $a_2(1320)$. The overview on all results is given in table 4.16 and figure 4.48.

	χ^2	$N_{\text{parameter}}$
Main fit	325 125	622
Without $a_1(1420)$	443 942	598
Without a_1'	372 180	596
Without a_2'	452 720	574

Table 4.15: χ^2 values for studies without selected resonances.

Resonance	Parameter	M[MeV/c^2]	A[MeV/c^2]	B[MeV/c^2]	C[MeV/c^2]
$a_1(1260)$	Mass	1286	1290	1300	1297
	Width	444	449	456	450
$a_1(1420)$	Mass	1408	—	1407	1404
	Width	157	—	157	162
a_1'	Mass	1752	1731	—	1721
	Width	257	250	—	274
$a_2(1320)$	Mass	1314	1314	1314	1318
	Width	108	108	108	122
a_2'	Mass	1648	1655	1651	—
	Width	430	453	454	—
$a_4(2040)$	Mass	1934	1933	1935	1934
	Width	357	359	354	353
$\pi(1800)$	Mass	1796	1792	1794	1787
	Width	217	218	219	221
$\pi_2(1670)$	Mass	1662	1666	1663	1662
	Width	293	283	289	279
$\pi_2(1880)$	Mass	1818	1819	1818	1809
	Width	347	350	351	367

Table 4.16: Resonance parameters for studies without selected resonances. M denotes the main fit. The others are studies leaving out the $a_1(1420)$ (A), the a_1' (B) and the a_2' (C).

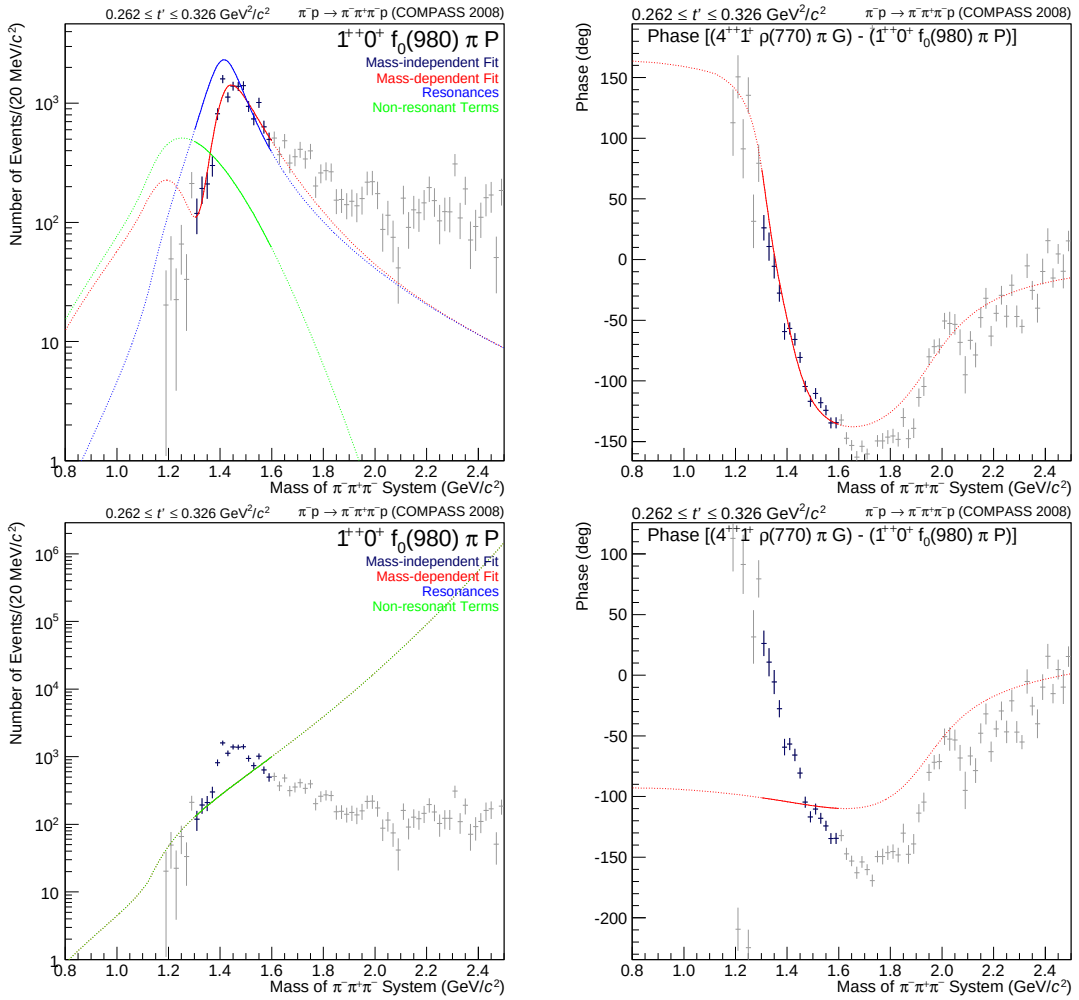

Figure 4.45: Intensity of the $1^{++}0^{+}f_0(980)\pi P$ wave (left) and its phase relative to the $4^{++}1^{+}\rho(770)\pi G$ wave (right) for the main fit (upper row) and the study without an $a_1(1420)$ (lower row) for an intermediate t' bin. The colour scheme is described in figure 4.2.

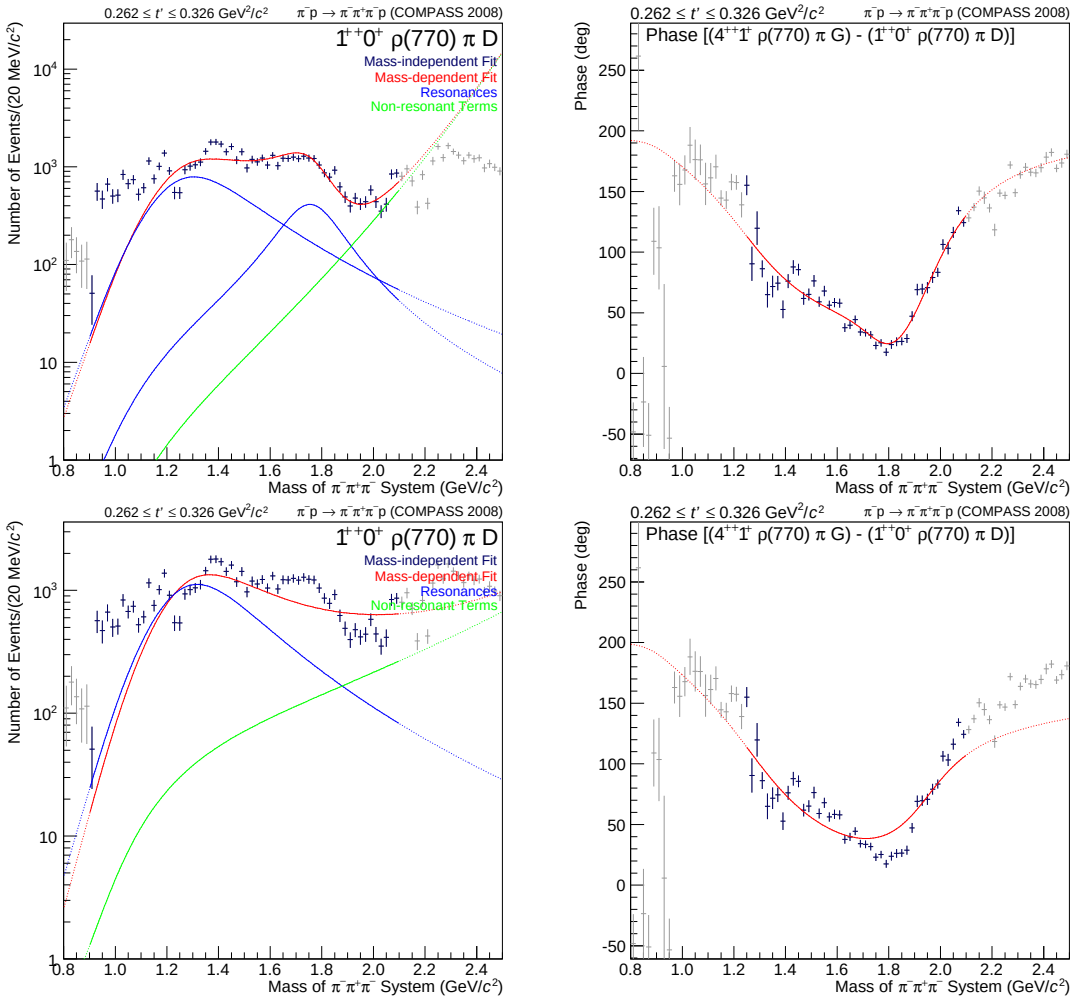

Figure 4.46: Intensity of the $1^{++}0^{+}\rho(770)\pi D$ wave (left) and its phase relative to the $4^{++}1^{+}\rho(770)\pi G$ wave (right) for the main fit (upper row) and the study without an a_1' (lower row) for an intermediate t' bin. The colour scheme is described in figure 4.2.

Besides the broadening of the $a_2(1320)$ two other peculiarities are observed in the study without an a_2'. First of all figure 4.50 shows that the best solution in terms of χ^2 was found only twice. However, since these two solutions are unphysical this is not an issue. Additionally figure 4.49 suggest that the cut on spurious solutions was requiring a too large number of equal χ^2 solutions, but again this is not a problem. One of the four missed solutions is unphysical, one has a χ^2 of roughly 640 000 and the other two are solutions, where the fitter missed another accepted solution by only 0.1 in χ^2. So the final result is robust against changes in the cut on spurious solutions.

Summarising the studies without selected resonances, it can be stated that all resonances are required and lead to a significant decrease in the χ^2 value.

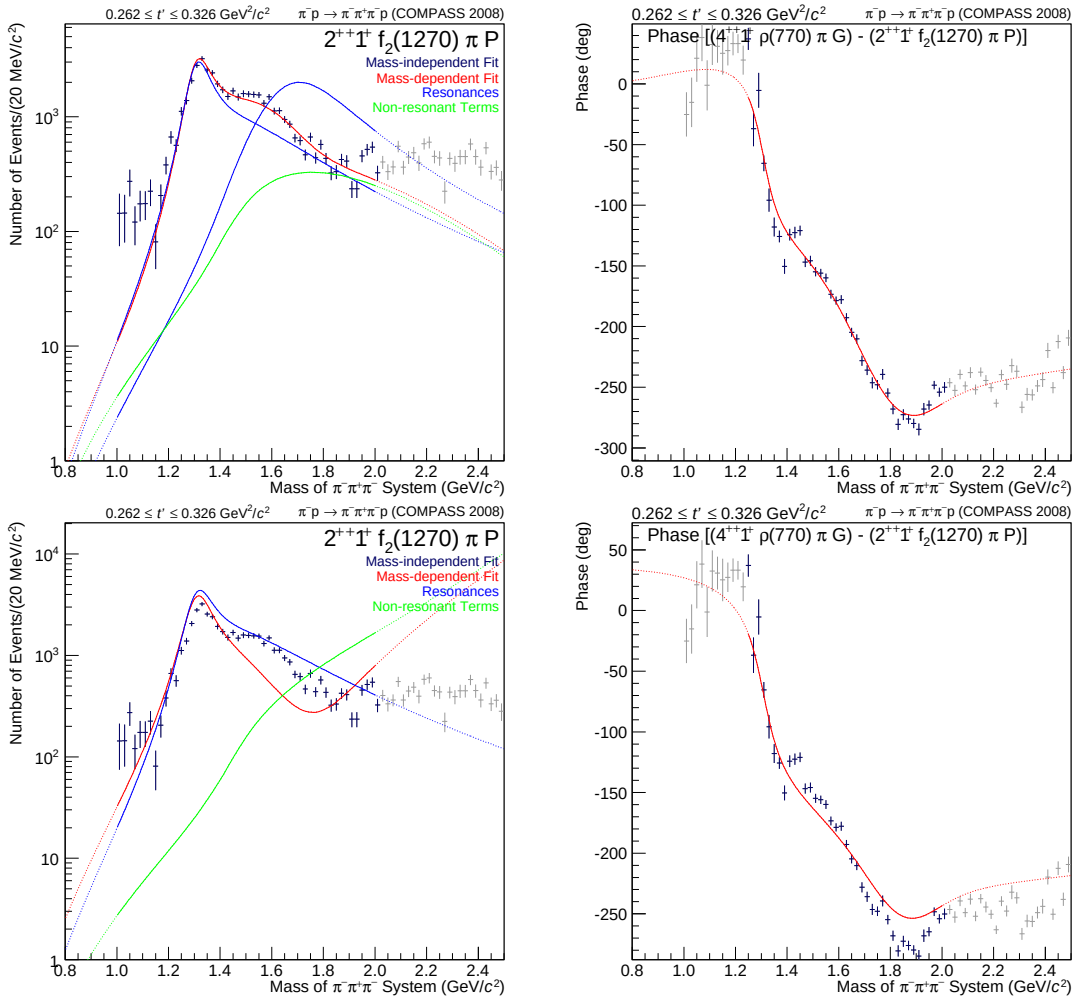

Figure 4.47: Intensity of the $2^{++}1^{+}f_2(1270)\pi P$ wave (left) and its phase relative to the $4^{++}1^{+}\rho(770)\pi G$ wave (right) for the main fit (upper row) and the study without an a_2' (lower row) for an intermediate t' bin. The colour scheme is described in figure 4.2.

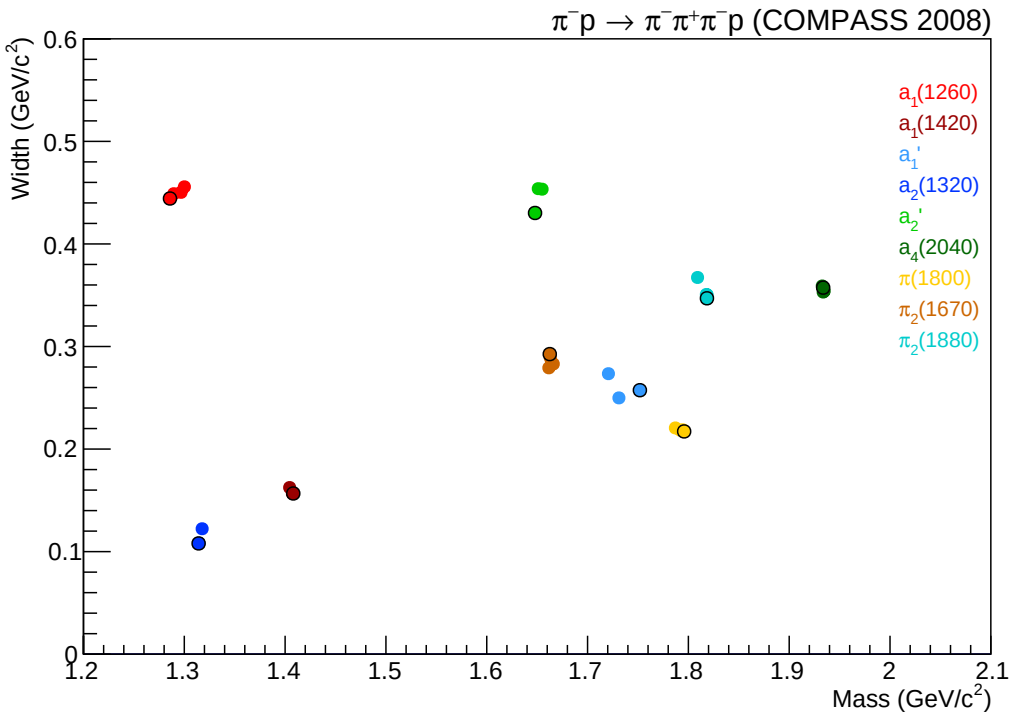

Figure 4.48: Resonance parameter overview for studies without selected resonances. The black circle around the dots marks the solution from the main fit.

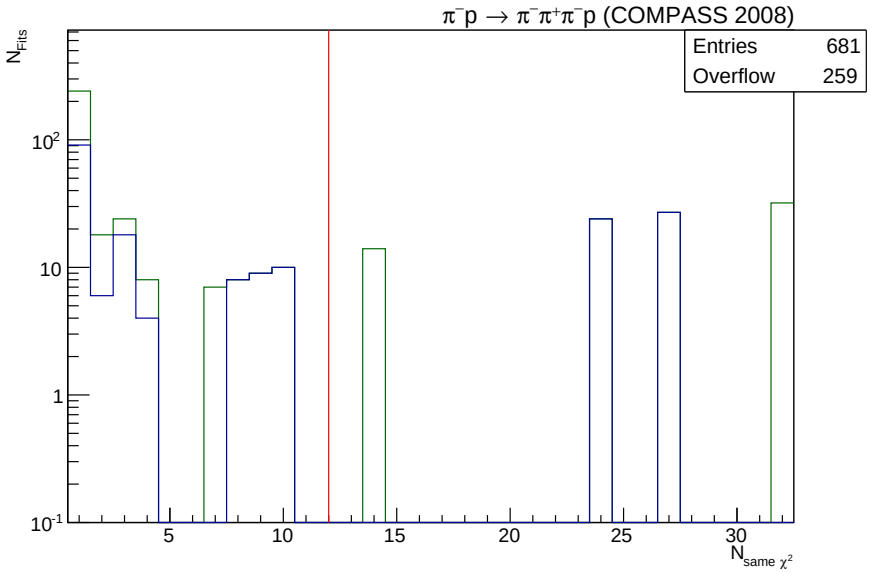

Figure 4.49: Projection of the distribution of χ^2 values in figure 4.50 on the y-axis followed by a multiplication of each $N_{\text{same}\chi^2}$ bin with its x-value $N_{\text{same}\chi^2}$. The histogram can be interpreted as a not normalised probability of a fit to result in a χ^2 interval with $N_{\text{same}\chi^2}$ values. The fits that are cut away (kept) by later applied physical and model-based restrictions are indicated in green (blue). The red line shows the cut on spurious solutions performed in the next step.

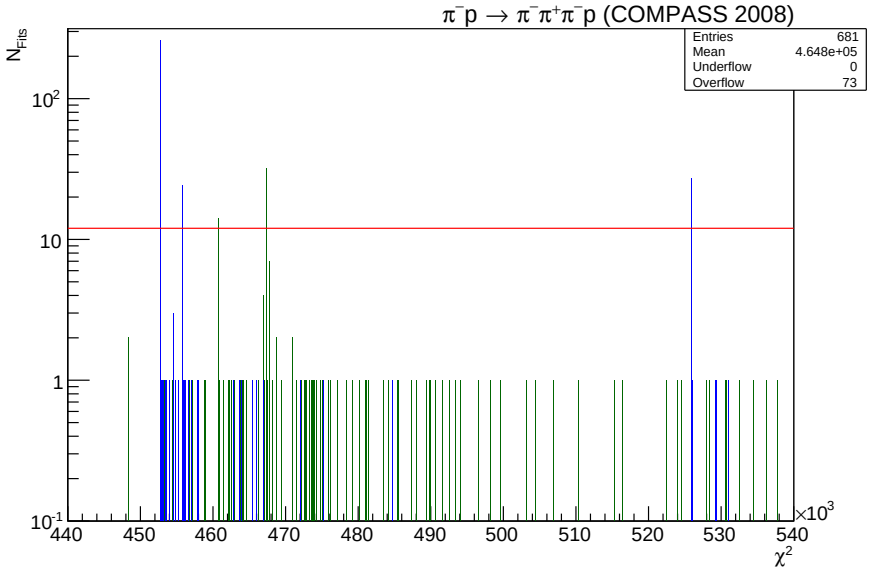

Figure 4.50: Distribution of χ^2 values before the removal of spurious solutions for the extended wave set without the a_2' resonance. The plotting scheme is described in figure 4.13.

4.4.6 Study on the Event Selection

Finally two studies have been performed on how robust the resonance parameters are against an increase of the incoherent background due to, for example, kaons or non-exclusive events. This is achieved by first removing the cuts on particle identification and on central production. In the second study additionally the condition on the coplanarity and the requirement of exactly on reconstructed track in the RPD were lifted. Thereby the fraction of non-exclusive events is increased. The total number of events is in the first study increased by approximately 26% and in the second study increased by approximately 76%. In both studies roughly 10% of the additional events are absorbed by the flat wave, which results in an increase of its relative total intensity from 3.09% to 4.78% and 5.63%. The rest is distributed over the other waves. Due to the nature of the background it typically does not interfere with the diffractive-dissociation process. However, since no incoherent terms are applied to the model, the fitter has to describe this background in terms of coherently summed contributions. In the ideal case this would completely be absorbed by the non-resonant terms. However, as can be seen in table 4.17 and figure 4.51 it also influences the resonance parameters. The magnitude of the changes is small compared to other studies, but the direction of the variations is especially for the $a_4(2040)$, $\pi(1800)$ and $\pi_2(1880)$ different than in the rest of the studies.

Resonance	**Parameter**	**M[MeV/c^2]**	**A[MeV/c^2]**	**B[MeV/c^2]**
$a_1(1260)$	Mass	1286	1295	1288
	Width	444	451	432
$a_1(1420)$	Mass	1408	1407	1406
	Width	157	150	146
a_1'	Mass	1752	1747	1747
	Width	257	209	212
$a_2(1320)$	Mass	1314	1314	1314
	Width	108	108	108
a_2'	Mass	1648	1652	1651
	Width	430	444	432
$a_4(2040)$	Mass	1934	1944	1944
	Width	357	350	345
$\pi(1800)$	Mass	1796	1802	1804
	Width	217	219	220
$\pi_2(1670)$	Mass	1662	1664	1664
	Width	293	282	283
$\pi_2(1880)$	Mass	1818	1834	1838
	Width	347	358	373

Table 4.17: Resonance parameters for study on event selection. M denotes the main fit. A removed the cuts due to particle identification and on central production in the event selection. For B the condition on the coplanarity and the requirement of exactly on reconstructed track in the RPD were lifted additionally.

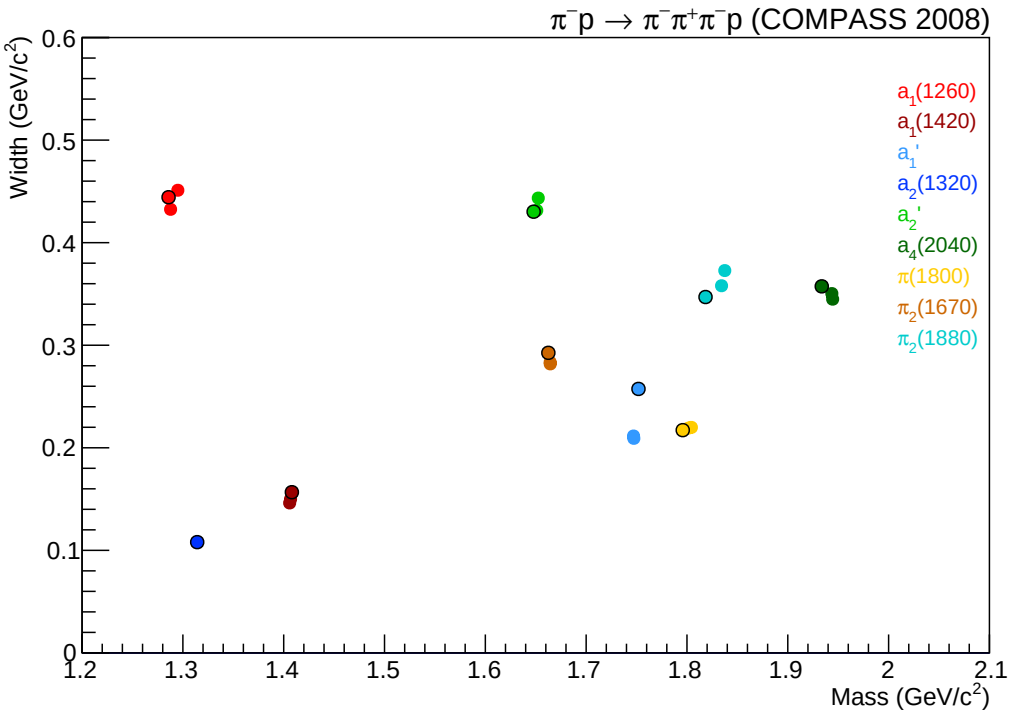

Figure 4.51: Resonance parameter overview for study on event selection. The black circle around the dots marks the solution from the main fit.

4.4.7 Comparison with the PDG 2012

Finally all studies are combined in a systematic error by using the largest deviation seen with respect to the main fit, which determines the central values. The results are listed in table 4.18 in combination with the corresponding averages from the PDG 2012 [13]. The comparison of the central values is visualised in form of an excitation spectrum in figure 4.52. For a representation including the errors the summary plot from the beginning of this chapter has been extended by adding the values from experiments that were used for averaging in the PDG 2012. In order to adapt the scale to the size of the individual spreads the plot is split into the five parts shown in figure 4.53, 4.54, 4.55, 4.56 and 4.57.

The $a_1(1260)$ results are at the high-mass side of the PDG 2012 estimate and most of the other experiments. However, since COMPASS for the first time performed an analysis in bins of t', which improves the separation of resonant and non-resonant contributions, this is not an unlikely effect. The errors are defined by two solutions. The broadest and lightest $a_1(1260)$ is from the study with the fixed-width parametrisation, which as stated before might overestimate the error. Whereas the narrowest and heaviest solution is related to the extremely broad a_1' from the study with only the $1^{++}0^+\rho(770)\pi S$ wave containing those two resonances.

The a_1' itself is more or less undetermined, therefore the values for the $a_1(1640)$ as well

Resonance	Parameter	COMPASS Result [MeV/c^2]	PDG 2012 [MeV/c^2]	
$a_1(1260)$	Mass	$1285.8\,^{+20.4}_{-53.9}$	1230 ± 40	
	Width	$444.3\,^{+31.8}_{-107.3}$	250 to 600	
$a_1(1420)$	Mass	$1408.1\,^{+11.1}_{-3.6}$	—	
	Width	$156.7\,^{+5.8}_{-19.8}$	—	
a_1'	Mass	$1751.9\,^{+204.5}_{-57.7}$	1647 ± 22	$1930\,^{+30}_{-70}$
	Width	$257.4\,^{+247.3}_{-132.4}$	254 ± 27	155 ± 45
$a_2(1320)$	Mass	$1314.2\,^{+3.5}_{-2.7}$	$1319.0\,^{+1.0}_{-1.3}$	
	Width	$108.0\,^{+14.3}_{-1.8}$	$105\,^{+1.6}_{-1.9}$	
a_2'	Mass	$1647.9\,^{+39.4}_{-0.0}$	1732 ± 16	
	Width	$430.2\,^{+35.5}_{-58.1}$	194 ± 40	
$a_4(2040)$	Mass	$1933.7\,^{+10.8}_{-15.8}$	$1996\,^{+10}_{-9}$	
	Width	$357.4\,^{+5.0}_{-14.8}$	$255\,^{+28}_{-24}$	
$\pi(1800)$	Mass	$1795.8\,^{+8.6}_{-8.7}$	1812 ± 12	
	Width	$217.2\,^{+3.4}_{-10.2}$	208 ± 12	
$\pi_2(1670)$	Mass	$1662.5\,^{+3.5}_{-30.6}$	1672.2 ± 3.0	
	Width	$292.6\,^{+20.0}_{-13.4}$	260 ± 9	
$\pi_2(1880)$	Mass	$1818.4\,^{+19.1}_{-9.3}$	1895 ± 16	
	Width	$347.0\,^{+25.8}_{-47.5}$	235 ± 34	

Table 4.18: Resonance parameters with systematic errors and values from the PDG 2012 [13]. For the $a_2(1320)$ the average for the 3π mode is stated and since the COMPASS parameters for the a_1' are spread so widely the values of the $a_1(1640)$ and the further state $a_1(1930)$ are presented.

as the ones for the $a_1(1930)$ are stated from the PDG 2012. The errors are mainly given by the study with only the $1^{++}0^+\rho(770)\pi S$ wave containing this resonance. The lowest mass, however, is from the solution without applied branchings. In order to improve the certainty of the parameters of this resonance as well as those of the $a_1(1260)$ additional studies including more waves and a more realistic description of the non-resonant terms are required.

Since it was newly discovered by COMPASS the $a_1(1420)$ is not listed in the PDG 2012. Nevertheless, owing to its well-pronounced phase motions, it is already quite well determined and fluctuations between different studies are small. The error is spanned by the light solution without an a_2' and the heavy solution with only two waves in the 2^{-+} sector.

As the most well-determined 3π resonance the $a_2(1320)$ is often used to check for

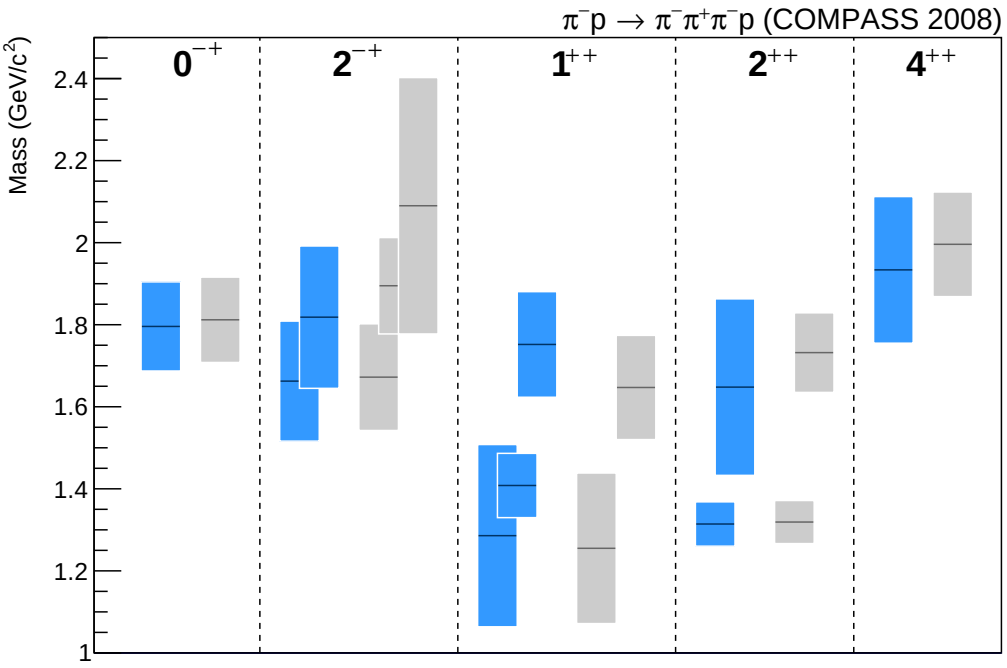

Figure 4.52: Comparison of the centre values from the COMPASS analysis given in table 4.18 (blue) with the PDG 2012 [13] (grey). The centres of the bars mark the masses of the resonances, while the full heights represent their widths. Since no central value is given for the PDG 2012 width estimate of the $a_1(1260)$, the parameters for this resonance are taken from the only experiment that is included in fits and limits. Due to the problems fitting three resonances in the same wave that are described in section 4.2 no COMPASS values for a third resonance with $J^{PC} = 2^{-+}$ are given.

problems in the analysis. While there is a deviation from the PDG 2012 3π average, looking at the individual measurements the COMPASS result is in quite good agreement. For nine of the thirteen measurements used for the average of mass and width the central value of this study lies within their 1σ error intervals. Furthermore it is interesting to see that the strong outlier due to a fit without an a_2' is within one σ of the PDG 2012 average. Considering that in general previous measurements did not include a second a_2 due to lack of data in the high-mass region of this wave the observed tension is less significant.

For the $a_2(1700)$, which is omitted from the PDG 2012 summary table, a clear discrepancy is observable for the COMPASS results with respect to the values from the PDG 2012. From the two measurements that are closest to the result of this thesis one is separated in terms of its errors by 0.3σ in mass and 2.1σ in width, while the other is 1.3σ away in mass and 3σ in width. However, the largest deviation for this resonance in the different studies are observed for the four different parametrisations of the non-resonant term, so

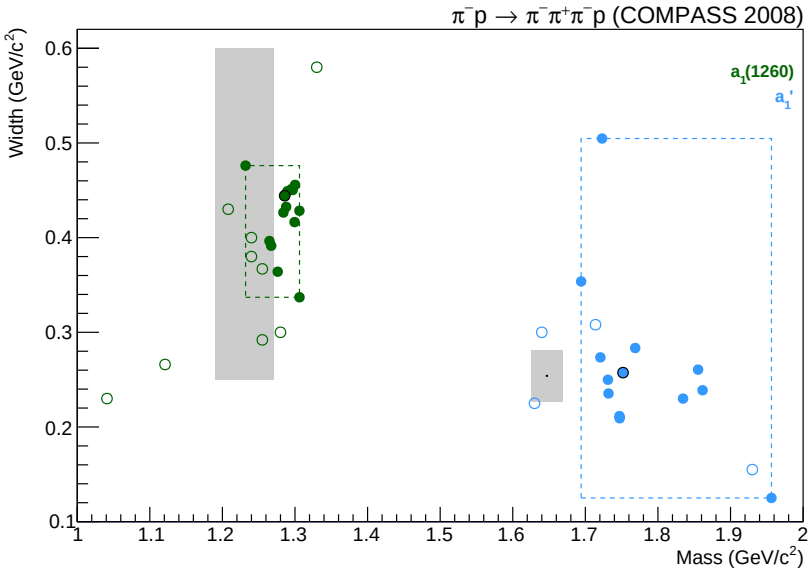

Figure 4.53: Comparison of the results from COMPASS with the PDG 2012 values [13] for the $a_1(1260)$ (green) and a_1' (blue). While the full circles mark the individual systematic studies performed for the COMPASS data, the open circles show the listed measurements of these resonances in the PDG 2012. Note that in general only the values used for the PDG 2012 average are shown. However, in the case of the $a_1(1260)$ no average is stated and therefore all scattering and proton-proton collision data are used. The average PDG 2012 value itself is marked by the black dots, whereas the respective errors are represented by the light grey boxes around them.

there is still quite some room for improvement for the $a_2(1700)$ parameters with a better characterisation of the non-resonant contribution.

The determined parameters of the $\pi(1800)$ are in quite good agreement with the PDG 2012 and the individual studies are distributed more or less homogeneously in the error interval.

For the $a_4(2040)$ on the contrary the deviation from the PDG 2012 is significant. However, the spread of values listed in the PDG 2012 is quite large. Nevertheless most experiments listed in the PDG 2012 find a higher mass then determined in this study with a deviation of up to 4σ in terms of their errors. Compared to this the divergence in between the individual systematic studies is rather small.

Finally the $\pi_2(1670)$ and $\pi_2(1880)$ are both significantly deviating from the PDG 2012 average by 3 to 5σ in mass and width. However, the largest shift in terms of resonance parameters is observed between six waves and thirteen waves for these resonances. The $\pi_2(1880)$ mass, for example, was at $1.94\,\mathrm{GeV}/c^2$ for the six-waves model, which is on the high-mass side of the PDG 2012 average and therefore significantly closer to two of the four listed experiments. Additionally the systematic error is mostly defined by the study leaving out two 2^{-+} waves and by the ones changing the non-resonant parametrisation

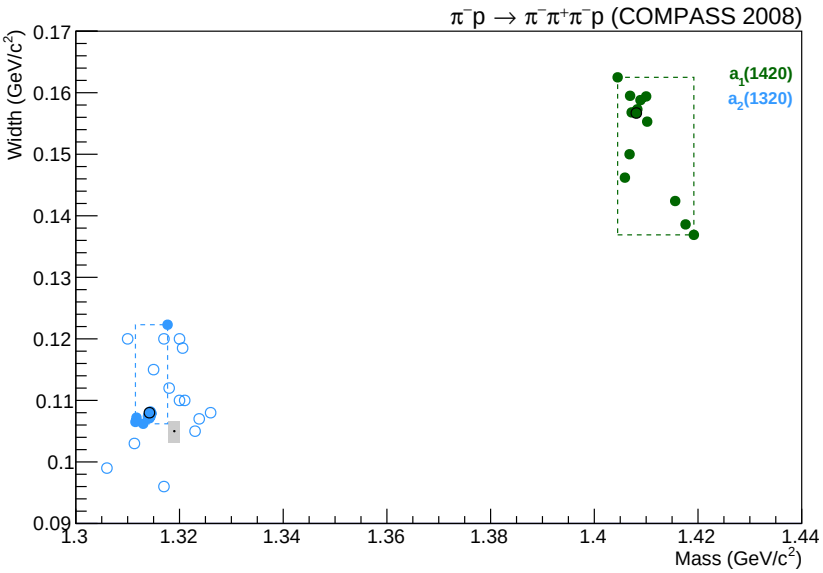

Figure 4.54: Comparison of the results from COMPASS with the PDG 2012 values [13] for the $a_2(1320)$ (blue). The new $a_1(1420)$ resonance (green) is plotted in addition. The plotting scheme is the same as previously in figure 4.53.

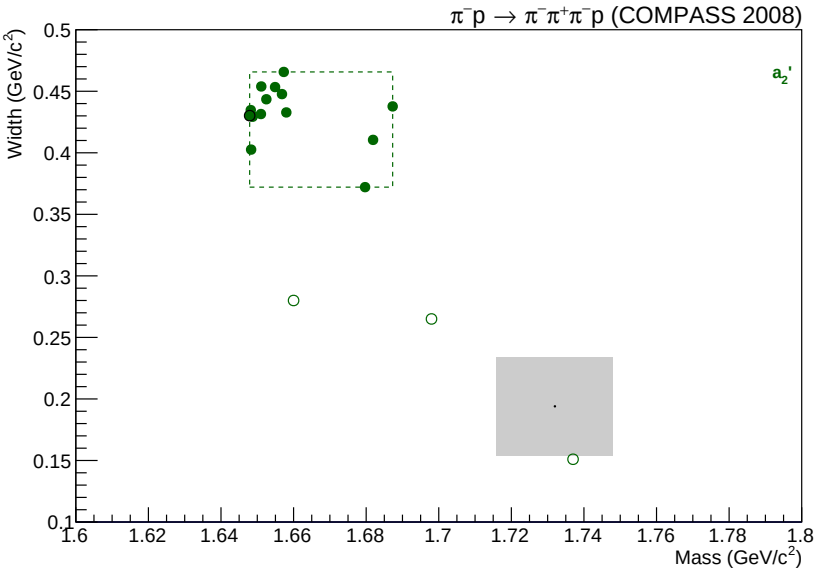

Figure 4.55: Comparison of the results from COMPASS with the PDG 2012 values [13] for the a_2'. The plotting scheme is the same as previously in figure 4.53.

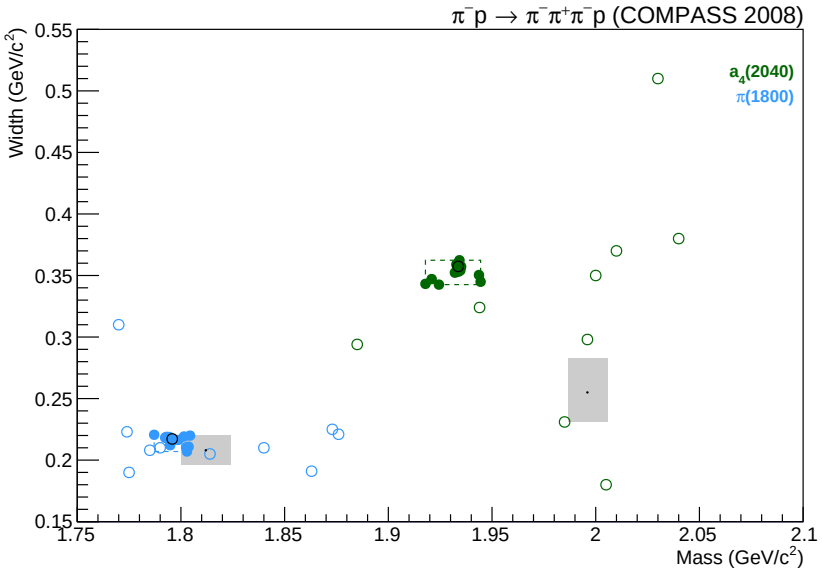

Figure 4.56: Comparison of the results from COMPASS with the PDG 2012 values [13] for the $a_4(2040)$ (green) and $\pi(1800)$ (blue). The plotting scheme is the same as previously in figure 4.53.

in, beside others, the $2^{-+}0^{+}f_2(1270)\pi S$ wave. In order to fully explain the deviation more dedicated studies are necessary.

Considering all resonances the fit result looks in general convincing. However, the seen deviations require further dedicated work that studies primarily the influences of the chosen wave set and improves the description of the non-resonant terms.

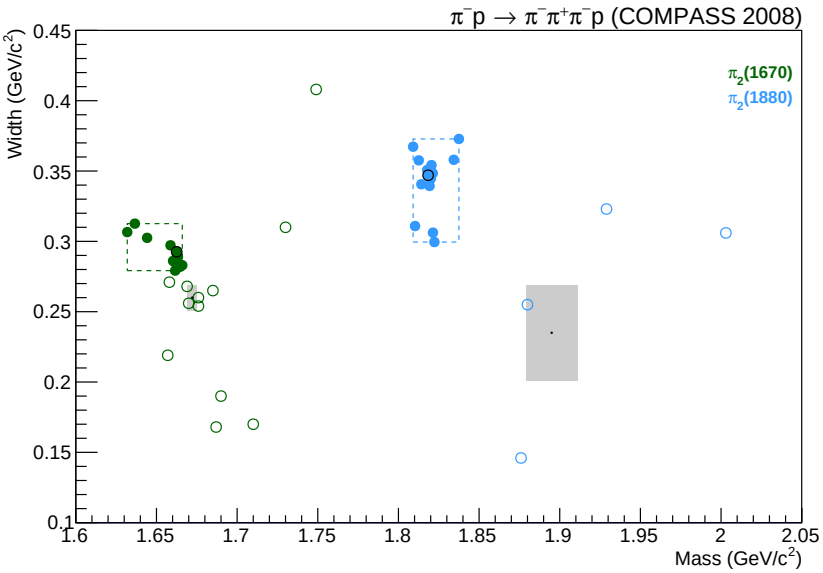

Figure 4.57: Comparison of the results from COMPASS with the PDG 2012 values [13] for the $\pi_2(1670)$ (green) and $\pi_2(1880)$ (blue). The plotting scheme is the same as previously in figure 4.53.

Chapter 5

Fit of t' Dependence

In contrast to the $m_{3\pi}$ distribution, which was used in the previous chapter to extract resonances, the topic of this chapter is the t' distribution. The simplest approach is to look at t' spectra for different slices of the $m_{3\pi}$ distribution like it is done, for example, in figure 5.1.

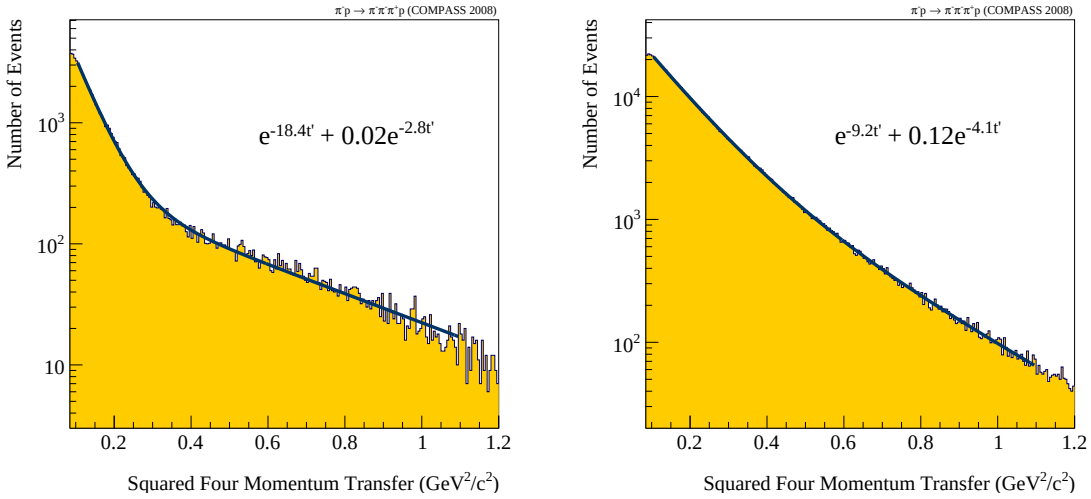

Figure 5.1: t' distribution in the kinematic range of $0.80 \leq m_{3\pi} \leq 0.81\,\mathrm{GeV}/c^2$ (left) and $1.60 \leq m_{3\pi} \leq 1.61\,\mathrm{GeV}/c^2$ (right) [17].

The ACCMOR Collaboration used this method for the so far most detailed parametrisation of the t' dependences [53]. However, the novel method including the t' binning in the resonance extraction now allows to study the t' dependences for individual resonant and non-resonant contributions. For this purpose for each t' bin the intensities of these components are integrated over the $m_{3\pi}$ fit range in the single waves.

The result for the $1^{++}0^+\rho(770)\pi S$ wave in the main fit from the previous section is given in figure 5.2. In addition to the $m_{3\pi}$-integrated intensities also the phases of the complex couplings of the individual contributions are plotted relative to the one of the $a_2(1320)$ in the $2^{++}1^+\rho(770)\pi D$ wave. Furthermore the intensity distributions are parametrised by an exponential distribution with slope parameter b. This parametrisation is motivated by a calculation of the t' dependence of the cross section assuming elastic scattering via Pomeron exchange and using the elastic form factor of the pion [39]. This results for a

fixed centre-of-mass energy and the $t' \lesssim 1\,\mathrm{GeV}^2/c^2$ range of diffractive scattering roughly in:

$$\frac{\mathrm{d}\sigma}{\mathrm{d}t'} \propto e^{-bt'}$$

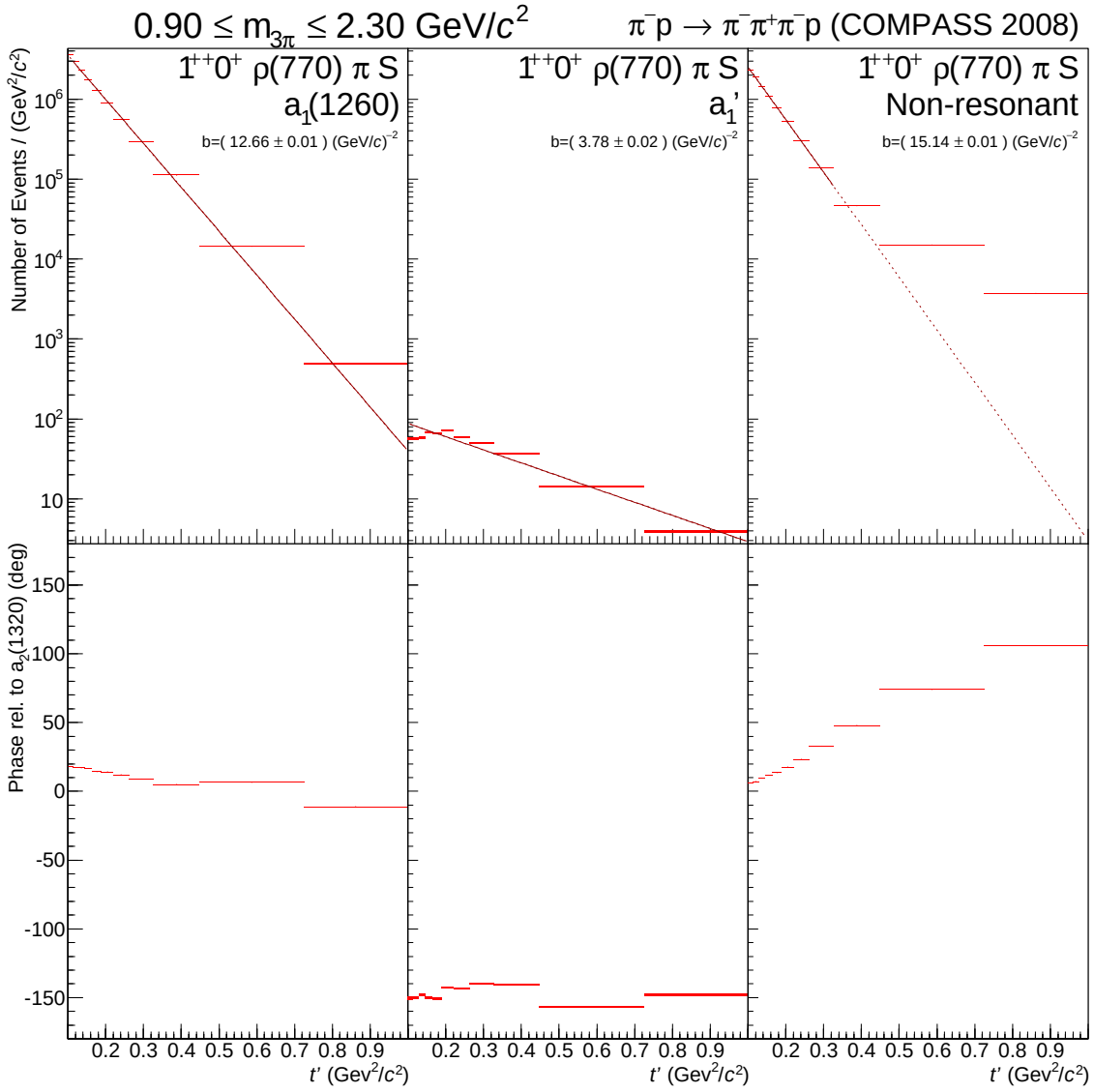

Figure 5.2: t' dependence of the $m_{3\pi}$-integrated intensity (upper row) and the phase (lower row) of the $a_1(1260)$ (left), the a_1' (centre) and the non-resonant term (right) in the $1^{++}0^+\rho(770)\pi S$ wave in the main fit. The red line indicates the fit of the single exponential parametrisation in equation 5.1 to the data represented by the red bars. The height of the bars shows the statistical error. Dotted lines indicate an extrapolation beyond the fit range.

However, applying this to states with a spin projection $M \neq 0$ an additional term is needed, since M introduces a dependence on the azimuthal angle ϕ in the intensity distribution. This angle is not defined in the forward limit of zero scattering angles

and therefore the intensity has to vanish in this limit. The suppression is realised by an additional factor $t'^{|M|}$ leading to the final parametrisation in the form:

$$\frac{\mathrm{d}\sigma}{\mathrm{d}t'} \propto t'^{|M|} e^{-bt'} \tag{5.1}$$

Especially for non-resonant terms it happens that a second component with a shallower slope is dominant for higher t'. Therefore bins at the end or to a limited extend also at the beginning of the accessed t' range have been excluded from the fit with equation 5.1.

Including all other solutions that were used to determine the systematic error for the resonance parameters leads from figure 5.2 to figure 5.3. It is striking that while the $a_1(1260)$ and the non-resonant term behave more or less stable, the a_1' distribution exhibits large fluctuations. This is not unexpected recalling the large spread in the a_1' resonance parameters. However, in contrast to the $a_1(1260)$ and the a_1' resonance, where the phase does not vary strongly with t', the phase of the non-resonant term significantly grows with t' in order to describe the peak shift of the $a_1(1260)$. This behaviour is also observed for the majority of the other resonances. However, in some waves the second resonance as well as the non-resonant term deviate from this behaviour. This indicates that the fitter has problems to disentangle them for these waves. One example for this is the a_2' in figure 5.5.

In the following the three waves defining the a_2 resonances, namely $2^{++}1^+\rho(770)\pi D$, $2^{++}2^+\rho(770)\pi D$ and $2^{++}1^+f_2(1270)\pi P$ are discussed. Their t' dependence is shown in figures 5.4, 5.5 and 5.6.

In figure 5.4 it can nicely be seen that all phases are given relative to the $a_2(1320)$ in the $2^{++}1^+\rho(770)\pi D$ wave. Therefore the phase of this resonance is completely flat by definition. The $a_2(1320)$ has been chosen as the reference, because it appears in one of the largest waves in the wave set, which is included in all systematic studies. Furthermore the $a_2(1320)$ is the clearest and best-known resonance in the 3π spectrum. In the intensities the effect of the $t'^{|M|}$ factor in the parametrisation is visible, which agrees well with the data. In figure 5.5 the effect is even stronger for $M = 2$.

The effect of the implemented branchings can be seen, for example, for the $2^{++}1^+f_2(1270)\pi P$ wave in figure 5.6. Apart from an offset the t' dependences of the phases of the $a_2(1320)$ and a_2' are the same as for the $2^{++}1^+\rho(770)\pi D$ wave, which is coupled to this wave via the branchings in equation 4.7. The only phase shift is visible for the systematic study without branchings. However, that this shift is rather small for the $a_2(1320)$, which has in its intensity peak from all observed resonances the smallest non-resonant contribution, further supports the separation of the dependence on the decay and t' performed in equation 4.7. The $M = 2$ wave in figure 5.5 shows a different t' dependence, because the spin projection enters in equation 5.1. However, the observed phase motion for the $a_2(1320)$ is still small.

It is also interesting to look at the interplay between the a_2' and the non-resonant term. While for the $2^{++}2^+\rho(770)\pi D$ and the $2^{++}1^+f_2(1270)\pi P$ waves, which mainly define the a_2', the phase of either the a_2' or the non-resonant term is strongly varying over t', they are both rather stable in the $2^{++}1^+\rho(770)\pi D$ wave. For the $2^{++}1^+f_2(1270)\pi P$ wave, where a variation of the a_2' is suppressed by the coupling to the $2^{++}1^+\rho(770)\pi D$ wave through the branchings, the changing component is the non-resonant term, whereas in the

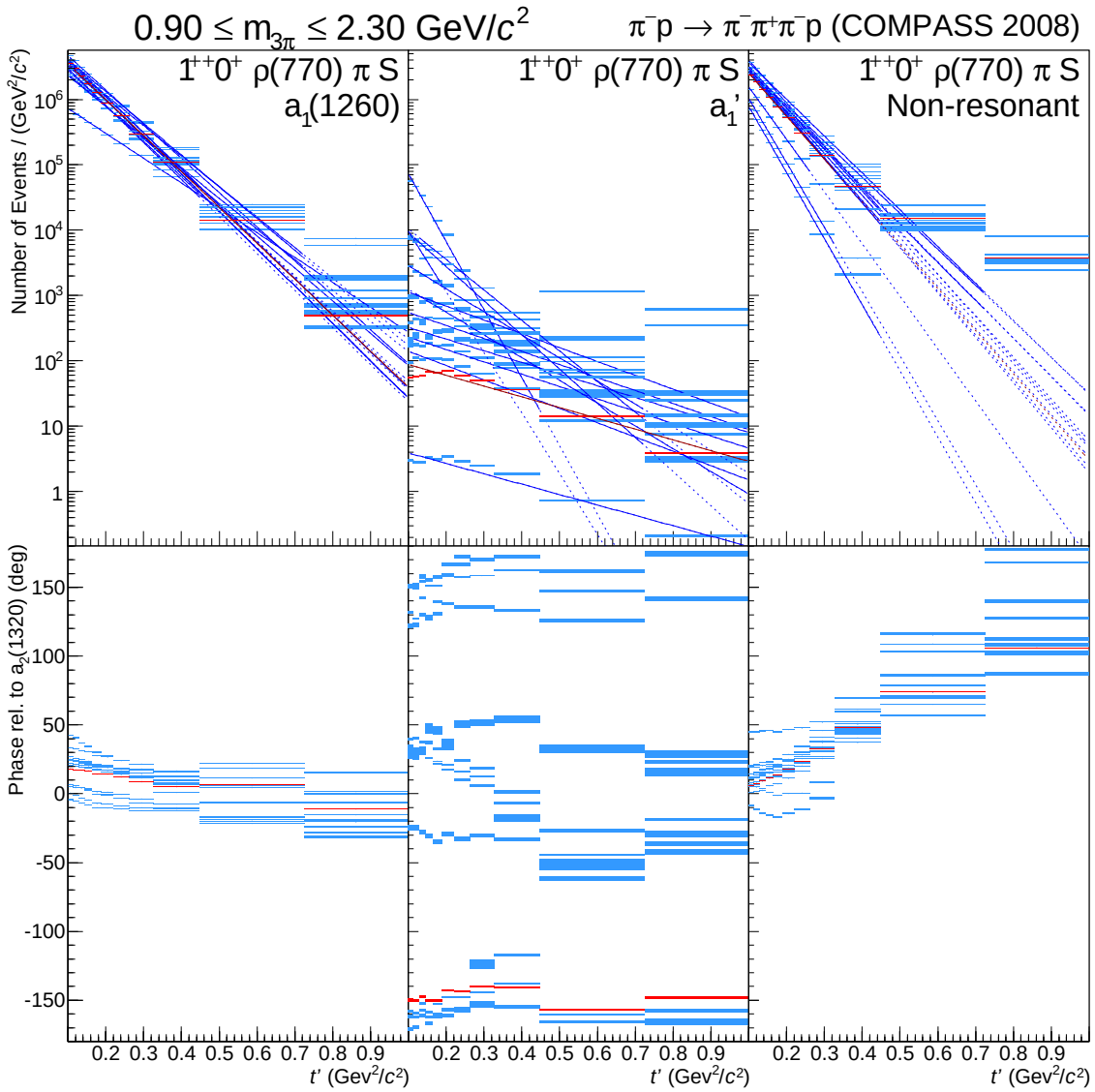

Figure 5.3: t' dependence of the intensity (upper row) and the phase (lower row) of the $a_1(1260)$ (left), the a_1' (centre) and the non-resonant term (right) in the $1^{++}0^+\rho(770)\pi S$ wave. Like in figure 5.2 the red line indicates the fit of the parametrisation in equation 5.1 to the data of the main fit shown in red. The systematic studies discussed in section 4.4 are plotted with blue lines and blue data bars. The height of the bars represents the statistical error. Dotted lines indicate an extrapolation beyond the fit range.

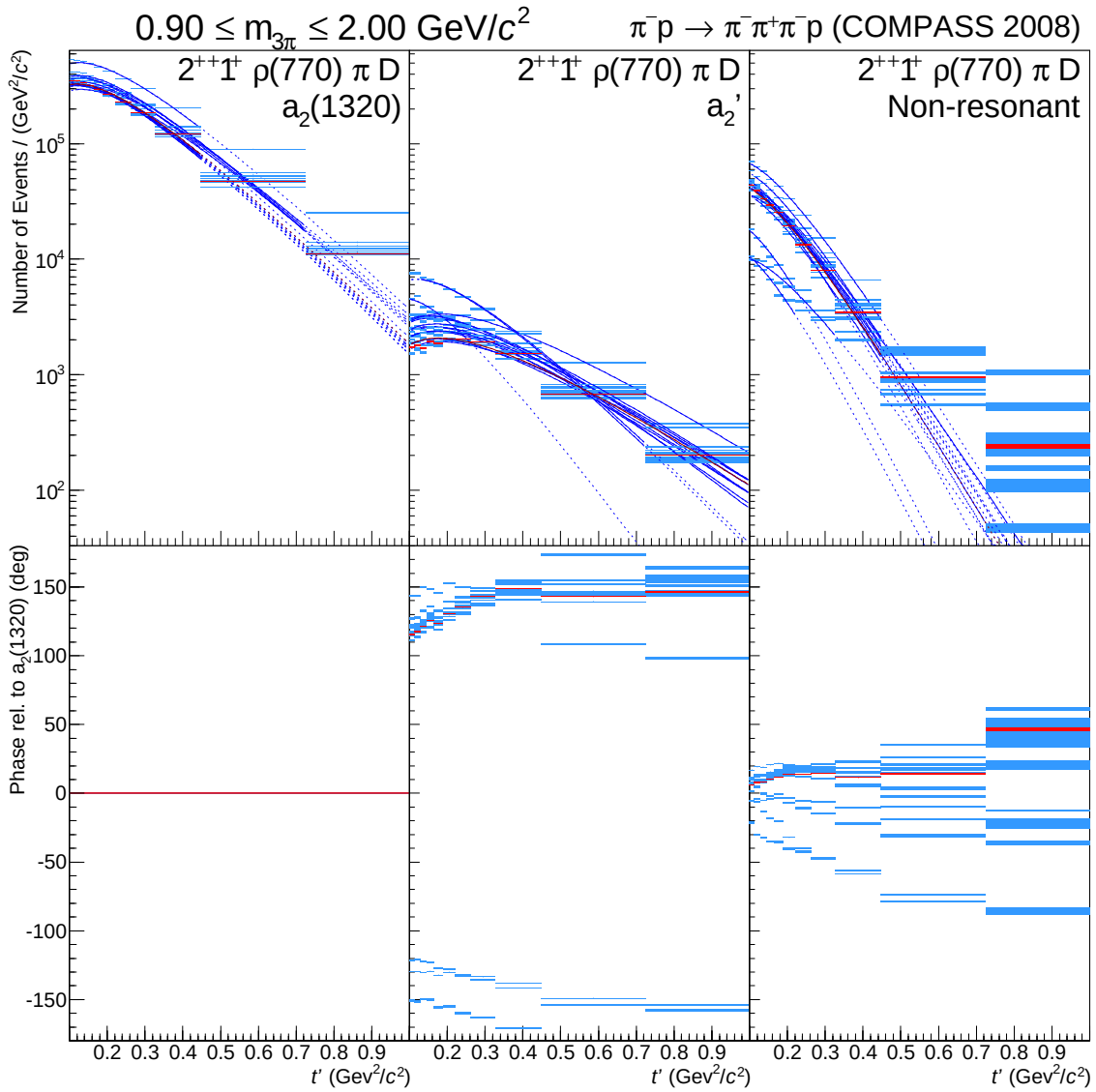

Figure 5.4: t' dependence of the intensity (upper row) and the phase (lower row) of the $a_2(1320)$ (left), the a_2' (centre) and the non-resonant term (right) in the $2^{++}1^{+}\rho(770)\pi D$ wave. The plotting scheme is the same as in figure 5.3.

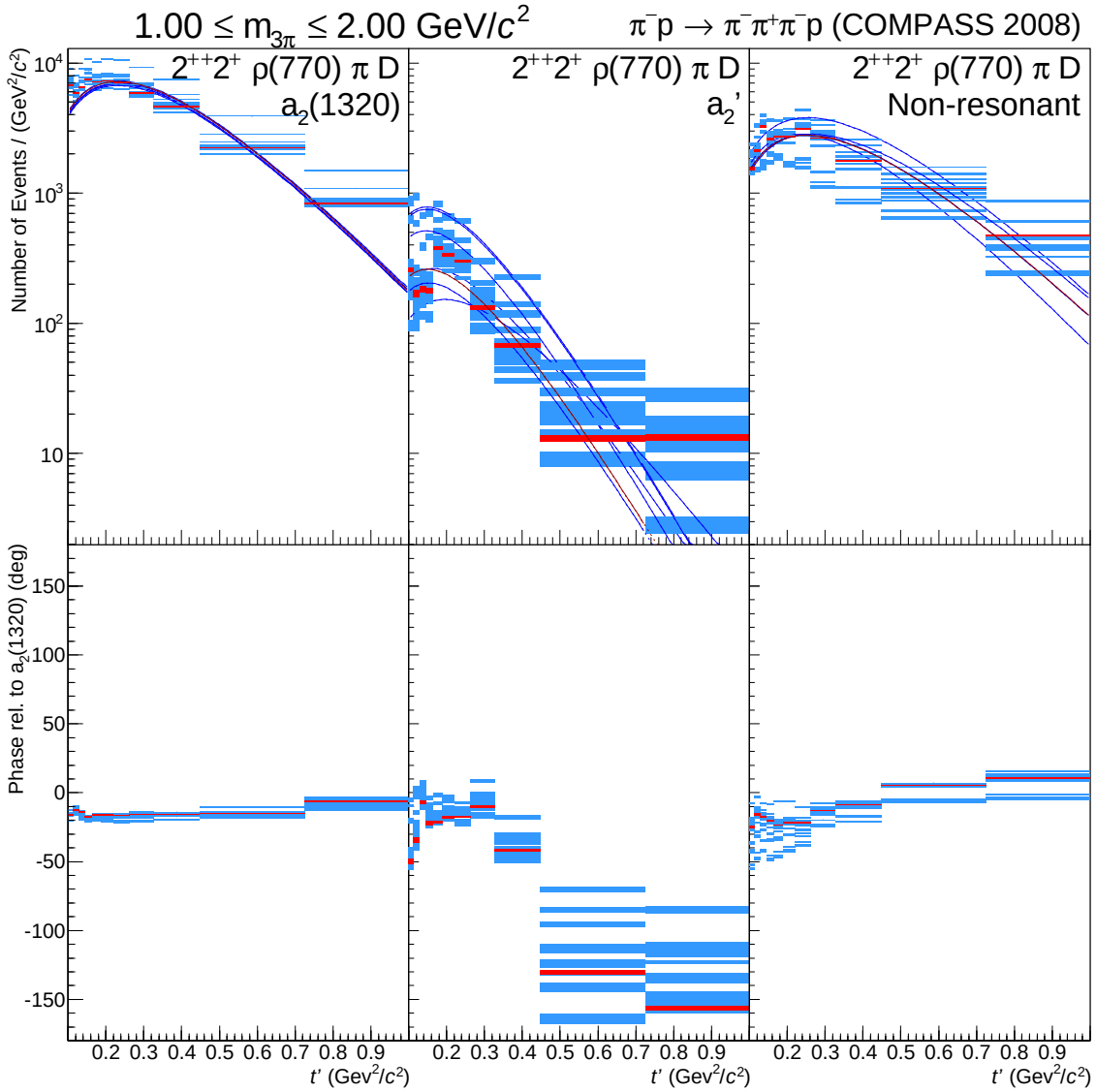

Figure 5.5: t' dependence of the intensity (upper row) and the phase (lower row) of the $a_2(1320)$ (left), the a_2' (centre) and the non-resonant term (right) in the $2^{++}2^{+}\rho(770)\pi D$ wave. The plotting scheme is the same as in figure 5.3.

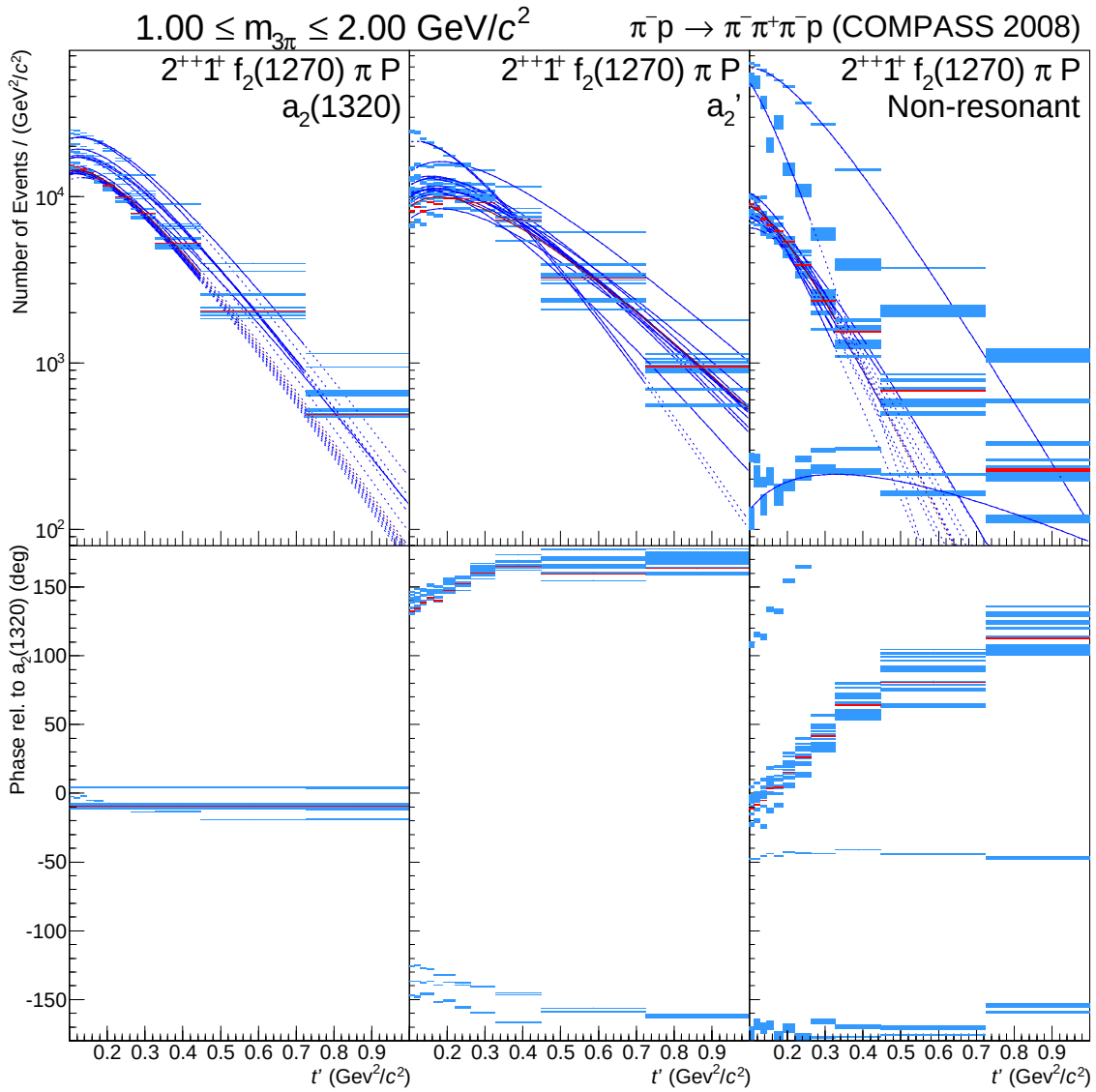

Figure 5.6: t' dependence of the intensity (upper row) and the phase (lower row) of the $a_2(1320)$ (left), the a_2' (centre) and the non-resonant term (right) in the $2^{++}1^{+}f_2(1270)\pi P$ wave. The plotting scheme is the same as in figure 5.3.

$2^{++}2^{+}\rho(770)\pi D$ wave that is not constraint via branchings it is the a_2'. This is again a sign that the fit has problems separating the a_2' from the non-resonant contributions.

Furthermore it is interesting that in the systematic study without an a_2' the phase of the non-resonant term in the $2^{++}1^{+}f_2(1270)\pi P$ wave is nearly constantly at about $-50°$, while most other studies show a significant growth with t'. The study without an a_2' also leads to the highest observed intensity for the non-resonant term in this wave, whereas the steepest slope is due to the study, in which the explicit t' dependence was removed from the parametrisation of the non-resonant terms. The shallowest slope and lowest intensity, however, is from the study leaving out two 2^{-+} waves.

The $2^{-+}0^{+}f_2(1270)\pi S$ wave, which is the third large wave in the wave set and the $1^{++}0^{+}f_0(980)\pi P$ wave, which contains the new $a_1(1420)$, are shown in figures 5.7 and 5.8. Both are rather stable. The only significant divergence can be seen for the study, where the $1^{++}0^{+}f_0(980)\pi P$ wave is fitted without the $a_1(1420)$. In this model the intensity of the non-resonant contribution increases drastically and also changes its phase behaviour.

The resulting exponential slopes from the fit with the parametrisation from equation 5.1 are listed for the resonances in table 5.1 and for the non-resonant terms in table 5.2. While the slopes of the resonances are mostly around $8\,(\mathrm{GeV}/c)^{-2}$, the ones for the non-resonant contributions are with a few exceptions above $11\,(\mathrm{GeV}/c)^{-2}$. This means that the intensity of the non-resonant parts drops in general faster with rising t' and therefore the spectrum is in general cleaner for higher t'. However, most non-resonant terms exhibit a second component with a significantly shallower slope above roughly $0.5\,\mathrm{GeV}^2/c^2$.

The largest systematic error, being $^{+20.2}_{-0.1}\,(\mathrm{GeV}/c)^{-2}$, occurs for the a_1', which is not surprising looking at figure 5.3. The statistical errors are with a maximum of $0.1\,(\mathrm{GeV}/c)^{-2}$for the resonant and $0.4\,(\mathrm{GeV}/c)^{-2}$for the non-resonant terms again mostly negligible and therefore are not listed.

For the non-resonant term in the $2^{-+}0^{+}\rho(770)\pi F$ wave no values are given. This is because of the determined t' dependence shown in figure 5.9. For most studies it is strongly curved, though for $M = 0$ only a straight line in the logarithmic representation is allowed in the parametrisation. Therefore the fitter is simply incapable of finding a valid solution. The large visible statistical errors for lower t' indicate problems of the mass-dependent fit determining this contribution, which most likely also lead to this unusual t' dependence and is an additional hint that the parametrisation of the non-resonant terms needs to be improved for further work.

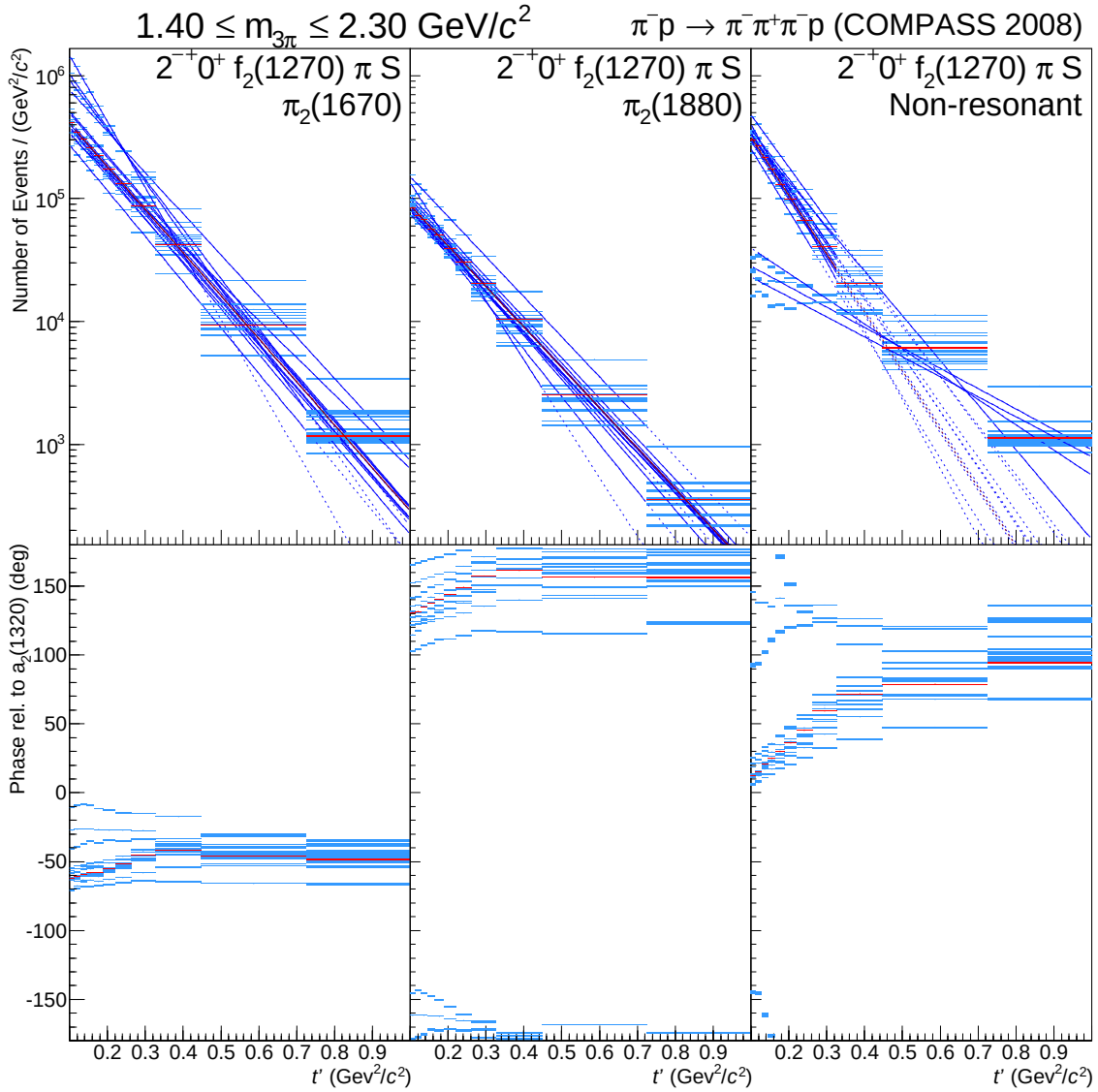

Figure 5.7: t' dependence of the intensity (upper row) and the phase (lower row) of the $\pi_2(1670)$ (left), the $\pi_2(1880)$ (centre) and the non-resonant term (right) in the $2^{-+}0^+ f_2(1270)\pi S$ wave. The plotting scheme is the same as in figure 5.3.

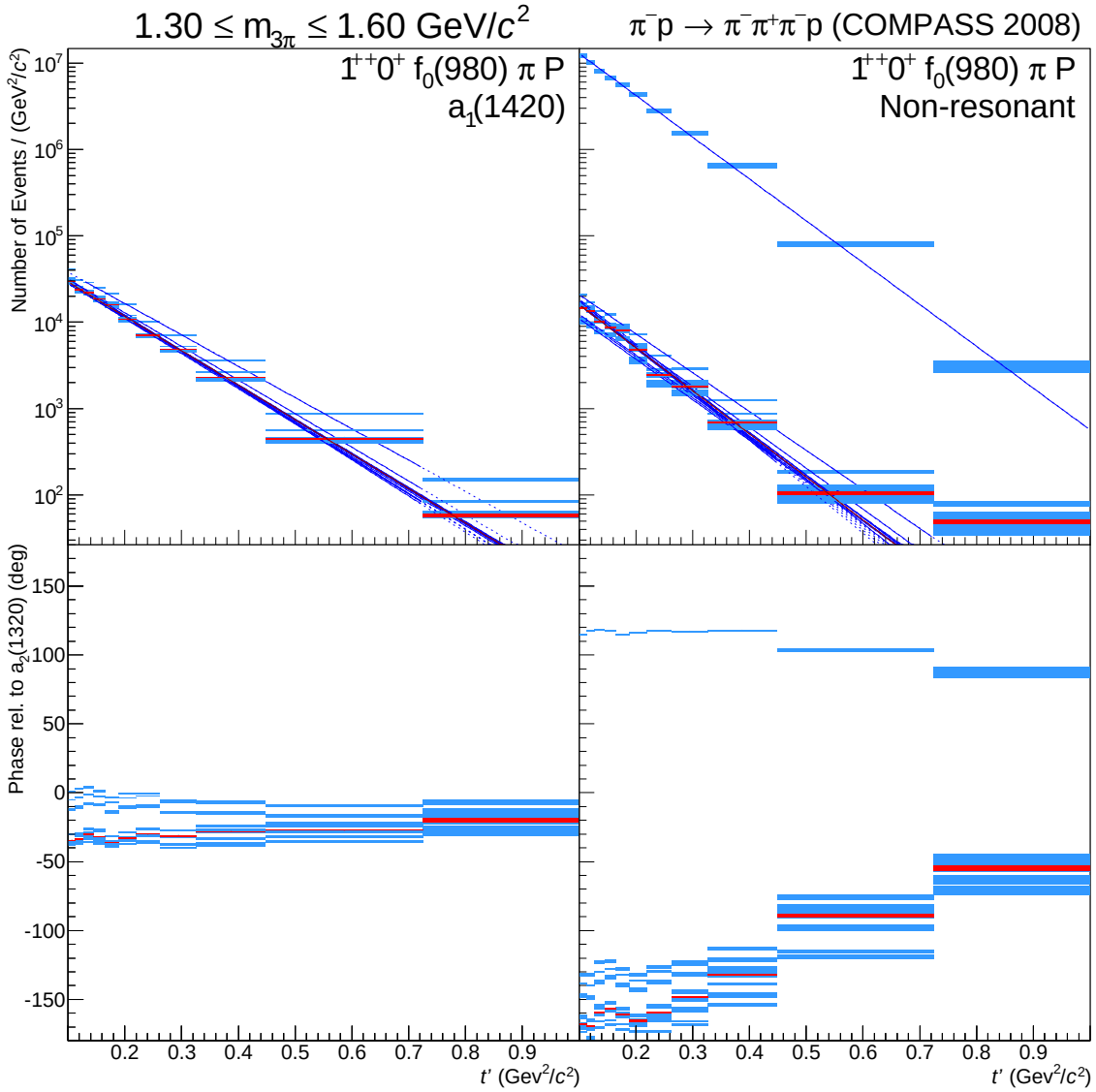

Figure 5.8: t' dependence of the intensity (upper row) and the phase (lower row) of the $a_1(1420)$ (left) and the non-resonant term (right) in the $1^{++}0^+ f_0(980)\pi P$ wave. The plotting scheme is the same as in figure 5.3.

Resonance	Partial Wave		Slope b [$(\mathrm{GeV/c})^{-2}$]
$a_1(1420)$	$1^{++}0^+ f_0(980)\pi P$		$9.2\,^{+0.5}_{-0.8}$
$a_1(1260)$	$1^{++}0^+ \rho(770)\pi S$	$*$	$12.7\,^{+0.5}_{-3.9}$
	$1^{++}0^+ \rho(770)\pi D$	$*$	$12.5\,^{+0.9}_{-1.7}$
a_1'	$1^{++}0^+ \rho(770)\pi S$	$*$	$3.8\,^{+20.2}_{-0.1}$
	$1^{++}0^+ \rho(770)\pi D$	$*$	$3.8\,^{+8.3}_{-1.2}$
$a_2(1320)$	$2^{++}1^+ \rho(770)\pi D$	$*$	$8.3\,^{+0.2}_{-0.7}$
	$2^{++}1^+ f_2(1270)\pi P$	$*$	$8.4\,^{+0.2}_{-0.8}$
	$2^{++}2^+ \rho(770)\pi D$		$8.6\,^{+0.0}_{-0.1}$
a_2'	$2^{++}1^+ \rho(770)\pi D$	$*$	$5.7\,^{+5.7}_{-0.2}$
	$2^{++}1^+ f_2(1270)\pi P$	$*$	$5.7\,^{+2.9}_{-0.2}$
	$2^{++}2^+ \rho(770)\pi D$		$13.4\,^{+0.4}_{-3.1}$
$a_4(2040)$	$4^{++}1^+ \rho(770)\pi G$	$*$	$8.5\,^{+1.7}_{-0.2}$
	$4^{++}1^+ f_2(1270)\pi F$	$*$	$8.5\,^{+2.3}_{-0.3}$
$\pi(1800)$	$0^{-+}0^+ f_0(980)\pi S$		$8.4\,^{+1.7}_{-0.3}$
$\pi_2(1670)$	$2^{-+}0^+ f_2(1270)\pi S$	$*$	$8.1\,^{+4.3}_{-1.1}$
	$2^{-+}0^+ f_2(1270)\pi D$	$*$	$8.1\,^{+4.2}_{-0.5}$
	$2^{-+}0^+ \rho(770)\pi F$	$*$	$8.1\,^{+1.9}_{-0.4}$
	$2^{-+}1^+ f_2(1270)\pi S$		$3.8\,^{+2.2}_{-0.4}$
$\pi_2(1880)$	$2^{-+}0^+ f_2(1270)\pi S$	$*$	$7.6\,^{+3.5}_{-0.1}$
	$2^{-+}0^+ f_2(1270)\pi D$	$*$	$7.6\,^{+3.5}_{-0.1}$
	$2^{-+}0^+ \rho(770)\pi F$	$*$	$7.6\,^{+1.3}_{-0.1}$
	$2^{-+}1^+ f_2(1270)\pi S$		$18.6\,^{+0.6}_{-4.3}$

Table 5.1: Slopes of the t' spectra of the resonances with systematic errors. The statistical errors are negligible. For the individual resonances the asterisks mark waves, which are coupled through the branchings. The slopes of resonances in coupled waves are not always exactly identical, because the relative errors are not increasing with the same rate with t' due to different intensities of the resonances in different waves.

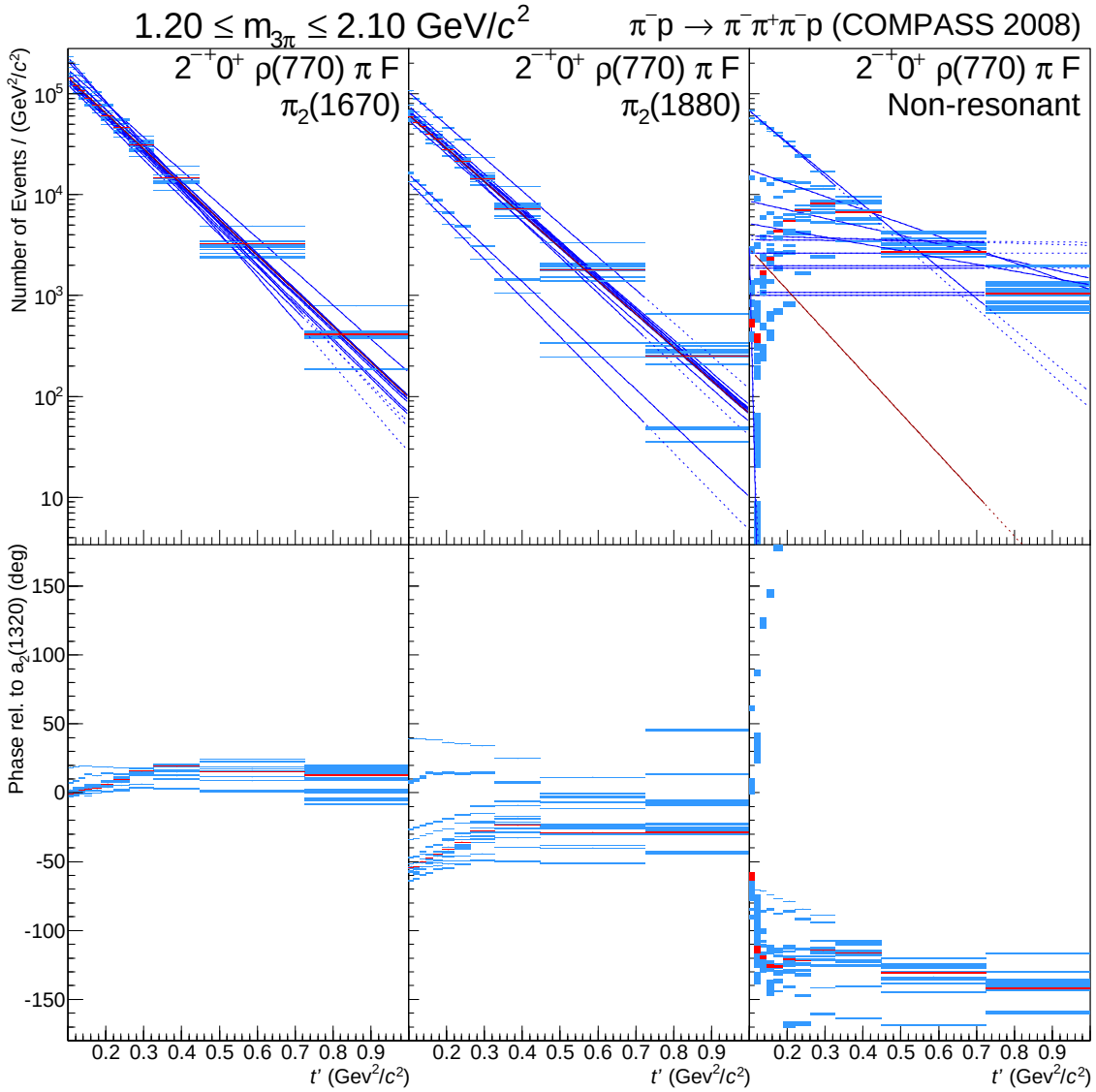

Figure 5.9: t' dependence of the intensity (upper row) and the phase (lower row) of the $\pi_2(1670)$ (left), the $\pi_2(1880)$ (centre) and the non-resonant term (right) in the $2^{-+}0^+\rho(770)\pi F$ wave. The plotting scheme is the same as in figure 5.3.

Partial Wave	**Slope b [$(\mathrm{GeV/c})^{-2}$]**
$1^{++}0^{+}f_0(980)\pi P$	$11.5\,^{+2.0}_{-1.1}$
$1^{++}0^{+}\rho(770)\pi S$	$15.1\,^{+11.0}_{-2.5}$
$1^{++}0^{+}\rho(770)\pi D$	$15.6\,^{+1.8}_{-12.0}$
$2^{++}1^{+}\rho(770)\pi D$	$13.9\,^{+7.0}_{-1.9}$
$2^{++}1^{+}f_2(1270)\pi P$	$12.2\,^{+5.6}_{-9.1}$
$2^{++}2^{+}\rho(770)\pi D$	$8.0\,^{+0.7}_{-0.4}$
$4^{++}1^{+}\rho(770)\pi G$	$17.1\,^{+1.5}_{-4.0}$
$4^{++}1^{+}f_2(1270)\pi F$	$11.5\,^{+4.7}_{-0.4}$
$0^{-+}0^{+}f_0(980)\pi S$	$24.2\,^{+4.8}_{-2.9}$
$2^{-+}0^{+}f_2(1270)\pi S$	$11.0\,^{+1.9}_{-7.2}$
$2^{-+}0^{+}f_2(1270)\pi D$	$15.1\,^{+2.1}_{-4.4}$
$2^{-+}0^{+}\rho(770)\pi F$	—
$2^{-+}1^{+}f_2(1270)\pi S$	$8.5\,^{+1.0}_{-2.1}$

Table 5.2: Slopes of the t' spectra of the non-resonant terms with systematic errors. The statistical errors are negligible. The non-resonant term in the $2^{-+}0^{+}\rho(770)\pi F$ wave is not compatible with the parametrisation in equation 5.1 (see figure 5.9).

Chapter 6

Conclusions

The large data set from the 2008 COMPASS hadron run permits to study the 3π spectrum in unprecedented detail. In combination with a novel analysis method that combines the information of several t' bins this leads on the one hand to a better separation of resonant and non-resonant components in the resonance parameter extraction and on the other hand allows for the first time to study in detail the t' dependences of the intensities and phases of individual components.

The new resonance denoted $a_1(1420)$, which has been found in the previous work [17], was confirmed in this thesis with parameters $m_{a_1(1420)} = 1408\,\mathrm{MeV}/c^2$ and $\Gamma_{a_1(1420)} = 157\,\mathrm{MeV}/c^2$. This resonance is highly peculiar, because whether models nor lattice calculations expect a resonance in this mass region. The fact that it is only observed in the decay mode to $f_0(980)\pi$ hints to an exotic nature of the $a_1(1420)$ or to coupled channel effects from the decay of the $a_1(1260)$ to $K^*(892)\overline{K}$ [54].

For the extraction of resonance parameters extensive systematic studies are extremely important, not just because the statistical errors are very small, but also because due to many local minima reproducible results are only achievable with a large number of different fits. This thesis presented a novel method using additional constraints in order to filter out the relevant solutions from the up to 10 000 fits created by random starting values and different orders of releasing the parameters of the dynamical terms during the fit.

Despite the selection criteria two ambiguous solutions remained for the original wave set, which includes six partial waves and is close to that of previous analyses, like [16]. In order to resolve these ambiguities the wave set was extended by seven further waves. To large extends the data could be well described without additional resonances. However, especially the results for $\pi_2(1670)$ and $\pi_2(1880)$ significantly deviate from the PDG 2012 [13]. This shift of the resonance parameters is caused by the additional constraints due to the enlarged wave set. Furthermore the systematic errors for the $a_1(1260)$ and the a_1' are still large. The main source for this are the uncertainties in the parametrisation of the non-resonant terms and the choice of the wave set.

6.1 Outlook

In order to reduce the systematic uncertainty caused by the choice of the wave set, further studies including more waves are planned. For the practical reason of computing time they will most likely be dedicated to individual sectors in J^{PC}. However, simultaneously

the non-resonant terms need to be improved. Two different ways to approach this are in preparation. One is to simulate the believed to be dominant source for non-resonant contributions, namely the Deck-effect, with **M**onte-**C**arlo (MC) methods and to decompose the MC data into partial wave amplitudes. The thereby achieved spectral distribution could then be used as a parametrisation for the non-resonant terms.

The other approach are so-called Pietarinen expansions, where resonances are described as poles in the complex energy plane. The amplitudes of the resonant and non-resonant terms are then described by the poles in combination with a number of Pietarinen power series. The Pietarinen functions are a complete set of functions with well-known analytic properties. By the use of this series the arbitrariness in the choice of parametrisations is avoided and the number of power series used is simply based on the maximally allowed deviation of the fit from the data. For further information please refer to [55, 56] and citations therein. This alternative approach looks most promising and was already successfully applied to baryon resonances, but whether and how it can be applied to the analysis presented here still has to be investigated.

Probably the first improvement that will be implemented is a redefinition of the χ^2 function used for minimisation. So far the χ^2 has been calculated comparing the real and imaginary parts of all elements of the spin-density matrix for model and data. While this is valid as a minimisation criterion, the interpretation of $\frac{\chi^2}{\mathrm{NDF}}$ is problematic, because the used data points are in general not independent. On the one hand the intensities of the individual waves are also influencing the off-diagonal elements, where just the phase information are independent from the intensities. On the other hand the phase between waves A and B as well as A and C already fully defines the one between B and C. A direct fit of selected phases is impractical, but another way to remove this redundant information is to select an anchor wave and fit only the real and imaginary parts of the elements, which include this wave, making use of the known covariance matrix.

Another source of uncertainty, but this time arising from the mass-independent fit, is the isobar model in combination with the isobar parametrisation. In order to improve the description a new kind of analysis method is currently developed [45] on the same data as used for this thesis. In this method the fixed amplitudes of the isobars are replaced by piece-wise constant functions, which then are determined by fits to the data, resulting in an bind isobar shape.

A further consistency check is to fit also the $\pi^-\pi^0\pi^0$ channel in the 2008 COMPASS data with the method presented in this thesis. Finally in order to contribute to the long-lasting discussion of the spin-exotic states, a study including the spin-exotic $1^{-+}1^+\rho(770)\pi P$ wave with the $\pi_1(1600)$ in the mass-dependent fit will soon be performed.

Appendix A

Spin-Density matrices

A.1 6 waves

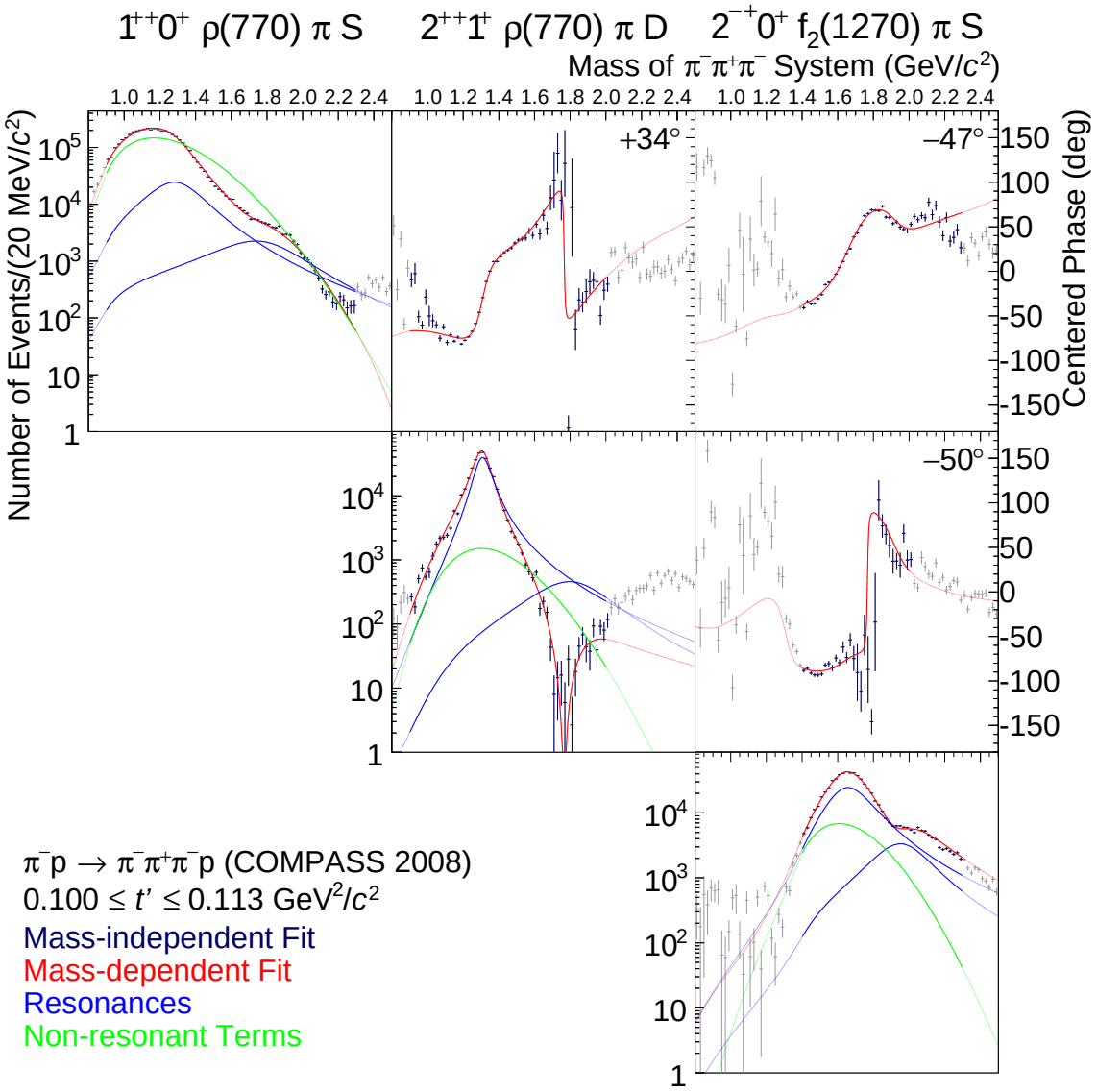

Figure A.1: Part 1 of 3 of the fitted spin-density matrix from figure 4.4. Please refer to the text there for further information.

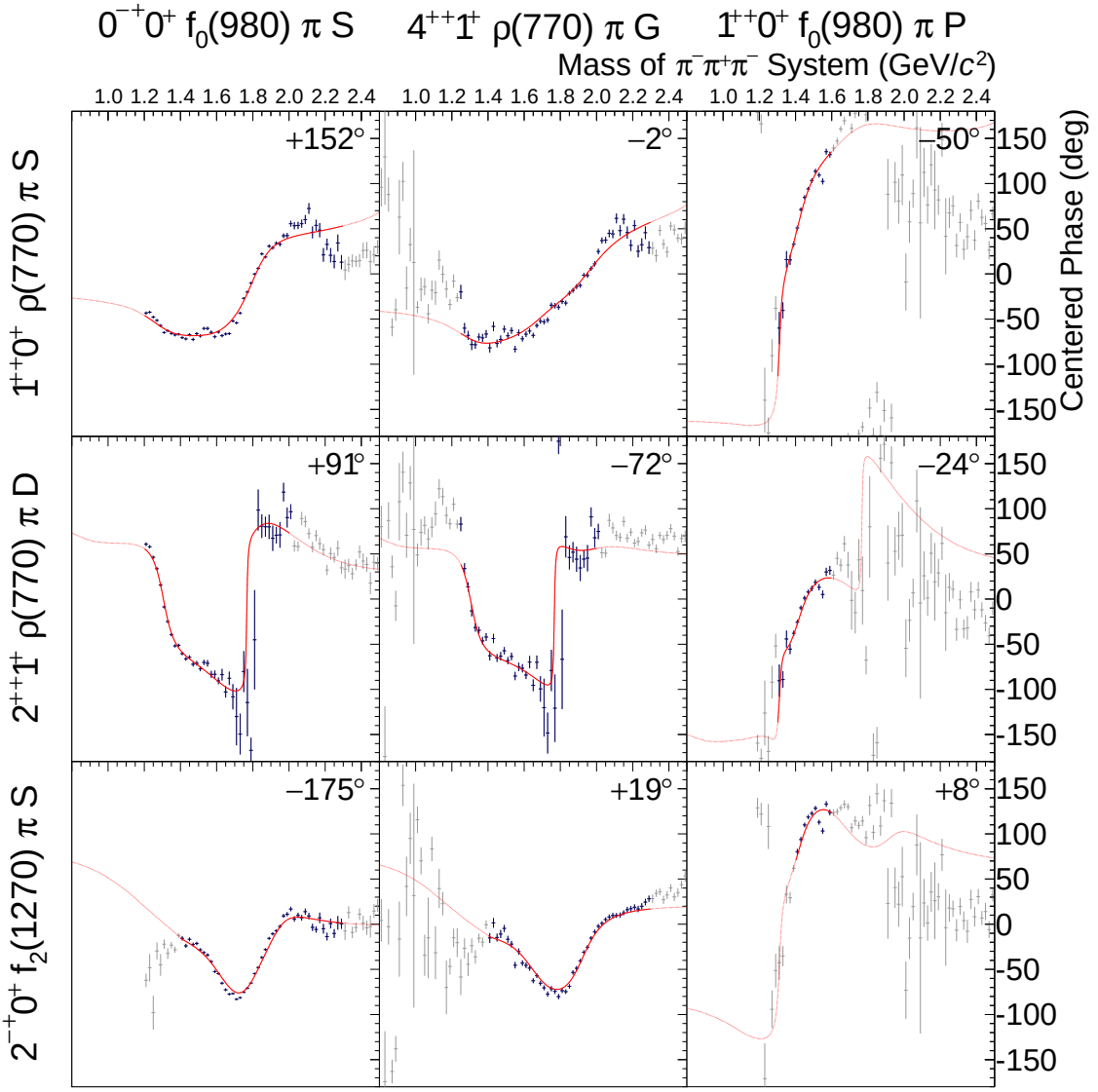

Figure A.2: Part 2 of 3 of the fitted spin-density matrix from figure 4.4. Please refer to the text there for further information.

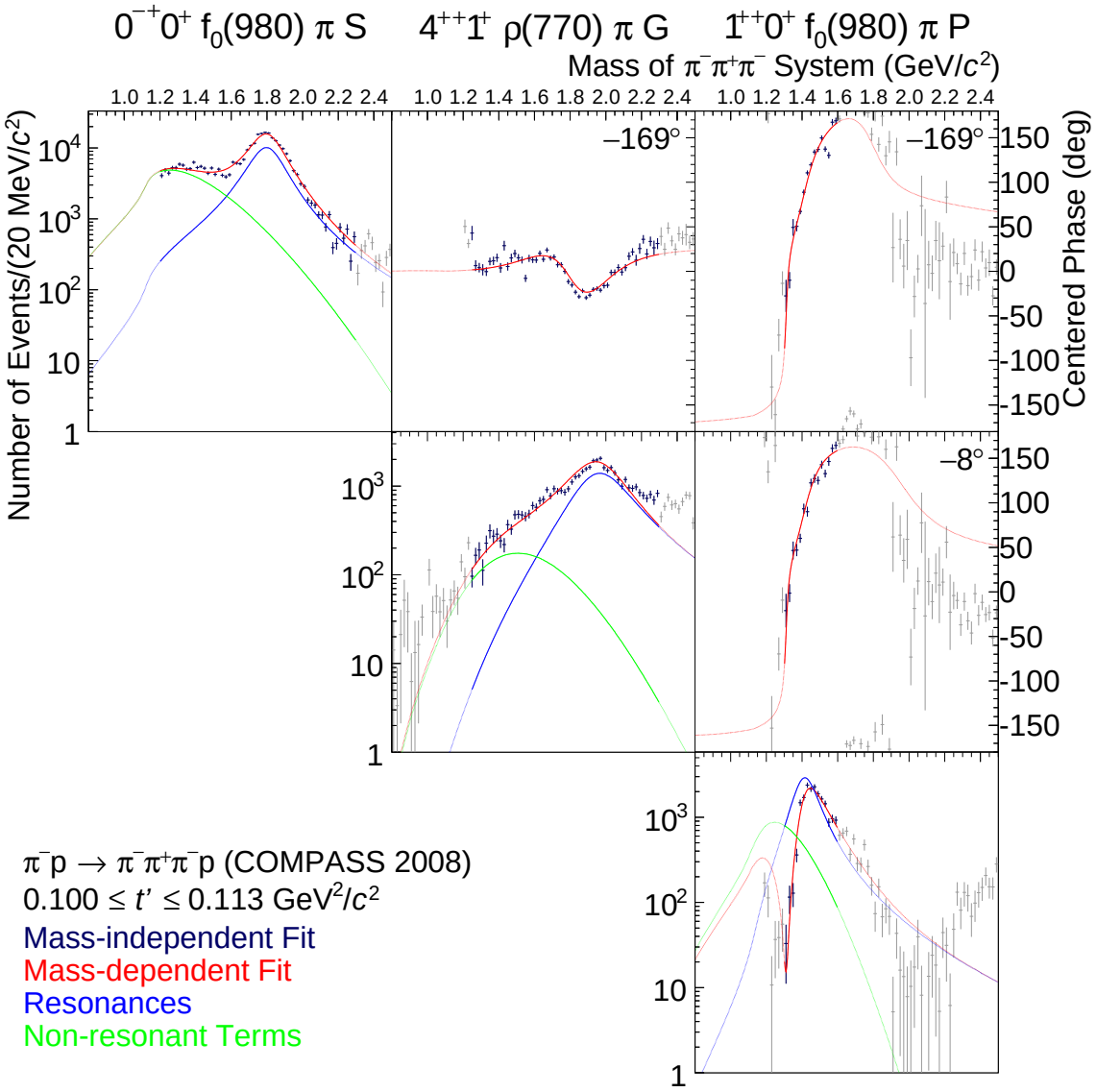

Figure A.3: Part 3 of 3 of the fitted spin-density matrix from figure 4.4. Please refer to the text there for further information.

A.2 13 waves

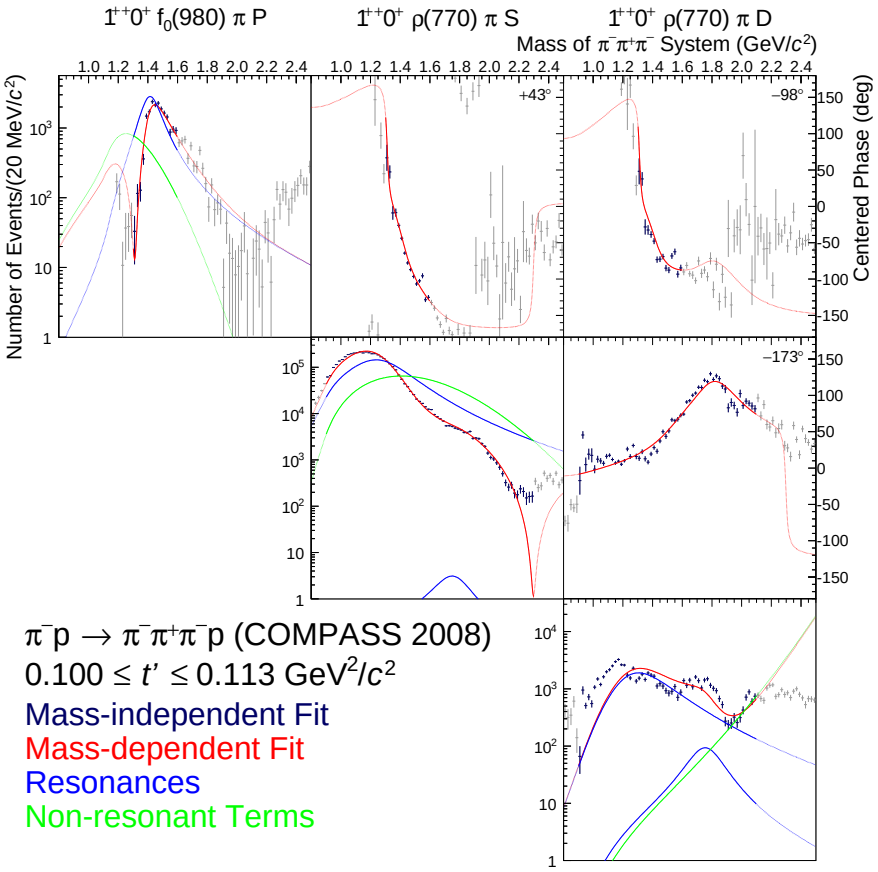

Figure A.4: Part 1 of 10 of the fitted spin-density matrix from figure 4.25. Please refer to the text there for further information.

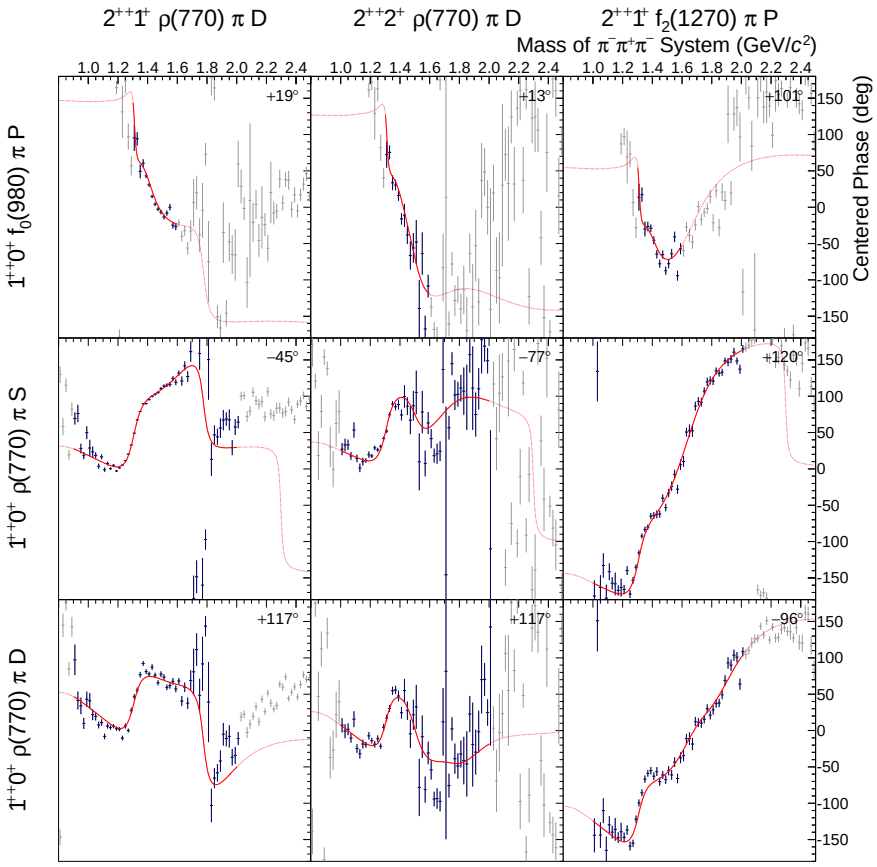

Figure A.5: Part 2 of 10 of the fitted spin-density matrix from figure 4.25. Please refer to the text there for further information.

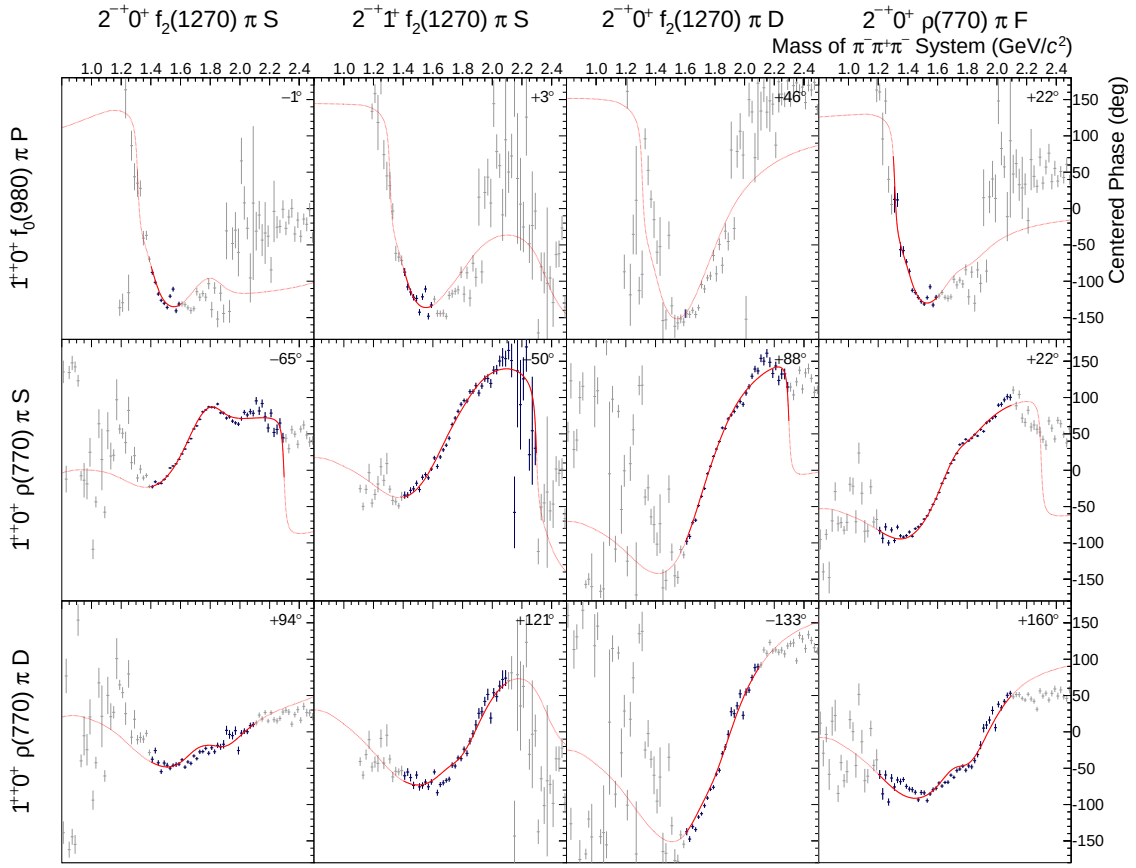

Figure A.6: Part 3 of 10 of the fitted spin-density matrix from figure 4.25. Please refer to the text there for further information.

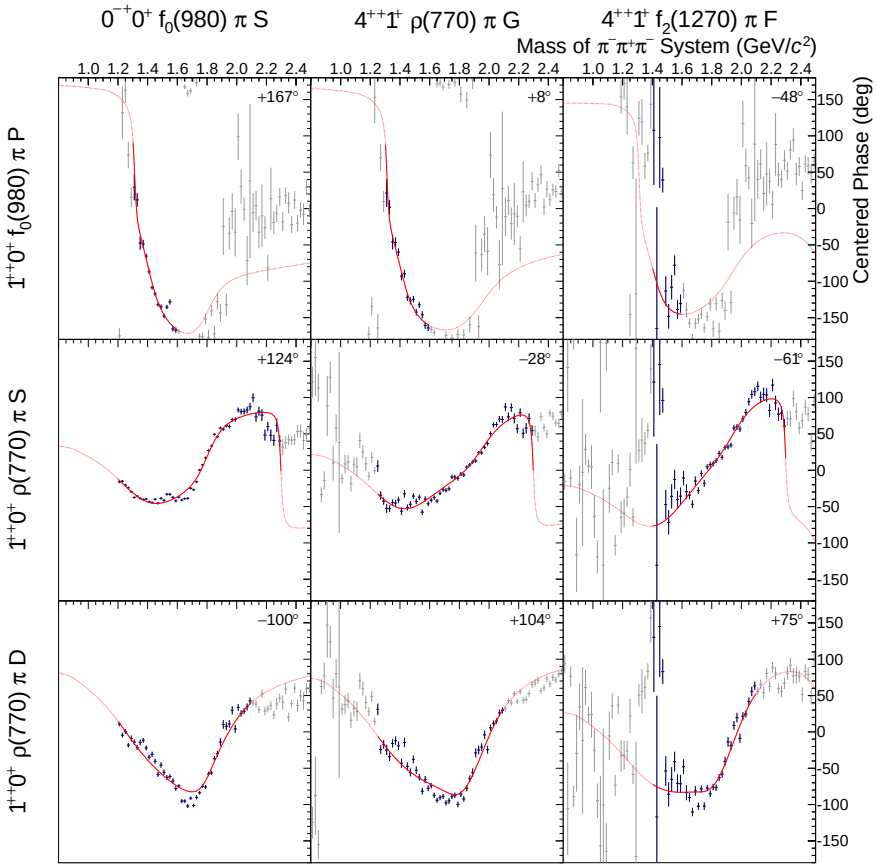

Figure A.7: Part 4 of 10 of the fitted spin-density matrix from figure 4.25. Please refer to the text there for further information.

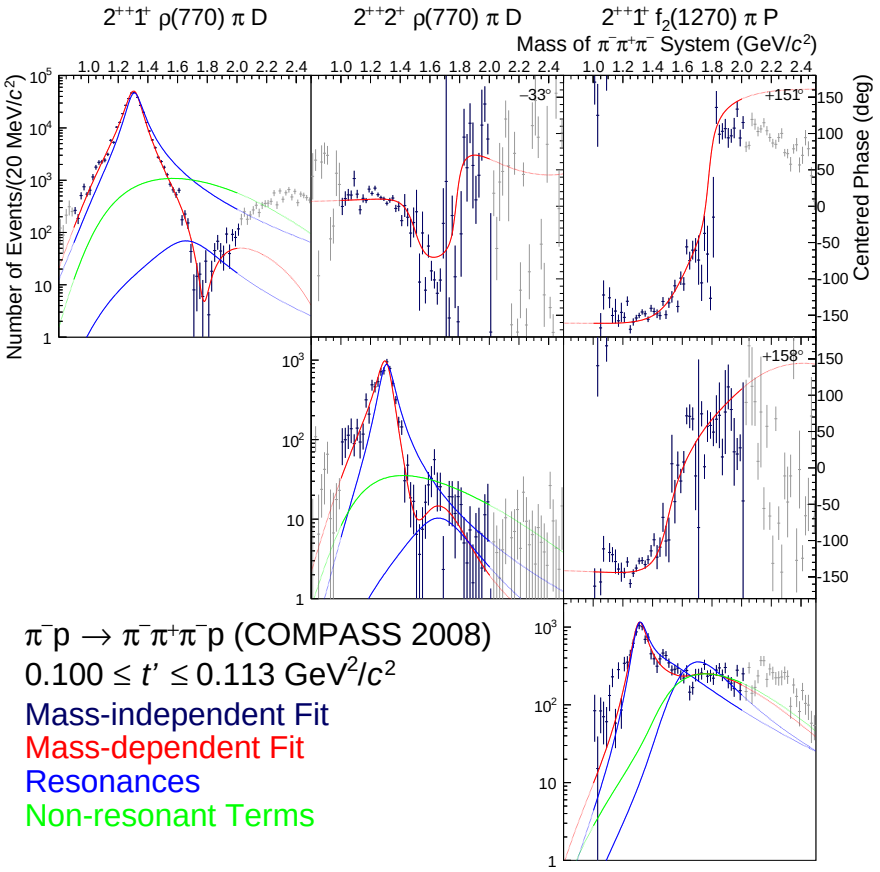

Figure A.8: Part 5 of 10 of the fitted spin-density matrix from figure 4.25. Please refer to the text there for further information.

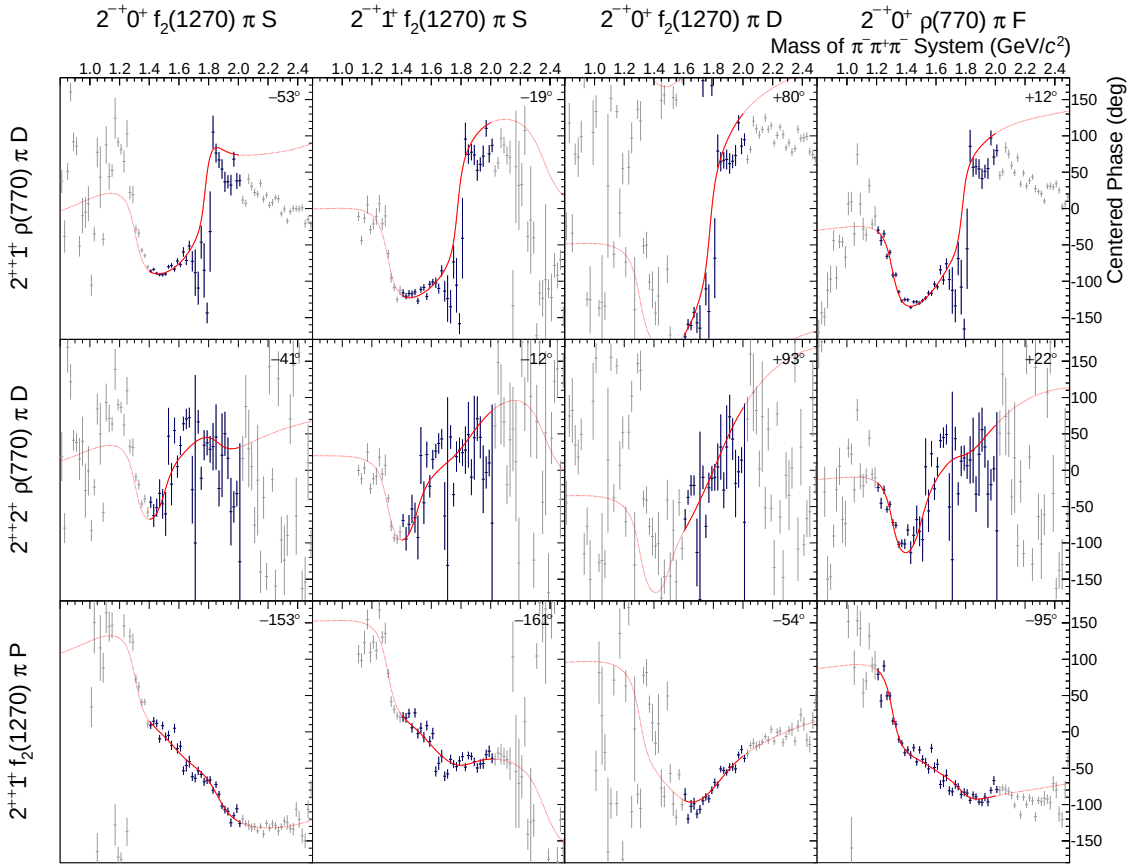

Figure A.9: Part 6 of 10 of the fitted spin-density matrix from figure 4.25. Please refer to the text there for further information.

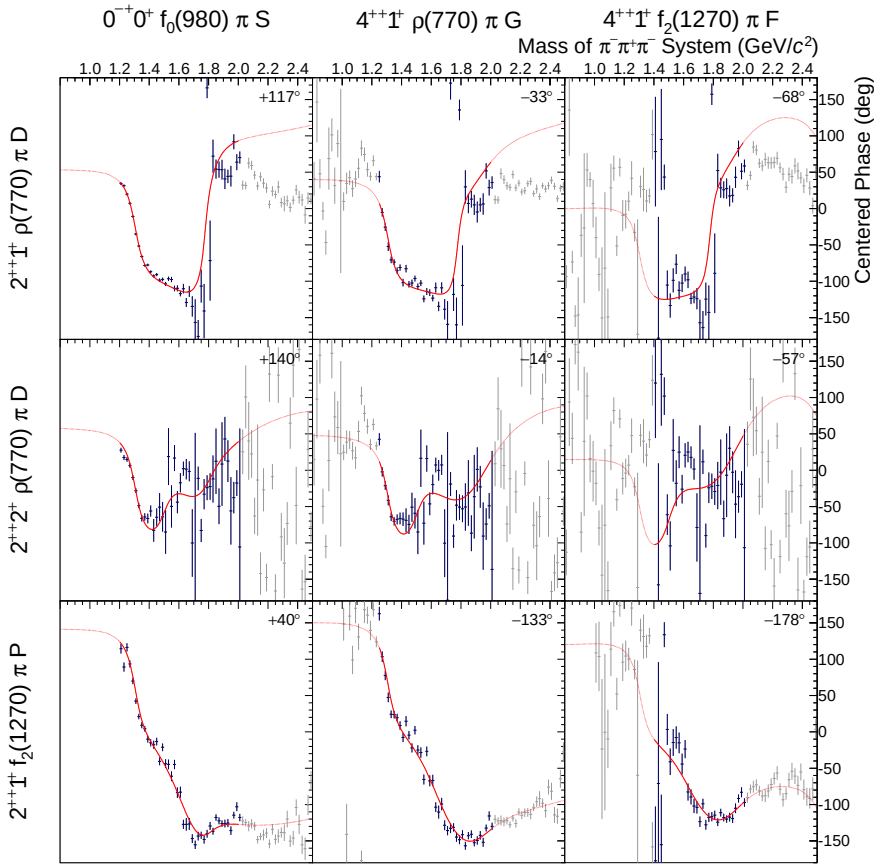

Figure A.10: Part 7 of 10 of the fitted spin-density matrix from figure 4.25. Please refer to the text there for further information.

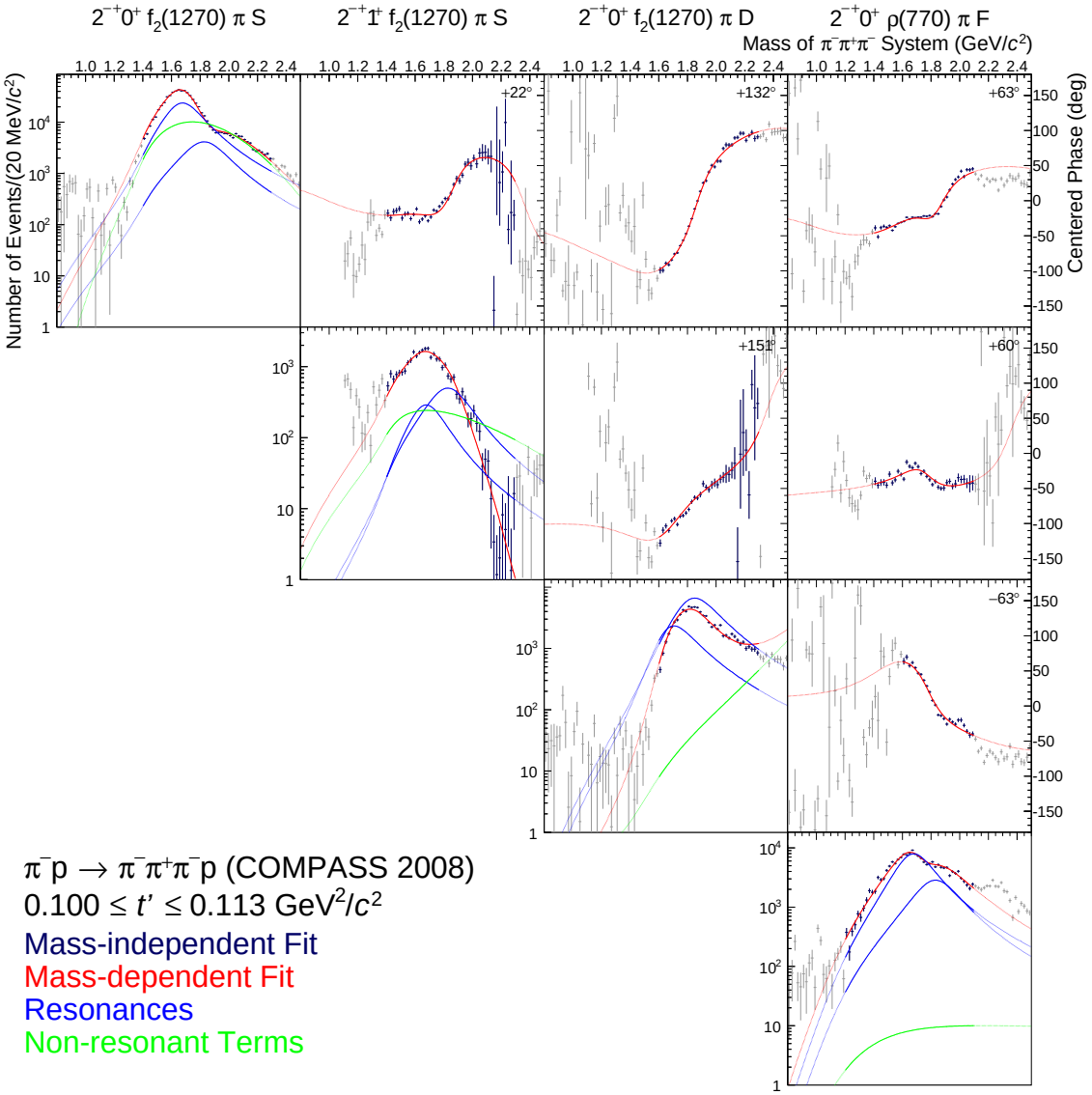

Figure A.11: Part 8 of 10 of the fitted spin-density matrix from figure 4.25. Please refer to the text there for further information.

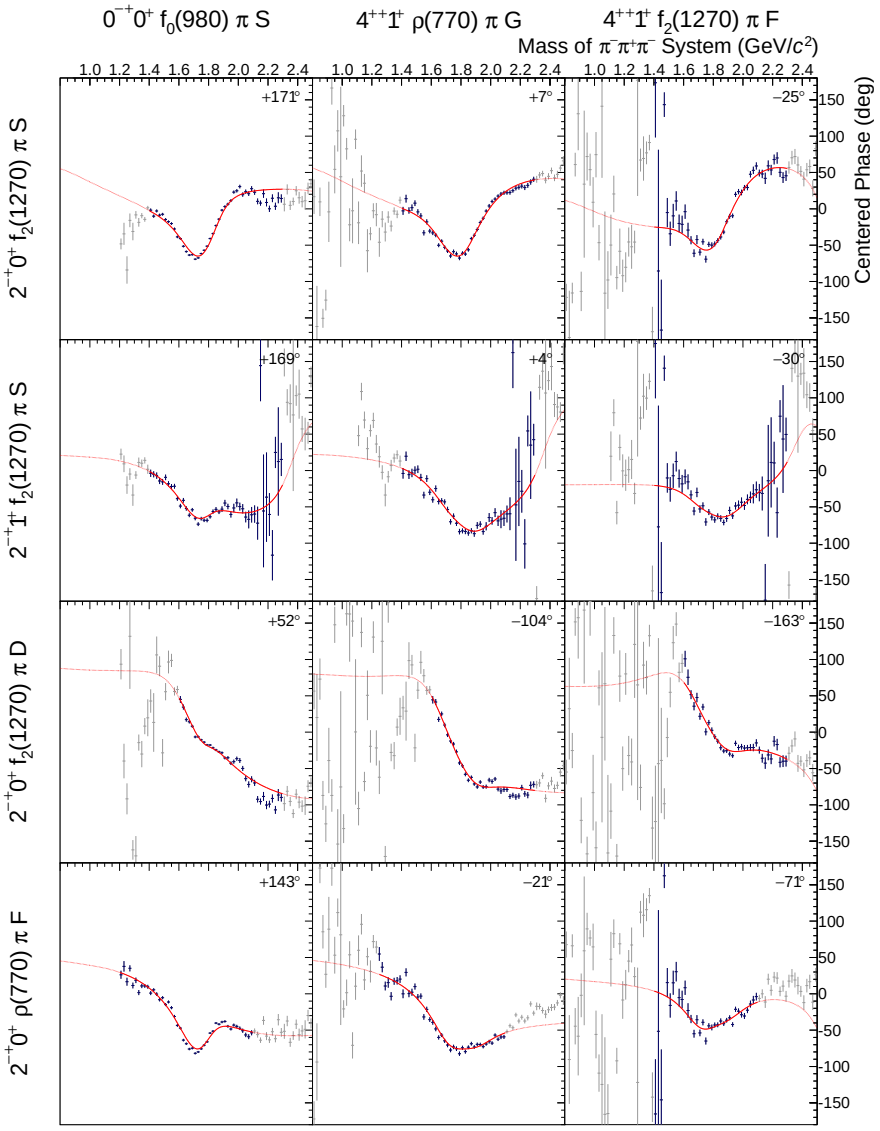

Figure A.12: Part 9 of 10 of the fitted spin-density matrix from figure 4.25. Please refer to the text there for further information.

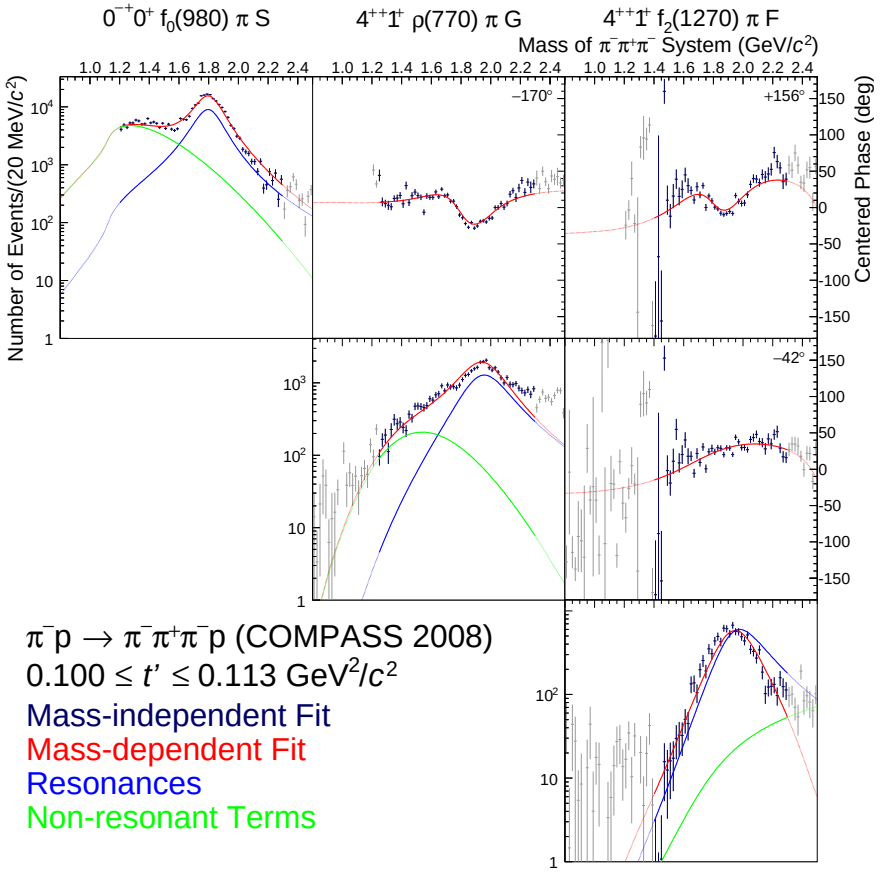

Figure A.13: Part 10 of 10 of the fitted spin-density matrix from figure 4.25. Please refer to the text there for further information.

List of Figures

List of Tables

Bibliography

[1] F. W. Bopp. *Kerne, Hadronen und Elementarteilchen*. Teubner Studienbuecher, 1989. ISBN 3-519-03068-3.

[2] S.U. Chung et al. Exotic and q anti-q resonances in the pi+ pi- pi- system produced in pi- p collisions at 18-GeV/c. *Phys.Rev.* **D65**, 072001 (2002).

[3] D.V. Amelin et al. Investigation of hybrid states in the VES experiment at the Institute for High Energy Physics (Protvino). *Phys. At. Nucl.* **68 3**, 359–371 .

[4] M. Gell-Mann. A schematic model of baryons and mesons. *Phys. Lett.* **8 3**, 214 – 215 (1964).

[5] G. Zweig. An SU_3 model for strong interaction symmetry and its breaking. oai:cds.cern.ch:352337; Part I. **CERN-TH-401**, 24 p Jan 1964.

[6] G. Zweig. An SU_3 model for strong interaction symmetry and its breaking. oai:cds.cern.ch:570209; Part II. **CERN-TH-412**, 80 p Feb 1964.

[7] J. Carlson, J. B. Kogut, and V. R. Pandharipande. Hadron spectroscopy in a flux-tube quark model. *Phys.Rev.* **D28**, 2807 (1983).

[8] N. Isgur and J. Paton. Flux-tube model for hadrons in QCD. *Phys.Rev.* **D31 11**, 2910 (1985).

[9] G. Roberts. Emergence of DSEs in Real-World QCD, 2012. Talk given at the USCS school on non-perturbative Physics.

[10] K. G. Wilson. Confinement of quarks. *Phys. Rev.* **D10**, 2445–2459 Oct 1974.

[11] G.P. Lepage. Lattice QCD for novices. *arXiv:hep-lat* , 49–90 (1998).

[12] J. J. Dudek. The lightest hybrid meson supermultiplet in QCD. *Phys.Rev.* **D84**, 074023 (2011).

[13] J. Beringer et al. Review of Particle Physics (RPP). *Phys.Rev.* **D86**, 010001 (2012).

[14] A.R. Dzierba et al. A Partial wave analysis of the pi- pi- pi+ and pi- pi0 pi0 systems and the search for a J**PC = 1-+ meson. *Phys.Rev.* **D73**, 072001 (2006).

[15] A. Zaitsev. Study of exotic resonances in diffractive reactions. *Nucl.Phys.* **A675**, 155C–160C (2000).

[16] M. G. Alekseev et al. Observation of a $J^{PC} = 1^{-+}$ Exotic Resonance in Diffractive Dissociation of 190 GeV/c π^- into $\pi^-\pi^-\pi^+$. *Phys. Rev. Lett.* **104**, 241803 Jun 2010.

[17] F. Haas. Two-Dimensional Partial-Wave Analysis of Exclusive 190 GeV $\pi^- p$ Scattering into the $\pi^-\pi^-\pi^+$ Final State at COMPASS (CERN). (2013). doctoral thesis.

[18] J. Dudek and A. Szczepaniak. The Deck effect in pi N –> pi pi pi N. *AIP Conference Proceedings* **814 1**, 587–591 (2006).

[19] E. Klempt and A. Zaitsev. Glueballs, Hybrids, Multiquarks. Experimental facts versus QCD inspired concepts. *Phys.Rept.* **454**, 1–202 (2007).

[20] M. G. Alekseev et al. First Measurement of Chiral Dynamics in $\pi^-\gamma \to \pi^-\pi^-\pi^+$. *Phys. Rev. Lett.* **108**, 192001 (2012).

[21] M. G. Alekseev et al. Measurement of radiative widths of $a_2(1320)$ and $\pi_2(1670)$. *The European Physical Journal A* **50**, 79 (2014).

[22] M. G. Alekseev et al. Measurement of the Charged-Pion Polarisability. *Phys. Rev. Lett.* (2014). to be submitted.

[23] A. Austregesilo. Central Production of Two-Pseudoscalar Final States at COMPASS. *arXiv:hep-ex* **1310.3190** (2013).

[24] A. Austregesilo. Phd thesis in preparation, Technische Universität München, 2014.

[25] COMPASS Collaboration. Odd and Even Partial Waves of $\eta\pi^-$ and $\eta'\pi^-$ in $\pi^- p \to \eta^{(\prime)}\pi^- p$ at 191 GeV/c. *Phys. Lett.* **B** . To be submitted.

[26] COMPASS Collaboration. Diffractive Resonance Production in $\pi^- + p \to \pi^-\pi^-\pi^+ + p_{recoil}$ at 190 GeV with COMPASS and Observation of a new Axial-Vector Meson $a_1(1420)$. (2014). in preparation.

[27] G. Baum, J. Kyynäräinen, and A. Tripet. COMPASS: a proposal for a COmmon Muon and Proton Apparatus for Structure and Spectroscopy. Technical Report CERN-SPSLC-96-14. SPSLC-P-297, CERN, Geneva, 1996.

[28] Overview of COMPASS Publications. http://wwwcompass.cern.ch/compass/publications/papers.

[29] Official Website of the COMPASS Experiment. http://wwwcompass.cern.ch.

[30] Letter of intent: semi-inclusive muon scattering from a polarised target. Technical Report CERN-SPSLC-95-27. SPSLC-I-204, CERN, Geneva, 1995.

[31] Yu. A. Alexandrov, F. Balestra, and M. Beck. CHEOPS: charm experiment with omnipurpose setup. Technical Report CERN-SPSLC-95-22. SPSLC-I-202, CERN, Geneva, 1995.

[32] S. Uhl. *Analysis of Exclusive Diffractive Events in the $\pi^-\pi^0\pi^0$ Final State*. Phd thesis in preparation, Technische Universität München, 2014.

[33] J. R. Cudell et al. Hadronic scattering amplitudes: Medium-energy constraints on asymptotic behavior. *Phys. Rev.* **D65**, 074024 Mar 2002.

[34] S. Neubert. *First Amplitude Analysis of Resonant Structures in the 5-Pion Continuum at COMPASS*. PhD thesis, Technische Universitat Munchen, 2012.

[35] H. Yukawa. On the Interaction of Elementary Particles. *Proc.Phys.Math.Soc.Jap* **17**, 48–56 (1935).

[36] T. Regge. Introduction to complex angular momenta. *Nuovo Cim.* **14**, 951 (1959).

[37] I. Y. Pomeranchuk. Equality between the interaction cross sections of high energy nucleons and antinucleons. *Zh. Eksp. Teor. Fiz.* **34**, 725 (1958).

[38] L. L. Foldy and R. F. Peierls. Isotopic spin of exchanged systems. *Phys. Rev.* **130 4**, 1585–1589 May 1963.

[39] S. Donnachie, G. Dosch, P. Landshoff, and O. Nachtmann. *Pomeron Physics and QCD*. Cambridge Monographs on Particle Physics, Nuclear Physics and Cosmology. Cambridge University Press, 2002.

[40] R. T. Deck. Kinematical interpretation of the first pi - rho resonance. *Phys.Rev.Lett.* **13**, 169–173 (1964).

[41] R. Ammar et al. Properties of $\pi_N(980)$. *Phys. Rev.* **B2**, 430 (1970).

[42] P. Abbon et al. The COMPASS experiment at CERN. *Nucl. Instrum. Methods* **577 3**, 455 – 518 (2007).

[43] COMPASS collaboration. The COMPASS Setup for Physics with Hadron Beams. *Nucl. Instrum. Methods* (2014). to be published.

[44] B. Grube. Hadron Spectroscopy in COMPASS, 2012. Talk given at Xth Quark Confinement and the Hadron Spectrum.

[45] F. Haas, D. Ryabchikov, et al. Diffractive Resonance Production in $\pi^- + p \to \pi^-\pi^-\pi^+ + p_{recoil}$ at 190 GeV with COMPASS and Observation of a new Axial-Vector Meson $a_1(1420)$. (2013). release note.

[46] Q. Weitzel. *Precision Meson Spectroscopy: Diffractive Production at COMPASS and Development of a GEM-based TPC for PANDA*. PhD thesis, Technische Universitat Munchen, 2008.

[47] L. Gatignon. private communication with F. Haas. M2 beam line liason physicist.

[48] K. Gottfried and J. D. Jackson. On the Connection between production mechanism and decay of resonances at high-energies. *Nuovo Cim.* **33**, 309–330 (1964).

[49] S. U. Chung and T. L. Trueman. Positivity conditions on the spin density matrix: A simple parametrization. *Phys. Rev.* **D11**, 633–646 Feb 1975.

[50] K. Peters. A Primer on Partial Wave Analysis. *arXiv:hep-ph* **0412069** (2004).

[51] M.G. Bowler. The {A1} revisited. *Phys. Lett.* **B182 3–4**, 400–404 (1986).

[52] F. Von Hippel and C. Quigg. Centrifugal-barrier effects in resonance partial decay widths, shapes, and production amplitudes. *Phys.Rev.* **D5**, 624–638 (1972).

[53] The ACCMOR Collaboration: C. Daum, L. Hertzberger, W. Hoogland, S. Peters, and P. van Deurzen. Diffractive production of 3π states at 63 and 94 GeV. *Nucl.Phys.* **B182**, 269–336 (1981).

[54] J.L. Basdevant and E. L. Berger. Unitary Coupled-Channel Analysis of Diffractive Production of the a1 Resonance. *Phys.Rev.* **D16**, 657 (1977).

[55] E. Pietarinen. Fixed momentum transfer analysis of pion-nucleon scattering. *Nucl.Phys.* **B107**, 21–44 (1976).

[56] A. Svarc, M. Hadimehmedovi, H. Osmanovi, and J. Stahov. A new method for extracting poles from single-channel data based on Laurent expansion of T-matrices with Pietarinen power series representing the non-singular part. *arXiv:nucl-th* **1212.1295v2** (2012).

Own Contributions

The analysis I performed is based on previous work that is described up to section 4.1. The decomposition in spin-parity states was finished and a first extraction of resonance parameters with six partial waves had been performed, but the usage of the fit program was quite time-consuming and error-prone.

In order to make large scale systematic studies possible I had to create a Python wrapper that automatically created the configuration files and provided, for example, the start parameters. Nearly 700 individual fits later trying out over 40 different models with 13 different release orders for the fit parameters I had to realise that there are a lot of local minima and no single order is able to reliably find the best χ^2. Therefore I implemented a more elaborated search for the global minimum, but with the first successes it became clear that the newly found best χ^2 values often were unphysical. So the major achievement of the first 8 months was to realise that with the employed minimisation method it is simply impossible to find central values with systematic errors for the resonance parameters without performing large-scale studies with random starting values and different release orders as described in section 4.2.

In order to finish these studies in time I had to implement the automatic generation and execution of fits with random starting values. The computing jobs had to be submitted to three completely different computing clusters (E18, CERN, C2PAP), since one single study with 10 000 fits needed roughly a week on 2000 cores. At the end I had to find appropriate criteria to select only the physical solutions.

Acknowledgement

First of all I would like to thank Stephan Paul for giving me the possibility to work on this interesting subject and for always finding the time to discuss the latest results. Furthermore I thank Boris Grube, who seems to know the answer for everything, for plenty of useful advice, guidance and gummy bears. Of course I would also like to thank Florian Haas on the one hand for providing all the ground work needed for this thesis by doing the mass-independent fit and on the other hand for always trying to motivate me, even when nothing seemed to work out. Additionally I thank Dmitri Ryabchikov for providing a lot of knowledge and the fit program as well as implementing quickly all needed new features to it.

Then I would like to thank Karin Frank for handling all the bureaucratic stuff so I was able to concentrate on this thesis. Furthermore I like to thank Christian Dreisbach, Julia Bloemer, Johannes Rauch and Stefan Lietzau for a pleasant atmosphere in our office. Additionally I thank all other persons at E18 that provided ideas, help and an a nice working environment.

Furthermore I acknowledge the support by the DFG Cluster of Excellence "Origin and Structure of the Universe". A large fraction of the systematic studies has been carried out on the computing facilities of the Computational Center for Particle and Astrophysics (C2PAP).

Finally I like to thank my family for always supporting me at whatever I do, so that I can live a life that suits me. Last but not least I thank Katharina Schneider for the last five wonderful years and for the many years, which are hopefully going to come.